

Akademiya Nauk SSSR

NASA
TT
F-558
c.1

A. S. Predvoditelev, Editor

HIGH-TEMPERATURE PROPERTIES OF GASES

Physical Gas Dynamics, Thermodynamics,
and Physics of Combustion



LOAN COPY: RETURN
AFWL (WLQ-2)
KIRTLAND AFB, N MEX

Translated from Russian

Published for the National Aeronautics and Space Administration
and the National Science Foundation, Washington, D.C.
by the Israel Program for Scientific Translations



AKADEMIYA NAUK SSSR · MINISTERSTVO ENERGETIKI I ELEKTR.
Energeticheskii institut im. G.M. Krzhizhanovskogo

Academy of Sciences of the USSR · Ministry of Power and Electrification of the USSR
G.M. Krzhizhanovskii Power Institute

A. S. Predvoditelev, Editor

HIGH-TEMPERATURE PROPERTIES OF GASES

Physical Gas Dynamics, Thermodynamics, and Physics
of Combustion

(Svoistva gazov pri vysokikh temperaturakh: fizicheskaya gazodinamika,
termodinamika i fizika goreniya)

Izdatel'stvo "Nauka"
Moskva 1967

Israel Program for Scientific Translations
Jerusalem 1969

NASA TT F-558
TT 69-55021

Published Pursuant to an Agreement with
THE NATIONAL AERONAUTIC AND SPACE ADMINISTRATION
and
THE NATIONAL SCIENCE FOUNDATION, WASHINGTON, D.C.

Copyright © 1969
Israel Program for Scientific Translations Ltd.
IPST Cat. No. 5437

Translated by A. Barouch
Edited by P. Greenberg

Printed in Jerusalem by IPST Press
Binding: Wiener Bindery Ltd., Jerusalem

Available from the
U.S. DEPARTMENT OF COMMERCE
Clearinghouse for Federal Scientific and Technical Information
Springfield, Va. 22151

Table of Contents

SAMUILOV, E.V. Effect of spherical conducting foreign particles on the electrical conductivity of gases	1
ROZHDESTVENSKII, I.B., V.P.SHEVELEV, and K.K.OLEVINSKII. Calculation of the composition and thermodynamic functions of general reacting gaseous systems	14
ROZHDESTVENSKII, I.B., K.K.OLEVINSKII, and V.P.SHEVELEV. Thermodynamic functions of the combustion products of the system liquid ethyl alcohol—gaseous oxygen	23
TSITELAURI, N.N. Interaction potential of CO molecules	28
GVOZDEVA, L.G. and O.A.PREDVODITELEVA. Parameters of carbon dioxide and nitrogen behind shock waves interacting with a wedge . .	33
NIKOLAEV, G.N. and V.P.POPOV. Nonequilibrium expansion of air in supersonic nozzles	51
NABOKO, I.M. and R.G.NEMKOV. Study of the flow state behind a shock front by means of frame-scan photography	59
NEMKOV, R.G. Effective profile of the Mach line in a relaxing gas	64
POLYAKOV, Yu.A. Shock-tube study of the stagnation-point heat exchange of a blunt body	71
KON'KOV, A.A., A.P.RYAZIN, and V.S.RUDNEV. Experimental study of the spectral properties of air at high temperatures	79
PLASTININ, Yu.A. Spectroscopic investigations of the emission of hot nitrogen	90
BASHILOV, V.A. and V.P.SHEVELEV. Flow structure of ionized gas in an electromagnetic shock tube	98
BASHILOV, V.A. Electron concentration behind a shock front and in a gas-discharge plasma in a magnetohydrodynamic shock tube	105
BAZHENOVA, T.V. and Yu.S.LOBASTOV. Rate of thermal ionization of nitrogen at 3000—5000°K	108
PETROVA, G.P. and E.K.CHEKALIN. Argon plasma flow in a channel with a transverse magnetic field	112
CHEKALIN, E.K. and V.S.SHUMANOV. Radiation of an exploding wire in vacuum	118
CHEKALIN, E.K. and V.S.SHUMANOV. Electric characteristics of an exploding wire in vacuum	122

VYGOVSKII, V.F., E.K.CHEKALIN, and V.S.SHUMANOV. Deformation of solids by an exploding wire	127
PREDVODITELEV, A.S. Ignition theory of two-phase mixtures	129
PREDVODITELEV, A.S. Ignition conditions in combustible gas mixtures . . .	137
SALAMANDRA, G.D. Vibrational flame propagation in a tube	148
SALAMANDRA, G.D. Obtaining color Schlieren photographs of rapid processes using the IAB-451 instrument	153
FEDOSEEVA, N.K. Apparatus for projecting stills	157
ZAITSSEV, S.G., E.V.LAZAREVA, and E.I.CHEBOTAREVA. The boundary layer behind a shock wave in argon and nitrogen	160
NEMKOV, R.G. A delay circuit for triggering shock-tube recording instruments, automatically controlled by the shock-wave velocity .	171
GUSEV, M.V., V.A.GORDYUSHIN, and V.D.LOBANOV. Pulse counting chronometer for shock-velocity measurements	175
GUSEV, M.V., V.D.LOBANOV, and V.A.GORDYUSHIN. An instrument for controlling the high-speed photorecording of the phases of a process	180
EROSHENKO, V.M., A.V.MORAR, and Yu.N.TERENT'EV. Front nature of the reaction surface with the medium	183
EROSHENKO, V.M. and Yu.N. TERENT'EV. The sublimation of solids in a supersonic stream	196
VORONTSOV, Yu.N., V.M.EROSHENKO, A.V.MORAR, and Yu.N. TERENT'EV. A method for visualizing isothermal surfaces	205

EXPLANATORY LIST OF ABBREVIATED NAMES OF U. S. S. R. INSTITUTIONS
AND PERIODICALS APPEARING IN THE BIBLIOGRAPHIES

Abbreviation	Full name (transliterated)	Translation
AN	Akademiya Nauk	Academy of Sciences
DAN	Doklady Akademii Nauk	Transactions of the Academy of Sciences
FIAN	Fizicheskii Institut Akademii Nauk [SSSR]	Physical Institute of the Academy of Sciences [of the USSR]
GEI	Gidroenergeticheskii Institut	Hydropower Institute
GITTL	Gosudarstvennoe Izdatel'stvo Tekhnicheskoi i Teoreti- cheskoi Literatury	State Publishing House of Technical and Theoretical Literature
IL	Izdatel'stvo Inostrannoi Literatury	Foreign Literature Publishing House
NIKFI	Vsesoyuznyi Nauchno- issledovatel'skii kinofotoinstitut	All-Union Scientific Research Institute of Motion Picture and Photography
PMM	Prikladnaya Matematika i mekhanika	[Journal of] Applied Mathe- matics and Mechanics
PMTF	Prikladnaya Mekhanika i Tekhnicheskaya Fizika	[Journal of] Applied Mecha- nics and Technical Physics
PTE	Priory i Tekhnika Eksperimenta	[Journal of] Experimental Instru- ments and Techniques
ZhRFKhO	Zhurnal Russkogo Fiziko- Khimicheskogo Obshchestva	Journal of the Russian Physicochemical Society

ANNOTATION

This collection contains theoretical and experimental investigations of the properties of gas flow at high temperatures, and the thermodynamic functions and physicochemical processes in gases and heterogeneous gas — solid systems. Experimental results regarding the ionization and dissociation of gases and the properties of jets of ionized gases in a magnetic field are presented. A method is outlined for improving the studies of rapid processes.

The collection is intended for scientists and engineers in gas dynamics.

E. V. Samuilov

***EFFECT OF SPHERICAL CONDUCTING FOREIGN
PARTICLES ON THE ELECTRICAL
CONDUCTIVITY OF GASES***

Conducting particles of small radius can be contained as natural impurities in the products of combustion of a solid or gaseous fuel, in high-temperature gas flows interacting destructively with surfaces. Particles are sometimes introduced artificially in the gas to increase its electrical conductivity.

The particles affect the conductivity of the gases as a result of thermal ionization (a considerable admixture of electrons is formed in the gas) and the effect of free electrons on the diffusion process.

It is assumed in what follows that the radius R of the particles is considerably smaller than the average distance r_{av} between electrons, ions, and charged particles.

**1. DYNAMICS OF THE COLLISIONS OF ELECTRONS
WITH THE PARTICLES**

It is assumed that the electron adheres to the particle on reaching its surface. Collisions in which the electron reaches the surface of the particle are termed inelastic, and those in which it does not reach the surface are elastic. The energy $\varphi(r)$ of an electron situated at a distance r from the center of a particle carrying charge Z^*e (Z^* is a positive or negative integer; e is the electron charge) in a fully or partially ionized gas with an admixture of charged particles can be approximated by the expression

$$\varphi(r) = -\frac{Z^*e^2e^{-\kappa(r-R)}}{r(1 + R\kappa)} - \frac{e^2R^2e^{-2\kappa(r-R)}}{2r^2(r^2 - R^2)}, \quad (1)$$

where κ is the Debye shielding constant given by

$$\kappa^2 = 4\pi e^2 \left[\frac{n_e}{kT_e} + \sum_Z \frac{N_Z Z^2}{kT_i} + \sum_{Z^*} \frac{n_{Z^*} Z^{*2}}{kT_p} \right]; \quad (2)$$

n_e is the electron density; N_Z , n_{Z^*} are the ion and particle densities of charges Ze , Z^*e respectively; T_e , T_i , T_p are the respective temperatures of the electrons, ions, and particles; k is the Boltzmann constant.

The first term in $\varphi(r)$ is the electron energy in the shielded Coulomb field of the particle /1/, and the second one the electron energy in the shielded image field /2/. The shielding factor $e^{-2\kappa(r-R)}$ in the second term corresponds to the case of a plane wall /3/. Expression (1) holds only for $r > R$, commencing at $r_0 \simeq R + \delta$, where $\delta = 2 \cdot 10^{-8}$ cm.

As explained below, the calculations involve function (1) near the particle surface, where it can be written in the form

$$\varphi(r) \approx -\frac{Ze^2}{r} - \frac{e^2}{4(r-R)}, \quad (3)$$

and $Z = Z^*/(1 + R\kappa)$. Function (3) will therefore replace (1) in what follows.

For $R \ll r_{av}$ the electron interacting with the particle may be considered as having come from infinity.

Following /4/, the motion of an electron in a field $\varphi(r)$ reduces to the motion of the electron in the effective field

$$\varphi_1(r) = \varphi(r) + M^2/2mr^2, \quad (4)$$

where $M = mbV$ is the moment of momentum of the electron; b is the impact parameter; V is the absolute value of the electron velocity at infinity; m is the electron mass.

The electron reaches the particle surface if

$$\frac{mV^2}{2} \geq \varphi_1(r_m^{(z)}), \quad (5)$$

where $r_m^{(z)}$ is the value of r for which $\varphi_1(r)$ is a maximum in the interval $r_0 \leq r \leq \infty$.

At given electron velocity there corresponds to each Z and R a maximum value of the impact parameter $b_m^{(z)}$ for which the electron becomes incapable of reaching the particle surface. The values of $b_m^{(z)}$ and $r_m^{(z)}$ are determined for given electron velocity from the system of equations

$$\varphi_1(r_m^{(z)}) = \frac{mV^2}{2}; \quad \left. \frac{\partial \varphi_1}{\partial r} \right|_{r=r_m^{(z)}} = 0, \quad (6)$$

which can be represented in the following dimensionless form:

$$\varphi_1^*(p_m) \equiv -\frac{Z}{1+p_m} - \frac{1}{4p_m} + \frac{B_{\max}}{2(1+p_m)^2} = E, \quad (7)$$

$$\Psi(p_m) = 0, \quad (8)$$

where $E = RmV^2/2e^2$; $B_{\max} = M_m^2/Rme^2$; $r_m/R = 1 + p_m$; $\psi(p_m) = 1 + 3p_m + (4Z - 4B_{\max} + 3)p_m^2 + (4Z + 1)p_m^3$.

For $p \geq \delta/R > 0$ ($p + 1 = r/R$), $Z \geq 0$ equation (8) has a solution for $\alpha = 4Z - 4B_{\max} + 3 < 0$. The function $\psi(p)$ then has two extrema at

$$p_{1,2} = -\frac{\alpha}{3(4Z+1)} \mp \sqrt{\left[\frac{\alpha}{3(4Z+1)}\right]^2 - \frac{1}{4Z+1}}. \quad (9)$$

Since $\psi(0) = 1$ and $\psi(\infty) = \infty$ equation (8) has no positive real solutions for $\psi(p_2) > 0$, while for $\psi(p_2) < 0$ two positive roots exist, of which p_m ,

situated in the range $p_1 < p_{m1} \leq p_2$, corresponds to the maximum value of the function φ_1 , and the other one $p_{m2} \geq p_2$ corresponds to its minimum value for $p_{m1} \leq p < \infty$. When $Z \leq -1$ equation (8) has only one positive root for $p_{m1} > p_2$. This root corresponds to the maximum of the function φ_1 .

The minimum value of the energy E_{\min} for which the electron is incident on the particle is as follows:

for $Z \geq 0$

$$E_{\min} = 0, \quad (10)$$

for $Z \leq -1$

$$E_{\min} = -\frac{Z}{1+p_0} - \frac{1}{4p_0}, \quad (11)$$

where

$$p_0 = -(1 + \sqrt{-4Z}) / (1 + 4Z).$$

By solving equation (8) relationships were derived for p_{m1} and p_{m2} as functions of B_{\max} for different Z . The values of $p_{m1} \ll 1$. The dependence of B_{\max} on E for different Z and finite ranges of values of E is approximated by a linear function of the form

$$B_{i,\max} = \alpha_i(Z)E + \beta_i(Z), \quad (12)$$

where $E_i \leq E \leq E_{i+1}$; $i \geq 0$.

Values of α_i, β_i, E_i are given in Table 1. Using these values and the relation

$$\sigma = \pi b_m^{(z)^2} \quad (13)$$

one can calculate the capture cross section of the electrons by the particle.

TABLE 1.

Z	i	E_i	α_i	β_i	Z	i	E_i	α_i	β_i
-10	0	7.09	2.61	-18.5	0	2	1.4	2.9	3.42
-10	1	12	2.38	-15.6	0	3	3	2.73	4.1
-5	0	3.09	4.3	-13.25	0	4	5	2.38	5.6
-5	1	3.32	3.43	-10.4	1	0	0	3.46	5.2
-5	2	3.6	2.82	-8.2	1	1	1	3.05	5.7
-5	3	6.4	2.56	-6.4	1	2	2	2.7	6.33
-5	4	12	2.35	-4	1	3	5	2.45	7.8
-1	0	0.25	5.21	-1.3	1	4	15	2.38	10
-1	1	0.6	3.93	-0.55	5	0	0	2.83	15.55
-1	2	1.2	3.18	0.35	5	1	2	2.57	16
-1	3	2	2.83	1.3	5	2	5	2.4	16.8
-1	4	5	2.63	2.9	5	3	15	2.26	19
-0	0	0	4.75	2.18	10	0	0	2.52	27.5
0	1	0.4	3.59	2.65	10	1	7	2.24	29.7

If, in expression (3), only the Coulomb interaction energy is considered, (12) is replaced by

$$B_{\max} = 2E + 2Z, \quad (14)$$

where $E_{\min} = 0$ for $Z \geq 0$, and $E_{\min} = -Z$ for $Z < 0$.

We shall calculate the number of electrons with velocities between \mathbf{V} and $\mathbf{V} + d\mathbf{V}$ incident per unit time on the particle. According to [5]

$$dN_{\text{inc}} = f(\mathbf{V}) V b db d\varepsilon dV, \quad (15)$$

where ε is the azimuthal angle; $f(\mathbf{V})$ is the distribution function of the electrons, normalized with respect to the number of electrons per unit volume:

$$n_e = \int f(\mathbf{V}) dV. \quad (16)$$

Only those electrons whose velocity and impact parameter satisfy condition (5) reach the particle surface. For the quasistationary state $T_e \neq T_p \neq T_i$ we have

$$f = n_e \left(\frac{m}{2\pi k T_e} \right)^{3/2} e^{-\frac{mV^2}{2kT_e}}. \quad (17)$$

For complete equilibrium

$$f \equiv f^{(0)} = n_e \left(\frac{m}{2\pi k T} \right)^{3/2} e^{-\frac{mV^2}{2kT}}. \quad (18)$$

Writing dV in spherical coordinates and transforming to the variables

$$M = mbV, \quad V = V, \quad (19)$$

expression (15) becomes

$$dN_{\text{inc}} = \frac{f}{m^2} VM dM dV d\varepsilon d\varepsilon^* \sin \theta d\theta, \quad (20)$$

where ε^*, θ are the angles in the spherical system of coordinates.

Transforming further to dimensionless variables

$$B = \frac{M^2}{mRe^2} \quad \text{and} \quad E = \frac{mV^2}{2} \frac{R}{e^2},$$

expression (20) takes the form

$$dN_{\text{inc}} = \frac{e^2}{2m^2} f \sin \theta d\theta d\varepsilon d\varepsilon^* dB dE. \quad (21)$$

Condition (5) has the following form in terms of the variables B, E :

$$E \geq -\frac{Z}{1+p} - \frac{1}{4p} + \frac{B}{2(1+p)^2} \equiv \Phi_1^*(p). \quad (22)$$

With the aid of (21), (22), (17), one may derive by integration the total number of electrons incident on the particle per unit time:

$$N_{\text{inc}} = n_e \frac{4\pi^2 e^4}{m^2} \left(\frac{m}{2\pi k T_e} \right)^{1/2} \int_{E_{\text{min}}}^{\infty} B_{\text{max}} e^{-x_e E} dE, \quad (23)$$

where E_{min} is selected according to (10) or (11); $x_e = e^2/RkT_e$.

In subsequent calculations we use the angle of deviation χ_z of the electrons during elastic collisions with the particle. This yields /5/

$$\chi_z = \pi - 2 \int_{r_{\text{min}}}^{\infty} \frac{b \frac{dr}{r^2}}{\sqrt{1 - \frac{b^2}{r^2} - \frac{2}{mV^2} \Phi(r)}}, \quad (24)$$

where r_{min} is the minimum distance between the electron and the particle during collision (the maximum positive root of the equation

$$1 - \left(\frac{b}{r}\right)^2 - \frac{2}{mV^2} \Phi(r) = 0).$$

The angle of deviation for the potential (1) can only be calculated numerically. For the potential (3) the expression for χ_z can be reduced to an elliptic integral. In terms of the variables E , B , $y = R/r$, expression (3) can be used to transform integral (24) to the form

$$\chi_z = \pi - 2 \sqrt{2B} \int_0^{y_2} \sqrt{\frac{1-y}{\Phi(y)}} dy, \quad (25)$$

where $\Phi(y) \equiv 4E - (4E - 4Z - 1)y - (2B + 4Z)y^2 + 2By^3$; y_2 is the minimum positive root of the equation

$$\Phi(y) = 0. \quad (26)$$

The angle of deviation χ for elastic collisions must be calculated for $B > B_{\text{max}}$. Equation (26) then has three roots, satisfying the inequality

$$1 > y_3 > y_2 > 0 > y_1. \quad (27)$$

Using (27), $\Phi(y)$ can be written in the form

$$\Phi(y) = (y - y_1)(y_2 - y)(y_3 - y). \quad (28)$$

Following /6/, integral (25) then equals

$$\chi_z = \pi - \frac{4\sqrt{2B}}{\sqrt{(1-y_2)(y_3-y_1)}} \left[(y_3 - y_2) \Pi\left(\gamma, \frac{y_2 - y_1}{y_3 - y_1}, r\right) + (1 - y_3) F(\gamma, r) \right], \quad (29)$$

where $\Pi(\varphi, n, k)$ is an elliptic integral of the third kind; $F(\varphi, k)$ is an elliptic integral of the first kind;

$$\gamma = \arcsin \sqrt{\frac{(y_3 - y_1)y_2}{(y_2 - y_1)y_3}}; \quad (30)$$

$$r = \sqrt{\frac{(1-y_3)(y_2-y_1)}{(1-y_2)(y_3-y_1)}}. \quad (31)$$

If only the first term is taken into account in (3), then

$$\chi_z = 2 \arcsin \frac{1}{\sqrt{1 + \frac{2EB}{Z^2}}}. \quad (32)$$

2. THERMIONIC EMISSION OF ELECTRONS FROM THE SURFACE OF THE PARTICLES

The number of electrons with velocities between \mathbf{U} and $\mathbf{U} + d\mathbf{U}$ emitted from the surface of a particle per unit time as a result of thermal ionization is equal to

$$dN_{\text{em}} = 4\pi r_0^2 \alpha \frac{2m^3}{h^3} \left[1 + e^{\frac{1}{kT_p} \left(\frac{mU^2}{2} + \Phi^* \right)} \right]^{-1} U_z d\mathbf{U}, \quad (33)$$

where \mathbf{U} is the electron velocity at distance δ from the particle surface; $U = |\mathbf{U}|$; U_z is the component of velocity \mathbf{U} along the z axis (the z axis is normal to the particle surface); h is Planck's constant; Φ^* is the work function, including the work to move the electron a distance δ from the particle surface; α is the surface efficiency coefficient.

For $\Phi^* \geq (3-4)kT_p$ one may neglect the one in the square brackets of expression (33). This expression then reduces to

$$dN_{\text{em}} = 4\pi r_0^2 \alpha \frac{2m^3}{h^3} e^{-\frac{1}{kT_p} \left(\frac{mU^2}{2} + \Phi^* \right)} U_z d\mathbf{U}. \quad (34)$$

The electron, on overcoming the potential barrier Φ^* , will leave the particle if

$$\frac{mU^2}{2} + \Phi(r_0) \geq \Phi_1(r_m^{(z)}). \quad (35)$$

The relationship

$$U_z d\mathbf{U} = U_z U^2 \sin \theta d\theta d\varepsilon dU = U^3 \cos \theta \sin \theta d\theta d\varepsilon dU \quad (36)$$

is valid, where θ, ε are the angles of the spherical system of coordinates whose axis z lies normal to the particle surface.

Transforming to the variables

$$M = U \sin \theta r_0 m, \quad U = U, \quad (37)$$

(36) becomes

$$\frac{U M}{(r_0 m)^2} dU dM d\varepsilon. \quad (38)$$

In terms of the variables V^2, M^2, ε , where $\frac{mV^2}{2} = \frac{mU^2}{2} + \varphi(r_0)$, (38) has the form

$$\frac{1}{4(r_0 m)^3} dV^2 dM^2 d\varepsilon. \quad (39)$$

After another transformation to the variables B and E (39) becomes

$$\frac{e^4}{2(r_0 m)^3} dB dE d\varepsilon. \quad (40)$$

As a result, (34) and (35) are replaced, respectively, by

$$dN_{\text{em}} = 4\pi\alpha e^4 \frac{m}{h^3} e^{-\frac{1}{kT} \left(\frac{mV^2}{2} + \Phi^* - \varphi(r_0) \right)} dB dE d\varepsilon; \quad (41)$$

$$E \geq \Phi_1^*(p). \quad (42)$$

From (41) it is easy to derive an expression for the number of electrons emitted from the particle surface in the solid angle $\sin \theta d\theta d\varepsilon/4\pi$:

$$\Delta dN_{\text{em}} = \alpha e^4 \frac{m}{h^3} e^{-\frac{1}{kT} \left(\frac{mV^2}{2} + \Phi^* - \varphi(r_0) \right)} \sin \theta d\theta d\varepsilon d\varepsilon^* dB dE. \quad (43)$$

From (15) and (21) we obtain

$$\sin \theta d\theta d\varepsilon d\varepsilon^* dB dE = \frac{2m^2}{e^4} Vb db d\varepsilon dV. \quad (44)$$

Therefore, (43) can be written in the form

$$\Delta dN_{\text{em}} = \alpha \frac{2m^3}{h^3} e^{-\frac{1}{kT} \left(\frac{mV^2}{2} + \Phi^* - \varphi(r_0) \right)} Vb db d\varepsilon dV. \quad (45)$$

From (42) and (41) we obtain

$$N_{\text{em}} = \alpha \frac{8\pi^2 m e^4}{h^3} e^{-\frac{\Phi^* - \varphi(r_0)}{kT}} \int_{E_{\text{min}}}^{\infty} B_{\text{max}} e^{-x_p E} dE, \quad (46)$$

where E_{min} is selected according to (10) or (11); $x_p = e^2/RkT_p$.

3. LAW OF MASS ACTION

If the particle charge varies only as a result of thermionic emission and the incidence of electrons on the particle, the following balance relation will be satisfied in the quasistationary case for $T_e \neq T_i \neq T_p$:

$$n_{Z+1} N_{\text{inc}}(Z+1) - n_Z N_{\text{inc}}(Z) = n_Z N_{\text{em}}(Z+1) - n_{Z-1} N_{\text{em}}(Z). \quad (47)$$

From (23), (46), (47) we obtain the following expression for the law of mass action:

$$n_e = 2\alpha \left(\frac{2\pi m k T_p}{h^2} \right)^{3/2} \frac{x_e}{x_p} e^{-\frac{\Phi^*}{k T_p}} \frac{n_Z e^{\frac{\varphi(r_0, Z+1)}{k T_p}} S(Z+1, x_p) - n_{Z-1} e^{\frac{\varphi(r_0, Z)}{k T_p}} S(Z, x_p)}{n_{Z+1} S(Z+1, x_e) - n_Z S(Z, x_e)}, \quad (48)$$

where

$$\frac{S(Z, x)}{x} = \int_{E_{\min}}^{\infty} B_{\max} e^{-xE} dE.$$

When $x_p = x_e$ expression (48) reduces to the known expression for the law of mass action for the ionization reaction. Using (12), the expression for $S(Z, x)$ becomes, after integration,

$$S(Z, x) = \sum_i \left(\frac{\alpha_i f_{\alpha}^{(i)}}{x} + \beta_i f_{\beta}^{(i)} \right), \quad (49)$$

where

$$f_{\alpha}^{(i)} = e^{-xE_i} [xE_i + 1 - e^{-x(E_{i+1}-E_i)}(xE_{i+1} + 1)];$$

$$f_{\beta}^{(i)} = e^{-xE_i} [1 - e^{-x(E_{i+1}-E_i)}].$$

If in expression (3) we take into account only the Coulomb interaction energy, we obtain the following with the aid of (14):
for $Z \geq 0$

$$S(Z, x) = \frac{2}{x} (1 + Zx);$$

for $Z \leq -1$

$$S(Z, x) = \frac{2}{x} e^{xZ}.$$

4. ELECTRON DISTRIBUTION FUNCTION

The Boltzmann equation for the electron distribution function has the form /5/

$$\frac{\partial f}{\partial t} + \mathbf{v} \frac{\partial f}{\partial \mathbf{r}} + \frac{e\mathbf{E}}{m} \frac{\partial f}{\partial \mathbf{v}} = \sum_{\alpha} \left(\frac{\partial f}{\partial t} \right)_{\alpha} + \sum_Z \left[\left(\frac{\partial f}{\partial t} \right)_{(Z-1)\text{em}} + \left(\frac{\partial f}{\partial t} \right)_{Z\alpha} + \left(\frac{\partial f}{\partial t} \right)_{Z\gamma} \right] + \left(\frac{\partial f}{\partial t} \right)_e, \quad (50)$$

where \mathbf{v} is the electron velocity; \mathbf{r} is the radius vector; \mathbf{E} is the electric field strength; $\left(\frac{\partial f}{\partial t} \right)_{\alpha}$, $\left(\frac{\partial f}{\partial t} \right)_e$, $\left(\frac{\partial f}{\partial t} \right)_{(Z-1)\text{em}}$, $\left(\frac{\partial f}{\partial t} \right)_{Z\alpha}$, $\left(\frac{\partial f}{\partial t} \right)_{Z\gamma}$ are the variations in the distribution function per unit time produced respectively by elastic collisions with atoms of ions of type α , electron-electron collisions,

thermionic emission of electrons from the surface of particles with effective charge $(Z-1)e$, inelastic collisions of electrons with particles of effective charge Ze , and elastic collisions of electrons with particles of effective charge Ze .

Inelastic collisions of the electrons with atoms or ions are not taken into account, since their relative weight is small for low values of E .

The following calculations are realized under the assumption $T_e = T_i = T_p = T$.

Using (45) and (15) (according to /5/), and taking into account that the mass of particle, atom, or ion $\mu \gg m$, we can write

$$\left(\frac{\partial f}{\partial t}\right)_{Zu} = -n_Z \int_0^{b_m^{(Z)}} \int_0^{2\pi} f V b db d\epsilon, \quad (51)$$

$$\left(\frac{\partial f}{\partial t}\right)_{Zv} = n_Z \int_0^{b_m^{(Z)}} \int_0^{2\pi} (f' - f) V b db d\epsilon, \quad (52)$$

$$\left(\frac{\partial f}{\partial t}\right)_{(Z-1)em} = n_{Z-1} \alpha \frac{2m^3}{\hbar^3} e^{-\frac{1}{kT} \left(\frac{mV^2}{2} + \Phi^* - \varphi(r_0) \right)} \int_0^{b_m^{(Z)}} \int_0^{2\pi} V b db d\epsilon, \quad (53)$$

$$\left(\frac{\partial f}{\partial t}\right)_* = n_* \int_0^\infty \int_0^{2\pi} (f' - f) V b db d\epsilon. \quad (54)$$

The quantity $\left(\frac{\partial f}{\partial t}\right)_e$ has the usual form

$$\left(\frac{\partial f}{\partial t}\right)_e = \iiint (f_1 f' - f_1 f) g b db d\epsilon dV_1. \quad (55)$$

In expressions (52), (54), (55) $f' \equiv f(V')$, where V' is the velocity of the electron relative to the particle after an elastic collision with it.

The solution of the Boltzmann equation (50) is taken in the form

$$f = f^{(0)}(1 + \Phi).$$

Under the assumptions made relative to the distribution function f , the left member of equation (50) can be written in the following form, using the standard transformation procedure /5/ of the kinetic theory of gases:

$$f^{(0)} \left[\frac{n}{n_e} (\mathbf{V} \mathbf{d}) + \left(b_e : \frac{\partial}{\partial \mathbf{r}} \mathbf{v}_0 \right) - \left(\frac{5}{2} - \frac{mV^2}{2kT} \right) \left(\mathbf{V} \frac{\partial \ln T}{\partial \mathbf{r}} \right) \right], \quad (56)$$

where

$$\mathbf{d} = \frac{\partial}{\partial \mathbf{r}} \left(\frac{n_e}{n} \right) + \left(\frac{n_e}{n} - \frac{n_e m}{\rho} \right) \frac{\partial \ln p}{\partial \mathbf{r}} - \frac{n_e m}{\rho p} \left[\frac{\rho}{m} e \mathbf{E} - \sum_Z n_Z Z e \mathbf{E} \right]; \quad (57)$$

b_e is a tensor; p is the total pressure; ρ is the density; n is the total number of particles per unit volume.

The sum of the integrals of the inelastic collisions in the left member of equation (50) is transformed to the form

$$\begin{aligned} & \sum_Z \left[\left(\frac{\partial f}{\partial t} \right)_{(Z-1)em} + \left(\frac{\partial f}{\partial t} \right)_{ZII} \right] = \\ & = \sum_Z \left\{ \left[2\alpha \left(\frac{2\pi m}{h^2} \right)^{3/2} (kT)^{3/2} e^{-\frac{\Phi^* - \Phi(r_0)}{kT}} - \frac{n_Z n_e}{n_{Z-1}} \right] n_{Z-1} f^{(0)} \int_0^{b_m^{(Z)}} \int_0^{2\pi} V b db d\epsilon - n_Z \int_0^{b_m^{(Z)}} \int_0^{2\pi} f^{(0)} \Phi V b db d\epsilon \right\}. \end{aligned} \quad (58)$$

The expression in brackets vanishes by the law of mass action. Therefore

$$\begin{aligned} & \sum_Z \left[\left(\frac{\partial f}{\partial t} \right)_{(Z-1)em} + \left(\frac{\partial f}{\partial t} \right)_{ZII} + \left(\frac{\partial f}{\partial t} \right)_{ZII'} \right] = \\ & = \sum_Z \left\{ -n_Z \int_0^{b_m^{(Z)}} \int_0^{2\pi} f^{(0)} \Phi V b db d\epsilon + n_Z \int_{b_m^{(Z)}}^{\infty} \int_0^{2\pi} f^{(0)} (\Phi' - \Phi) V b db d\epsilon \right\}. \end{aligned} \quad (59)$$

The collision integrals (54), (55) are transformed to

$$\left(\frac{\partial f}{\partial t} \right)_\alpha = n_\alpha \int_0^{\infty} \int_0^{2\pi} f^{(0)} (\Phi' - \Phi) V b db d\epsilon, \quad (60)$$

$$\left(\frac{\partial f}{\partial t} \right)_e = \iiint f_1^{(0)} f^{(0)} (\Phi_1' + \Phi' - \Phi_1 - \Phi) g b db d\epsilon d\mathbf{V}_1. \quad (61)$$

In accordance with the form (56) the solution of the integral equation for Φ may be represented as

$$\Phi = -A \frac{\partial \ln T}{\partial \mathbf{r}} - B_e : \frac{\partial}{\partial \mathbf{r}} \mathbf{v}_0 + n C d, \quad (62)$$

where A, B_e, C are functions of the velocity, local composition of the mixture, and temperature.

In particular

$$C = W C(W^2), \quad (63)$$

where $W^2 = mV^2/2kT$.

To calculate the electrical conductivity the function C must be determined. Substituting (62) in (59), (60), (61), and replacing the left member of (50) by (56) and rewriting the right member of (50) with the aid of (59)–(61), we obtain an integral equation for the function C :

$$-\frac{4}{n_e} \mathbf{V} f^{(0)} = C Q_1(V) + C Q_2(V) + \iiint f_1^{(0)} f^{(0)} (C_1 + C - C_1' - C') g b db d\epsilon d\mathbf{V}_1, \quad (64)$$

where

$$Q_1(V) = 2\pi f^{(0)} \sum_{\alpha} n_{\alpha} \int_0^{\infty} (1 - \cos \chi_Z) V b db; \quad (65)$$

$$Q_2(V) = 2\pi f^{(0)} \sum_Z n_Z \left\{ \int_0^{\infty} (1 - \cos \chi_Z) V b db + \int_0^{b_m^{(Z)}} V b db \right\}. \quad (66)$$

Following /5/, equation (64) can be solved by a variational method. To that end we represent C in terms of Sonin's polynomials $S_{3/2}^{(m)}(W^2)$ as follows:

$$C = W \sum_{m=0}^{\xi-1} C_m(\xi) S_{3/2}^{(m)}(W^2), \quad (67)$$

where $C_m(\xi)$ are the coefficients of expansion which must be determined.

Omitting the details of solving equation (64) by the variational method /5/, we give the final system of linear algebraic equations from which the coefficients $C_m(\xi)$ can be determined:

$$R^m + \sum_{m'=0}^{\xi-1} C_m(\xi) Q^{m',m} = 0, \quad m = 0; 1; \dots; \xi-1, \quad (68)$$

where

$$R^m = \frac{1}{n_e} \int W V f^{(0)} S_{3/2}^{(m)}(W^2) dV; \quad (69)$$

$$Q^{m',m} = Q_1^{m',m} + Q_2^{m',m} + Q_e^{m',m}; \quad (70)$$

$$Q_{1,2}^{m',m} = \int W^2 S_{3/2}^{(m)}(W^2) S_{3/2}^{(m')}(W^2) Q_{1,2}(V) dV; \quad (71)$$

$$Q_e^{m',m} = n_e^2 [W S_{3/2}^{(m')}(W^2), W S_{3/2}^{(m)}(W^2)]_1. \quad (72)$$

The expression in brackets represents the known integral operator of the kinetic theory of gases, whose meaning is explained in /5/. When calculating $Q_2^{m',m}$ one should bear in mind that the limits of integration with respect to V must be selected to be consistent with E_{\min} in (10) or (11). Hence,

$$\begin{aligned} Q_2^{m',m} = & n_e R^2 \left(\frac{2\pi kT}{m} \right)^{1/2} x^3 \times \\ & \times \left\{ \sum_{Z \geq 0} n_Z \int_0^{\infty} e^{-xZ} E S_{3/2}^{(m)}(xE) S_{3/2}^{(m')}(xE) \left(B_{\max}^{(Z)} + \int_{B_{\max}^{(Z)}}^{\infty} [1 - \cos \chi_Z] dB \right) dE + \right. \\ & + \sum_{Z < 0} n_Z \left[\int_{E_{\min}}^{\infty} e^{-xZ} E S_{3/2}^{(m)}(xE) S_{3/2}^{(m')}(xE) \left(B_{\max}^{(Z)} + \int_{B_{\max}^{(Z)}}^{\infty} [1 - \cos \chi_Z] dB \right) dE + \right. \\ & \left. \left. + \int_0^{E_{\min}} \int_0^{\infty} e^{-xZ} E (1 - \cos \chi_Z) S_{3/2}^{(m)}(xE) S_{3/2}^{(m')}(xE) dB dE \right] \right\}, \quad (73) \end{aligned}$$

where $x = e^2/RkT$.

5. ELECTRICAL CONDUCTIVITY

The current density is

$$\mathbf{j} = n_e e \bar{\mathbf{V}}, \quad (74)$$

where $\bar{\mathbf{V}} = \frac{1}{n_e} \int \mathbf{V} d\mathbf{V}$. Using (57), (62), (67), we obtain for the ohmic component of the current density

$$\mathbf{j} = -\frac{1}{2} \frac{n_e n_s^2}{p} \left(\frac{2kT}{m} \right)^{1/2} e^2 C_0(\xi) \mathbf{E} \equiv \vartheta(\xi) \mathbf{E}. \quad (75)$$

The expression for the conductivity ϑ can be obtained in a first approximation by calculating $C_0(\xi)$. This results in

$$\vartheta^{(1)} = \frac{3}{8} \frac{n_e e^2}{p} \left(\frac{kT}{2\pi m} \right)^{1/2} \left(\sum_{\alpha} x_{\alpha} \Omega_{\alpha}^{(1,1)*} \sigma_{\alpha}^2 + \sum_Z x_Z \Omega_Z^{(1,1)*} R^2 \right)^{-1}, \quad (76)$$

where $x_{\alpha} = n_{\alpha}/n$; $x_Z = n_Z/n$; σ_{α} is a characteristic parameter of the interaction potential of the electron with the particle α , having the dimension of length;

$$\Omega_Z^{(1,1)*} = \frac{x^3}{4} \int_0^{\infty} e^{-xZ} E \left(B_{\max}^Z + \int_{B_{\max}^{(Z)}}^{\infty} [1 - \cos \chi_Z] dB \right) dE, \quad Z \geq 0; \quad (77)$$

$$\begin{aligned} \Omega_Z^{(1,1)*} &= \frac{x^3}{4} \left\{ \int_{E_{\min}}^{\infty} e^{-xZ} E \left(B_{\max}^{(Z)} + \int_{B_{\max}^{(Z)}}^{\infty} [1 - \cos \chi_Z] dB \right) dE + \right. \\ &\quad \left. + \int_0^{E_{\min}} \int_0^{\infty} e^{-xZ} [1 - \cos \chi_Z] E db dE \right\}, \quad Z < 0; \end{aligned} \quad (78)$$

$\Omega_{\alpha}^{(1,1)*}$ is the integral of the collisions of the electrons with atoms or ions of type α having the usual form /5/.

We shall calculate $\Omega_Z^{(1,1)*}$, retaining only the first term in (3). Using (14), (32), (77), and (78), we obtain

$$\Omega_Z^{(1,1)*} = 1 + \frac{Zx}{2} + \frac{(Zx)^2}{4} \ln \frac{(Zx)^2 + 16}{(Zx)^2 + 8Zx + 16}, \quad Z \geq 0; \quad (79)$$

$$\begin{aligned} \Omega_Z^{(1,1)*} &= \frac{1}{2} [xE_{\min} (xE_{\min} + 2) + 2] e^{-xE_{\min}} + \frac{Zx}{2} (xE_{\min} + 1) e^{-xZ} + \\ &+ \frac{(Zx)^2}{4} \left\{ \ln \left(1 + \frac{16}{(Zx)^2 (\kappa R)^2} \right) - e^{-xE_{\min}} \ln \left(1 + \frac{8}{Zx} + \frac{16}{(Zx)^2} \right) \right\}, \quad Z < 0. \end{aligned} \quad (80)$$

When calculating the integrals with respect to E the value of E under the \ln sign is replaced by $2/x$, as is usual in /5/. For $Zx \sim 1$ all the terms in expressions (79)–(80) are of the same order of magnitude.

If electrons are produced only by the thermal ionization of the particles, then for $n_e \simeq 0.3 n_s$ (n_s is the saturation number of electrons per unit volume) $Zx \simeq 1$, for $n_e = n_s$ $Zx \ll 1$, for $n_e \ll n_s$ $Zx \gg 1/7$.

In conclusion estimates of the magnitudes figuring in (76) are given. For Argon, according to [8], $\sum_a x_a \Omega_x^{(1,1)*} \sigma_x^2 \simeq 10^{-17} \text{ cm}^2$; therefore for $n_e = 10^{12} \text{ cm}^{-3}$, $R = 10^{-5} \text{ cm}$, $p = 1 \text{ atm}$ and $T = 2000^\circ \text{ K}$ we have $\sum x_z \Omega_z^{(1,1)*} R^2 \simeq 10^{-17} \text{ cm}^2$.

Bibliography

1. Semenchenko, V.K. Fizicheskaya teoriya rastvorov (Physical Theory of Solutions).—Moskva-Leningrad, Gostekhizdat. 1941.
2. Landau, L.D. and E.M. Lifshits. Electrodynamics of Continuous Media.—Pergamon Press, Oxford. 1960.
3. Buff, F.P. and F.H. Stillinger. Surface Tension of Ionic Solution.—J. Chem. Phys., 25(2):312—318. 1956.
4. Landau, L.D. and E.M. Lifshits. Mechanics.—Pergamon Press, Oxford. 1960.
5. Herschfelder, J., C. Curtiss, and R. Bird. Molecular Theory of Gases and Liquids.—John Wiley and Sons, New York. 1949.
6. Gradshtein, I.S. and I.M. Ryzhik. Tablitsy integrallov, summ, ryadov i proizvedenii (Tables of Integrals, Sums, Series and Products).—Moskva, Gosudarstvennoe Izdatel'stvo Fiziko-Matematicheskoi Literatury. 1963.
7. Williams, H., J.D. Lewis, and R.M. Hobson. The Influence of Thermal Ionization Processes on the Design of a Fossil Fuelled MHD Power Generator.—In "Advanced Magnetohydrodynamics." Oxford-London-N.Y.-Paris, Pergamon Press. pp. 65—78. 1963.
8. Pack, J.Z. and A.V. Phelps. Drift Velocities of Slow Electrons in Helium, Neon, Argon, Hydrogen and Nitrogen.—Phys. Rev., Vol. 121, No. 3. 1961.

I. B. Rozhdestvenskii, V. P. Shevelev, K. K. Olevinskii

**CALCULATION OF THE COMPOSITION AND THERMO-
DYNAMIC FUNCTIONS OF GENERAL
REACTING GASEOUS SYSTEMS**

The thermodynamic functions of ideal reacting gaseous systems at high temperatures can be calculated by the methods of statistical physics /1/.

In the range of temperatures and pressures met in combustion chambers, in the nozzles of MHD-generators, and behind shock waves, the thermodynamic functions can be calculated with sufficient accuracy by assuming that the gas is ideal. This assumption is also useful in extreme cases, since it is possible to introduce in the resulting values corrections allowing for the nonideality /2, 3/. We shall accordingly consider below a chemically reacting gas in an ideal state.

Data on the thermodynamic functions of pure components are given in several sources /4-6/.

The calculation of the composition is linked with considerable difficulties in view of its nonlinear dependence on the thermodynamic parameters of the system.

The simplification of the computing model by means of neglecting various components can lead to considerable errors. This simplification is particularly undesirable when estimating the degree of ionization of negligible admixtures and in many problems of chemical kinetics. Calculations have shown /7/ that the optimum amounts of easily ionized admixtures, giving maximum conductivity, do not exceed several per cent. Thus, when determining the electron fraction one must account for all the possible reactions of ionization and the formation of negative ions of negligible admixtures.

By an arbitrary gaseous system is understood a system consisting of k types of atoms (including electrons) and i different components. The numbers i and k are arbitrary. In such a system there can take place $i-k$ reversible reactions of dissociation, ionization of arbitrary order, and formation of negative ions, likewise of arbitrary order. The component i can contain an arbitrary number of atoms of type k . For such a system it is possible to write $k-1$ equations of material balance, one equation of charge conservation (equation of matter balance for the electrons) and a norming condition (the Dalton law). These equations are completed by $i-k$ equations of the law of mass action.

This system has been solved by numerous authors. In /8/ the equations of chemical equilibrium were established in a symmetrical form, from which much data was derived /9, 10/.

In this paper we derive a more general notation of the system of equations of chemical equilibrium, on which the mathematical model rests. At the

end of the paper examples are considered of realizing this model in a three-address computer.

1. THE EQUATIONS OF CHEMICAL EQUILIBRIUM

The equations of chemical equilibrium have (in the approximation considered) the form

$$\sum_i x_i - 1 = 0, \quad (1)$$

$$\sum_i A_{ij}x_i - C_{jk-1} \sum_i A_{ijk-1}x_i = 0, \quad (2)$$

$$\sum_i A_{ijk}x_i = 0, \quad (3)$$

$$\prod_i x_i^{v_{is}} = K_{p_s} p^{-\sum_i v_{is}}, \quad (4)$$

where x_i is the molar fraction of component i ; A_{ij} is an element of the matrix of stoichiometric coefficients; C_{jk-1} is a material constant, equal to the ratio of the number of atoms of type j to the number of atoms of type $k-1$; K_{p_s} is the equilibrium constant at constant pressure; v_{is} are the stoichiometric coefficients in reaction s . The index j takes values from 1 to $k-2$.

The solution of system (1)–(4) presents some difficulties in view of its nonlinearity. One of the methods for solving it consists in eliminating $i-k$ unknowns in (1)–(3) with the aid of (4), and then applying Newton's method [1] to the nonlinear system of k equations. Different possibilities exist involving various difficulties, e.g., the convergence of the method of successive approximations, the selection of the independent variables, etc.

We selected a method by means of which this system can be solved by orientation on any set of k independent components from the whole set i .

The composition of the general i -th component $[x_i]$ of the reacting mixture can be represented in the form

$$[x_i] = A_{i1}e_1 + A_{i2}e_2 + \dots + A_{ik}e_k = \sum_k A_{ik}e_k, \quad (5)$$

where e_k is a symbol designating the type of atom k , and A_{ik} is the number of given atoms in the i -th component (in all there are $k-1$ types of atoms; the last index k always corresponds to electrons).

It is likewise possible to expand $[x_i]$ not only with respect to all the atoms entering the mixture composition, but also with respect to $k-1$ molecular components selected in some specific way. The molecular symbols are designated by e'_k . Then

$$[x_i] = \sum'_k \Phi_{ik}e'_k. \quad (6)$$

Thus, all the components allowed for in the calculation are represented by the matrices $\|A_{ik}\|$ or $\|\Phi_{ik}\|$. Expression (5) corresponds to the orientation of (1)–(3) on atoms, and expression (6) to the orientation on molecules. The transition from one orientation to the other is realized by the laws of

linear algebra, where $[x_i]$ is regarded as a vector in the space of base e'_k or e_k .

To that end we select the matrix* $\|A_{ik}\|$ containing initial information on the composition.

In order to transform to a general $\|\Phi_{ik}\|$ one must find the transformation matrix $\|B_{ik}\|$, which is the inverse of the transposed matrix consisting of the coefficients A_{ik} for any base e'_k in the space of base e_k . It is only necessary that the molecules forming e'_k contain at least once any atom e_k and not be a linear combination of each other (such as O_2 and O).

We shall give an example of such a transformation. Take three types of atoms O , N , C , and e^- , and consider the combinations CO_2 , CO , N_2 , N_2O^+ , C_2N_2 , e^- . The matrix $\|A_{ik}\|$ will have respectively the following form for them:

$$\|A_{ik}\| = \begin{array}{c|c} & \begin{array}{c} O \quad N \quad C \quad e^- \end{array} \\ \hline \begin{array}{c} CO_2 \\ CO \\ N_2 \\ N_2O^+ \\ C_2N_2 \\ e^- \end{array} & \begin{array}{cccc} 2010 & & & \\ 1010 & & & \\ 0200 & & & \\ 120 & -1 & & \\ 0220 & & & \\ 0001 & & & \end{array} \end{array}$$

Take now as e'_1, e'_2, e'_3, e'_4 respectively CO_2 , CO , N_2 and e^- .

The transformation matrix $\|B_{ik}\|$ is then found from the matrix

$$\begin{array}{c} \left| \begin{array}{c} 2010 \\ 1010 \\ 0200 \\ 0001 \end{array} \right| \end{array}$$

This matrix** is now transposed and its inverse found:

$$\|B_{ik}\| = \begin{array}{c|c} & \begin{array}{cc} 10 & -10 \end{array} \\ \hline \begin{array}{c} -10 \\ 0 \\ 0 \\ 0 \end{array} & \begin{array}{cc} 20 & 00 \\ \frac{1}{2} & 00 \\ 00 & 01 \end{array} \end{array}$$

The elements of Φ_{ik} for N_2O^+ are hence found as

$$\Phi_{N_2O^+, 1} = 1 \times 1 + 0 \times 2 + (-1) \times 0 + 0 \times (-1) = 1,$$

$$\Phi_{N_2O^+, 2} = (-1) \times 1 + 0 \times 2 + 2 \times 0 + 0 \times (-1) = -1,$$

$$\Phi_{N_2O^+, 3} = 0 \times 1 + \frac{1}{2} \times 2 + 0 \times 0 + 0 \times (-1) = 1,$$

$$\Phi_{N_2O^+, 4} = 0 \times 1 + 0 \times 2 + 0 \times 0 + 1 \times (-1) = -1.$$

For C_2N_2 Φ_{ik} is similarly determined, $k = -2, 4, 1, 0$.

Thus, the components of any vector i , written in the space e_k , are transformed uniquely into components of this vector in the space e'_k by

* A matrix corresponding to an arbitrary orientation could be selected here.

** The determinant of this matrix is nonzero (-2) , i. e., the matrix is nondegenerate.

multiplying these vectors by the matrix $\|B_{ik}\|$. The latter can easily be found with the aid of the adjoint of the matrix $\|A_{ik}\|_{e_k}$, i.e., the matrix formed of the coefficients A_{ik} in the space e_k :

$$\|B_{ik}\| = \frac{1}{d} \|A_{ik}\|_{e_k}^* \quad (7)$$

where $\|A_{ik}\|_{e_k}^*$ is the adjoint matrix, and d is the determinant of the matrix $\|A_{ik}\|_{e_k}$.

With the aid of the matrices $\|A_{ik}\|$ or $\|\Phi_{ik}\|$ the fraction of an arbitrary component x_i is written as follows on the strength of the law of mass action:

$$x_i = K_{p_{iA}} \rho^{\sum_k A_{ik} - 1} \prod_k x_k^{A_{ik}}, \quad (8)$$

or

$$x_i = K_{p_{i\Phi}} \rho^{\sum_k \Phi_{ik} - 1} \prod_k x_k^{\Phi_{ik}}. \quad (9)$$

The quantities $K_{p_{iA}}$ and $K_{p_{i\Phi}}$ represent the equilibrium constants at the corresponding orientation and are calculated with the aid of data relative to the pure components (the enthalpy and entropy or the reduced thermodynamic potential); for instance

$$K_{p_i} = \exp \left\{ - \left[H_i - TS_i - \sum_k \Phi_{ik} (H_k - TS_k) \right] / RT \right\}. \quad (10)$$

In the case of orientation on the atoms $\|\Phi_{ik}\| \equiv \|A_{ik}\|$. It is easily seen that $K_{p_k} \equiv 1$, i.e., that the equilibrium constant of the base component, calculated according to (10), is always equal to unity. We have then $x_k \equiv x_k$ from (8) and (9). Thus, the representation (8), (9), (10) has an obvious advantage over other notations, since one may eliminate $i - k$ unknowns in (1)–(3) and conduct the calculation for the orientation on any set of k independent components. In addition, in this notation the orientation can be easily altered in the course of the calculation.

The selection of the k base components is subject only to the requirement $d \neq 0$, i.e., the matrix $\|A_{ik}\|_{e_k}$ must be nondegenerate; otherwise it does not possess an inverse matrix. The simplest matrix is $\|A_{ik}\|$ (orientation on atoms). The transformation in the course of the calculation to the orientation $\|\Phi_{ik}\|$ gives however a gain in computing time and expands the region of convergence of Newton's method, if we select as base components the predominant components [1].

2. THE COMPOSITION OF A GENERAL GASEOUS SYSTEM

Consider the simple relations

$$\sum_i N_i - N = 0, \quad (11)$$

$$\sum_i A_{ij} N_i - c_j N^0 = 0, \quad (12)$$

where N_i is the number of moles of component i ; N is the total number of moles; A_{ij} are the elements of the matrix of stoichiometric coefficients; c_j are the material constants. For the electrons $c_j = 0$. The index j takes the values 1 to k . The components i in these relations are expressed, with the aid of the law of mass action, in terms of k arbitrary components, but include necessarily each type of the k atoms and electrons.

For determinacy we shall express the components i in terms of the number of moles of atoms and electrons (cf. above):

$$N_i = K_{pi} p^{\sum_k \Phi_{ik} - 1} N^{\sum_k \Phi_{ik}} \prod_k N_k^{\Phi_{ik}}. \quad (13)$$

For the quantities with index k from the totality i we obtain, with the aid of (13), the identity $N_k \equiv N_k$ and $K_{pk} = 1$. Substituting (13) in (11) and (12), we obtain a system of $k + 1$ nonlinear algebraic equations for determining the unknowns N_1, N_2, \dots, N_k, N . The system (11), (12) will be completely determined if the set of numbers c_j , the equilibrium constants K_{pi} , and the matrix of stoichiometric coefficients Φ_{ik} are specified.

Applying Newton's method to (11), (12) and solving this system with respect to the logarithmic corrections $\Delta \ln N_k$, $\Delta \ln N$, we obtain

$$\sum_k \Delta \ln N_k \sum_i \Phi_{ik} N_i + \Delta \ln N \left[\left(1 - \sum_i \Phi_{ik} \right) N_i - N \right] + \left(\sum_i N_i - N \right) = 0, \quad (14)$$

$$\sum_k \Delta \ln N_k \sum_i A_{ij} \Phi_{ik} N_i + \Delta \ln N \left[\sum_i A_{ij} \left(1 - \sum_k \Phi_{ik} \right) N_i \right] + \left(\sum_i A_{ij} N_i - c_j N^0 \right) = 0. \quad (15)$$

System (14), (15) is linear with respect to the corrections $\Delta \ln N_k, \Delta \ln N$ and can be solved by one of the standard methods. The iterated magnitudes are the logarithms of N_1, N_2, \dots, N_k . The requirement that the iteration converges is equivalent to a comparison with the reference logarithmic correction

$$\left| \frac{\Delta N_k}{N_k} \right| \leq \varepsilon, \quad \left| \frac{\Delta N}{N} \right| \leq \varepsilon. \quad (16)$$

Thus, the determination of the composition reduces to the following sequence of operations:

- 1) initial approximations $\ln N_1, \dots, \ln N$ are assumed;
- 2) we calculate

$$N_i = \exp \left\{ \ln K_{pi} + \left(\sum \Phi_{ik} - 1 \right) \ln p + \left(1 - \sum \Phi_{ik} \right) \ln N + \sum \Phi_{ik} \ln N_k \right\}. \quad (17)$$

Here $\ln K_{pi}$ is calculated with the aid of (10);

3) solving (14), (15), we find $\Delta \ln N_k, \Delta \ln N$;

4) we realize the relative control (16);

5) if $|\Delta \ln N_k| > \varepsilon, |\Delta \ln N| > \varepsilon$, we form the next approximation, i. e.,

$$\ln N_k^{(n+1)} = \ln N_k^{(n)} + \Delta \ln N_k^{(n)}, \quad (18)$$

$$\ln N^{(n+1)} = \ln N^{(n)} + \Delta \ln N^{(n)}. \quad (19)$$

The second and fourth operations are now carried out successively until requirement (16) is finally satisfied. The right sides of (14), (15) then vanish, and the approximate composition is derived. We further calculate the molar fractions $x_i = N_i/N$ and the integral thermodynamic characteristics

$$\mu = \mu_0 N^0 / N, \quad (20)$$

$$h = \frac{1}{\mu} \sum_i H_i x_i, \quad (21)$$

$$u = h - RT / \mu, \quad (22)$$

$$s = \frac{1}{\mu} \left[\sum_i S_i x_i - R \ln \mu - R \sum_i x_i \ln x_i \right]. \quad (23)$$

3. CALCULATIONS IN DIFFERENTIAL THERMODYNAMICS

There are several methods of calculating the differential thermodynamic characteristics, differing in programming ease and computing time. One of them is the procedure used in [1, 2, 8–10], where the derivatives

$1/N \left(\frac{\partial N_i}{\partial T} \right)_p$ and $1/N \left(\frac{\partial N_i}{\partial T} \right)_v$ were calculated. The determinants of the linear systems for the composition and the derivatives turned out to be different.

It is however known that the specific heats and the sound velocity can also be calculated by a different procedure, with the aid of the derivatives $\left(\frac{\partial N_i}{\partial T} \right)_p$ and $\left(\frac{\partial N_i}{\partial p} \right)_T$ or $\left(\frac{\partial \ln N_i}{\partial \ln T} \right)_p$ and $\left(\frac{\partial \ln N_i}{\partial \ln p} \right)_T$ /11/. In this case the determinants for the composition and the derivatives coincide. In fact, if in (11) and (12) N_i is replaced by $\exp(\ln N_i)$ and N by $\exp(\ln N)$, and we then differentiate allowing for (13) and (14), there results

$$\begin{aligned} \sum_k \left(\frac{\partial \ln N_k}{\partial \ln T} \right)_p \sum_i \Phi_{ik} N_i + \left(\frac{\partial \ln N}{\partial \ln T} \right)_p \left[\sum_i \left(1 - \sum_k \Phi_{ik} \right) N_i - N \right] + \\ + \frac{1}{RT} \sum_i \left(H_i - \sum_k \Phi_{ik} H_k \right) N_i = 0, \end{aligned} \quad (24)$$

$$\begin{aligned} \sum_k \left(\frac{\partial \ln N_k}{\partial \ln T} \right)_p \sum_i A_{ij} \Phi_{ik} N_i + \left(\frac{\partial \ln N}{\partial \ln T} \right)_p \left[\sum_i A_{ij} \left(1 - \sum_k \Phi_{ik} \right) N_i \right] + \\ + \frac{1}{RT} \sum_i A_{ij} \left(H_i - \sum_k \Phi_{ik} H_k \right) N_i, \end{aligned} \quad (25)$$

$$\begin{aligned} \sum_k \left(\frac{\partial \ln N_k}{\partial \ln p} \right)_T \sum_i \Phi_{ik} N_i + \left(\frac{\partial \ln N}{\partial \ln p} \right)_T \left[\sum_i \left(1 - \sum_k \Phi_{ik} \right) N_i - N \right] + \\ + \sum_i \left(\sum_k \Phi_{ik} - 1 \right) N_i = 0, \end{aligned} \quad (26)$$

$$\begin{aligned} \sum_k \left(\frac{\partial \ln N_k}{\partial \ln p} \right)_T \sum_i A_{ij} \Phi_{ik} N_i + \left(\frac{\partial \ln N}{\partial \ln p} \right)_T \left[\sum_i A_{ij} \left(1 - \sum_k \Phi_{ik} \right) N_i \right] + \\ + A_{ij} \left(\sum_k \Phi_{ik} - 1 \right) N_i = 0. \end{aligned} \quad (27)$$

Thus, it is easily seen that the determinants of systems (24), (25), and (26), (27) coincide with that of system (14), (15) in the last iteration cycle.

When using the standard subroutines for solving systems of linear equations, the matrix of coefficients is not conserved in the course of the

calculations and cannot be used for solving other systems. It is therefore advisable to include the solution of the system with respect to the derivatives in every cycle of iterations of the system for composition (14), (15). Since the systems differ in their right sides, it is convenient to use a solution program based on the Gauss method with selection of the main element and with many right sides (cf. below). The solution of the system with respect to the derivatives is obtained in this case in the last cycle of iterations of the composition system. The matrix of coefficients of the determinants and the matrix of the right sides of the systems are

$$\begin{vmatrix} \sum_i \Phi_{ik} N_i & \sum_i (1 - \Phi_{ik}) N_i - N \\ \sum_i A_{ij} \Phi_{ik} N_i & \sum_i A_{ij} (1 - \sum_k \Phi_{ik}) N_i \end{vmatrix}, \quad (28)$$

$$\begin{vmatrix} N - \sum_i N_i & \frac{1}{RT} \sum_i (\Phi_{ik} H_k - H_i) N_i & \sum_i (1 - \sum_k \Phi_{ik}) N_i \\ C_i - \sum_j A_{ij} N_j & \frac{1}{RT} \sum_j A_{ij} (\Phi_{jk} H_k - H_i) N_j & \sum_j A_{ij} (1 - \sum_k \Phi_{jk}) N_j \end{vmatrix} \quad (29)$$

The calculation of the derivatives has thus been reduced to the same sequence of operations as the calculation of the composition.

This calculation yields together with N_i , N also $\left(\frac{\partial \ln N_k}{\partial \ln T}\right)_p$, $\left(\frac{\partial \ln N}{\partial \ln T}\right)_p$ and $\left(\frac{\partial \ln N_k}{\partial \ln p}\right)_p$, $\left(\frac{\partial \ln N}{\partial \ln p}\right)_T$. It is now easy to calculate $\left(\frac{\partial \ln N_i}{\partial \ln T}\right)_p$ and $\left(\frac{\partial \ln N_i}{\partial \ln p}\right)_T$. These quantities can likewise be determined in parallel with the iteration cycle.

Allowing for (10), we obtain from (13)

$$\left(\frac{\partial \ln N_i}{\partial \ln T}\right)_p = \frac{1}{RT} \left[H_i - \sum_k \Phi_{ik} H_k \right] + \left(1 - \sum_k \Phi_{ik}\right) \left(\frac{\partial \ln N}{\partial \ln T}\right)_p + \sum_k \Phi_{ik} \left(\frac{\partial \ln N_k}{\partial \ln T}\right)_p, \quad (30)$$

$$\left(\frac{\partial \ln N_i}{\partial \ln p}\right)_T = \left(\sum_k \Phi_{ik} - 1\right) + \left(1 - \sum_k \Phi_{ik}\right) \left(\frac{\partial \ln N}{\partial \ln p}\right)_T + \sum_k \Phi_{ik} \left(\frac{\partial \ln N_k}{\partial \ln p}\right)_T. \quad (31)$$

Finally, the formulas for calculating c_p , c_v , a are given as follows:

$$c_p = \frac{1}{\mu_0 N^0} \left[\sum_i C_{pi} N_i + \sum_i H_i \frac{1}{T} N_i \left(\frac{\partial \ln N_i}{\partial \ln T}\right)_p \right], \quad (32)$$

$$c_v = c_p + \frac{R}{\mu_0 N^0} \left[\left(1 + \left(\frac{\partial \ln N}{\partial \ln T}\right)_x\right)^2 - \left(\frac{\partial \ln N}{\partial \ln p}\right)_T - 1 \right], \quad (33)$$

$$a^2 = \frac{\gamma RT}{\mu} \frac{1}{1 - \left(\frac{\partial \ln N}{\partial \ln p}\right)_T}, \quad (34)$$

where $\gamma = c_p/c_v$.

4. REALIZATION OF THE MATHEMATICAL MODEL

The following must be borne in mind when the mathematical model described is programmed in a computer language. The program must yield

the thermodynamic quantities and composition of the mixture corresponding to given T and p . It can also be used as a subroutine in the program to solve the gas-dynamic problem. Both when used independently and as a subroutine, the program necessitates as input data, in addition to T and p , also the initial approximation N_1, N_2, \dots, N_k, N . The program itself uses the library of standard subroutines available in the IS-2 system, and also a program for solving a system of linear equations by the Gauss method with selection of the main element. The advantages of this program, besides the accuracy, are twofold: first, the selection of the main element, which makes it possible to avoid division by zero when dividing by an arbitrary element of the system determinant; second, by the Gauss method the expanded matrix comprising the determinant coefficients and of several right sides is inverted, which enables the computing time to be considerably reduced.

Several comments are now made as regards the possibility of using the program with a computer having an internal memory of about 4000 three-address cells. We recall that the formation of the coefficients of linear-system matrices is realized with the aid of the matrix of stoichiometric coefficients A_{ik} . This matrix occupies ik cells. Since it is constantly in use, it must be stored in the internal memory. For small values of i and k ($i \simeq 100$, $k \simeq 10$) the matrix A_{ik} is stored in such a way that a cell corresponds to every matrix element. For numbers i and k such that $ik \geq 1000$, several cell digits are assigned to each matrix element, which is coded in binary form. Every vector i in space k is stored in two cells of the memory, and as a result the matrix occupies $2i$ cells. Provision was made for modifying the number of digits assigned to each element A_{ik} , depending on the maximum content of the atom of type k in particle i . Independently of the method of coding the matrix A_{ik} , this unit realizes the formation of the matrix of determinant coefficients and the right sides of linear systems and their distribution in a definite order for arbitrary i and k . Note that the maximum order of the linear system for the existing standard subroutines does not exceed 60. We shall consider two optimum possibilities of the program. In the first case the matrix A_{ik} is stored in ik cells, and the coefficients of the polynomials $\varphi_i^{(m)}$ are stored in the internal memory (i.e., the whole program is stored in the internal memory). Possible i and k can then be determined from the approximation relation $15i + ik + k + 10k \simeq 3200$.

For $k = 10$, we obtain $i \simeq 120$; for $k = 15$, $i \simeq 90$.

In the second case the matrix A_{ik} is stored in $2i$ cells, and the coefficients of the polynomials $\varphi_i^{(m)}$ are stored in the internal memory (i.e., the program occupies the internal memory and one group of drums). In this case possible i and k are determined from the relation $7i + k^2 + 10k \simeq 3200$.

For $k = 20$, we obtain $i \simeq 370$; for $k = 40$ $i = 170$.

Bibliography

1. Stupochenko, E. V., I. P. Stakhanov, E. V. Samuilov, A. S. Pleshanov, and I. B. Rozhdestvenskii. Termodinamicheskie svoystva vozdukh v intervale temperatur 1000—1200°K (Thermodynamic Properties of Air in the Temperature Range 1000—1200°K).—Sbornik "Fizicheskaya gazodinamika," Moskva, Izdatel'stvo AN SSSR. 1959.

2. Stupochenko, E. V., E. V. Samuilov, A. S. Pleshanov, and I. B. Rozhdestvenskii. *Termodinamicheskie funktsii vozdukh pri vysokikh temperaturakh* (Thermodynamic Functions for Air at High Temperatures).—*Zhurnal Fizicheskoi Khimii*, Vol. 34, No. 6. 1960.
3. Hirschfelder, J., C. Curtiss, and R. Bird. *Molecular Theory of Gases and Liquids*.—John Wiley and Sons, New York. 1949.
4. Gurvich, L. V. and others. *Termodinamicheskie svoistva individual'nykh veshchestv* (Thermodynamic Properties of Individual Substances).—Moskva, Izdatel'stvo AN SSSR. 1962.
5. Gurvich, L. V. and N. P. Rtishcheva. *Analiticheskoe predstavlenie tabulirovannykh znachenii termodinamicheskikh svoistv gazov* (Analytic Representation of the Tabulated Values of the Thermodynamic Properties of Gases).—*Teplofizika vysokikh temperatur*, No. 6. 1964.
6. Samuilov, E. V. and K. K. Olevinskii. *Tablitsy summ dlya rascheta termodinamicheskikh svoistv gazov* (Tables of Sums for Calculating the Thermodynamic Properties of Gases).—Moskva, Izdanie VTs AN SSSR. 1963.
7. Aravin, G. S. and V. P. Shevelev. *Termicheskaya ionizatsiya i elektroprovodnost' nekotorykh smesei i produktov sgoraniya* (Thermal Ionization and Electrical Conductivity of Some Mixtures and Combustion Products).—*PMTF*, No. 2. 1962.
8. Pleshanov, A. S. *Obshchii raschet sostava i termodinamicheskii analiz proizvod'nykh reagiruyushchikh gazovykh sistem* (General Calculation of the Composition and Thermodynamic Analysis of General Reacting Gaseous Systems).—*Sbornik "Fizicheskaya gazodinamika,"* Moskva, Izdatel'stvo AN SSSR. 1962.
9. Pleshanov, A. S. and S. G. Zaitsev. *Sostav, termodinamicheskie i gazodinamicheskie svoistva uglekislogo gaza pri vysokikh temperaturakh* (Composition, Thermodynamic, and Gas-Dynamic Properties of Carbonic Acid at High Temperatures).—*Sbornik "Fizicheskaya Gazodinamika,"* Moskva, Izdatel'stvo AN SSSR. 1962.
10. Pleshanov, A. S. *Sostav, termodinamicheskie i gazodinamicheskie svoistva azota pri vysokikh temperaturakh* (Composition, Thermodynamic, and Gas-Dynamic Properties of Nitrogen at High Temperatures).—*Sbornik "Fizicheskaya gazodinamika,"* Moskva, Izdatel'stvo AN SSSR. 1962.
11. Epshtein, P. S. *Kurs termodinamiki* (A Course of Thermodynamics).—Moskva-Leningrad, GITTL. 1948.

I. B. Rozhdestvenskii, K. K. Olevinskii, V. P. Shevelev

**THERMODYNAMIC FUNCTIONS OF THE COMBUSTION
PRODUCTS OF THE SYSTEM LIQUID ETHYL
ALCOHOL—GASEOUS OXYGEN**

This paper presents (in Figure 1) the $h-s$ diagram of the products of combustion (for $\alpha = 1$), a graph (in Figure 2) of the composition of the combustion products as a function of α ($0.1 \leq \alpha \leq 3$) for the theoretical combustion temperature T_c , and other curves (Figures 3—7). These data can be used in calculations regarding combustion chambers and the isentropic flow of the products of combustion. The following 29 components were taken into account in the calculation: CO_2 , CO , CH , CH_2 , CH_3 , CH_4 , H_2O , H_2O_2 , HO_2 , HCO , H_2 , O_2 , O_3 , OH , O , H , C , e^- , CO^+ , OH^+ , O_2^+ , H^+ , O^+ , C^+ , OH^- , O_2^- , H^- , O^- , C^- . The data on the composition can be used for an improved calculation of the kinetic coefficients of the combustion products of the system. The computation was performed on a computer by the same method /1/ with orientation on CO_2 , CO , H_2 , e^- for $\alpha \leq 1$, and on CO_2 , O_2 , H_2O , e^- for $\alpha \geq 1$.

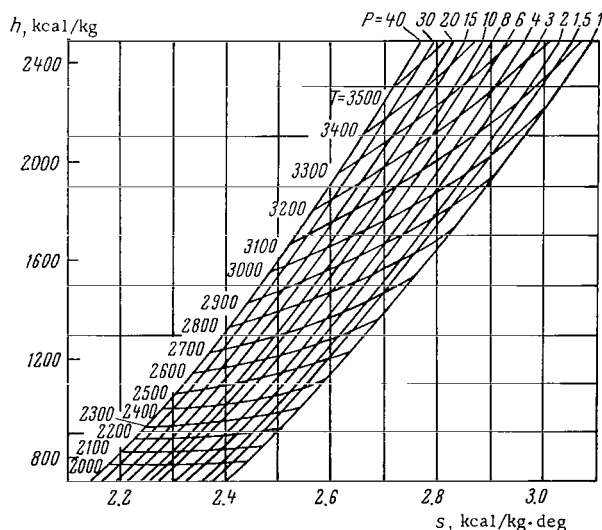
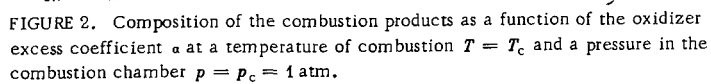


FIGURE 1. $h-s$ -diagram of the combustion products.

The following quantities were calculated: composition (molar fractions), enthalpy h (cal/g), internal energy u (cal/g), entropy s (cal/g·deg),



molecular weight μ (g/mole), specific heats c_p, c_v (cal/g·deg), $\gamma = c_p/c_v$, sound velocity a (m/sec), density ρ (g/cm³). The calculations were conducted as a function of the oxidizer excess coefficient α for the following pressures in the combustion chamber: $p_c = 1, 1.5, 2, 3, 4, 6, 8, 10, 15, 20, 30, 40$ atm. The thermodynamic functions of the pure components (polynomial coefficients) for h and s were taken from a handbook [2]. The equilibrium constants for the reactions $O_2 + e^- \rightleftharpoons O_2^- \rightleftharpoons O$ and $C + e^- \rightleftharpoons C^- \rightleftharpoons O$ are taken from [3]. The dissociation or ionization energies and the enthalpy reference levels at 0°K are given in the table for the main components.

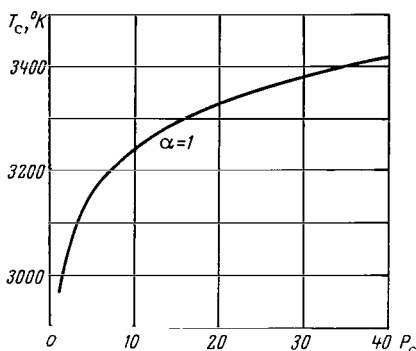


FIGURE 3. Combustion temperature at $\alpha = 1$ as a function of the pressure in the combustion chamber.

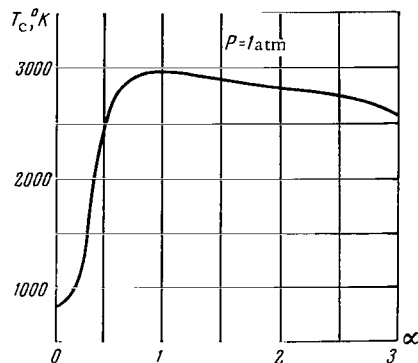
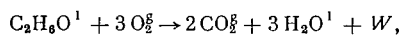


FIGURE 4. Combustion temperature $p_c = 1$ atm as a function of the oxidizer excess coefficient.

Component	Dissociation, ionization energy, cal/mole	Enthalpy at 0°K, cal/mole	Component	Dissociation, ionization energy, cal/mole	Enthalpy at 0°K, cal/mole
CO ₂	381 543	0	O ₂	117 973	0
CO	255 790	66 766.5	HCO	285 596	117 157.5
H ₂	103 264	57 130	O	—	58 986.5
CH ₄	290 581	213 580	H	—	80 197
H ₂ O ₂	252 282	26 085	C	—	263 570
H ₂ O	219 361	0	e	—	0
HO ₂	165 000	33 170	CO ⁺	323 179	389 945.4
CH ₂	206 849	217 115	OH ⁺	304 000	341 824
O ₃	141 828	35 131.5	O ₂ ⁺	278 545	278 544
CH ₃	392 118	192 240	H ⁺	313 600	393 797
CH	80 000	263 767	O ⁺	314 052	373 038.5
OH	101 360	37 824	C ⁺	259 845	523 415

The complete combustion of pure (100 %) ethyl alcohol can be described by the stoichiometric equation



where the superscripts l and g refer to liquid and gas respectively.

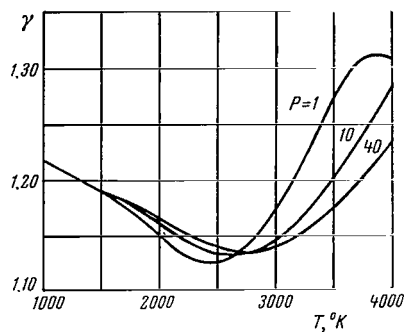


FIGURE 5. Specific-heat ratio $\gamma = c_p/c_v$ of the combustion products at $\alpha = 1$ as a function of the temperature for $p_c = 1, 10, 40$ atm.

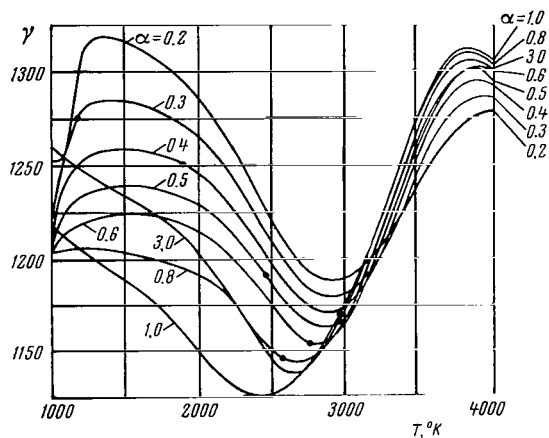


FIGURE 6. Specific-heat ratio $\gamma = c_p/c_v$ of the combustion products at $p = 1$ as a function of the temperature for different α .

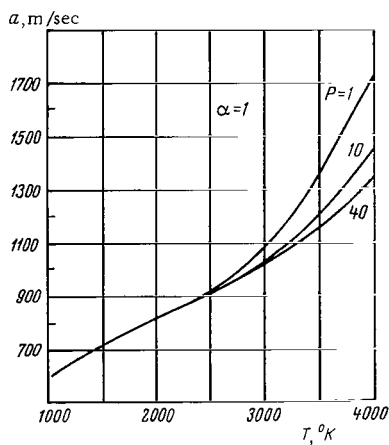
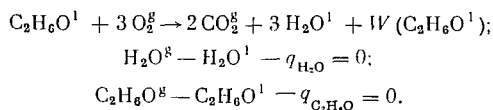


FIGURE 7. Equilibrium sound velocity of the combustion products as a function of the temperature for $\alpha = 1$ and $p_c = 1, 10, 40$ atm.

The heats of combustion of C_2H_6O in liquid and gaseous states for $T = 298^\circ K$, following [4], are equal respectively to $W(C_2H_6O^l) - 326.66 \pm 0.10$ kcal/mole, $W(C_2H_6O^g) - 336.78 \pm 0.10$ kcal/mole. It follows that the heat of evaporation of alcohol at $298^\circ K$ ($q_{C_2H_6O}$) is equal to 10.12 kcal/mole. The products of combustion are in both cases liquid water and gaseous carbon dioxide. The heat of evaporation of H_2O at $298^\circ K$ (q_{H_2O}) is equal to 10.503 ± 0.006 kcal/mole.

We can thus write the following reaction equations:



These equations yield $W - W(C_2H_6O^l) + q_{C_2H_6O} - 3 q_{H_2O} = 305.271$ kcal/mole for the heat of combustion of gaseous alcohol into gaseous products. At the enthalpy reference levels adopted the enthalpy of $C_2H_6O^g$ at $298^\circ K$ is found to have the value 310.628 kcal/mole ($H_{C_2H_6O}^{298} = 310,628$ cal/mole).

The calculation was performed for 96 % (by volume) alcohol. The quantity W includes the heat of evaporation of the water contained in 96 % alcohol. The theoretical combustion temperature was determined by linear interpolation of the enthalpy values with simultaneous calculation of the $h-s$ -diagrams of the combustion products.

The range of the $h-s$ diagram (cf. Figure 1) which is of practical interest for calculating the efflux through a nozzle is the lower region, lying beneath the horizontal line of the corresponding combustion temperature ($h_{in} = h_{pr}$).

Bibliography

1. Rozhdestvenskii, I.B., V.P. Shevelev, and K.K. Olevinskii. Raschet sostava i termodinamicheskikh funktsii proizvol'nykh reagiruyushchikh gazovykh sistem (Calculation of the Composition and Thermodynamic Functions of General Reacting Gaseous Systems).—In this collection, p. 14.
2. Gurvich, L.V. and others. Termodinamicheskie svoistva individual'nykh veshchestv (Thermodynamic Properties of Individual Substances).—Moskva, Izdatel'stvo AN SSSR. 1962.
3. Pleshanov, A.S. and S.G. Zaitsev. Sostav, termodinamicheskie i gazodinamicheskie svoistva uglekislogo gaza dlya temperatur ot 1000 do 12,000°K i davlenii ot 10^{-2} to 10^3 atm (Composition, Thermodynamic, and Gas-Dynamic Properties of Carbonic Acid for Temperatures between 1000 and 12,000°K and Pressures between 10^{-2} and 10^3 atm).—Sbornik "Fizicheskaya gazodinamika," Moskva, Izdatel'stvo AN SSSR. 1962.
4. Lewis, B. and G. von Elbe. Combustion, Flames and Explosions of Gases.—Academic Press, New York. 1951.

N. N. Tsitelauri

INTERACTION POTENTIAL OF CO MOLECULES

The kinetic theory of rarefied gases provides a means for calculating the transfer coefficients if the intermolecular interaction forces are known /1/. The available interaction potentials for most gases correspond however to moderate and low temperatures, and their extrapolation to higher temperatures is unsatisfactory. Several theoretical and experimental methods were developed for obtaining the interaction forces at high temperatures. The most valuable experimental approach in this respect is the study of the elastic scattering of a high-velocity neutral beam of particles /2/, and measurements of the relaxation time of the vibrational energy of the molecules. Another suitable method for obtaining the interaction potential is to use data about the viscosity or other transfer coefficients; however, these data are difficult to obtain at high temperatures.

In this paper the interaction potential of CO molecules was determined by studying the vibrational relaxation in CO behind a shock wave. This procedure was dictated by the available experimental data, and also by the following reasons: the chemical inertness of CO satisfies the theoretical assumption that the effect of chemical affinity can be neglected when describing molecular collisions; the high chemical stability of CO enables one to conduct shock-tube studies of the vibrational relaxation over a wide temperature range.

The parameters of the interaction potential of CO can be obtained from measurements of the vibrational relaxation time, using the relations of the theory of vibrational relaxation founded by Landau and Teller /3/. They proved that the probability of exciting molecular vibrations during collisions depends strongly on the intermolecular forces, mainly in the excitation of vibrations pertaining to the repulsive forces, while the attractive forces only accelerate the colliding molecules. This result is obtained by both classical and quantum-mechanical calculations. It is assumed that the kinetic energy of the molecules in collisions which excite vibrations is much higher than the vibrational quantum. This theory contains many simplifications, and its results as regards the probability of exciting vibrations in the molecule only coincide with the experimental results in order of magnitude. Some of the discrepancies can be attributed to inaccurate potentials. Besides the inaccuracies of the theory, discrepancies also arise due to experimental errors linked both with incorrect measurements and with the strong effect of impurities on the value of the time of vibrational relaxation /4/. It is therefore essential to ensure the purity of the gas under investigation.

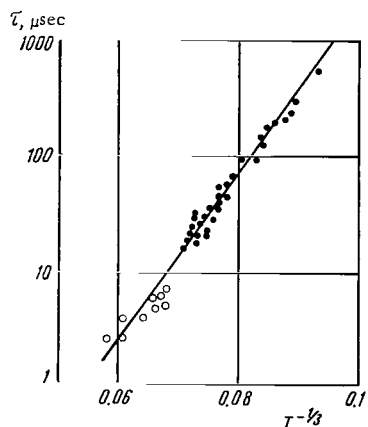


FIGURE 1. Vibrational relaxation time of CO molecules as a function of temperature.

for sodium /7/ and by interferometry /8/. The experimental results of /5/, divided by the atmospheric pressure, have been plotted as a curve of $\lg \tau$ against $T^{-1/2}$ (Figure 1). The points lie approximately on the straight line

$$\lg \tau = 75.8T^{-1/2} - 10.16. \quad (1)$$

The slope of this line determines the radius of the exchange interaction forces of the molecules. These results cover the temperature range 1100—4900°K and represent initial data for calculating the interaction potential of CO molecules.

The following relationship between the vibrational relaxation time of the molecules and the temperature was derived for the model of two colliding diatomic molecules with exponential central forces of repulsion located at the centers of the atoms /4, 9/:

$$\tau = \frac{\sqrt{3}}{64\pi^3} \left(\frac{L}{r_c} \right)^2 \frac{h\alpha^3}{p\chi^2} \exp \left(3\chi - \frac{\Delta E}{2kT} - \frac{3L^2\alpha}{8r_c} \right) \left[1 - \exp \left(- \frac{\Delta E}{kT} \right) \right]; \quad \chi = \left(\frac{2\pi^2\mu\Delta E^2}{\alpha^2 h^2 k T} \right)^{1/2}, \quad (2)$$

where L is the equilibrium internuclear distance in the molecule; r_c is the distance between the mass centers of the molecules at the classical reversal point; h is Planck's constant; k is the Boltzmann constant; p is the gas pressure; α is the reciprocal of the radius of action of the exchange forces between the atoms of the interacting molecules; μ is the reduced mass of the colliding molecules; ΔE is the vibrational quantum; T is the gas temperature.

The following assumptions were made in the derivation of the formula:

the main contribution toward exciting the vibrations were the repulsive forces, which decrease exponentially with increasing distance between the particles;

the largest contribution is made by those collisions for which the axes of the molecules are arranged along the same line;

the internuclear distances are sufficiently large compared with the radius of action α^{-1} of the intermolecular forces, and therefore only the interaction of the nearest atoms is important, while that of the second atoms can be neglected.

The full intermolecular potential will then equal the interatomic potential given by

$$V = V_0 \exp(-\alpha R),$$

where α , V_0 are constant over the given temperature range; R is the distance between the mass centers of the atoms of the interacting molecules.

The attraction is allowed for by increasing the energy of the colliding particles by the depth of the minimum ϵ in the Lennard-Jones (6, 12) potential [1], i.e.,

$$V = V_0 \exp(-\alpha R) - \epsilon. \quad (3)$$

The attraction forces are allowed for by introducing in (2) the factor $\exp(-\frac{\epsilon}{kT})/4$. The reduction in the vibrational relaxation time caused by the conversion of rotational energy into vibrational energy is allowed for by introducing a constant factor A smaller than unity. This factor is selected to compensate for other inaccuracies of the theory as well.

It is often convenient to use the total interaction energy averaged over all the orientations, the so-called "effective" spherical symmetrical potential. The averaging can be realized by the method of Amdur [2].

The effective potential is obtained in the form $U = U_0 e^{-\alpha_M r}$, where α_M is the reciprocal of the radius of action of the exchange forces between the molecules; r is the distance between the mass centers of colliding molecules.

The averaging leads naturally to an additional error, since the intermolecular potential CO is not spherically symmetrical.

It is seen from formula (2) that the dependence of the relaxation time on temperature is mainly determined by the factor $\exp(3\chi)$. Taking the logarithm of expression (2) and transferring to the left side all the terms except 3χ , we derive

$$\begin{aligned} \ln \left[r_c^2 \tau(T) \frac{1 - \exp(-\frac{\Delta E}{kT})}{T^2} \right] + \frac{3I^2 \alpha}{8r_c^2} + \frac{\epsilon}{kT} - \frac{43}{3} \ln \alpha + \frac{\Delta E}{2kT} + \\ + \ln \frac{64\pi^3 p \gamma^2}{\sqrt{3} I^2 h} - \ln A = \frac{3\gamma}{\alpha^2} T^{-1/2}; \quad \gamma = \left[\frac{2\pi^4 \mu \Delta E^2}{h^2 k} \right]^{1/2}. \end{aligned} \quad (4)$$

The quantity $\tau(T)$ is found from Figure 1 or equation (1) for the corresponding temperature. If the left side of equation (4) is designated by $\varphi - \ln A$, then the following linear equation is obtained:

$$\varphi - \ln A = (3\gamma / \alpha^{3/2}) T^{-1/2}. \quad (5)$$

Several equations analogous to (5) can be written for different temperatures to give a system of linear equations which can be approximately solved by the method of least squares. The zero approximation for α and r_c in (4) or (5) is obtained by using method B, described in [4, 8], to select an exponential potential for the Lennard-Jones (6, 12) potential. The

required values of α are then found from equation (4) by the method of successive approximations for a given r_c . The following approximations of r_c are linked with the parameters of the effective intermolecular potential. This potential can be obtained by the method of Amdur, developed in /10/ for the exponential potential:

$$U = U_0 \exp(-\alpha_m r) = 4V_0 e^{-\alpha_m r} \frac{2(\alpha r + 2)(\exp \alpha L - 1) - 2\alpha L \exp \alpha L}{\alpha^2 r L^2}. \quad (6)$$

First V_0 is found from the condition $V = V_0 \exp(-\alpha R) - \varepsilon = 0$ for $r = \sigma$. Hence, since $R = r - L$,

$$V_0 = \varepsilon \exp[\alpha(\sigma - L)]. \quad (7)$$

Here σ is the parameter of the Lennard-Jones potential /1/.

Next, writing equation (6) for different r , we find α_m and U_0 . The quantity r_c can then be derived from the condition

$$U_0 \exp(-\alpha_m r_c) = E^* = \frac{\mu v^{*2}}{2}, \quad (8)$$

where $v^* = (4\pi^2 kT \Delta E / ah\mu)^{1/2}$ is the velocity of the molecules which are most effective in exciting vibrations /4/.

The whole procedure is then repeated with the new values of r_c . This process converges fairly rapidly.

As a result the following values were obtained for the interactions of C and O atoms contained in different colliding molecules: $\alpha = 4.899 \text{ \AA}^{-1}$, $V_0 = 2.624 \cdot 10^{-8} \text{ erg}$; the corresponding values for the molecules are $\alpha_m = 4.629 \text{ \AA}^{-1}$, $U_0 = 3.158 \cdot 10^{-8} \text{ erg}$. The value of the correction factor A in equation (4) is equal to 0.2. The effective interaction potential obtained for the CO molecules,

$$U = 19700 \exp(-4.629 r) \text{ eV} \quad (9)$$

corresponds (following (8)) to intermolecular distances $1.95 \leq r \leq 2.2 \text{ \AA}$. Figure 2 shows a curve of the potential U along with the Lennard-Jones (6, 12) potential. It is seen that the Lennard-Jones potential gives overestimated results.

The figure also shows a plot of the interaction potential of the N_2 molecules, obtained from the experimental data on vibrational relaxation /10/.

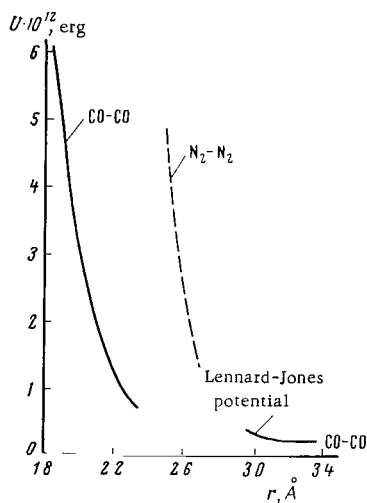


FIGURE 2. Curves of the interaction potential of the molecules.

Bibliography

1. Hirschfelder, J., C. Curtiss, and R. Bird. Molecular Theory of Gases and Liquids.—John Wiley and Sons, New York. 1949.
2. Amdur, I., E.A. Mason, and J.E. Jordan. Scattering of High Velocity Neutral Particles: He-N₂; A-N₂. The N₂-N₂ Interaction.—J. Chem. Phys., Vol. 27, No. 2. 1957.
3. Landau, L. and E. Teller. Zur Theorie der Schalldispersion.—Phys. Z. Sowjetunion, Vol. 10, No. 1. 1936.
4. Herzfeld, K.F. and T.A. Litovitz. Dispersion and Absorption of Ultrasonic Waves, N.Y.—London. 1959.
5. Millican, R.C. and W.J. Hooker. Shock-tube Study of Vibrational Relaxation in Carbon Monoxide for the Fundamental and First Overtone.—J. Chem. Phys., Vol. 38, No. 1. 1963.
6. Windsor, M.W., N. Davidson, and R.L. Taylor. A Study of Vibrational Relaxation in Carbon Monoxide by Shock Waves and Infrared Emission.—Seventh Symposium (International) on Combustion, London. 1959.
7. Gaydon, A.G. and I.R. Hurle. Measurement of Times of Vibrational Relaxation and Dissociation behind Shock Waves in N₂, O₂, Air, CO, CO₂ and H₂.—Eighth Symposium (International) on Combustion, Baltimore. 1962.
8. Matthews, D.L. Vibration Relaxation of Carbon Monoxide in the Shock Tube.—J. Chem. Phys., Vol. 34, No. 2. 1961.
9. Herzfeld, K.F. Deactivation of the Vibration during Collision of Two Diatomic Molecules.—Z. Phys., Vol. 156, p. 265. 1959.
10. Vanderslice, J.T., E.A. Mason, and E.R. Lippincott. Interaction between Ground State Nitrogen Atoms and Molecules.—J. Chem. Phys., Vol. 30, No. 1. 1959.

L. G. Gvozdeva, O. A. Predvoditeleva

PARAMETERS OF CARBON DIOXIDE AND NITROGEN BEHIND SHOCK WAVES INTERACTING WITH A WEDGE

The gas-dynamic quantities behind shock waves, propagating in a gas with initial temperatures of 300—3000°K, have been tabulated under different assumptions as regards the thermodynamic state of the gas. Tabulated data are used for calculating different shock configurations generated during the flow of shock waves past a wedge.

The interaction of the shock wave with a wedge consists in a reflected wave from the wedge surface and the flow of hot gas past the wedge behind the incident shock wave. This pattern depends substantially, as shown in /1, 2/, on the extent of the physicochemical transformations in the heated gas. The positioning of the reflected wave in the Mach configuration and the angle of inclination of the attached wave at the wedge are sensitive functions of the state of the gas in the regions bounded by these waves. This may lead to the detachment of the reflected and attached waves, and the formation of a second triple wave configuration.

Studies of the Mach configuration and the attached waves reveal regions in which double Mach configurations can exist.

Investigations were undertaken for carbon dioxide and nitrogen. In the range considered the physicochemical transformations in these gases affect the gas parameters considerably.

Every type of physicochemical transformation has its own relaxation time. The relaxation times of different processes sometimes vary widely. As a result, one can observe quasiequilibrium states in a gas heated by a shock wave, in which some processes have already been completed while others continue /3/; it can happen that the molecular vibrations have been fully excited, but no dissociation has taken place.

When considering shocks propagating in a gas preheated by a shock wave it was assumed that the state on the wave varies such that equilibrium is established immediately behind the wave with respect to the degrees of freedom excited behind the incident shock wave.

1. THE GAS STATE BEHIND SHOCK WAVES FOR DIFFERENT INITIAL STATES OF THE GAS

The state of the gas behind shock waves was calculated from the conservation laws of energy, mass, and momentum, by the method of successive approximations /4, 5/. The calculations for carbon dioxide were based on the following assumptions: all the vibrational modes are

excited in a stable manner behind the wave, and dissociation has taken place (variant I); all the vibrational modes are stable behind the wave, and there is no dissociation (variant II); neither dissociation has taken place nor have asymmetric valent vibrations been excited in the gas behind the wave (variant II'). The graphs compare curves for a constant specific-heat ratio $\gamma = 1.4$ during transition across the shock (variant III). Variant II was used for nitrogen, since the degree of dissociation of nitrogen molecules is low for the corresponding shock velocities. The calculation of the values of the enthalpy and molecular weight for variant I is described below. The values of the enthalpy for variant II were taken from the tables in /6/, and the values of the enthalpy for variant II' from /7/.

The calculations were first conducted for the gas state in front of the shock with $p_{in} = 1.68 \cdot 10^{-2}$ atm and $T_{in} = 293^\circ K$, and wave velocities between 1000 and 3000 m/sec. Calculations were also performed for shocks under higher initial temperatures and pressures. These initial states are obtained as a result of the passage through a gas (whose initial temperature is $293^\circ K$) of shock waves moving at one of the following velocities: $u = 1.0, 1.3, 1.6, 1.9, 2.2, 2.5, 2.8$ km/sec.

TABLE 1. CO_2 . Variant I

u, km/sec	$T_{in}, ^\circ K$														
	293			1770			2120			2385			2690		
	P_{in}, atm														
	0.0168			0.995			1.34			1.75			2.21		
	T_b/T_{in}	p_b/p_{in}	ρ_b/ρ_{in}	T_b/T_{in}	p_b/p_{in}	ρ_b/ρ_{in}	T_b/T_{in}	p_b/p_{in}	ρ_b/ρ_{in}	T_b/T_{in}	p_b/p_{in}	ρ_b/ρ_{in}	T_b/T_{in}	p_b/p_{in}	ρ_b/ρ_{in}
0.7	1.84	7.2	4.23	1.03	1.33	1.29	1.00	1.22	1.22	1.00	1.04	1.04	—	—	—
0.8	2.08	10.2	4.92	1.07	1.73	1.61	1.03	1.47	1.43	1.02	1.25	1.23	1.006	1.14	1.14
0.9	2.36	13.1	5.61	1.11	2.20	1.97	1.06	1.85	1.74	1.04	1.58	1.51	1.02	1.40	1.35
1.0	2.62	16.1	6.16	1.15	2.72	2.36	1.08	2.28	2.09	1.06	1.97	1.84	1.04	1.74	1.66
1.1	2.93	19.6	6.69	1.19	3.31	2.77	1.11	2.76	2.45	1.08	2.40	2.19	1.06	2.11	1.96
1.2	3.26	23.4	7.17	1.22	3.96	3.21	1.14	3.29	2.83	1.10	2.87	2.55	1.07	2.53	2.30
1.3	3.60	27.5	7.65	1.26	4.67	3.65	1.17	3.88	3.24	1.12	3.38	2.93	1.09	2.96	2.63
1.4	3.97	32.0	8.06	1.30	5.42	4.11	1.20	4.50	3.65	1.14	3.93	3.33	1.11	3.44	2.98
1.5	4.35	36.8	8.46	1.33	6.26	4.59	1.22	5.20	4.13	1.16	4.52	3.74	1.13	3.96	3.25
1.6	4.75	42.0	8.85	1.37	7.14	5.06	1.23	5.94	4.63	1.18	5.15	4.16	1.14	4.52	3.77
1.7	5.19	47.5	9.16	1.41	8.08	5.53	1.27	6.70	5.02	1.20	5.82	4.59	1.17	5.10	4.12
1.8	5.62	52.3	9.45	1.45	9.08	6.03	1.29	7.54	5.54	1.23	6.53	5.02	1.18	5.74	4.56
1.9	6.04	59.2	9.81	1.49	10.1	6.48	1.31	8.43	6.11	1.25	7.29	5.47	1.20	6.39	4.93
2.0	6.42	65.8	10.2	1.52	11.2	6.97	1.34	9.34	6.52	—	—	—	1.22	7.09	5.34
2.1	6.83	72.7	10.6	1.56	12.4	7.47	—	—	—	—	—	—	—	—	—
2.2	7.23	80.0	10.9	1.59	13.6	7.95	—	—	—	—	—	—	—	—	—
2.3	7.58	87.7	11.4	1.63	14.9	8.42	—	—	—	—	—	—	—	—	—
2.4	7.88	95.7	11.8	1.66	16.3	8.89	—	—	—	—	—	—	—	—	—
2.5	8.14	104	12.3	1.69	17.7	9.38	—	—	—	—	—	—	—	—	—
2.6	8.45	113	12.7	1.72	19.2	9.88	—	—	—	—	—	—	—	—	—
2.7	8.70	122	13.2	1.75	20.7	10.3	—	—	—	—	—	—	—	—	—
2.8	8.94	131.5	13.6	1.78	22.2	10.7	—	—	—	—	—	—	—	—	—
2.9	9.16	141	14.1	1.81	23.9	11.1	—	—	—	—	—	—	—	—	—
3.0	9.39	151	14.6	1.84	25.6	11.6	—	—	—	—	—	—	—	—	—

The tables give the ratios of the pressure p_b , the temperature T_b , and the density ρ_b behind the wave to the initial pressure p_{in} , temperature T_{in} ,

and density ρ_n , respectively, as a function of the wave velocity u . The initial pressure and temperature are indicated for variant I. For variants II and II' only the initial temperature T_n is indicated, since in this case the specific enthalpy of the gas behind the wave is a function of temperature alone, and the given ratios depend only on the velocity of the shock and the initial temperature. The calculations have an error of 1–2%. The data can be used for determining the gas parameters behind reflected waves in a shock tube, and behind waves at obstacles, when a hot gas flows past them. These results were used to determine the gas parameters for shock diffraction at a wedge (Tables 1–4).

TABLE 2. CO₂. Variant II

u , km/sec	T_n , °K													
	293		767		1055		1390		1780		2220		2730	
	T_b/T_n	ρ_b/ρ_n	T_b/T_n	ρ_b/ρ_n	T_b/T_n	ρ_b/ρ_n	T_b/T_n	ρ_b/ρ_n	T_b/T_n	ρ_b/ρ_n	T_b/T_n	ρ_b/ρ_n	T_b/T_n	ρ_b/ρ_n
0.7	1.84	4.23	1.22	2.45	1.145	1.82	1.02	1.77	—	—	—	—	—	—
0.8	2.08	4.92	1.31	3.02	1.20	2.30	1.07	2.14	1.07	1.59	1.04	1.30	1.01	1.11
0.9	2.36	5.61	1.40	3.58	1.26	2.83	1.12	2.57	1.12	1.91	1.08	1.57	1.04	1.34
1.0	2.62	6.16	1.50	4.15	1.33	3.40	1.17	3.03	1.16	2.27	1.12	1.91	1.08	1.61
1.1	2.93	6.69	1.61	4.69	1.40	3.95	1.23	3.46	1.21	2.66	1.15	2.26	1.11	1.90
1.2	3.26	7.17	1.73	5.22	1.48	4.50	1.24	3.92	1.26	3.10	1.20	2.61	1.15	2.19
1.3	3.60	7.65	1.85	5.73	1.57	4.95	1.36	4.38	1.31	3.50	1.24	2.95	1.19	2.49
1.4	3.97	8.06	1.98	6.24	1.66	5.48	1.43	4.82	1.37	3.89	1.29	3.31	1.22	2.82
1.5	4.35	8.46	2.11	6.73	1.76	5.91	1.51	5.25	1.43	4.28	1.33	3.68	1.26	3.16
1.6	4.75	8.85	2.27	7.14	1.87	6.30	1.59	5.67	1.49	4.68	1.38	4.05	1.30	3.49
1.7	5.19	9.16	2.44	7.50	1.98	6.70	1.68	6.05	1.56	5.08	1.43	4.41	1.35	3.81
1.8	5.55	9.55	2.61	7.85	2.11	7.15	1.77	6.46	1.63	5.45	1.49	4.76	1.39	4.14
1.9	6.00	9.83	2.79	8.20	2.24	7.42	1.86	6.84	1.70	5.81	1.55	5.09	1.44	4.47
2.0	6.50	10.1	2.96	8.58	2.37	7.80	1.96	7.19	1.78	6.16	1.62	5.43	1.49	4.79
2.1	7.00	10.3	—	—	—	—	—	—	—	—	—	—	—	—
2.2	7.50	10.6	—	—	—	—	—	—	—	—	—	—	—	—
2.3	8.05	10.8	—	—	—	—	—	—	—	—	—	—	—	—
2.4	8.65	11.0	—	—	—	—	—	—	—	—	—	—	—	—
2.5	9.25	11.2	—	—	—	—	—	—	—	—	—	—	—	—
2.6	9.85	11.3	—	—	—	—	—	—	—	—	—	—	—	—
2.7	10.4	11.5	—	—	—	—	—	—	—	—	—	—	—	—
2.8	11.2	11.6	—	—	—	—	—	—	—	—	—	—	—	—
3.0	12.6	11.9	—	—	—	—	—	—	—	—	—	—	—	—
3.3	14.9	12.2	—	—	—	—	—	—	—	—	—	—	—	—
3.6	17.2	12.5	—	—	—	—	—	—	—	—	—	—	—	—
3.8	19.0	12.7	—	—	—	—	—	—	—	—	—	—	—	—

2. THE EQUILIBRIUM THERMODYNAMIC FUNCTIONS OF CARBON DIOXIDE IN THE TEMPERATURE RANGE 1100–4500°K FOR PRESSURES 0.1–13 atm

The thermodynamics and composition of CO₂ were calculated by the method described in [4]. The following reactions are assumed to occur in carbon dioxide at temperatures of the order of 1000–4000°K:

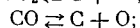
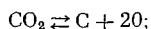


TABLE 3. CO₂. Variant II

u, km/sec	T _{in} , °K									
	293		1900		2390		2965		3610	
	T _b /T _{in}	ρ _b /ρ _{in}	T _b /T _{in}	ρ _b /ρ _{in}	T _b /T _{in}	ρ _b /ρ _{in}	T _b /T _{in}	ρ _b /ρ _{in}	T _b /T _{in}	ρ _b /ρ _{in}
1.0	—	—	1.16	2.14	1.11	1.75	1.07	1.44	1.046	1.23
1.1	—	—	1.21	2.49	1.16	2.05	1.11	1.70	1.07	1.45
1.2	—	—	1.26	2.86	1.20	2.35	1.15	1.98	1.11	1.67
1.3	—	—	1.32	3.21	1.25	2.69	1.19	2.27	1.14	1.91
1.4	—	—	1.38	3.57	1.30	3.00	1.23	2.54	1.18	2.16
1.5	—	—	1.45	3.92	1.35	3.33	1.27	2.83	1.21	2.42
1.6	—	—	1.52	4.26	1.40	3.65	1.32	3.12	—	—
1.7	—	—	1.59	4.60	1.46	3.95	1.37	3.40	—	—
1.8	—	—	1.66	4.93	1.53	4.25	1.42	3.69	—	—
1.9	6.49	9.05	1.74	5.25	1.59	4.55	1.47	3.98	—	—
2.0	7.00	9.31	1.83	5.55	1.66	4.83	—	—	—	—
2.1	7.54	9.47	—	—	—	—	—	—	—	—
2.2	8.16	9.69	—	—	—	—	—	—	—	—
2.3	8.81	9.81	—	—	—	—	—	—	—	—
2.4	9.45	9.95	—	—	—	—	—	—	—	—
2.5	10.1	10.1	—	—	—	—	—	—	—	—
2.6	10.8	10.2	—	—	—	—	—	—	—	—
2.7	11.5	10.3	—	—	—	—	—	—	—	—
2.8	12.3	10.4	—	—	—	—	—	—	—	—
2.9	13.1	10.5	—	—	—	—	—	—	—	—

TABLE 4. N₂. Variant II

u, km/sec	T _{in} , °K													
	293		740		1030		1400		1800		2270		2810	
	T _b /T _{in}	ρ _b /ρ _{in}	T _b /T _{in}	ρ _b /ρ _{in}	T _b /T _{in}	ρ _b /ρ _{in}	T _b /T _{in}	ρ _b /ρ _{in}	T _b /T _{in}	ρ _b /ρ _{in}	T _b /T _{in}	ρ _b /ρ _{in}	T _b /T _{in}	ρ _b /ρ _{in}
0.7	—	—	1.16	1.50	—	—	—	—	—	—	—	—	—	—
0.8	—	—	1.27	1.84	1.13	1.54	1.04	1.28	1.01	1.11	—	—	—	—
0.9	—	—	1.38	2.17	1.23	1.68	1.11	1.45	1.04	1.24	—	—	—	—
1.0	2.52	3.75	1.49	2.49	1.33	1.97	1.16	1.73	1.10	1.35	1.04	1.21	—	—
1.1	2.83	4.09	1.62	2.81	1.40	2.33	1.24	1.97	1.16	1.59	1.085	1.35	1.035	1.19
1.2	3.15	4.37	1.74	3.16	1.48	2.66	1.32	2.19	1.21	1.85	1.14	1.54	1.075	1.32
1.3	3.5	4.64	1.87	3.46	1.58	2.95	1.40	2.41	1.26	2.11	1.19	1.74	1.12	1.51
1.4	3.9	4.87	2.02	3.73	1.67	3.25	1.49	2.65	1.33	2.34	1.24	1.94	1.16	1.69
1.5	4.3	5.09	2.18	3.99	1.77	3.50	1.56	2.91	1.40	2.54	1.30	2.15	1.21	1.84
1.6	4.7	5.25	2.34	4.23	1.90	3.75	1.65	3.17	1.48	2.74	1.35	2.35	1.26	2.02
1.7	5.15	5.45	2.52	4.45	2.03	3.98	1.73	3.43	1.56	2.93	1.41	2.57	1.30	2.25
1.8	5.6	5.62	2.71	4.64	2.17	4.16	1.82	3.66	1.63	3.15	1.46	2.80	1.36	2.42
1.9	6.1	5.80	2.91	4.81	2.33	4.31	1.91	3.89	1.70	3.39	1.52	3.01	1.42	2.58
2.0	6.6	5.92	3.11	5.01	2.48	4.52	2.03	4.07	1.77	3.63	1.59	3.20	1.47	2.76
2.1	7.15	6.05	3.31	5.20	2.62	4.72	2.16	4.22	1.87	3.77	1.67	3.33	1.52	2.95
2.2	7.72	6.17	3.53	5.37	2.78	4.90	2.28	4.39	1.97	3.95	1.74	3.52	1.58	3.12
2.3	8.3	6.28	3.76	5.52	2.94	5.06	2.39	4.58	2.06	4.12	1.82	3.71	1.64	3.36
2.4	8.95	6.39	4.01	5.63	3.12	5.21	2.52	4.74	2.16	4.30	1.89	3.88	1.70	3.47
2.5	9.55	6.48	4.27	5.74	3.29	5.37	2.65	4.89	2.26	4.47	1.975	4.04	1.77	3.63
2.6	10.22	6.56	4.52	5.88	3.47	5.50	2.78	5.05	2.36	4.62	2.06	4.19	1.84	3.79
2.7	10.85	6.64	4.76	6.02	3.66	5.63	2.92	5.19	2.47	4.77	2.15	4.34	1.91	3.95
2.8	11.55	6.72	5.04	6.12	3.86	5.74	3.07	5.32	2.59	4.90	2.24	4.49	1.98	4.09
2.9	12.25	6.79	5.34	6.20	4.06	5.86	3.22	5.44	2.70	5.04	2.33	4.64	2.06	4.23
3.0	13.0	6.86	5.63	6.29	4.27	5.97	3.37	5.56	2.82	5.17	2.42	4.78	2.13	4.37

The thermodynamic equations of the system of gases are

$$\begin{aligned}\frac{X_C X_O^2}{X_{CO_2}} &= \frac{K_{pCO_2}}{p^2}, & X_{CO_2} + X_{CO} + X_{O_2} + X_C + X_O &= 1, \\ \frac{X_O^2}{X_{O_2}} &= \frac{K_{pO_2}}{p}, & \frac{X_{CO_2} + X_{CO} + X_C}{3X_{CO_2} + X_{CO} + 2X_{O_2} + X_O} &= \frac{1}{2}, \\ \frac{X_O X_C}{X_{CO}} &= \frac{K_{pCO}}{p},\end{aligned}$$

where X designates the molar fraction of a component, and K_p the equilibrium constant of the corresponding reaction.

If the equilibrium constants K_p are known, one can determine from this system the gas composition as a function of temperature and pressure.

When the gas composition is known, its specific enthalpy h and molecular weight μ can be found in the form

$$\begin{aligned}h &= \frac{1}{\mu} \sum_n H_n X_n, \\ \mu &= \sum_n \mu_n X_n,\end{aligned}$$

where H_n is the molar enthalpy of the components; μ_n is the molecular weight of the components; n is the number of components.

Such calculations were conducted for $T = 1100 - 4500^\circ\text{K}$ with increments of 200° and pressures of 0.1, 0.5, 1, 5, 7, 9, 11, 13 atm.

Tables 5—11 give data for h , μ , X_{CO_2} , X_{CO} , X_{O_2} , X_O , X_C .

The numerical material of the tables is given in normalized form.

The enthalpy of the gas CO_2 at $T_0 = 293.16^\circ\text{K}$ was taken as 43.485 cal/g.

The thermodynamic functions of the mixture components, given in /6/, were used to calculate the composition and thermodynamic properties of carbon dioxide.

The reference levels of the enthalpies of the components, and the values of the dissociation energies of the main components, are given in Table 12.

A comparison of the results obtained with those of /6/, which allows for a large number of possible reactions but gives values of the enthalpy for temperature increments of 1000° , showed that the failure to allow for the gas components figuring in very low concentrations is unimportant over these temperature ranges. The discrepancy does not exceed 1%. The values of the enthalpies calculated in our case differ by 10—20% from the values obtained in /6/ by linear interpolation, in particular over the temperature range $2000 - 3000^\circ\text{K}$.

3. THE GAS STATE BEHIND AN ATTACHED SHOCK AT A WEDGE AND THE ANGLE OF INCLINATION OF THE ATTACHED SHOCK

Consider the interaction between a shock wave and a wedge (Figure 1). Let the shock wave SA be incident on a wedge of apex angle α_0 , and let the wave velocity be u_0 . An attached shock wave ON is then formed.

TABLE 5. $h = A \cdot 10^7$, cal/g

T, °K	p, atm									
	0.1		0.5		1		2		3	
	A	r	A	r	A	r	A	r	A	r
1700	0.457	3	0.454	3	0.453	3	0.452	3	0.452	3
1800	0.496	3	0.491	3	0.489	3	0.487	3	0.487	3
1900	0.542	3	0.531	3	0.527	3	0.525	3	0.524	3
2100	0.663	3	0.629	3	0.619	3	0.611	3	0.607	3
2300	0.848	3	0.786	3	0.742	3	0.722	3	0.713	3
2500	0.113	4	0.963	3	0.914	3	0.873	3	0.854	3
2700	0.151	4	0.124	4	0.115	4	0.108	4	0.104	4
2900	0.199	4	0.159	4	0.145	4	0.134	4	0.129	4
3100	0.251	4	0.200	4	0.182	4	0.166	4	0.158	4
3300	0.302	4	0.244	4	0.222	4	0.203	4	0.192	4
3500	0.345	4	0.289	4	0.264	4	0.241	4	0.229	4
3700	0.375	4	0.330	4	0.306	4	0.281	4	0.266	4
3900	0.393	4	0.364	4	0.343	4	0.318	4	0.304	4
4100	0.405	4	0.388	4	0.373	4	0.352	4	0.338	4
4300	0.414	4	0.405	4	0.395	4	0.379	4	0.368	4
4500	0.422	4	0.417	4	0.411	4	0.400	4	0.392	4

TABLE 6. $\mu = A \cdot 10^7$

T, K°	p, atm									
	0.1		0.5		1		2		3	
	A	r	A	r	A	r	A	r	A	r
1700	0.439	2	0.440	2	0.440	2	0.440	2	0.440	2
1800	0.438	2	0.439	2	0.439	2	0.439	2	0.439	2
1900	0.436	2	0.438	2	0.438	2	0.439	2	0.439	2
2100	0.428	2	0.433	2	0.435	2	0.436	2	0.437	2
2300	0.412	2	0.423	2	0.427	2	0.429	2	0.431	2
2500	0.386	2	0.406	2	0.412	2	0.418	2	0.420	2
2700	0.353	2	0.381	2	0.391	2	0.400	2	0.404	2
2900	0.317	2	0.352	2	0.365	2	0.377	2	0.383	2
3100	0.285	2	0.321	2	0.336	2	0.351	2	0.359	2
3300	0.258	2	0.293	2	0.309	2	0.324	2	0.333	2
3500	0.240	2	0.269	2	0.284	2	0.300	2	0.309	2
3700	0.230	2	0.250	2	0.263	2	0.278	2	0.287	2
3900	0.225	2	0.237	2	0.248	2	0.260	2	0.268	2
4100	0.222	2	0.229	2	0.236	2	0.246	2	0.253	2
4300	0.221	2	0.225	2	0.229	2	0.236	2	0.241	2
4500	0.221	2	0.223	2	0.225	2	0.230	2	0.233	2

TABLE 7. $X_{CO_2} = 4 \cdot 10^7$

T, °K	p, atm																			
	0.1		0.5		1		2		3		5		7		9		11		13	
	A	r	A	r	A	r	A	r	A	r	A	r	A	r	A	r	A	r	A	r
1700	0.993	0	0.996	0	0.997	0	0.998	0	0.998	0	0.998	0	0.998	0	0.998	0	0.999	0	0.999	0
1800	0.986	0	0.992	0	0.993	0	0.995	0	0.995	0	0.996	0	0.997	0	0.997	0	0.997	0	0.997	0
1900	0.973	0	0.984	0	0.987	0	0.990	0	0.991	0	0.993	0	0.993	0	0.994	0	0.994	0	0.995	0
2100	0.921	0	0.953	0	0.962	0	0.970	0	0.974	0	0.978	0	0.980	0	0.982	0	0.983	0	0.984	0
2300	0.815	0	0.886	0	0.909	0	0.927	0	0.936	0	0.945	0	0.951	0	0.955	0	0.958	0	0.960	0
2500	0.649	0	0.773	0	0.815	0	0.849	0	0.867	0	0.886	0	0.898	0	0.905	0	0.911	0	0.916	0
2700	0.449	0	0.617	0	0.679	0	0.734	0	0.763	0	0.795	0	0.814	0	0.827	0	0.838	0	0.845	0
2900	0.266	0	0.442	0	0.518	0	0.589	0	0.628	0	0.673	0	0.701	0	0.721	0	0.736	0	0.748	0
3100	0.136	0	0.283	0	0.358	0	0.435	0	0.479	0	0.534	0	0.569	0	0.594	0	0.613	0	0.629	0
3300	0.622	-1	0.164	0	0.226	0	0.296	0	0.339	0	0.396	0	0.433	0	0.461	0	0.482	0	0.501	0
3500	0.265	-1	0.870	-1	0.131	0	0.187	0	0.224	0	0.275	0	0.310	0	0.337	0	0.359	0	0.377	0
3700	0.112	-1	0.437	-1	0.718	-1	0.141	0	0.139	0	0.180	0	0.210	0	0.234	0	0.254	0	0.271	0
3900	0.490	-2	0.214	-1	0.378	-1	0.631	-1	0.827	-1	0.113	0	0.136	0	0.156	0	0.172	0	0.186	0
4100	0.227	-2	0.106	-1	0.197	-1	0.349	-1	0.477	-1	0.685	-1	0.855	-1	0.999	-1	0.112	0	0.124	0
4300	0.112	-2	0.540	-2	0.104	-1	0.193	-1	0.271	-1	0.408	-1	0.524	-1	0.626	-1	0.718	-1	0.801	-1
4500	0.587	-3	0.288	-2	0.562	-2	0.108	-1	0.155	-1	0.241	-1	0.318	-1	0.388	-1	0.452	-1	0.511	-1

TABLE 8. $X_{O_2} = 4 \cdot 10^7$

T, °K	p, atm																			
	0.1		0.5		1		2		3		5		7		9		11		13	
	A	r	A	r	A	r	A	r	A	r	A	r	A	r	A	r	A	r	A	r
1700	0.225	-2	0.132	-2	0.105	-2	0.833	-3	0.728	-3	0.614	-3	0.549	-3	0.505	-3	0.472	-3	0.447	-3
1800	0.465	-2	0.273	-2	0.217	-2	0.173	-2	0.151	-2	0.127	-2	0.114	-2	0.105	-2	0.980	-3	0.927	-3
1900	0.886	-2	0.523	-2	0.416	-2	0.331	-2	0.289	-2	0.244	-2	0.218	-2	0.201	-2	0.188	-2	0.178	-2
2100	0.259	-1	0.156	-1	0.125	-1	0.995	-2	0.872	-2	0.738	-2	0.661	-2	0.608	-2	0.570	-2	0.539	-2
2300	0.592	-1	0.370	-1	0.299	-1	0.241	-1	0.212	-1	0.180	-1	0.162	-1	0.149	-1	0.140	-1	0.133	-1
2500	0.107	0	0.719	-1	0.594	-1	0.487	-1	0.432	-1	0.371	-1	0.335	-1	0.310	-1	0.291	-1	0.276	-1
2700	0.154	0	0.116	0	0.994	-1	0.838	-1	0.754	-1	0.656	-1	0.597	-1	0.556	-1	0.525	-1	0.500	-1
2900	0.175	0	0.157	0	0.141	0	0.124	0	0.114	0	0.101	0	0.935	-1	0.878	-1	0.835	-1	0.799	-1
3100	0.157	0	0.177	0	0.171	0	0.159	0	0.150	0	0.138	0	0.130	0	0.123	0	0.118	0	0.114	0
3300	0.111	0	0.168	0	0.178	0	0.178	0	0.174	0	0.167	0	0.160	0	0.155	0	0.150	0	0.146	0
3500	0.638	-1	0.135	0	0.159	0	0.175	0	0.179	0	0.180	0	0.178	0	0.175	0	0.173	0	0.170	0
3700	0.320	-1	0.925	-1	0.124	0	0.152	0	0.164	0	0.175	0	0.179	0	0.181	0	0.181	0	0.181	0
3900	0.153	-1	0.559	-1	0.851	-1	0.117	0	0.135	0	0.154	0	0.164	0	0.170	0	0.174	0	0.177	0
4100	0.746	-2	0.314	-1	0.530	-1	0.815	-1	0.101	0	0.123	0	0.138	0	0.148	0	0.155	0	0.160	0
4300	0.379	-2	0.173	-1	0.312	-1	0.526	-1	0.686	-1	0.913	-1	0.107	0	0.118	0	0.127	0	0.135	0
4500	0.202	-2	0.961	-2	0.181	-1	0.326	-1	0.445	-1	0.633	-1	0.776	-1	0.889	-1	0.982	-1	0.106	0

TABLE 9. $X_{CO} = 4 \cdot 10^6$

T, °K	p, atm									
	0.1		0.5		1		2		3	
	A	r	A	r	A	r	A	r	A	r
1700	0.451	-2	0.264	-2	0.210	-2	0.167	-2	0.146	-2
1800	0.934	-2	0.548	-2	0.435	-2	0.346	-2	0.302	-2
1900	0.178	-1	0.105	-1	0.834	-2	0.663	-2	0.579	-2
2100	0.526	-1	0.314	-1	0.251	-1	0.200	-1	0.175	-1
2300	0.122	0	0.753	-1	0.607	-1	0.487	-1	0.428	-1
2500	0.229	0	0.149	0	0.122	0	0.997	-1	0.882	-1
2700	0.353	0	0.250	0	0.210	0	0.175	0	0.156	0
2900	0.455	0	0.357	0	0.312	0	0.268	0	0.243	0
3100	0.510	0	0.447	0	0.406	0	0.362	0	0.335	0
3300	0.524	0	0.502	0	0.476	0	0.441	0	0.417	0
3500	0.519	0	0.524	0	0.514	0	0.494	0	0.478	0
3700	0.510	0	0.524	0	0.526	0	0.520	0	0.512	0
3900	0.505	0	0.517	0	0.524	0	0.527	0	0.520	0
4100	0.503	0	0.510	0	0.517	0	0.523	0	0.526	0
4300	0.501	0	0.506	0	0.510	0	0.517	0	0.521	0
4500	0.501	0	0.503	0	0.506	0	0.511	0	0.515	0

TABLE 10. $X_O = 4 \cdot 10^6$

T, °K	p, atm									
	0.1		0.5		1		2		3	
	A	r	A	r	A	r	A	r	A	r
1700	0.666	-5	0.228	-5	0.144	-5	0.906	-6	0.691	-6
1800	0.261	-4	0.894	-5	0.563	-5	0.355	-5	0.271	-5
1900	0.882	-4	0.303	-4	0.191	-4	0.120	-4	0.920	-5
2100	0.703	-3	0.244	-3	0.154	-3	0.974	-4	0.744	-4
2300	0.379	-2	0.134	-2	0.853	-3	0.541	-3	0.415	-3
2500	0.149	-1	0.546	-2	0.351	-2	0.225	-2	0.173	-2
2700	0.445	-1	0.173	-1	0.113	-1	0.734	-2	0.568	-2
2900	0.104	0	0.440	-1	0.300	-1	0.200	-1	0.154	-1
3100	0.196	0	0.932	-1	0.648	-1	0.442	-1	0.351	-1
3300	0.302	0	0.166	0	0.121	0	0.855	-1	0.691	-1
3500	0.391	0	0.254	0	0.195	0	0.145	0	0.120	0
3700	0.446	0	0.339	0	0.278	0	0.217	0	0.184	0
3900	0.475	0	0.405	0	0.354	0	0.293	0	0.257	0
4100	0.488	0	0.448	0	0.411	0	0.360	0	0.326	0
4300	0.494	0	0.471	0	0.448	0	0.411	0	0.384	0
4500	0.497	0	0.484	0	0.470	0	0.446	0	0.425	0

TABLE 11. $X_C = 4 \cdot 10^7$

T, °K	p, atm															
	0.1		0.5		1		2		3		5		7		9	
	A	r	A	r	A	r	A	r	A	r	A	r	A	r	A	r
1700	0.488	-22	0.167	-22	0.105	-22	0.663	-23	0.506	-23	0.360	-23	0.288	-23	0.243	-23
1800	0.186	-20	0.635	-21	0.400	-21	0.252	-21	0.193	-21	0.137	-21	0.109	-21	0.926	-22
1900	0.481	-19	0.165	-19	0.104	-19	0.655	-20	0.500	-20	0.356	-20	0.284	-20	0.241	-20
2100	0.127	-19	0.436	-17	0.275	-17	0.174	-17	0.133	-17	0.945	-18	0.756	-18	0.639	-18
2300	0.124	-14	0.434	-15	0.275	-15	0.174	-15	0.133	-15	0.948	-16	0.759	-16	0.642	-16
2500	0.571	-13	0.203	-13	0.129	-13	0.823	-14	0.631	-14	0.452	-14	0.362	-14	0.307	-14
2700	0.144	-11	0.526	-12	0.338	-12	0.217	-12	0.167	-12	0.120	-12	0.964	-13	0.818	-13
2900	0.228	-10	0.848	-11	0.551	-11	0.357	-11	0.276	-11	0.200	-11	0.161	-11	0.137	-11
3100	0.254	-9	0.939	-10	0.614	-10	0.401	-10	0.312	-10	0.227	-10	0.184	-10	0.157	-10
3300	0.223	-8	0.778	-9	0.507	-9	0.332	-9	0.259	-9	0.190	-9	0.154	-9	0.132	-9
3500	0.168	-7	0.521	-8	0.332	-8	0.216	-8	0.168	-8	0.123	-8	0.100	-8	0.861	-9
3700	0.111	-6	0.300	-7	0.184	-7	0.116	-7	0.898	-8	0.654	-8	0.532	-8	0.456	-8
3900	0.645	-6	0.155	-6	0.898	-7	0.545	-7	0.414	-7	0.297	-7	0.240	-7	0.205	-7
4100	0.327	-5	0.724	-6	0.399	-6	0.230	-6	0.171	-6	0.119	-6	0.952	-7	0.808	-7
4300	0.145	-4	0.306	-5	0.162	-5	0.895	-6	0.645	-6	0.437	-6	0.342	-6	0.287	-6
4500	0.566	-4	0.117	-4	0.604	-5	0.322	-5	0.226	-5	0.148	-5	0.114	-5	0.943	-6

TABLE 12.

Component	Reaction	Dissociation energy at 0°K, cal/mole	$H_T = 0$	Component	Reaction	Dissociation energy at 0°K, cal/mole	$H_T = 0$
CO ₂	$-\text{CO}_2 + \text{CO} + \frac{1}{2} \text{O}_2 \rightleftharpoons 0$	66767	0	C ₂	$-\text{C}_2 + 2\text{C} \rightleftharpoons 0$	143170	—
CO	$-\text{CO} + \text{C} + \text{O} \rightleftharpoons 0$	255790	66767	O	—	—	58986
O ₂	$-\text{O}_2 + 2\text{O} \rightleftharpoons 0$	117973	0	C	—	—	263571

Designate by ρ, u, p, T, μ, h the density, velocity, pressure, temperature, molecular weight, and specific enthalpy of the gas.

The subscripts 0, 1, 2, 3, 4, 5 refer respectively to the gas state ahead of the incident wave, behind the incident shock wave, behind the reflected wave, behind the Mach wave, ahead of the Mach wave (this state coincides with state 0), and behind the attached wave.

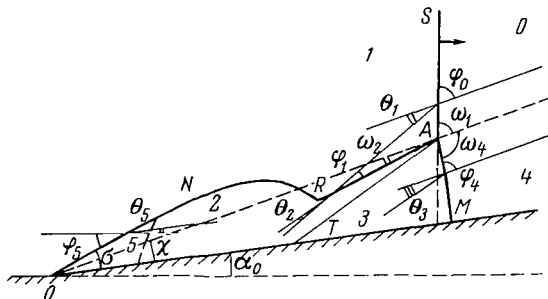


FIGURE 1. Diffraction pattern of a shock wave on a wedge.

Consider a coordinate frame linked with the wedge. The attached wave ON is immobile in this frame. The gas flows into the wave at an angle φ_5 and is deflected through an angle θ_5 equal to the wedge angle α_0 .

It follows from the continuity equation that

$$\theta_5 = \arctg \left[\frac{\left(1 - \frac{\rho_1}{\rho_5}\right) \tg \varphi_5}{1 + \frac{\rho_1}{\rho_5} \tg^2 \varphi_5} \right].$$

First the gas parameters in region 1 are determined from the velocity of the incident wave (cf. Figure 1, Tables 1–4), i. e., we obtain the gas velocity u_1 in the coordinate frame linked with the wedge, and the density ρ_1 . We then specify some angle φ_5 of the attached wave; the normal component of the flow incident on the attached wave is then

$$u_{in}' = u_1 \sin \varphi_5.$$

In the coordinate frame linked with the gas particles in region 1 it is the shock wave which will move at this velocity u_{in}' . The parameters behind it are determined from Tables 1–4. Substituting the values obtained in the continuity equation, we obtain $\theta_5 = \alpha_0$. Tables 13–16 give the values thus obtained for the angle φ_5 of the attached wave at the wedge and the pressure and temperature behind the wave, p_5 and T_5 , as a function of the wedge angle.

The pressure and temperature in the gas stream impinging on the wedge and the velocity of the incident shock wave are given.

The last line gives the "limiting" values of the parameters, which are determined with a lower accuracy than the other parameters. The term "limiting" implies the flow conditions under which the attached shock becomes detached. It is seen from the calculations that the physicochemical transformations sometimes substantially alter the pattern of the gas-dynamic

TABLE 13. CO₂. Variant I

θ_s	u_s , km/sec											
	1.9			2.1			2.5			2.8		
	φ_s	p_s , atm	T_s , °K	φ_s	p_s , atm	T_s , °K	φ_s	p_s , atm	T_s , °K	φ_s	p_s , atm	T_s , °K
0°00'	20°54'	0.995	1770	20°06'	1.22	2000	17°54'	1.76	2385	16°54'	2.22	2620
5 00	24 36	1.31	1830	23 06	1.63	2120	21 24	2.50	2450	20 06	3.12	2680
10 00	28 12	1.72	1890	26 48	2.18	2150	25 00	3.34	2520	23 48	4.22	2750
15 00	32 24	2.26	1970	31 00	2.86	2200	28 48	4.32	2590	27 36	5.72	2830
20 00	37 06	2.86	2050	35 18	3.60	2270	33 24	5.60	2660	32 12	7.40	2910
25 00	42 12	3.60	2120	40 18	4.53	2340	38 00	7.04	2720	37 00	9.40	2990
30 00	47 36	4.38	2210	45 36	5.60	2420	43 00	8.60	2800	41 48	11.65	3070
35 00	54 12	5.26	2285	51 36	6.72	2490	48 48	10.5	2880	47 24	14.2	3150
40 00	58 24	6.40	2370	55 36	7.94	2570	52 24	12.45	2970	—	—	—
41 30	41 48	7.10	2430	—	—	—	—	—	—	—	—	—
44 00	—	—	—	70	9.7	2680	—	—	—	—	—	—

TABLE 14. CO₂. Variant II

θ_s	u_s , km/sec											
	1.9			2.2			2.5			2.8		
	φ_s	p_s , atm	T_s , °K	φ_s	p_s , atm	T_s , °K	φ_s	p_s , atm	T_s , °K	φ_s	p_s , atm	T_s , °K
0°00'	21°24'	0.71	1390	20°30'	0.98	1780	20°30'	1.33	2220	19°48'	1.72	2730
5 00	25 00	0.98	1420	25 00	1.30	1850	24 06	1.82	2330	23 06	2.37	2850
10 00	28 36	1.24	1450	29 00	1.72	1930	27 48	2.44	2430	27 00	3.20	2980
15 00	33 00	1.54	1480	33 00	2.24	2025	31 48	3.14	2535	31 12	4.20	3125
20 00	37 48	1.90	1540	37 42	2.86	2120	36 24	4.00	2645	35 48	5.40	3275
25 00	43 12	2.36	1610	42 48	3.55	2210	41 36	5.05	2770	41 00	6.80	3430
30 00	49 06	2.86	1690	48 30	4.36	2320	47 00	6.20	2910	46 18	8.33	3620
35 00	56 30	3.50	1790	55 48	5.35	2470	53 36	7.44	3080	52 48	10.1	3830
40 00	—	—	—	—	—	—	63 12	9.20	3295	61 00	12.3	4080
38 36	—	—	—	—	—	—	—	—	—	—	—	—
39 24	—	—	—	69 00	6.85	2660	—	—	—	—	—	—
40 54	—	—	—	—	—	—	67 00	9.9	3380	—	—	—

TABLE 15. CO₂. Variant II'

θ_s	u_0 , km/sec								
	1.9			2.2			2.5		
	φ_s	p_s , atm	T_s , °K	φ_s	p_s , atm	T_s , °K	φ_s	p_s , atm	T_s , °K
0°00'	22°48'	0.99	1900	22°00'	1.34	2390	21°12'	1.74	2970
5 00	26 24	1.34	1990	25 12	1.80	2490	24 36	2.34	3110
10 00	30 12	1.72	2080	29 00	2.36	2610	28 24	3.10	3260
15 00	34 12	2.20	2170	33 15	3.00	2740	32 30	4.02	3420
20 00	38 48	2.76	2260	38 00	3.82	2890	37 00	5.10	3600
25 00	44 12	3.47	2380	43 12	4.84	3040	42 30	6.4	3800
30 00	50 36	4.30	2500	49 24	6.00	3215	48 24	7.88	4040
35 00	58 48	5.26	2680	57 00	7.28	3445	55 42	9.60	4300
37 18	68 00	6.10	2840	—	—	—	—	—	—
38 06	—	—	—	67 12	8.80	3680	—	—	—

TABLE 16. N₂. Variant II

θ_s	u_0 , km/sec														
	1.3			1.6			1.9			2.2			2.5		
	φ_s	p_s , atm	T_s , °K	φ_s	p_s , atm	T_s , °K	φ_s	p_s , atm	T_s , °K	φ_s	p_s , atm	T_s , °K	φ_s	p_s , atm	T_s , °K
10°00'	49°36'	0.40	1100	43°24'	0.64	1520	41°06'	0.96	2010	38°48'	1.29	2550	37°48'	1.76	3140
15 00	61 36	0.57	1240	51 24	0.84	1640	47 36	1.23	2140	44 24	1.62	2720	43 36	2.22	3350
20 00	—	—	—	—	—	—	56 30	1.56	2300	51 48	2.1	2900	50 18	2.78	3580
25 00	—	—	—	—	—	—	—	—	—	—	—	—	60 48	3.60	3930
19 00	—	—	—	65 00	1.20	1820	—	—	—	—	—	—	—	—	—
22 12	—	—	—	—	—	—	65 30	1.85	2420	—	—	—	—	—	—
24 36	—	—	—	—	—	—	—	—	—	65 48	2.93	3180	—	—	—
25 36	—	—	—	—	—	—	—	—	—	—	—	—	66 00	3.85	4010

process. Thus, for a velocity of the incident shock wave equal to $1.9 \cdot 10^5$ m/sec (Figure 2), the change in the specific-heat ratio γ caused by exciting the vibrational levels of the CO_2 molecules causes the shock at the wedge apex to remain attached up to wedge angles $\alpha_0 = \theta_0 = 41^\circ 31'$.

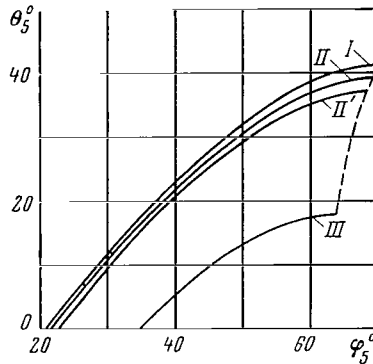


FIGURE 2. Angle of the attached wave as a function of the wedge angle $\alpha_0 = \theta_0$ for diffraction of a shock wave at the wedge:

Gas CO_2 , $u_0 = 1.9 \cdot 10^5$ m/sec. Curves I, II, II' were calculated for the corresponding variants, and curve III for an ideal gas $\gamma = 1.4$.

TABLE 17. CO_2 . Variant I

ω_1	ω_2	ω_3	$T_2, ^\circ\text{K}$	$P_2 = P_3, \text{atm}$	$T_3, ^\circ\text{K}$	$u_M \frac{\text{km}}{\text{sec}}$	θ_3
$u_0 = 1.9 \text{ km/sec}$ $P_1 = 0.995 \text{ atm}$ $T_1 = 1770^\circ \text{ K}$							
35°	7°36'	91°12'	2085	3.12	2950	3.31	16°48'
40	—10 00	91 48	2005	2.50	2730	2.97	22 00
45	—12 12	92 30	1940	2.05	2550	2.70	27 30
50	—12 48	93 24	1900	1.74	2380	2.49	32 18
55	—12 42	94 30	1860	1.51	2240	2.32	37 48
60	—10 00	95 54	1830	1.33	2110	2.19	42 42
65	—4 30	98 12	1805	1.205	1980	2.08	48 24
$u_0 = 2.1 \text{ km/sec}$ $P_1 = 1.22 \text{ atm}$ $T_1 = 2000^\circ \text{ K}$							
45°	—13°36'	92°24'	2170	2.50	2730	2.97	28°18'
50	—14 36	93 06	2130	2.115	2570	2.74	33 06
55	—14 36	94 12	2100	1.83	2440	2.56	38 30
60	—12 42	95 30	2070	1.64	2320	2.41	43 30
65	—6 42	97 18	2050	1.48	2220	2.30	48 06
$u_0 = 2.5 \text{ km/sec}$ $P_1 = 1.75 \text{ atm}$ $T_1 = 2385^\circ \text{ K}$							
50°	—18°30'	92°54'	2500	3.00	2930	3.26	35°42'
55	—19 00	93 54	2460	2.63	2780	3.04	41 00
60	—17 30	94 54	2450	2.33	2670	2.88	45 30
65	—13 54	96 36	2425	2.12	2580	2.74	50 24

4. THE TRIPLE CONFIGURATION USING SHOCK POLARS

The system of waves in the neighborhood of a triple point was calculated using shock polars [8].

Consider a coordinate frame linked to the triple point (cf. Figure 1). In such a frame the gas flows into the incident wave with velocity $u_0/\sin \omega_1$, at an angle $\varphi_0 = \omega_1$. During its transition through the incident wave the flow is deflected through an angle θ_1 . This angle is determined from the continuity equation

$$\frac{\lg (\varphi_0 - \theta_1)}{\lg \varphi_0} = \frac{\rho_0}{\rho_1}.$$

The gas velocity behind the shock wave SA in the coordinate frame linked with the triple point is

$$\bar{u}_1 = \sqrt{u_1^2 + u_0^2 \operatorname{ctg}^2 \varphi_0},$$

where \bar{u}_1 is the gas velocity in the coordinate frame linked with the incident wave.

Construct the shock polar for the reflected wave in (p, θ) coordinates. Let the reflected wave lie at an angle φ_1 to the flow incident with velocity \bar{u}_1 ; the normal component of the flow velocity will then be $u_{1n} = \bar{u}_1 \sin \varphi_1$.

The value of p_2 behind the reflected wave is determined from Tables 1—4 and θ_2 from the continuity equation.

For different φ_1 , a number of values of u_{1n} can be derived for corresponding θ_2 and p_2 , i. e., the shock polar in the p - θ plane. Construct now the shock polar for the Mach wave. If the Mach wave lies at an angle φ_4 to the incident flow, the normal velocity component to the Mach wave will be $u_M = u_0 (\sin \varphi_4 / \sin \omega_1)$.

By assuming different values for u_M , one can construct the shock polar for the Mach wave in (p, θ) coordinates, using Tables 1—4 and the continuity equation.

In order to find the required solution the compatibility condition must be fulfilled, namely, equality of the pressures and parallelism of the flows in regions 2 and 3; $p_2 = p_3$ and $\theta_3 = \theta_1 - \theta_2$.

These conditions are fulfilled at the intersection point of the shock polars for the reflected wave and the Mach wave.

The intersection point of the polars yields the required values of u_M and u_{1n} .

All the angles of the Mach configuration are determined from the expressions

$$\begin{aligned} \sin \varphi_3 &= \frac{\bar{u}_{1n}}{u_1}, & \omega_2 &= \varphi_2 - \theta_1, \\ \sin \varphi_4 &= \frac{u_M}{u_0} \sin \omega_1, & \omega_3 &= \varphi_4. \end{aligned}$$

Tables 17—20 give the results obtained using this method, and also the values of the gas-dynamic parameters and the angles between the shock waves forming the triple configuration as a function of the velocity of the incident wave.

TABLE 18. CO₂. Variant II

ω_1	ω_2	ω_3	$T_1, ^\circ\text{K}$	$p_1 = p_2, \text{ atm}$	$T_1, ^\circ\text{K}$	$u_M \frac{\text{km}}{\text{sec}}$	θ_1
$u_0 = 1.0 \text{ km/sec}$			$T_1 = 767^\circ \text{ K}$		$P_1 = 0.27 \text{ atm}$		
30°	2°54'	90°48'	1000	1.09	1920	2.00	6°54'
35	1 00	91 30	945	0.83	1560	1.74	11 54
40	—0 48	92 24	905	0.66	1340	1.55	17 06
45	—0 48	93 18	870	0.54	1180	1.41	21 54
50	—0 24	94 30	845	0.46	1060	1.30	26 30
55	1 06	95 54	830	0.40	970	1.21	30 54
60	8 12	97 12	820	0.36	900	1.14	35 18
65	24 12	99 48	810	0.32	850	1.09	39 00
$u_0 = 1.3 \text{ km/sec}$			$T_1 = 1055^\circ \text{ K}$		$P_1 = 0.46 \text{ atm}$		
30°	—1°11'	91°06'	1360	1.86	3360	2.60	9°30'
35	—3 46	91 36	1290	1.41	2350	2.26	15 06
40	—4 44	92 24	1235	1.12	1950	2.02	20 00
45	—6 33	93 24	1200	0.92	1690	1.83	25 42
50	—6 08	94 24	1150	0.78	1500	1.69	30 24
55	—5 24	95 48	1120	0.68	1370	1.58	35 54
60	—1 47	97 42	1095	0.61	1270	1.48	41 00
65	1 40	100 00	1090	0.55	1180	1.41	45 06
$u_0 = 1.9 \text{ km/sec}$			$T_1 = 1390^\circ \text{ K}$		$P_1 = 0.706 \text{ atm}$		
30°	—4°36'	91°00'	2280	4.03	5560	3.80	11°54'
35	—7 24	91 36	2150	3.06	4380	3.30	17 12
40	—10 06	92 18	2050	2.41	3600	2.95	22 42
45	—12 00	93 00	1980	1.98	3060	2.68	28 06
50	—12 48	93 54	1920	1.68	2690	2.47	33 12
55	—12 30	95 00	1870	1.47	2420	2.31	38 18
60	—10 00	96 18	1840	1.30	2210	2.18	43 06
65	—4 30	98 24	1820	1.17	2030	2.07	48 12
$u_0 = 2.2 \text{ km/sec}$			$T_1 = 1780^\circ \text{ K}$		$P_1 = 0.98 \text{ atm}$		
35°	—8°42'	91°36'	2660	5.650	4.12	3.83	17°48'
40	—11 30	92 12	2540	4.620	3.28	3.42	23 18
45	—13 36	92 54	2470	3.870	2.65	3.11	28 54
50	—14 42	93 48	2400	3.430	2.27	2.86	34 36
55	—15 00	94 54	2340	3.060	1.97	2.67	39 54
60	—12 54	96 18	2300	2.790	1.75	2.52	44 48
65	—8 30	98 06	2260	2.560	1.59	2.40	49 24
$u_0 = 2.5 \text{ km/sec}$			$T_1 = 2220^\circ \text{ K}$		$P_1 = 1.33 \text{ atm}$		
40°	—12°06'	92°12'	3110	5.800	4.24	3.89	23°48'
45	—14 12	92 54	3030	4.880	3.50	3.53	28 54
50	—15 48	93 48	2935	4.269	2.92	3.26	34 42
55	—15 48	94 30	2880	3.770	2.55	3.04	39 42
60	—14 12	95 48	2835	3.440	2.28	2.87	44 42
65	—9 42	97 54	2790	3.165	2.05	2.73	50 24

TABLE 19. CO₂. Variant II

ω_1	ω_2	ω_3	$T_2, ^\circ\text{K}$	$p_2 = p_3, \text{ atm}$	$T_3, ^\circ\text{K}$	$u_M, \frac{\text{km}}{\text{sec}}$	ϕ_3
$u_0 = 1.9 \text{ km/sec}$			$p_1 = 0.986 \text{ atm}$		$T_1 = 1900^\circ \text{ K}$		
40°	-8°36'	92°24'	2220	2.40	3970	2.95	21°42'
45	-11 00	93 18	2125	1.97	3340	2.68	27 30
50	-12 18	94 18	2055	1.67	2900	2.47	32 54
55	-12 18	95 36	2010	1.46	2590	2.31	38 24
60	-10 00	97 06	1975	1.30	2360	2.18	43 30
65	4 30	99 12	1950	1.17	2170	2.07	47 54
$u_0 = 2.2 \text{ km/sec}$			$p_1 = 1.33 \text{ atm}$		$T_1 = 2390^\circ \text{ K}$		
50°	-13°00'	94°12'	2590	2.25	3760	2.86	33°42'
55	-12 42	95 24	2530	1.97	3320	2.67	38 48
60	-10 42	96 48	2490	1.75	3010	2.52	43 42
65	-5 06	98 54	2450	1.57	2770	2.40	48 36
$u_1 = 2.5 \text{ km/sec}$			$p_1 = 1.72 \text{ atm}$		$T_1 = 2965^\circ \text{ K}$		
60°	-11°12'	96°42'	3090	2.26	3760	2.87	44°24'
65	-6 06	98 42	3030	2.05	3440	2.73	49 18

TABLE 20. CO₂. Variant II

ω_1	ω_2	ω_3	$T_2, ^\circ\text{K}$	$T_3, ^\circ\text{K}$	$p_2 = p_3, \text{ atm}$	$u_M \text{ km/sec}$
$u_0 = 1.3 \text{ km/sec}$			$T_1 = 1030^\circ \text{ K}$		$p_1 = 0.275 \text{ atm}$	
30°	9°54'	90°36'	1560	3000	1.13	2.60
35	8 30	91 36	1415	2380	0.85	2.26
45	8 12	94 12	1230	1707	0.55	1.83
50	10 12	95 30	1190	1500	0.465	1.69
55	14 12	97 48	1142	1344	0.405	1.57
60	24 12	100 54	1110	1230	0.36	1.48
65	44 54	108 54	1050	1100	0.30	1.36
$u_0 = 1.6 \text{ km/sec}$			$T_1 = 1400^\circ \text{ K}$		$p_1 = 0.416 \text{ atm}$	
30°	7°06'	90°54'	2110	4240	1.70	3.20
35	5 06	91 54	1910	3360	1.30	2.79
40	4 00	93 00	1745	2790	1.03	2.48
45	3 42	94 24	1630	2360	0.84	2.26
50	4 36	95 54	1560	2080	0.71	2.08
55	7 06	97 54	1495	1850	0.61	1.93
60	13 42	100 24	1460	1680	0.54	1.82
$u_0 = 1.9 \text{ km/sec}$			$T_1 = 1800^\circ \text{ K}$		$p_1 = 0.59 \text{ atm}$	
35°	2°24'	92°00'	2390	4500	1.82	3.31
40	1 36	93 06	2240	3680	1.445	2.95
45	1 24	94 18	2135	3140	1.20	2.68
50	2 06	95 54	2035	2740	1.01	2.47
55	4 18	95 48	1965	2440	0.87	2.30
60	7 12	100 12	1900	2220	0.77	2.16
65	17 18	103 30	1835	2020	0.685	2.04
$u_0 = 2.2 \text{ km/sec}$			$T_1 = 2270^\circ \text{ K}$		$p_1 = 0.80 \text{ atm}$	
40°	-0°12'	93°06'	2830	4720	1.94	3.42
45	-0 36	94 18	2680	4080	1.60	3.10
50	0 00	95 36	2580	3500	2.14	2.86
55	2 12	97 18	2440	3120	1.18	2.66
60	6 48	99 36	2380	2800	1.04	2.50
$u_0 = 2.5 \text{ km/sec}$			$T_1 = 2810^\circ \text{ K}$		$p_1 = 1.025 \text{ atm}$	
50°	-1°34'	95°48'	3160	4340	1.75	3.25
55	0 42	97 24	3050	3850	1.53	3.03
60	5 29	99 30	2965	3480	1.35	2.85

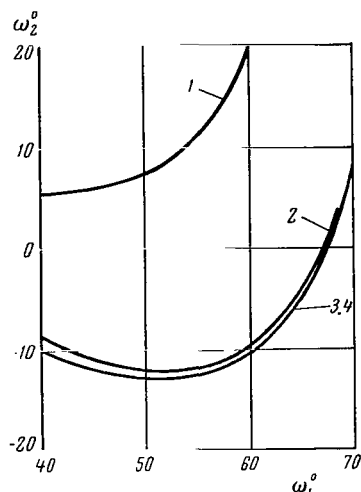


FIGURE 3. The reflection angle ω_2 vs. the incidence angle ω_1 :

1—ideal gas $\gamma = 1.4$; 2—unexcited asymmetric vibrations of the molecules and no dissociation; 3, 4—the curves overlap, the vibrations are excited, there is no dissociation, and complete equilibrium.

The results shown in Figure 3 indicate that under certain conditions the angle ω_2 becomes negative, i. e., the reflected wave is situated lower than the motion trajectory of the triple point. Under these conditions the appearance of a double Mach configuration becomes unavoidable.

Bibliography

1. Gvozdeva, L.G. and O.A. Predvoditeleva. Eksperimental'noe issledovanie makhovskogo otrazheniya udarnykh voln pri skorosti 1000—3000 m/sec v uglekislom gaze, azote i vozdukhe (Experimental Study of the Mach Reflection of Shock Waves at Velocities of 1000—3000 m/sec in Carbon Dioxide, Nitrogen, and Air).—Doklady AN SSSR, Vol. 163, No. 5. 1965.
2. Gvozdeva, L.G. and O.A. Predvoditeleva. Osobennosti makhovskogo otrazheniya udarnykh voln, dvizhushchikhsya v uglekislom gaze so skorostyami poryadka 2000 m/sec (Special Features of the Mach Reflection of Shock Waves Propagating in Carbon Dioxide and Nitrogen at Velocities of the Order of 2000 m/sec).—Sbornik "Issledovaniya po fizicheskoi gazodinamike," Moskva, Izdatel'stvo "Nauka." 1966.
3. Zel'dovich, Ya.B. and Yu.P. Raizer. Fizika udarnykh voln i vysokotemperaturnykh gidrodinamicheskikh yavlenii (Physics of Shock Waves and High-Temperature Hydrodynamic Phenomena).—Moskva, Fizmatgiz. 1963.

4. Rozhdestvenskii, I.B. Termodinamicheskie i gazodinamicheskie svoistva potoka vozdukha za pryamym skachkom uplotneniya s uchetom dissotsiatsii i ionizatsii vozdukha (Thermodynamic and Gas-Dynamic Properties of the Air Flow behind a Normal Compression Shock Allowing for the Dissociation and Ionization of the Air).—Sbornik "Fizicheskaya gazodinamika i teploobmen", Moskva, Izdatel'stvo AN SSSR. 1959.
5. Bazhenova, T.V. and O.A. Predvoditeleva. Znacheniya parametrov vozdukha za pryamym skachkom uplotneniya i za otrazhennoi udarnoi volnoi pri ravnovesnoi i zamorozhennoi dissotsiatsii (Values of the Air Parameters behind a Normal Compression Shock and Behind a Reflected Shock Wave at Equilibrium and Frozen Dissociation).—Sbornik "Fizicheskaya gazodinamika i teploobmen," Moskva, Izdatel'stvo AN SSSR. 1959.
6. Gurvich, L.V. et al. Termicheskie svoistva individual'nykh veshchestv (Thermal Properties of Individual Substances). Vol. II.—Moskva, Izdatel'stvo AN SSSR. 1962.
7. Naboko, I.M. Issledovanie sostoyaniya gaza za udarnoi volnoi po obtekaniyu prepyatstviya, pomeschennogo v udarnuyu trubu (Study of the Gas State behind a Shock Wave from the Flow Past an Obstacle in a Shock Tube).—Sbornik "Issledovaniya po fizicheskoi gazodinamike", Moskva, Izdatel'stvo AN SSSR. 1965.
8. Courant, R. and K. Friedrichs. Supersonic Flow and Shock Waves.—Interscience Publishers, New York. 1948.

G. N. Nikolaev, V. P. Popov

NONEQUILIBRIUM EXPANSION OF AIR IN SUPERSONIC NOZZLES

A basic difficulty exists when simulating the conditions of hypersonic flow in wind tunnels with a high air stagnation temperature. At high temperatures, air represents a mixture of products of dissociation of oxygen and nitrogen and a certain amount of nitric oxide NO (not taking into account admixtures of argon, carbon, dioxide, etc.). In addition to cooling of the gas and a decrease in its density, physicochemical processes take place in the course of the expansion, e.g., recombination of atomic components, reactions with the participation of NO, deactivation of the vibrational degrees of freedom of the molecules. These processes occur at a finite velocity, and it has been shown [1, 2] that for very rapid expansions in nozzles the degree of their completion may not correspond to the local values of the gas temperature and pressure. The gas state will be characterized by nonequilibrium values of the component concentrations. The main effect of this type is to freeze the oxygen dissociation levels, as a result of which the other thermo- and gas-dynamic flow parameters (pressure, temperature, flow and sound velocities) differ from the conditions of equilibrium expansion.

Since calculations of these phenomena are based on the rate constants of the chemical reactions, whose values are unreliable, it is important to study experimentally air expansion in nozzles.

The first published data showed that [3], according to static pressure measurements, the air flow in supersonic nozzles is not in equilibrium under certain conditions.

In this paper the Mach number (the parameter sensitive to nonequilibrium effects) is determined from the angle of inclination of the weak disturbance propagating in the supersonic flow. This method is considerably simpler, since the manufacture and assembly of pressure gages is very complicated. The disturbances are recorded optically, which enables nozzles of small dimensions to be used.

The values of the static pressure derived from experimental data on the Mach numbers agree qualitatively with the results in [3] and the recently published paper [7], in which the static pressure of the air flow in nozzles was measured, and results based on a more accurate theoretical analysis of the process were given.

1. EXPERIMENTAL SET-UP

The supersonic expansion of the air was studied by means of an intermittent laboratory wind tunnel, combining in its design a shock tube and a

supersonic nozzle. The shock wave was reflected from a wall with a small orifice (occupying in area 3 % of the total cross section of the shock-tube channel). The region behind the reflected shock served as an air reservoir, heated to a high temperature. The apparatus and method of study are described in /5, 6/. The state of the gas at the nozzle exit was determined

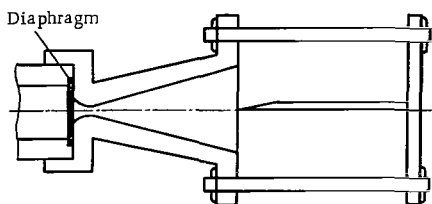


FIGURE 1. Mounting of the axisymmetrical nozzle and the model at the end of the shock tube.

by the Mach number of the flow, which in turn was found from the angle of inclination of the weak disturbance at a wedge located near the nozzle exit such that one of its edges was parallel to the plane of symmetry of the flow. The Mach angle was determined from photographs (taken with an exposure of the order of $3\mu\text{sec}$) of the flow pattern past the wedge, visualized by Töpler's method (Apparatus IAB-451).

The low-pressure chamber of the shock tube was separated from the nozzle by an additional thin diaphragm, burst by the oncoming shock wave. This diaphragm ensured the creation inside both the nozzle and pressure chamber of a sufficient rarefaction, independent of the initial pressure in the shock tube. As a result nozzles with a high degree of expansion of the flow could be used, independently of the pressure developed behind the reflected shock waves. Such a nozzle set-up attached to a shock tube is now widely used /7, 8, 9, 4/. Figure 1 shows the nozzle mounting at the end of the shock tube and the location of the diaphragm; the wedge was fastened on holders directly to the nozzle and was not connected to the pressure chamber. The latter was connected to the shock tube through a rubber sealing ring with the aid of a sleeve.



FIGURE 2. Exterior of the nozzle with model, set up at the end of the shock tube.

Figure 2 shows a nozzle with a wedge in its working position at the end of the shock tube (the pressure chamber is removed). Figure 3 depicts the working section of the apparatus in assembled form.

The nozzles were axisymmetrical, the cross-sectional radius along the axis obeying the hyperbolic law

$$r^2 = r_{cr}^2 + (K_N^2 / \pi) x^2,$$

where x is the distance from the critical section; r is the cross-sectional radius corresponding to the coordinate x ; $K_N = \sqrt{\pi} \operatorname{tg} \delta$; δ is the half-angle of the asymptotic cone of the unparted hyperboloid of revolution represented by the nozzle in its supersonic part.



FIGURE 3. Working section of an intermittent wind tunnel. The nozzle and model are inside a pressure chamber, vacuum-sealed tightly to the shock tube.

Table 1 gives the geometrical dimensions of the nozzles.

TABLE 1.

Nozzle expansion ratio	Cross-sectional diameter, mm		Distance from throat to exit, mm	Nozzle expansion ratio	Cross-sectional diameter, mm		Distance from throat to exit, mm
	throat	exit			throat	exit	
8.1	10.44	29.7	80	54.1	10.31	76.0	200
26.6	10.15	52.3	135	62.1	5.67	44.7	125

The full angle of the asymptotic cone was 20° in all cases.

2. EXPERIMENTAL DATA

A study was made of the efflux from a supersonic nozzle of air heated by a reflected shock wave. The gas state behind the reflected wave was calculated with the aid of tables of thermodynamic functions of air [10] based on the conservation laws on the shock wave, using the measured initial gas parameters (pressure and temperature) in a low-pressure chamber and the velocity of the traveling shock wave. A regime of flow was created such that in the region behind the reflected wave the air temperature was $T_0 = 5700^\circ\text{K}$ and the pressure $P_0 = 12$ atm, which was achieved for a temperature of 290°K and a pressure of 8 mm mercury in the low-pressure chamber, and a velocity of 3200 m/sec for the traveling shock wave. The following chemical composition (in molar fractions) corresponded to the air parameters behind the reflected wave: $X_{O_2} = 0.005$; $X_{N_2} = 0.616$; $X_{NO} = 0.036$; $X_{Ar} = 0.008$; $X_O = 0.302$; $X_N = 0.032$. The flow

Mach number at the nozzle exit was determined by the method described above.

In order to assign the measured value of M to some specific cross section of the flow it is insufficient to know just the ratio of the nozzle areas at the exit and throat [the expansion ratio]. The displacement thickness of the boundary layer was estimated (under the assumption of equilibrium flow) with the aid of relationships given in /11, 12/. The calculation made use of the effective gas enthalpy in the boundary layer /13, 14/.

The variation of M has been plotted in Figure 4 for three different nozzles, whose geometries are given in Table 1.

A complete analysis of the errors in the determination of M is given in /6/. The corresponding corrections due to the boundary layer have been taken into account when marking the points on the graph.

The experimental and theoretical values of the Mach number were compared by plotting curves corresponding to various assumptions about

the types of chemical transformations in the air flow inside the nozzle. All the curves were calculated to a one-dimensional approximation, which is quite common for studies of expanding flows in nozzles; the results coincide satisfactorily both with experimental data /4, 7, 8, 15/ and with more accurate calculations. The Mach number M was calculated as a function of the dimensionless nozzle area for an equilibrium air expansion, the initial state being a temperature of 6670°K and a pressure of 82 atm. The results of this calculation were compared with data obtained in /2/ by the method of finite differences for a nozzle of cross-sectional radius along the axis obeying a hyperbolic law, and a total angle of the asymptotic cone equal to 12°40' for the same initial

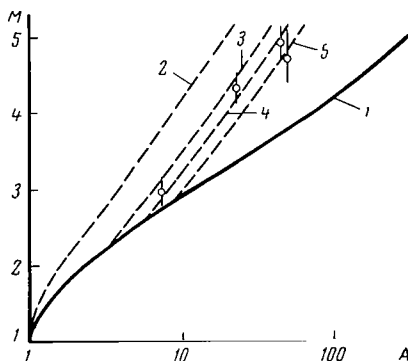


FIGURE 4. Mach number of the air flow as a function of the dimensionless nozzle area:

Stagnation temperature 5700°K in the reservoir; stagnation pressure 12 atm.

conditions. The values of M obtained by both methods did not differ by more than 6 %, which in our opinion justifies the use of the one-dimensional model.

The quantities M in Figure 4 were obtained by dividing the flow velocity by the frozen sound velocity, following the theoretical concepts about the propagation of disturbances in reactive media /16—20/, which have also been corroborated experimentally /21, 22/. According to these concepts, the slope of the Mach line is determined in some neighborhood of the source of weak disturbances in a supersonic flow by the velocity of the acoustic waves; translational and rotational degrees of freedom of the molecules are excited, while the gas does not undergo either vibrational excitations or any variation in its chemical composition.

Curve 1 in Figure 4 corresponds to the assumption of full thermodynamic equilibrium in the gas flow, i. e., infinite rate of the chemical reactions. Curve 2 assumes complete freezing of the composition, i. e., that the chemical reactions of formation of the molecules O_2 and N_2 and dissociation

of NO cannot be completed by the time the gas has flowed through the nozzle. It was assumed in the calculations that the vibrational degrees of freedom are permanently half-excited (the Lighthill model) /23/.

The experimental data presented in Figure 4 implies that the state of the gas flowing out of the nozzle not only differs noticeably from the equilibrium state, but does not correspond to the conditions of frozen flow. Such a process of nonequilibrium gas expansion, in which physicochemical transformations proceed at a finite rate, is described by a system of equations including the kinetic equations of the chemical reactions /1, 8/. The calculations involved are very cumbersome and the data on the reaction rates is unreliable; an attempt has therefore been made to simplify the description of the given process.

The simplification reduces basically to the following:

- 1) if the temperature is not too high, only one chemical reaction is important from the point of view of the energy balance, namely, the recombination of the atomic oxygen through triple collisions (the amount of atomic nitrogen and NO is negligible);
- 2) the nonequilibrium effects are only connected with the recombination of oxygen. As to the vibrational degrees of freedom, they are either in equilibrium with the translational and rotational degrees of freedom or are considered permanently half excited;
- 3) by analogy with the results /8, 24-27/ for simple diatomic dissociating gases, the instantaneous freezing model of oxygen recombination is considered sufficiently close to the real process. The possibilities and conditions of application of the instantaneous freezing model of one reaction to the processes taking place in gaseous mixtures, and in particular in air, are examined in detail in /25, 28/.

For temperatures up to 6000° air approximately satisfies the above-described model of physicochemical transformations at rapid expansions. It is possible in this case to calculate the variation in the parameters of the air expanding in the supersonic nozzle, assuming an overall equilibrium flow up to some section of the nozzle, after which the flow proceeds independently of any energy variation due to the chemical activity of the components.

The results of calculating the Mach numbers M by this approximate method are shown in Figure 4 (curves 3, 4, 5). They correspond to the interruption of the oxygen recombination, originating at a section of dimensionless area 2.7, 5.4, and 8.3.

A comparison of the obtained experimental data with these curves leads to the conclusion that a sharp slowing down of the oxygen recombination occurs at the nozzle section of area equal to 3-7 times the throat area. In our opinion the best representation of the experimental results is curve 4.

3. DISCUSSION OF THE RESULTS

Despite the wide scatter of the results, an attempt was made to compare them with the data of other experimental studies dealing with the nonequilibrium expansion of air. The distribution of the static pressure was calculated during the expansion of air from the same initial conditions, for equilibrium up to the section of dimensionless area $A = 5.4$, and then according to the

middle curve of Figure 4, corresponding to the instantaneous freezing model of the physicochemical transformations.

Table 2 presents the measured values of the static pressure given in the published papers, together with the calculated values for a nonequilibrium flow based on measurements of the Mach number M . The expansion ratio, relative to which all the data of Table 2 refer, has been so selected as to enable a comparison to be made with the results of /3/. Under the air efflux conditions created by us and the expansion ratio selected for comparison, the pressure turns out to be lower than the equilibrium pressure by a factor of 2—2.5 (in the case of complete freezing it is lower than the equilibrium pressure by almost a factor of 4). With due allowance for the inaccuracy in determining the freezing section from the data on M , our result can be considered as agreeing satisfactorily with that in /3/. The computed data of /3, 4/, given in Table 3, have been measured from the curves given in these papers, and therefore the third figure in the values given is only tentative. The experimental values have an error of the order of $\pm 10\%$. The values of the pressure derived from measurements of the Mach number M are less reliable, since the instantaneous freezing section is determined with a considerable error. Thus, for freezing in the section at which $A = 2.72$, the static pressure in the section corresponding to $A = 144$ will be 30 % lower than the value indicated in Table 2; nevertheless the result agrees well with the values obtained by direct measurements of the static pressure.

TABLE 2.

$T_0, ^\circ\text{K}$	P_0, atm	Ratio of the static pressure in the nozzle section of dimensionless area $A = 144$ to the pressure in the reservoir $(P/P_0) \cdot 10^4$			
		for equilibrium expansion (calculation)	experiment	source of the experimental results	for a frozen chemical composition from the start of the expansion (calculation)*
7000	17	4.80	2.26	Paper /4/	1.37
			1.50	Extrapolation of the data in /3/	
5700	12	5.17	2.42	Calculation of the static pressure based on measurements of the Mach number M in this paper	1.39
			1.95	Paper /3/	
4000	35	2.80	2.55	Paper /4/	1.46
			2.58	Paper /3/	

* The results of the calculations for $T_0 = 7000$ and 4000°K are taken from /4/, where it was assumed that the chemical composition was invariable and the excitation of the vibrations was in equilibrium. The result for $T_0 = 5700^\circ\text{K}$ presupposes that the vibrations are likewise frozen.

CONCLUSIONS

Under experimental conditions the expansion of air in nozzles is a thermodynamically nonequilibrium process, a fact connected with the lag in the recombination of atomic oxygen. A sharp slowing down of the recombination takes place when the ratio of the local cross section to the throat area lies between 3 and 7. The subsequent expansion takes place with a constant (nonequilibrium) chemical composition.

Bibliography

1. Eschenroeder, A.Q., D.W. Boyer, and J.G. Hall. Nonequilibrium Expansions of Air with Coupled Chemical Reactions.—Phys. of Fluids, Vol. 5. 1962.
2. Breiner, G. and E. Levinskii. Vyazkie i nevyazkie neravnovesnye techeniya v soplakh (Viscous and Nonviscous Nonequilibrium Flows in Nozzles).—Raketnaya Tekhnika i Kosmonavtika, No. 11. 1963. [Russian translation.]
3. Nagamatsu, J.B., J.B. Workman, and R.E. Sheer. Hypersonic Expansion of Air in Nozzles, Accompanied by Recombination of Atoms.—J. Aeronaut. Sci., Vol. 28. 1961.
4. Duffy, R.E. Experimental Study of Nonequilibrium Expanding Flows.—AIAAJ., Vol. 3. 1965.
5. Ionov, V.P., G.N. Nikolaev, M.V. Gusev, and O.I. Luneva. Izuchenie potokov gaza v udarnoi trube pri pomoshchi skhemy Teplera i skorostnogo kadrovogo fotografirovaniya (Study of Gas Flows in a Shock Tube by the Töpler Method and High-Speed Frame Photography).—Sbornik "Fizicheskaya gazodinamika i svoystva gazov pri vysokikh temperaturakh," Moskva, Izdatel'stvo "Nauka." 1964.
6. Ionov, V.P. and G.N. Nikolaev. Eksperimental'noe issledovanie istecheniya dissotsirovannykh gazov cherez sverkhzvukovye sopla (Experimental Study of the Flow of Dissociated Gases through Supersonic Nozzles).—Sbornik "Issledovaniya po fizicheskoi geodinamike," Moskva, Izdatel'stvo, "Nauka". 1965.
7. Nagamatsu, H., R. Geiger, and R.E. Sheer. A Hypersonic Shock Tube.—ARSJ., Vol. 29. 1959.
8. Hurle, I.R., Russo, A.L., and J.G. Hall. Spectroscopic Studies of Vibrational Nonequilibrium in Supersonic Nozzle Flows.—J. Chem. Phys., Vol. 40. 1964.
9. Kamimoto, G., T. Akamatsu, and T. Hasegawa. Triple-Diaphragm Type Hypersonic Shock Tunnel.—Dept. Aeronaut. Engng., Kyoto University, Current Papers, Kyoto. 1962.
10. Predvoditelev, A.S., E.V. Stupochenko, A.S. Pleshanov, E.V. Samuilov, and I.B. Rozhdestvenskii. Tablitsy termodynamicheskikh funktsii vozdukha (Tables of the Thermodynamic Functions of Air).—Moskva, Izdatel'stvo AN SSSR. 1962.
11. Hall, G.H. Application of Boundary Layer Theory to Explain Some Nozzle and Venturi Flow Peculiarities.—Proc. Inst. Mech. Engrs., Vol. 173, No. 36. 1959.

12. Sichel, M. Leading Edge of a Shock-Induced Boundary Layer.—
Phys. of Fluids, Vol. 5. 1962.
13. Burke, A. and K. Bird. Primeni konicheskikh i profilirovannykh
sopel v giperzvukovykh ustanovkakh (Use of Conic and Profiled
Nozzles in Hypersonic Installations).—Sbornik "Sovremennaya
tekhnika aerodinamicheskikh issledovaniy pri giperzvukovykh
skorostyakh," Moskva, Izdatel'stvo "Mashinostroyeniye." 1965.*
14. Hayes, W.D. and R.F. Probstein. Hypersonic-Flow Theory.—
Acad. Press, New York. 1959.
15. Vidavskii, A., R. Osvaldt, and J. Harn. Eksperimental'noe
opredeleniye konstanty rekombinatsii vodoroda (Experimental
Determination of the Hydrogen Recombination Constants).—
Raketnaya Tekhnika i Kosmonavtika, No. 12. 1962.*
16. Stupochenko, E. V. and I. P. Stakhanov. Ob uravneniyakh
relaksatsionnoi gidrodinamiki (Equations of Relaxation Hydro-
dynamics).—Doklady AN SSSR, No. 4, p. 134. 1960.
17. Stakhanov, I. P. and E. V. Stupochenko. O strukture linii
Makha v relaksiruyushchikh sredakh (Structure of the Mach Lines
in Relaxing Media).—Doklady AN SSSR, No. 5, p. 134. 1960.
18. Wood, W.W. and F.R. Parker. Structure of a Centered Rarefaction
Wave in a Relaxing Gas.—Phys. of Fluids, Vol. 1. 1958.
19. Moore, F.K. and W.E. Gibson. Propagation of Weak Disturbances
in a Gas Subject to Relaxation Effects.—J. Aerospace Sci.,
Vol. 27. 1960.
20. Broer, L.J.F. Characteristics of the Equations of Motion of a
Reacting Gas.—J. Fluid Mech., Vol. 4. 1958.
21. Wilson, J. An Experiment to Measure the Recombination Rate of
Oxygen.—J. Fluid Mech., Vol. 15. 1963.
22. Wegener, P.P. Supersonic Nozzle Flow with a Reacting Gas
Mixture.—Phys. of Fluids, Vol. 2. 1959.
23. Lighthill, M. Dynamics of a Dissociating Gas: Part I. Equilibrium
Flow.—J. Fluid Mech., Vol. 2. 1957; Part II. Quasiequilibrium
Transfer Theory.—J. Fluid Mech., Vol. 8. 1960.
24. Bray, K.N.C. Atomic Recombination in a Hypersonic Wind-Tunnel
Nozzle.—J. Fluid Mech., Vol. 6. 1959.
25. Bray, K.N.C. Sudden-Freezing Analysis for Nonequal Nozzle Flows.—
Amer. Rocket Soc. J., Vol. 31. 1961.
26. Hall, J.G. and A.L. Russo. Proceedings of the First Conference
on Kinetics, Equilibria, and Performance of High Temperature
Systems.—Butterworth Scientific Publications, London. 1960.
27. Lordi, J. Comparison of Exact and Approximate Solutions for Non-
Equilibrium Flows in Nozzles.—Raketnaya Tekhnika, No. 8.
1962.*
28. Bray, K. Ninth Symposium (International) on Combustion.
N. Y. — London, Academic Press. 1963.

* [Russian translation.]

I. M. Naboko, R. G. Nemkov

**STUDY OF THE FLOW STATE BEHIND A SHOCK
FRONT BY MEANS OF FRAME-SCAN
PHOTOGRAPHY**

In /1—3/ the state of the flow behind a shock wave was estimated from the angle made by the Mach line leaving the leading edge of the half-wedge, located in the section of the shock tube under consideration. The position of the Mach line was recorded by a series of still photographs. In addition to the still photographs, the flow may be easily recorded by frame-scan photography. The Schlieren frame-scan photograph of the flow past an obstacle enables an independent determination to be made of the flow velocity and the propagation velocity of the weak disturbance (the sound velocity) in addition to measurements of the angle made by the Mach line with the flow axis.

Experiments to record the flow continuously were conducted on the UT-2 apparatus /4/, to which was attached a cylinder of 40 liter capacity, separated from the low-pressure chamber by a celluloid diaphragm and evacuated to a pressure of 10^{-1} mm mercury. The vacuum-sealed connection of the cylinder with the low-pressure chamber was facilitated by suspending the cylinder on a trolley which moved along the rails of the shock tube stand.

A stabilizer enabled a higher initial pressure to be used in the low-pressure chamber. This somewhat reduced the effects due to the development of the boundary layer, and lowered the requirements regarding the intensity of the short-exposure lamp.

A delay with an automatic control based on the shock velocity was used to synchronize accurately the flash of the lamp with some specific position of the shock wave, independently of the wave velocity /5/. The use of such a delay turned out to be very convenient. In fact, since the aperture in the blind covering the tube section under investigation had to be as narrow as possible, the period of maximum lamp intensity had to be synchronized with the most interesting stage of the process.

The synchronization is shown in Figure 1. On passing the sensor *b*, the shock wave triggered a signal proportional to the time of its passage between sensors *a* and *b*. As a result the pulse which lit the short-exposure lamp was delayed during a time

$$T = s/v - \tau', \quad (1)$$

where τ' is the experimentally determined delay time of the lamp; v is the velocity of the shock wave.

The set-up for obtaining the Schlieren frame-scan photograph of the Mach line is shown in Figure 2. The distance between the aperture and

the nearest generatrix of the half-wedge was measured before the experiment. Together with a knowledge of the distance between the apertures α, β, γ (which served to obtain reference lines) this made it possible to record the real scale of the phenomenon on the film. The Mach number of the flow was determined from the relations

$$\left. \begin{aligned} M &= (\sin \alpha_M)^{-1} = u/c, \\ \alpha_M &= \arctg(d/l), \\ l^*/l &= l_{\alpha\gamma}^*/l_{\alpha\gamma}, \end{aligned} \right\} \quad (2)$$

where the asterisk implies distances on the film.

The beginning of the formation of the Mach line as an acoustic disturbance moving with the flow at velocity u corresponds to the instant at which the shock wave passes the leading edge of the half-wedge. If the effective length of the relaxation zone behind the shock wave is sufficiently small compared with l and d , this disturbance will obey some stationary conditions most of the time until it reaches the aperture. The sound velocity c and the flow velocity u can then be found directly from photographs of the flow past the half-wedge and referred to the indicated stationary state. The sound velocity thus determined is actually the velocity c_∞ of propagation of some effective (sufficiently strong) leading Mach front.

The value of u can frequently be determined from the frame-scan photograph of the process [6].

Since the Mach line is inclined at an angle to the aperture, its width is mainly determined by the width of this aperture, which equals 0.5 mm.

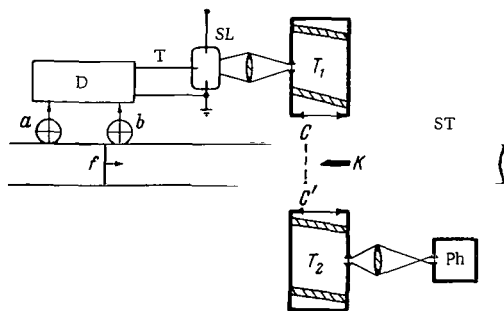


FIGURE 1. Synchronization set-up:

ST—shock tube; a, b—sensors; K—half-wedge; D—delay; SL—short-exposure lamp; T—output of the delay, triggering the illumination; f—shock front; T_1, T_2 —IAB-451 apparatus; Ph—photorecorder.

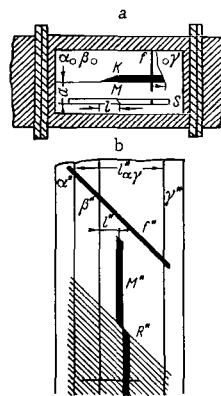


FIGURE 2. Outline of the Mach line;

a—chamber; b—film; S—aperture; K—half-wedge; M—Mach line; M^* —trace of the Mach line on the film; R^* —trace of the contact surface; $\alpha^*, \beta^*, \gamma^*$ —reference lines.

Figure 3 shows a typical frame-scan photograph of the flow past a half-wedge (shock wave in CO_2 , $M_0=7.45$ is Mach number of the shock wave). The Mach line is indicated on Figure 3 by the letter M .

The photograph indicates the vibrations of the Mach line in the CO_2 flow, which point to an inhomogeneity of the other flow parameters. Such vibrations are absent in an N_2 flow.



FIGURE 3. Frame-scan Töpler photograph of the Mach line.

The existence of a periodical variation in the inclination of the Mach line in CO_2 is consistent with the density fluctuations observed by other authors using interferometry /7/ and electron-beam absorption /8/.

Note also the systematic, although negligible, decrease in the angle α_M toward the end of the plug, which may result from the increase in the flow velocity accompanying the development of the boundary layer. The part played by diffusion and heat conduction apparently becomes substantial in the narrow region adjoining the contact surface.

The data obtained were processed by the method described in /2, 3/. A number of curves $M = f(M_0, \lambda)$ were plotted, where $M = u/c_\infty$ and λ is the state of the flow.

The flow state is characterized by a set of conditions: E_{ω_i} represents the internal energy of the molecular vibration of frequency ω_i in a frozen state. The state of the flow could be estimated by comparing the experimental and theoretical values of M .

Gas	M_0	M	$c, \text{ m/sec}$		Gas	M_0	M	$c, \text{ m/sec}$	
			calcu- lation	experi- ment*				calcu- lation	experi- ment*
N_2	4.14	1.73	710	710	CO_2	6.2	2.1—2.3	640	660
N_2	4.66	1.92	780	770	CO_2	7.03	2.42	—	720
N_2	6.73	1.97	—	982	CO_2	7.45	2.1—2.35	740	750
CO_2	4.8	1.3—1.50	540	560	CO_2	7.75	2.2—2.35	760	770
CO_2	5.14	2.08	—	580					

* The accuracy of the experimental values is $\pm 10\%$.

The results are given in the table, where M corresponds to some intermediate part of the plug, in which the flow parameters are almost constant with time. When calculating c , all the internal degrees of freedom except the rotational ones were considered frozen, i. e., $\gamma = (c_p/c_v) = 1.4$.

CONCLUSIONS

The following conclusions about the state of the gas flow behind the incident shock wave can be drawn from the results of the investigations.

1. Behind the shock front in CO_2 at pressures of 1–3 atm and Mach numbers $M = 5-8$, the angle of inclination of the Mach line has a variable component, a fact apparently connected with the existence of waves disturbing the plug, generated as the boundary layer thickens behind the shock wave, and also during the formation of the shock wave after the diaphragm bursts. In nitrogen such periodical variations of the Mach number are almost absent.

2. The average state of the CO_2 flow (assuming $\gamma = 1.4$ in the sound wave) is close to the frozen state of the asymmetric valent vibrations of the molecules and the lag of the dissociation. This result agrees with [2, 3], and is corroborated to a certain extent by an independent measurement of the mean value of the propagation velocity of the leading front of the signal.

Bibliography

1. Fel'dman, S. Eksperimental'noe izucheniye khimicheskikh reaktsii v vozdukh pri vysokikh temperaturakh (Experimental Study of the kinetics of Chemical Reactions in Air at High Temperatures).— VRT, No. 1 (49). 1959.
2. Bazhenova, T. V. and I. M. Naboko. K voprosu o skorosti fiziko-khimicheskikh prevrashchenii molekul CO_2 za udarnoi volnoi pri temperaturakh 2000–4000°K (Rate of Physicochemical Transformations of CO_2 Molecules behind a Shock Wave at Temperatures of 2000–4000°K).— Doklady AN SSSR, Vol. 154. No. 2.
3. Naboko, I. M. Issledovanie sostoyaniya gaza za udarnoi volnoi po kartine obtekaniya prepyatstviya, pomeschennogo v udarnuyu trubu (Study of the Gas State behind a Shock Wave from the Flow Pattern Past an Obstacle in a Shock Tube).— Sbornik "Issledovaniya po fizicheskoi gazodinamike," Moskva, Izdatel'stvo "Nauka," 1966.
4. Bazhenova, T. V., I. M. Naboko, and O. A. Predvoditeleva. Vliyanie dissipatsii na parametry potoka za skachkom v udarnoi trube (Effect of Dissipation on the Flow Parameters behind a Shock in a Shock Tube).— Sbornik "Fizicheskaya gazodinamika i svoystva gazov pri vysokikh temperaturakh," Moskva, Izdatel'stvo AN SSSR, 1963.
5. Nemkov, R. G. Skhema zaderzhki dlya sinkhronizatsii zapuska registriruyushchei apparatury (A Delay Circuit for Triggering Shock-Tube Recording Instruments, Automatically Controlled by the Shock-Wave Velocity).— In this collection, p. 171.

6. Bazhenova, T. V. Izmenenie skorosti potoka gaza za skachkom v udarnoi trube (Variation in the Gas Flow Velocity behind a Shock in a Shock Tube).—Sbornik "Fizicheskaya gazodinamika i teploobmen," Moskva, Izdatel'stvo AN SSSR. 1961.
7. Zaitsev, S. G., E. V. Lazareva, and A. P. Shatilov. Issledovanie normal'nogo otrazheniya udarnykh voln v udarnoi trube (Study of the Normal Reflection of Shock Waves in a Shock Tube).—PMTF, No. 4. 1964.
8. Busygin, E. P. and G. K. Tumakaev. Izmerenie plotnosti gaza za udarnoi volnoi v udarnoi trube metodom elektronnoy luchy (Measurement of the Gas Density behind a Shock Wave in a Shock Tube Using an Electron Beam).—Zhurnal Tekhnicheskoi Fiziki, Vol. 34, No. 1. 1964.

R. G. Nemkov

EFFECTIVE PROFILE OF THE MACH LINE IN A RELAXING GAS

It was shown in /1/ that in a relaxing gas the Mach line occupies a whole region (the cone AOB in the figure). It was also established that in the cases $(x, y) \rightarrow 0$ and $(x, y) \rightarrow \infty$ the structure of the disturbance region (emanating from a source at $x = y = 0$) is such that a clearly expressed disturbance maximum exists and is localized along the frozen Mach line (cf. the line OA in Figure 1) and correspondingly along the equilibrium Mach line (the line OB).

Thus, in these two limiting cases the introduction of the concept of an "effective" Mach line as some one-dimensional region, given by

$$y = \varphi(x; u; c_\infty; c_0; \tau), \quad (1)$$

can be justified, where u is the flow velocity; c_∞, c_0 are the frozen and equilibrium sound velocities; τ is the relaxation time.

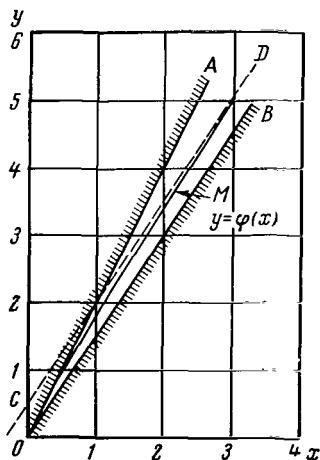


FIGURE 1. The Mach line M , calculated by formula (25) for $p=1$, $c=0.5$, $\sqrt{M_0^2-1}=1.5$.

An attempt is made in this paper to find the profile of the effective Mach line (as the curve describing the propagation of the wave packet center), i. e.,

the function (1), over the entire range of values of x . The same assumptions are used as in /1/, namely, the relaxing substance (gas) is described by the Kneser model, and the Mach line corresponds to such small disturbances that it can be described by some linear acoustic equation. The effective Mach line in dispersive media is considered.

1. LINEAR ACOUSTIC EQUATION OF A RELAXING GAS

It is assumed that the required Mach line can be found from the linear acoustic equation of relaxing media. Since the experimentally observed Mach line corresponds to some finite disturbance, this assumption may raise objections (e.g., the critical observations in /2/ on the analogous question of applying linear equations to a dispersive plasma). Nevertheless, the solution of the linear acoustic equation approximates the exact solution for sufficiently small ($x < L, y < L$) distances from the source. The relationship $L = L(A)$, where A is the disturbance amplitude, can only be evaluated quantitatively from the initial nonlinear equations. This problem is beyond the scope of the present paper. The acoustic equation for a relaxing gas (in rheological terms—for the Kneser model) has been derived in several papers (cf. for instance /3–5/). For our purposes a different form of this equation is more convenient, namely, a second-order partial integro-differential equation. To the best of our knowledge such a form of the acoustic equation has not been used before. A brief derivation of this equation will accordingly be given.

The gas is assumed to be inviscid with zero thermal conductivity. The following equation is then derived from the continuity equation, the Euler equation, and the condition that small disturbances are adiabatic /6/:

$$\left. \begin{aligned} [(1/c^2) \partial^2 / \partial t^2 - \nabla^2] \Phi(\vec{r}, t) &= 0, \\ c &= V(d\rho/dp)_s, \end{aligned} \right\} \quad (2)$$

where Φ is understood as the flow velocity (density ρ , pressure p), and c is not explicitly determined at this stage.

Let the relaxation properties of the substance be determined by a single relaxation parameter. Using the linear relaxation equation, it can be shown /6/ that c is determined from the relation

$$\left. \begin{aligned} \Phi(\vec{r}, t) &= (1/2\pi) \int \Phi(\omega, \vec{r}) e^{i\omega t} d\omega, \\ c^{-2}(\omega) &= \left(\frac{c_0^2 + i\omega\tau c_\infty^2}{1 + i\omega\tau} \right)^{-1} = \frac{c_0^{-2} - c_\infty^{-2}}{1 + i\omega\theta} + c_\infty^{-2}, \\ \theta &= \tau(c_\infty/c_0)^2 \end{aligned} \right\} \quad (3)$$

as a function of the frequency of the process.

The following form will then be equivalent to (2):

$$\left\{ \int [(1/c^2(\omega)) \partial^2 / \partial t^2 - \nabla^2] \Phi(\omega, \vec{r}) e^{i\omega t} d\omega \right\} = 0. \quad (4)$$

Applying the convolution theorem to the functions $c^{-2}(\omega)$ and $\Phi(\omega)$, and using the relation

$$\int \frac{e^{i\omega t}}{1 + i\omega\theta} d\omega = \begin{cases} \frac{2\pi}{\theta} e^{-t/\theta}; & t > 0, \\ 0; & t < 0, \end{cases} \quad (5)$$

it is easily derived that equation (4) is equivalent to a second-order integro-differential equation with retarded argument:

$$\left. \begin{aligned} [(1/\hat{c}^2)\partial^2/\partial t^2 - \vec{\nabla}^2] \Phi(\vec{r}, t) &= 0, \\ \hat{c}^2 &= (c_0^2 - c_\infty^2) \hat{\theta} + c_\infty^2, \\ \hat{\theta} &= [1 + \theta(\partial/\partial t)]^{-1}, \\ \hat{\theta}\Phi(t) &= \int_0^\infty [\exp(-z/\theta)/\theta] \Phi(t-z) dz. \end{aligned} \right\} \quad (6)$$

To the best of our knowledge equation (6) has not been used in gas-dynamic studies. Similar acoustic equations have however been used to describe viscoelastic media (according to the Maxwell model) in /7, 8/.

Multiplying (6) by the operator $[1 + \theta(\partial/\partial t)]$, we obtain the third-order partial differential equation

$$\left\{ \theta \left(\frac{\partial}{\partial t} \right) \left[(1/c_\infty^2) \frac{\partial^2}{\partial t^2} - \vec{\nabla}^2 \right] + \left[(1/c_0^2) \frac{\partial^2}{\partial t^2} - \vec{\nabla}^2 \right] \right\} \Phi = 0 \quad (7)$$

with no retarded term. Such an equation has often been used /3-5/. Equation (6) is more convenient here, since the link between the retardation effects and the relaxation is explicit.

Equation (6) describes the propagation of acoustic disturbances in a medium at rest. The transformation $\partial/\partial t \rightarrow \partial/\partial t - u\partial/\partial x$ defines a coordinate frame in which the substance moves with a velocity u along the x axis, and if $\partial/\partial t \equiv 0$ (we seek only stationary disturbances), the equation

$$\left. \begin{aligned} [(\hat{M}^2 - 1) \partial^2/\partial x^2 - \partial^2/\partial y^2] \Phi(x, y) &= 0, \\ \hat{M}^2 - 1 &= (M_0^2 - M_\infty^2) \hat{l} + (M_\infty^2 - 1), \\ \hat{l} &= [1 + l(\partial/\partial x)]^{-1}, \\ \hat{l}\Phi(x) &= \int_0^\infty [\exp(-z/l)/l] \Phi(x-z) dz, \\ l &= u\theta, \quad M_0 = u/c_0, \quad M_\infty = u/c_\infty, \end{aligned} \right\} \quad (8)$$

is derived in which only the case $\vec{r} = (x, y)$ is considered.

Equation (8) describes the propagation of stationary acoustic disturbances in a supersonic stream and is fundamental in the subsequent treatment. When (8) is multiplied by $[1 + l(d/dx)]$ the equation

$$\left\{ l \frac{\partial}{\partial x} \left[(M_\infty^2 - 1) \frac{\partial^2}{\partial x^2} - \frac{\partial^2}{\partial y^2} \right] + \left[(M_0^2 - 1) \frac{\partial^2}{\partial x^2} - \frac{\partial^2}{\partial y^2} \right] \right\} \Phi = 0 \quad (9)$$

is obtained (without pronounced retardation); this equation has been used in a number of papers, for instance /1/.

2. EQUATIONS OF THE EFFECTIVE CHARACTERISTICS IN DISPERSIVE MEDIA

Equations (8) indicate that a point disturbance source ($x = y = 0$) creates an acoustic field, whose intensity differs from zero (for $\tau \neq 0$) over a two-dimensional cone between the lines

$$OA \quad y = x / \sqrt{M_\infty^2 - 1}, \quad (10)$$

$$OB \quad y = x / \sqrt{M_0^2 - 1}, \quad (11)$$

where OA (cf. the figure) is the frozen Mach line and OB the equilibrium line.

This fact can also be derived intuitively. When $x \approx 0$ the disturbance $\Phi(x, y)$, i. e., $(1/2\pi) \int \Phi(\omega) \exp(i(\omega x - k(\omega)y)) d\omega$, is localized in a small spatial region, and in this wave packet all the frequencies participate with equal intensity (i. e., $\Phi(\omega) = \text{const}$). Each frequency then propagates with its particular velocity, which determines the indicated shape of the disturbance region.

An unavoidable consequence of the dispersion is the subsequent spreading of the disturbance as a wave packet. However, for any fixed x there exists some center of this wave packet, which, as can be shown, moves at the group velocity, i. e., along the ray of geometrical optics. Our separation of the effective Mach line (as a one-dimensional region) from the whole disturbance region is based on this fact. The trajectory $y = y(x)$, a ray of geometrical optics, is associated with the effective Mach line.

It is natural also to attempt to find an equation governing the motion of the wave packet center, and hence the form of the effective Mach line. This equation will be called the equation of the effective characteristics. Only the case when the effective characteristics are real quantities is considered, i. e., when the initial equation is hyperbolic in this sense.

Equation (6) will be used to illustrate how the equation of the effective characteristics is derived. In this case the effective characteristic will be some curve $\vec{r} = \vec{r}(t)$, along which

$$\frac{d\vec{r}(t)}{dt} = \vec{V} = \frac{d\omega}{dk}, \quad \left(\frac{d\omega}{dk} \sim \frac{\omega}{k} \right), \quad (12)$$

where the group velocity $(d\omega/dk)$ is determined by

$$\left. \begin{aligned} \omega &= -\partial\psi / \partial t, \\ \vec{k} &= \vec{\nabla}\psi, \\ \Phi(\vec{r}, t) &= A e^{i\psi} \end{aligned} \right\} \quad (13)$$

in terms of the eikonal ψ of the field Φ .

Equation (6), written as a geometrical acoustics approximation (i. e., in terms of ψ , where $\psi \sim \text{const}$ along (12)), takes the form

$$(1/\hat{c}^2) \omega^2 = (\vec{k}^2). \quad (14)$$

The required equation follows from (14):

$$(1/\hat{c}^2) \left[\frac{d\vec{r}(t)}{dt} \right]^2 = 1. \quad (15)$$

By analogy, the effective characteristics of equation (8) are the solutions of

$$(\hat{M}^2 - 1) \left[\frac{dy(x)}{dx} \right]^2 = 1. \quad (16)$$

Following this procedure, the effective characteristics of (9) can also be derived; they naturally coincide with (16).

Suppose $c(\omega)$ is the phase velocity as a function of the frequency. The function $c(\omega)$ is a consequence of the dispersion relation resulting from the equation studied (an example is the relation between (3) and (6)).

Consider now the problem of finding curves $\vec{r} = \vec{r}(t)$ such that the equation

$$\frac{d\vec{r}(t)}{dt} = \vec{V}_M \quad (17)$$

is satisfied along them, where \vec{V}_M is determined from

$$\left. \begin{aligned} \vec{V} &= (1/2\pi) \int \vec{V}(\omega) e^{i\omega t} d\omega, \\ \vec{V}_M &= \vec{V}(\omega_M), \\ \text{Rec}(\omega_M) &= \max_{\omega} \text{Rec}(\omega) \end{aligned} \right\} \quad (18)$$

as a group velocity for some narrow group of waves near the frequency for which the phase velocity is a maximum.

The curves satisfying (17) represent the leading front of the disturbance, along which the "signal" (as understood in information theory) propagates, irrespective of the energy carried by this signal. It is therefore natural to assume that the partial differential equations (17) establish their characteristics (in the usual sense). The general proof of this assertion will not be given; we note only that the characteristics (7), determined from

$$\frac{dr(t)}{dt} \begin{cases} \pm c_{\infty}, & \tau > 0, \\ \pm c_0, & \tau = 0, \end{cases} \quad (19)$$

do in fact coincide with the curves determined by (17).

Relation (17) is convenient in view of the fact that it is also applicable to the integro-differential equation (6). It is easily seen that the same equation (19) is obtained. The characteristics of equation (8) are found in exactly the same way; they satisfy the equation

$$\frac{dy(x)}{dx} = \begin{cases} \pm (1/\sqrt{M_{\infty}^2 - 1}), & \tau > 0, \\ \pm (1/\sqrt{M_0^2 - 1}), & \tau = 0. \end{cases} \quad (20)$$

Thus, starting from two physically different requirements, i. e., from (17) and (12), equations were derived for two generally speaking different curves, namely, the characteristics and the effective characteristics.

If $c(\omega) = \text{const}$ satisfies the initial equation, its effective characteristics coincide with the characteristics given in /6/ (the characteristics were derived from (12) and (13) for a quasilinear second-order partial differential equation).

3. PROFILE OF THE EFFECTIVE MACH LINE IN A RELAXING GAS

Consider now equation (16). Note first that from the condition $y(x) = 0$ for $x < 0$ it follows that

$$\left. \frac{dy(x)}{dx} \right|_{x=0} = \frac{\pm 1}{\sqrt{M_\infty^2 - 1}}. \quad (21)$$

The operator \hat{l} may be assumed to be determined by the relations

$$\begin{aligned} \hat{l} &= \lim_{\Delta \rightarrow 0} \hat{l}_\Delta, \quad (\Delta > 0), \\ \hat{l}_\Delta \psi(x) &= \int_{\Delta}^{\infty} [\exp(-z/l)/l] \psi[x - (z + \Delta)] dz. \end{aligned} \quad (22)$$

It follows from (22) that if $\psi(x) \equiv 0$ for $x < 0$, then

$$\hat{l}_\Delta \psi(x) \equiv 0, \quad (0 < x < \Delta), \quad (23)$$

i. e., in the interval $0 < x < \Delta$ equation (16) takes the form

$$\frac{dy(x)}{dx} = \frac{\pm 1}{\sqrt{M_\infty^2 - 1}}. \quad (24)$$

Relation (21) follows from (24).

Equation (16) is easily solved with the aid of (21). Its solution, valid for $y \geq 0$, is given by

$$\left[\frac{dy(x)}{dx} \right]^2 = \begin{cases} 0, & x < 0 \\ \frac{1}{M_0^2 - 1} + qe^{-px}, & x > 0, \end{cases} \quad (25)$$

where q and p are determined by

$$\left. \begin{aligned} p &= [(M_0^2 - 1)/(M_\infty^2 - 1)] (1/l), \\ q &= [(1/M_\infty^2 - 1) - (1/M_0^2 - 1)]. \end{aligned} \right\} \quad (26)$$

We shall discuss the relation obtained. The fact that $y(x) = 0$ when $x < 0$ implies that the only liquid particles which interact directly with the source are those situated (for $x < 0$) on the line $y = 0$.

It follows further from (25) that in the limiting cases ($x \rightarrow 0$, $x > 0$, $x \rightarrow \infty$) the direction of the Mach line coincides (asymptotically) with the direction of the frozen (9) and equilibrium (10) Mach lines. The Mach line itself tends asymptotically to the line

$$\tilde{y}(x) = \frac{x}{\sqrt{M_0^2 - 1}} + m, \quad (m > 0), \quad (27)$$

i. e., to a line lying above the equilibrium Mach line. This is seen in the figure, where the effective Mach line is designated by the letter M , and CD represents the line given by (27).

As $\tau \rightarrow 0$ we obtain the equilibrium Mach line, and as $\tau \rightarrow \infty$ the frozen line is derived. The limit of $y'_x(\tau)$ as $\tau \rightarrow 0$,

$$\lim_{\tau \rightarrow 0} y'_x(\tau) = \begin{cases} 1/\sqrt{M_0^2 - 1}, & x > 0, \\ 1/\sqrt{M_\infty^2 - 1}, & x = 0 \end{cases} \quad (28)$$

is discontinuous at $x = 0$. However, this in no way impairs the validity of our assertion that the effective Mach line of a relaxing medium transforms into the equilibrium Mach line. In fact, $x = y = 0$ is the point at which the source operates, and it therefore is not a proper part of the Mach line.

We shall consider briefly the frequently discussed assertion that in relaxation acoustics the characteristic is no longer a line of propagation of small disturbances (i. e., is not a Mach line /4-9/). This follows from the fact that the characteristics of equations (8) and (9), according to (19) and (20), do not tend to the equilibrium ($\tau \equiv 0$) characteristics as $\tau \rightarrow 0$ ($\tau \neq 0$). This is not only true in relaxation gas dynamics proper (i. e., including the effects of exciting internal degrees of freedom of the molecules), but is related at times to the asymptotic paradox of hydrodynamics /10/.

In our opinion, the correct interpretation of this paradox is that one can only associate an effective Mach line with an effective characteristic for the line of propagation of the disturbance-energy center. Only for such a line would its discontinuity at $\tau = 0$ constitute a paradox. The characteristics of equations (8) and (9) determine the leading front of the disturbance, whose intensity differs from zero (although it is very close to zero) for any nonzero τ .

Bibliography

1. Stakhanov, I. P. and E. V. Stupochenko. O strukture linii Makha v relaksiruyushchikh sredakh (Structure of the Mach Lines in Relaxing Media).—Doklady AN SSSR, Vol. 134, No. 5. 1960.
2. Zakharov, V. E. Ob evolyutsii volnovogo paketa v gidrodinamike s dispersiei zvuka (Evolution of the Wave Packet in Hydrodynamics with Sound Dispersion).—PMTF, No. 3. 1964.
3. Moore, F. K. Propagation of Weak Waves in a Dissociated Gas.—J. Aeronaut. Sci., Vol. 25, No. 4. 1958.
4. Stupochenko, E. V. and I. P. Stakhanov. Ob uravneniyakh relaksatsionnoi gidrodinamiki (Equations of Relaxation Hydrodynamics).—Doklady AN SSSR, Vol. 134, No. 4. 1960.
5. Clarke, J. F. On the Propagation of Small Disturbances in a Relaxing Gas with Heat Addition.—J. Fluid Mech., Vol. 20, Part 2. 1964.
6. Landau, L. D. and E. M. Lifshitz. Mekhanika sploshnykh sred (Mechanics of Continuous Media).—Moskva, GTTI. 1954.
7. Sips, R. Propagation Phenomena in Elastic Viscous Media.—J. Polymer Sci., Vol. 6, No. 3. 1951.
8. Davis, J. L. On Wave Propagation in Viscoelastic Media.—J. Polymer Sci., Vol. 50, No. 4. 1961.
9. Broer, L. J. F. Characteristics of the Equations of Motion of a Reacting Gas.—J. Fluid Mech., Vol. 4, Part 2. 1958.
10. Anderson, G. D. and W. Band. Compressible Fluid Flow and the Theory of Characteristics.—Amer. Phys., Vol. 30, No. 11. 1962.

Yu. A. Polyakov

SHOCK-TUBE STUDY OF THE STAGNATION-POINT HEAT EXCHANGE OF A BLUNT BODY

The shock tube provides a means for simulating the conditions of heat exchange with respect to the stagnation parameters in the neighborhood of the stagnation point of axisymmetrical bodies moving at high velocities. The initial parameters and wave velocity in the tube must be correctly selected to correspond completely to the conditions of motion of the body.

In /1/ the simulation conditions are derived from the main relations on the shock front for an ideal gas. Such a formulation of the problem is incorrect for regimes with dissociation of the gas molecules.

The thermodynamic and gas-dynamic parameters for air, published in /2/, enable one to derive the corresponding relations for simulating the conditions of heat exchange from the flight velocity and altitude in the presence of thermochemical reactions in the gas.

The interference with the heat exchange at high M is mainly due to:

- 1) the appearance of electrons during ionization, whose high mobility may lead to an increase in convective heat transfer;
- 2) the influence of the diffusion of the reacting gas components toward the wall on the magnitude and character of the heat flux;
- 3) the catalytic effect of the body wall material on the recombination of atoms at its surface;
- 4) the appearance of additional heat flux due to radiation from the shock layer;
- 5) the variation in the kinetic coefficients of the polycomponent medium as a function of temperature and pressure;
- 6) the absence of thermochemical equilibrium both in the gas layer behind the shock front and in the boundary layer over some parts of the trajectories.

In addition to problems on the interaction of a high-temperature reacting gas with the body, there exist experimental investigations /3, 4/ of the total value of the heat flux at the stagnation point of a blunt body.

A shock tube enables one to simulate intermittently the heat exchange for high velocities of the body over a very wide range of velocities and pressures.

The present paper presents an attempt to simulate conditions for heat exchange at the stagnation point of blunt bodies.

1. DERIVATION OF THE SIMULATION RELATIONS

To derive the simulation conditions of heat transmission with respect to the stagnation parameters one requires the main gas-dynamic relations for

a plane shock front propagating along the tube channel and the corresponding equations for the detached compression shock around the blunt body under flight conditions.

The bending of the shock wave discontinuity around the blunt body is neglected when establishing the correspondence between the stagnation enthalpies of the gas in the shock tube (in the plug) and under flight conditions.

Thus, if v_2 is the gas velocity in the plug for a laboratory coordinate frame, the stagnation enthalpy in the region before the stagnation point is given by

$$h^* = \frac{v_2^2}{2} + h_2, \quad (1)$$

where h_2 is the enthalpy of the plug gas.

On the other hand, for a coordinate frame linked with the shock front,

$$\frac{V_s^2}{2} = \frac{u_2^2}{2} + h_2, \quad (2)$$

where V_s is the velocity of the shock wave.

In equation (2) the velocity of the gas impinging on the motionless front,

$$u_2 = V_s - v_2, \quad (3)$$

is the gas velocity behind the wave front.

Therefore, from (1) and (2)

$$h^* = \frac{v_2^2}{2} + \frac{V_s^2}{2} - \frac{u_2^2}{2},$$

or, taking into account (3),

$$h^* = \frac{v_2^2}{2} + \frac{V_s^2}{2} - \frac{(V_s - v_2)^2}{2} = V_s v_2.$$

The stagnation enthalpy at the stagnation point of a flying vehicle will be realized at a flight velocity V_f and will be equal to

$$h^* \simeq V_f^2 / 2 = V_s v_2.$$

Thus, the connection between the flight velocity and the gas-dynamic flow characteristics in the shock tube is expressed as

$$V_f = \sqrt{2V_s v_2}.$$

To ensure the heat-exchange simulation conditions with respect to the flight and experimental stagnation parameters, one must know the velocity of the shock wave V_s in the tube and the gas velocity v_2 in the plug. Present-day pulse techniques for recording the parameters of transient processes enables these magnitudes to be measured experimentally to a high degree of accuracy.

In the absence of data on the gas velocity in the plug, this velocity can be eliminated with the aid of the mass-conservation equation on the front, namely,

$$V_s \rho_1 = (V_s - v_2) \rho_2. \quad (4)$$

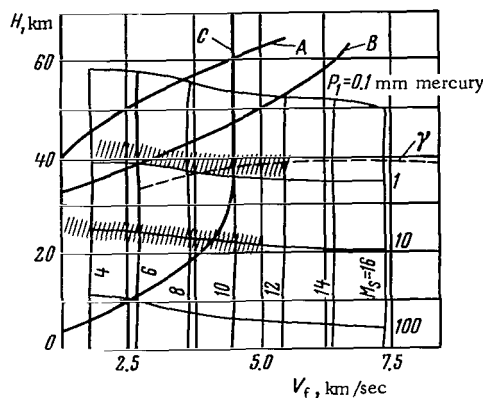


FIGURE 1. Correspondence between the stream parameters in the shock tube and the supersonic-flight conditions at different altitudes with respect to the stagnation parameters;

Shaded regions—simulation conditions; A—typical trajectory of an earth satellite; B—gliding vehicle; C—ballistic vehicle; γ —maximum altitude of the equilibrium boundary layer.

Hence

$$v_2 = V_s \left(1 - \frac{1}{\delta}\right), \quad (5)$$

where $\delta = \rho_2/\rho_1$ is a function of M and p_1 , and found from gas-dynamic tables which allow for dissociation (/2/ or /5/).

As a result

$$V_f = V_s \sqrt{2 \left(1 - \frac{1}{\delta}\right)}. \quad (6)$$

When $M_s > 10$, $V_f \approx V_s \sqrt{2}$ to the experimental accuracy.

The simulation condition with respect to density (altitude) is derived from the equation of mass conservation in flight. In the stagnation-point region for the central flow

$$\rho_f V_f = \rho_s V_s,$$

where ρ_s, V_s are the density and velocity of the gas in the vicinity of the stagnation point behind the compression shock under flight conditions.

The model of supersonic plug-gas flow can be simulated by

$$\rho_2 v_2 = \rho_s V_s.$$

Then

$$\frac{\rho_2}{\rho_1} \rho_1 v_2 = \rho_f V_f,$$

or

$$\frac{\rho_f}{\rho_1} = \frac{\delta v_2}{V_f}.$$

On the strength of (5) and (6), we can write

$$\frac{\rho_f}{\rho_1} = \sqrt{\frac{\delta}{2}(\delta-1)}, \quad (7)$$

which, with the aid of /2/ or /5/, shows that even for $M_s > 10$ we can take

$$\frac{\rho_f}{\rho_1} \approx \frac{\delta}{\sqrt{2}}. \quad (8)$$

For an initial pressure p_1 (ρ_1) in the shock tube, we can find (taking into consideration δ , whose variation with M allows for chemical reactions in the gas) a relation between the flight altitude and pressure p_1 in the tube, given by

$$\rho_f = \rho_1 \sqrt{\frac{\delta}{2}(\delta-1)}$$

or

$$p_f = p_1 \sqrt{\frac{\delta}{2}(\delta-1)}, \quad (9)$$

where p_f is the air pressure at altitude H for the corresponding flight velocity. The relationship between p_f and H can be found from the tables in /6/.



FIGURE 2. Model with heat transducer.

On the strength of (6) and (9), Figure 1 shows curves of altitude, initial shock-tube pressure, flight velocity and M_s for the shock wave in the tube. Several typical flying-vehicle trajectories are represented /7/, in addition to the equilibrium boundary layer near the surface of a body of radius $R = 0.3$ m.

The operating range of the shock tube easily includes the trajectories of different hypersonic vehicles at entry into the dense layers of the atmosphere.

2. EXPERIMENTAL TECHNIQUES

The experimental apparatus used to study heat exchange in the neighborhood of the stagnation point of a blunt body is described in /4/. A shock tube with an inner diameter of 50 mm enabled the Mach number to be varied between 3 and 13 in the course of the experiments; the initial air pressure p_1 varied between 0.00013 and 0.13 atm.

The two regimes $p_1 = 10^{-3}$ atm and $p_1 = 1.3 \cdot 10^{-2}$ atm were investigated. That with $p_1 = 1.3 \cdot 10^{-2}$ atm made it possible to compare heat-flux measurements with the results of /1/, obtained by calorimetric sensors; thanks to the high sensitivity of the film transducers, data was obtained for relatively low values of M_∞ (up to 3).

The regime with $p_1 = 10^{-3}$ atm yields data for relatively high altitudes, at which the flying vehicles begins to brake for reentry. The experiments were conducted with cylindrical glass models (Figure 2) of 11 mm diameter with a semispherical head, to which a platinum film transducer of thickness $l \leq 0.1 \mu$ was fastened in the form of a strip through the stagnation point. The technology for obtaining such instruments is described in /4/.

The contacts were glued by a special glue, and as a result the measuring zone occupied about 50 % of the film length. The resistance of the working zone of the transducer was measured by means of molten electrodes made from a low-melting metal.

The heat transducer, connected as a resistance thermometer, recorded the transient temperature of the model surface after the shock front reached the stagnation point. The heat exchange was observed during the unsteady flow past the model (Figure 3).

The Schlieren photograph indicated that the period during which a detached compression shock forms about the body

does not exceed 5—10 μ sec; at high M_∞ this initial period may represent a considerable fraction of the duration of homogeneous flow. The time for a boundary layer to form on the body is likewise important. The Navier-Stokes equation was used to demonstrate that the time during which a boundary layer forms is of the same order as the time that it takes a compression shock to develop about the model.

Rose and Stark /1/ established that the pressure distribution about the model is Newtonian for shock-tube conditions.

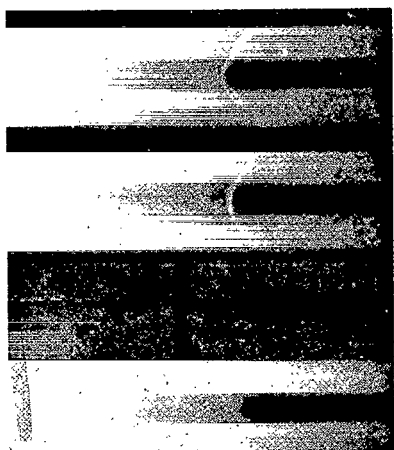


FIGURE 3. Schlieren photograph of the supersonic flow past the model in a shock tube.

$M_\infty = 6.6$; $p_1 = 10^{-1}$ atm.

The method of measuring heat exchange by film transducers provides a means for detecting minute variations in the surface temperature. The oscillogram in Figure 4 clearly shows the vertical jump of the film temperature at the moment the shock wave touches the model. The analysis of /4/ and the many oscillograms for different regimes show that the time constant of the film transducer does not exceed $1 \mu\text{sec}$.

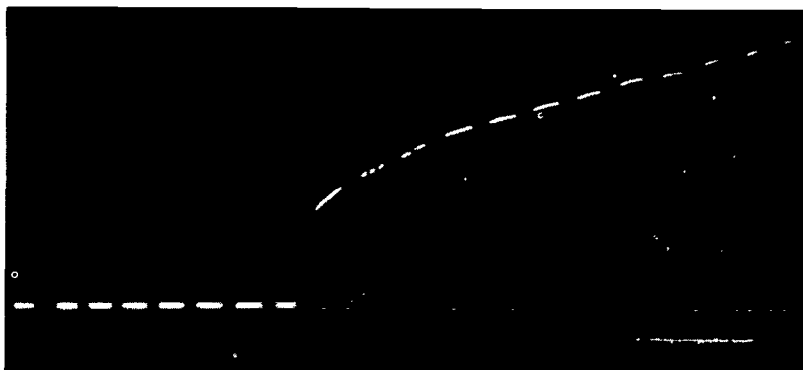


FIGURE 4. Oscillogram of the pulse from a heat transducer near the stagnation point of a blunt body:

$M_s = 6.6$; $p_1 = 10^{-3}$ atm; marker frequency $10 \mu\text{sec}$.

After converting the pulses to temperature it was established that the temperature of the model surface is proportional to $\sqrt{\tau}$. This means that during steady flow past the model the heat flux is constant.

Any deviation from a steady state is immediately reflected in the character of the pulse; the law $q = \text{const}$ is then disturbed. It is known that the duration of the parabolic form of a pulse indicates the length of the plug /8/.

3. EXPERIMENTAL RESULTS

The heat fluxes were calculated by the formula /9/

$$q_s = \frac{[t(0, \tau) - t_0] \lambda_w}{2 \cdot 0.5642 \sqrt{a_w \tau}}.$$

Figure 5 shows the dependence of the heat flux on the Mach number M_s of the shock wave and on the flight velocity, calculated from the relations governing the simulation conditions. Rose and Stark's results are also presented; they were obtained by means of calorimeters on models of 12.7 mm diameter /1/. It is seen that the film transducers provide a means for studying the heat exchange at lower M_s and Re .

Up to flight velocities $V_f = 6 \text{ km/sec}$ the experimental results coincide satisfactorily with the theory of Fay and Riddell /10/ for the equilibrium boundary layer. The calculation was realized in /4/.

To obtain quantitative data on the heat flux for the leading part of a flying vehicle a correction must be introduced to allow a correction for the body geometry. Then

$$q^* = q_s \sqrt{\frac{r_m}{R_l}},$$

where r_m is the model radius; R_l is the radius of the leading part of the body.

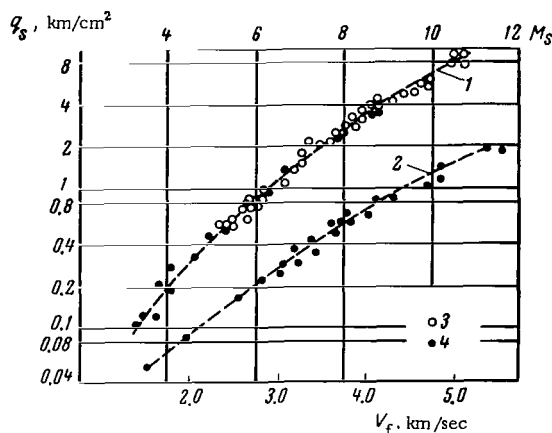


FIGURE 5. Heat flux near the stagnation point of the model as a function of the shock-wave Mach number M :

1— $p_1 = 1.3 \cdot 10^{-2}$ atm, $H \approx 22-28$ km; 2— $p_1 = 10^{-3}$ atm, $H \approx 35-40$ km; 3—results of /1/; 4—the author's results.

Figure 5 shows that at altitudes of the order of 35—40 km the heat flux in the neighborhood of the stagnation point increases by a factor of almost two as the flight velocity increases from 1 to 5 km/sec. Air dissociation at high velocities leads to no anomalies in the behavior of the function q_s . The experimentally found heat fluxes can be used when calculating the heat shielding of high-velocity flying vehicles.

The simulation conditions with respect to the stagnation parameters can be extended to other gases, the heat exchange in supersonic flows being studied in a shock tube.

Bibliography

1. Rose, P. and W. Stark. Stagnation Point Heat-Transfer Measurements in Dissociated Air.—J. Aeronaut. Sci., Vol. 25, No. 2, 1958.
2. Predvoditelev, A.S., E.V. Stupchenko, E.V. Samuilov, A.S. Pleshanov, and I.B. Rozhdestvenskii. Tablitsy termodinamicheskikh i gazodinamicheskikh svoistv potoka vozdukh za pryamym skachkom uplotneniya (Tables of Thermodynamic and Gas-Dynamic Properties of the Air Flow behind a Normal Compression Shock).—Moskva, Izdatel'stvo AN SSSR, 1960.

3. Offenhartz, E., H. Weisblatt, and R. Flagg. Stagnation-Point Heat-Transfer Measurements at Super-Satellite Speed.—J. Roy. Aeronaut. Soc., Vol.66, No. 1. 1962.
4. Polyakov, Yu.A. Primenenie plenochnykh datchikov dlya izucheniya teploobmena v dissotsirovannom potoke gaza (Use of Film Transducers for Studying Heat Exchange in a Dissociated Gas Flow).—Sbornik "Fizicheskaya gazodinamika, teploobmen i termodinamika gazov vysokikh temperatur." Moskva, Izdatel'stvo AN SSSR. 1962.
5. Rozhdestvenskii, I.B. Termodinamicheskie i gazodinamicheskie svoistva potoka vozdukha za pryamym skachkom uplotneniya s uchetom dissotsiatsii i ionizatsii vozdukha (Thermodynamic and Gas-Dynamic Properties of the Air Flow behind a Normal Compression Shock allowing for Dissociation and Ionization of the Air).—Sbornik "Fizicheskaya gazodinamika," Moskva, Izdatel'stvo AN SSSR. 1959.
6. Ostoslavskii, I.V. and I.V. Strazheva. Dinamika poleta. Traektorii letatel'nykh apparatov (Flight Dynamics. Trajectories of Flying Vehicles).—Moskva, Oborongiz. 1963.
7. Cheng, H.K. Recent Advances in Hypersonic Flow Research.—AIAA Journal, Vol. 1, No. 2. 1963.
8. Polyakov, Yu.A., I.M. Naboko, and Yu.V. Makarov. Eksperimental'noe opredelenie rabocheho vremeni udarnoi truby metodom teplovogo zonda (Experimental Determination of the Operating Time of a Shock Tube Using a Heat Probe).—Teplofizika vysokikh temperatur, No. 3. 1965.
9. Lykov, A.V. Teoriya teploprovodnosti (Theory of Heat Conduction).—Moskva, GITTL. 1952.
10. Fay, J.A. and F.R. Riddell. Theory of Stagnation Point Heat Transfer in Dissociated Air.—J. Aero. Sci., Vol. 25. 1958.

A.A. Kon'kov, A.P. Ryazin, V.S. Rudnev

EXPERIMENTAL STUDY OF THE SPECTRAL PROPERTIES OF AIR AT HIGH TEMPERATURES

The spectral absorption coefficients of air and the absorption of cross sections of its components have been calculated by different authors [1-4], and their results diverge widely. The squares of the matrix elements representing the dipole moments of the electron transitions of the molecules form the basis of the calculations, but their measurement accuracy is however not always satisfactory. Differences also exist in the calculation methods. An experimental determination of the radiant heat flux [5] at the stagnation point of a model under conditions corresponding to a flight altitude of 37 km and a Mach number equal to 28 showed that the radiant heat flux is dominant. A comparison of the experimental value of the heat flux with the value calculated under the assumption of thermodynamic equilibrium showed that the theoretical values are twice as large as the experimental ones. The value of the radiant heat flux is determined by the spectral absorption coefficients. The spectral absorption coefficients of air at temperatures above 10,000°K have not been found experimentally. The present paper aims at filling this gap.

1. EXPERIMENTAL SET-UP

The shock tube used in our experiments is described in detail in [6]. Its basic design parameters are: length of the low-pressure chamber, 170 cm; internal diameter, 3 cm. The high-pressure chamber was filled with either hydrogen (for pressures up to 150 atm), or a mixture of 10 % oxygen, 20 % hydrogen, and 70 % helium (for pressures up to 40 atm).

The range of shock-wave velocities which could be realized was 2—10 km/sec. The velocity of the shock wave was measured by a system of sensors. Photo-ionization sensors were used. The sensor comprised two electrodes set at a distance of about 2 mm from each other to which a voltage of about 100 v was applied. The shock wave generated a current in the sensor circuit; the resulting voltage pulse on the load resistance was recorded on an oscillograph. The photosensors were FEU-29 photomultipliers. The signals were recorded on an IO-4 oscillograph. The parameters of the gas heated by the reflected shock wave were calculated from the velocity of the incident shock. The accuracy of this calculation was corroborated by direct measurements of the temperature, whose results are given below.

2. SPECTRAL COMPOSITION OF THE RADIATION AND DEPENDENCE OF THE ABSORPTION COEFFICIENT OF AIR ON WAVELENGTH

The spectral properties of air were studied by time-resolved spectrogram recordings taken simultaneously with the absolute intensity of the radiation for some region of the spectrum.

The use of spectrograms with time resolution is described in [6]. Basically, it consists in the following: an inclined slit moves perpendicularly to the spectrograph slit, and uncovers different portions of the entrance slit at various instances of time; as a result, the photographic film records the time-resolved radiation spectrum of the gas. A similar device enabled time-resolved spectrograms to be obtained with a resolving time of $5\text{--}10\mu\text{sec}$ and a total operating time of $40\text{--}200\mu\text{sec}$.

The absolute radiation intensity was measured with the aid of a photomultiplier-monochromator system, graduated with the aid of an SI-8-200 tungsten band lamp.

The general layout of the experimental apparatus is shown in Figure 1. The shock wave, on passing the ionization sensor, initiated a pulse which triggered the synchronization unit 6. Over definite time intervals, the latter sent pulses to the supply unit 7 of the spectrum shutter 9, and also

triggered the sweep of the oscillographs measuring the intensity of the air radiation and the shock velocity. The spectrograms were recorded by means of the ISP-28 spectroscope 8 on an X-panchromatic film of sensitivity 1000 GOST* units. The photoelectric channel of the apparatus comprised the following elements: the lens 12, projecting the image of the radiating gas volume on the entrance slit; the neutral light filters 13, which made it possible to vary the sensitivity of the system within wide limits; the ZMR-3 monochromator 1; the FEU-29 photomultiplier 2; the supply unit 3 of the photomultiplier; the IO-4 oscillograph. The monochromator was placed such that its optical axis coincided with the

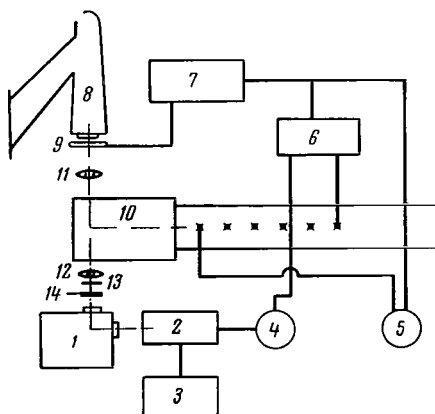


FIGURE 1. Apparatus for studying the spectral characteristics of gases.

optical axis of the spectrograph and was perpendicular to the shock-tube axis. The image of the gas layer, located 5 mm from the end of the shock tube, was projected on the entrance slit of the monochromator. Accordingly, a slit of about 1 mm width was placed at a distance of 5 mm from the end on the outer surface of the observation window.

Figure 2 shows the time resolution of the radiation spectrum of air heated by a reflected shock wave. The first negative bands of nitrogen are identified in the spectrum, as well as the lines of the impurities — iron, chrome, calcium, etc. The impurity lines were identified in several stages. First,

* [Gosudarstvennyi obshchesoyuznyi standart — All-Union State Standard.]

using the reference lines of iron, the wavelengths of all the lines in the air spectra were interpreted and determined. The impurity lines in the air radiation spectra were highly broadened, and it was consequently difficult to accurately determine their wavelength. We therefore obtained /7/ the radiation spectra of krypton and xenon at 20000—25000°K, where the lines of the impurities only appear in the absorption spectrum. The reversed lines are quite narrow, and the accuracy in finding their wavelength is much higher than determining it from the radiation spectra. If the mutual spacing of the lines was the same in the spectra of air, krypton, and xenon, and the wavelength coincided with that of the impurity line, it was considered as established that the given line belongs to the impurity.

The spectrograms were processed using heterochromatic photometry /6/. The graphic variant of this method was used: using an MF-4 microphotometer, microphotograms of the spectra of the SI-8-200 tungsten band lamp were recorded on the same plate with the aid of a nine-step attenuator on the same film as the spectrum being studied. The dependence of the emission power of tungsten on the wavelength is well known, and so these microphotograms enable transformations to be made from the blackening in the spectrum of the gas studied to the dependence of the intensity in relative units on the wavelength.

This variant of the method frees us from the cumbersome and time-consuming construction of the characteristic curves of the film for every wavelength. As indicated above, the relative dependence of the intensity on the wavelength was normalized to absolute values with the aid of data from a photoelectric channel. The spectrum zone of width 10 Å about the wavelength 4850 Å was selected for the normalization, because it is free of impurity lines, as seen from the spectrogram (Figure 2). The emissive power was thus obtained as a function of wavelength. The dependence of the absorption coefficient on the wavelength was derived using the laws of Kirchhoff and Beer.

This method of finding the absorption coefficients presupposes a known gas temperature. Under the given experimental conditions, there are insufficient grounds for taking the air temperature equal to the value calculated on the basis of the conservation laws; accordingly, the accuracy of such a calculation was corroborated by direct measurements of the gas temperature, whose results are presented below.

Figure 3 (curve 1) gives the experimental relationship between the air absorption coefficient and the wavelength for a temperature of 11500°K and a pressure of 60 atm. The air absorption coefficients, obtained by directly measuring the spectrogram blackenings, are given here. The vertical lines give the values of the absorption coefficients measured at the points of the spectrum where the impurity lines lie. The

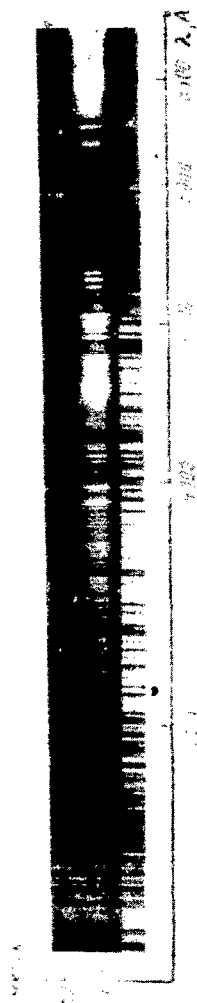


FIGURE 2. Time-resolved air radiation spectrum; the temperature is 11500°K and the pressure 60 atm.

height of the lines corresponds to the value of the absorption coefficient measured directly at the given point of the spectrum. It follows from an examination of both this curve and the spectrogram (cf. Figure 2) that very few zones are free of impurity lines.

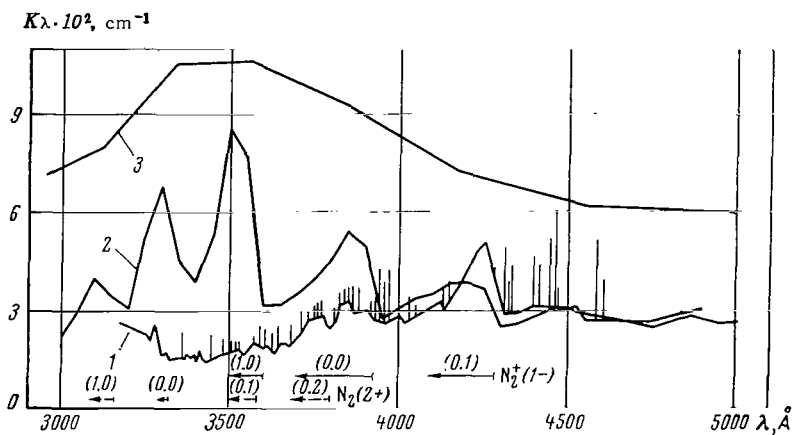


FIGURE 3. The air absorption coefficient as a function of the wavelength:

1—experimental data of the present paper, temperature 11500°K, pressure 60 atm; 2—theoretical values according to /2, 3/, temperature 12000°K, pressure 50 atm; 3—theoretical values according to /4/, temperature 12000°K, pressure 50 atm.

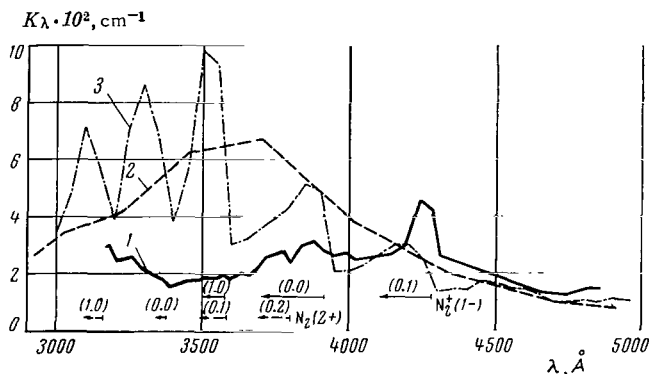


FIGURE 4. The air absorption coefficient as a function of the wavelength:

1—experimental data of the present paper, temperature 10500°K, pressure 50 atm; 2—theoretical values according to /2, 3/, temperature 10000°K; 3—theoretical values according to /4/, temperature 10000°K.

The widely used method of studying the emissive power of gases by measuring the emission at different zones of the spectrum without simultaneous spectrogram recordings contains a considerable indeterminacy, since considerable quantities of the impurity lines are present (as seen from Figures 2 and 3) and contribute to the emissive power.

Figure 4 (curve 1) shows the experimental relationship between the air absorption coefficient and the wavelength at temperature 10500°K and pressure 50 atm. The impurity lines have been excluded from consideration here and the given values of the absorption coefficient only correspond to air.

The accuracy of the absorption coefficients is determined by the accuracies of the heterochromatic photometry and the normalizing factor. The accuracy of the heterochromatic photometry is determined by the graduation accuracy of the standard source, and the measurement accuracy of blackening by a microphotometer, and forms $\pm 20\%$. The measurement accuracy of the normalizing factor is determined by the accuracy with which the standard source is set up, its graduation, the measurement of the potential by an oscillograph, and the determination of the gas parameters, and forms $\pm 25\%$.

3. MEASUREMENT OF THE TEMPERATURE OF AIR HEATED BY A REFLECTED SHOCK WAVE

The temperature of air heated by a reflected shock wave was measured with the aid of Kirchhoff's law. The temperature was obtained from simultaneous and independent measurements of the emissive and absorptive powers of air for a given wavelength. Their ratio, according to Kirchhoff's law, is the Planck function, depending at given fixed wavelength only on the temperature of the radiating object.

The general set-up of the apparatus is shown in Figure 5. There are two channels: the first was used for recording the absorptive power of the gas, and the second for recording its emissive power. To that end the

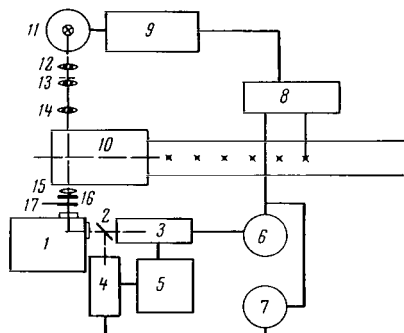


FIGURE 5. Apparatus for measuring the air temperature.

entrance and exit slits of the monochromator were divided into two parts, and two recording channels were installed behind the exit slit. The first channel functioned as follows. The image of the probing pulse light source 11 was projected by the lenses 12-14 roughly on the axis of the shock tube, after which lens 15 projected it on the upper part of the entrance slit of a ZMR-3 monochromator 1. After the radiation passed the monochromator and was reflected by the revolving mirror, it entered the FEU-29 photomultiplier 4 and was recorded by an IO-4 oscillograph 7. The radiation from the object under observation

entered the lower part of the slit of monochromator 1, and was then recorded by the second channel, consisting of an FEU-29 photomultiplier 3 and an IO-4 oscilloscope 7. The photomultipliers were fed by the VS-16 unit 5. The operation of both channels and the pulse light source was synchronized by an electronic unit 8. The system was graduated in absolute units by means of an SI-8-200 tungsten band lamp, which was inserted at the intersection of the axes of the shock tube and the optical system, while the other parameters of the optical system remained the same as during the experiment.

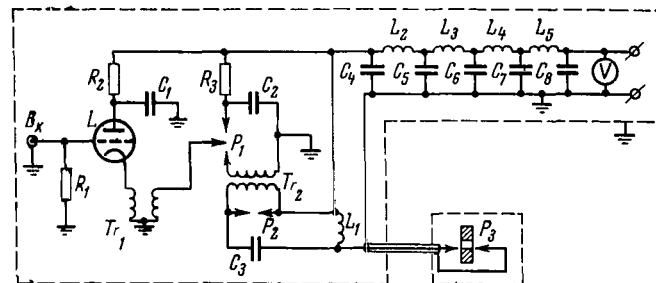


FIGURE 6. Electric circuit of the pulse light source.

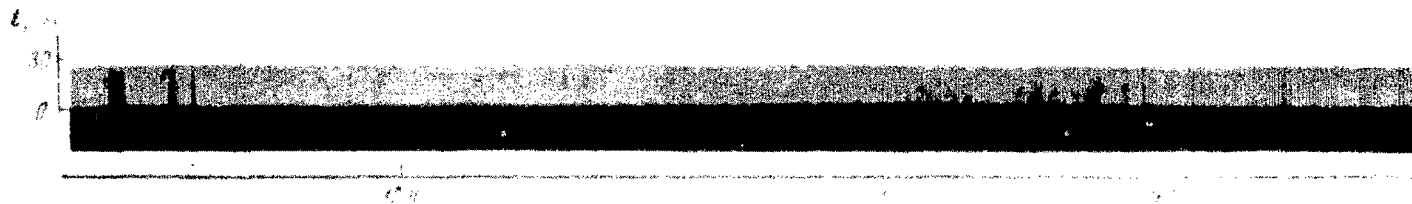


FIGURE 7. Time resolution of the emission spectrum of a pulse light source.

The auxiliary pulse source functioned according to the scheme in Figure 6. A series of five LC circuits was discharged through a textolite capillary tube of diameter 2–3 mm. The pulse source elements functioned in the following sequence. The pulse from the synchronization unit reached the grid of the thyatron L , the thyatron opened and the capacitor C_1 was discharged through it. As a result, a voltage pulse was generated on the secondary transformer winding Tr_1 , which initiated the breakdown of the spark gap P_1 , and high-frequency oscillations appeared in the circuit comprising the capacitor C_2 and the primary transformer winding Tr_2 . The voltage was then increased on the secondary transformer winding Tr_2 . The gap of the spark gap P_2 was selected to obtain a breakdown voltage of 20 kv. After the breakdown, the high-frequency oscillations appearing in the C_3L_1 circuit initiate the breakdown of the spark gap of the capillary tube P_3 . The series of five LC cells charged to a voltage of 3 kv was discharged through the capillary tube.

The emission spectrum of the pulse source (Figure 7) is continuous with a small number of reversed lines. Its brightness and color temperatures coincide within the error limits and are equal to 30000°K.

It follows that the source radiates as a black body of temperature 30000°K. The emission pulse of the source has a trapezoidal form, and its duration is about 300 μ sec, the radiation remaining constant for about 200 μ sec.

The experiment was conducted as follows. When the shock wave reached the ionization sensor, the latter triggered the synchronization unit, which in its turn triggered the supply unit of the pulse light source and the sweep of the oscillographs. The time intervals were selected so that the instant at which the reflected shock wave arrived coincided with the zone at constant radiation of the capillary source. The first channel recorded the quantity $[I_{\lambda_0}(1 - A_{\lambda}) + cI_{\lambda}]$, and the second one I_{λ} , where I_{λ} is the radiation intensity of the capillary source; A_{λ} is the absorptive power of the gas; I_{λ} is the emissive power of the gas; c is the ratio of the sensitivities of the channels.

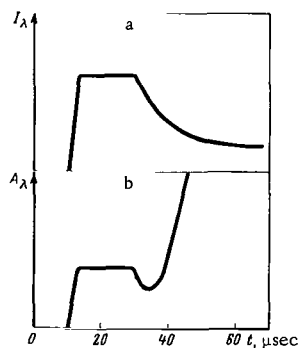


FIGURE 8. Radiation intensity (a) and absorptive power (b) as a function of time.

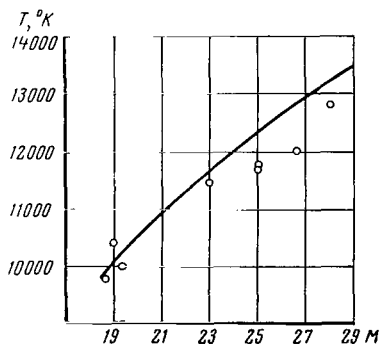


FIGURE 9. Temperature of the air heated by a reflected shock wave as a function of the Mach number of the incident shock wave.

Since $c \ll 1$, in a first approximation the data obtained from the first channel yield the value of the absorptive power, while the emissive power

can be calculated from the data of the second one. After measuring the ratio of sensitivities of the channel, one can, if necessary, suitably correct the values obtained from the first channel.

The air temperature in the section situated 4 mm from the end of the shock tube, was measured. A spectrum zone of width 5 \AA was selected near 4238 \AA for measuring the temperature. The spectrogram (Figure 2) and the dependence of the absorption coefficient on the wavelength (Figure 3) show that the given spectrum zone is free from impurity lines and corresponds to the absorption maximum (0.1) of the first negative band of nitrogen.

The radiation intensity (a) and the absorptive power (b) have been plotted in Figure 8 as a function of time. The curves show that after the arrival of the reflected shock wave the radiation remains constant for a period of $10\text{--}30 \mu\text{sec}$ (at times considerably longer), then drops rapidly to a relatively small value, and remains at that level for a considerable time. The absorption is constant for $10\text{--}30 \mu\text{sec}$ after the arrival of the reflected shock wave, and then starts to increase to unity. The same shielding effect of the radiation of the auxiliary source by the gas being studied after the reflected shock wave and the contact surface meet, was observed earlier in /6/. No reliable interpretation of this effect has so far been given.

The experimental values of the air temperature are represented by dots in Figure 9. The initial air pressure in the low-pressure chamber was 5 mm mercury. The accuracy of the temperature measurement was $\pm 10000^\circ$. The continuous curve represents the dependence of the temperature of the air heated by the reflected shock wave on the Mach number of the incident wave. These data are taken from /8/, where the temperature was calculated from the conservation laws. The theoretical values of the temperature are given in /8/ for Mach numbers up to 24; the values corresponding to higher Mach numbers were obtained by extrapolation.

The theoretical air temperature is seen to coincide with the experimental value up to Mach number 23. For higher Mach numbers a systematic discrepancy is observed; however, taking into account the accuracy of the temperature measurement and the fact that the theoretical values in this region are extrapolated, it is impossible to state with certainty that a discrepancy does indeed exist.

4. DISCUSSION OF THE RESULTS

The data of /1/ are out of date and are therefore not considered.

It follows from an examination of the curves in Figure 3 that the values of the absorption coefficient obtained on the basis of /4/ lie above the experimental values in the whole region of the spectrum under investigation. This is due to the absorption cross section of the negative nitrogen ion used in /4/, which is taken from /9/, and is assumed to be independent of the wavelength and equal to $4 \cdot 10^{-17} \text{ cm}^2$. At 10000°K the emission of the negative nitrogen ion was disregarded, and therefore in the region of $4000\text{--}5000 \text{ \AA}$ the experimental and theoretical values agree satisfactorily. The data of /2, 3/ in the region of $4000\text{--}5000 \text{ \AA}$ describe satisfactorily the experimental data. In the region of $3000\text{--}4000 \text{ \AA}$ a discrepancy is observed between the experimental and theoretical values. In /2, 4/ the oscillator strength of the second positive system of nitrogen is taken near the value 0.057 obtained in /10/. However, this paper does not analyze the possible

effect of impurities, whose emission can make an additional contribution, which makes it necessary to consider this value of the oscillator strength of the second positive system of nitrogen as the upper limit. The above-mentioned papers imply that the value nearest the true value is 0.039 obtained in /11/, where the lifetime of the excited state of the second positive system of nitrogen was measured. The oscillator strength of the first negative system of nitrogen was taken as 0.035 in /4/, according to the data of /11/. The adiabatic approximation is assumed correct. The authors

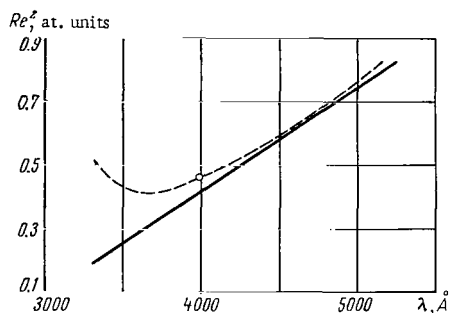


FIGURE 10. Dependence of the square of the matrix element of the dipole moment of electron transition of the first negative system of nitrogen on the wavelength.

of /2/ assumed the same value for the oscillator strength of the first negative system of nitrogen, but assumed in addition that the square of the matrix element of the dipole transition moment Re^2 depends on the internuclear distance; the assumed relationship is represented by the dotted line in Figure 10.

Hence, the values 0.032–0.035 and 0.039 are the best approximations of the oscillator strength of the first negative and second positive nitrogen systems respectively. Since no radiation increase was observed in the region of 3500 Å in the present study, the relationship represented by the solid line in Figure 10 was

adopted as expressing the square of the matrix element of the first negative system of nitrogen as a function of the wavelength.

It was therefore found advisable to introduce the following changes in the computed values of /2/ and /4/:

- 1) to exclude the contribution of the negative nitrogen atom from the data of /4/;
- 2) to take 0.039 as the oscillator strength for the second positive system of nitrogen;
- 3) to assume that the square of the matrix element is given by the solid curve in Figure 10.

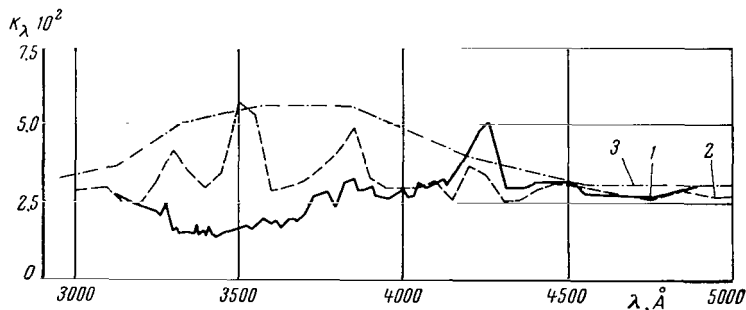


FIGURE 11. Dependence of the absorption coefficient of air on the wavelength:

- 1—experimental data of the present study, temperature 11500°K, pressure 60 atm; 2—according to the data of /2, 3/ with the changes indicated in this paper, temperature 12000°K, pressure 50 atm; 3—according to /4/ with the changes indicated in this paper, temperature 12000°K, pressure 50 atm.

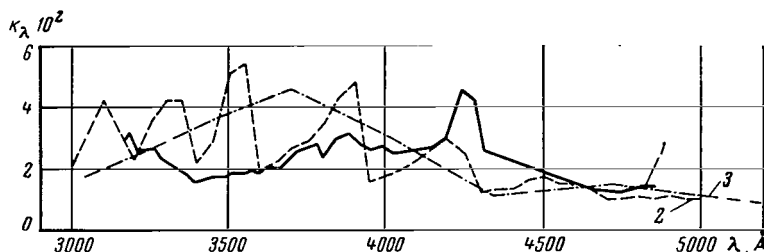


FIGURE 12. Dependence of the absorption coefficient of air on the wavelength:

1—experimental data of the present study, temperature 10500°K, pressure 50 atm; 2—according to the data of /2, 3/ with the changes indicated in this paper, temperature 10000°K; 3—according to /4/ with the changes indicated in this paper, temperature 10000°K.

The indicated changes were introduced in the calculations of /2/ and /4/. The dependences of the absorption coefficient on the wavelength obtained after these changes were compared with the experimental data. The results of this comparison are shown in Figures 11 and 12, from which it follows that the changes yield satisfactory agreement between experimental and theoretical data, with the exception of the region of 3500 Å.

CONCLUSION

1. The temperature of air heated by a reflected shock wave was measured for Mach numbers of the incident shock wave between 20 and 30. Satisfactory agreement between experimental and theoretical data was observed up to Mach number 24, while for higher Mach numbers a systematic discrepancy existed between the measured and theoretical values of the temperature. This discrepancy, however, remained within the limits of the measurement errors.

2. A comparison of the experimental and theoretical values of the spectral absorption coefficients of air established that the values used in /4/ for the absorption cross section of the negative nitrogen ion were overestimated, and that the values used in /2, 4/ for the absorption cross sections of the second positive nitrogen system were likewise overestimated. Calculations for the air absorption coefficients in the temperature range 1000—2400°K and for densities 10^{-6} — 10^1 of the normal are given in /12/. A comparison of the data of /12/ with that of /2, 3/ showed that their numerical values are close.

The authors acknowledge the assistance of A. A. Volkov in conducting this study.

Bibliography

1. Armstrong, B. H., I. Sokoloff, R. W. Nicholls, D. H. Holland, and R. E. Meyerott. Radioactive Properties of High Temperature Air.— J. Quant. Spectr. Radiative Transfer, Vol. 1, No. 1/2. 1961.

2. Plastinin, Yu. A. and G. G. Baula. Secheniya pogloshcheniya elektronnykh sistem polos dvukhatomnykh molekul (Absorption Cross Sections of the Electron Band Systems of Diatomic Molecules).—Sbornik "Issledovaniya po fizicheskoi gazodinamike, Moskva, Izdatel'stvo "Nauka." 1965.
3. Nikolaev, V. M. and Yu. A. Plastinin. Vychisleniya poperechnykh sechenii fotoionizatsii atomov azota i kisloroda i ikh ionov, nakhodyashchikhsya v vozbuzhdennykh sostoyaniyakh (Calculations of the Photo-Ionization Cross Sections of Nitrogen and Oxygen Atoms and their Ions in Excited States).—Sbornik "Issledovaniya po fizicheskoi gazodinamike." Moskva, Izdatel'stvo "Nauka." 1965.
4. Biberman, L. M. and A. Kh. Mnatsakanyan. Teplofizika vysokikh temperatur (High-Temperature Physics), Vol. 4, No. 2. 1966.
5. Flagg, R. F. Stagnation-Point Radioactive Heat-Transfer Measurements at Supersatellite Velocities.—IEEE Trans. Nucl. Sci., Vol. II, No. 1. 1964.
6. Ambartsumyan, E. N., P. V. Ionov, and A. A. Kon'kov. Issledovanie spektral'nykh kharakteristic gazov, nagretykh sil'nymi udarnymi volnami (Spectral Characteristics of Gases Heated by Strong Shock Waves).—Sbornik "Issledovaniya po fizicheskoi gazodinamike." Moskva, Izdatel'stvo "Nauka." 1965.
7. Kon'kov, A. A., A. P. Ryazin, and V. S. Rudnev. Eksperimental'noe issledovanie spektral'nykh svoistv inertnykh gazov, nagretykh otrazhennoi udarnoi volnoi (Experimental Study of the Spectral Properties of Inert Gases Heated by a Reflected Shock Wave).—Sbornik "Fizicheskaya gazodinamika ionizirovannykh i khimicheski reagiruyushchikh gazov," Moskva, Izdatel'stvo "Nauka."
8. Ferri, A., ed. Fundamental Data Obtained from Shock-Tube Experiments.—Pergamon Press, London. 1961.
9. Boldt, G. Rekombinations-und "Minus"-Kontinuum der Stikstoffatome.—Z. Phys., 154(3):330. 1959.
10. Reis, V. H. Oscillator Strengths for the N_2 Second Positive and N_2^+ First Negative Systems from Observations of Shock Layers about Hypersonic Projectiles.—J. Quant. Spectr. Radiative Transfer, Vol. 4, No. 6. 1964.
11. Bennett, R. G. and F. W. Dalby. Experimental Determination of the Oscillator Strength of the First Negative Bands of N_2^+ .—J. Chem. Phys., Vol. 31, No. 2. 1959.
12. Churchill, D. R., B. H. Armstrong, R. R. Johnston, and K. G. Müller. Absorption Coefficients of Heated Air: A Tabulation to 24000°K.—J. Quant. Spectr. Radiative Transfer, Vol. 1, No. 3/4. 1961.

Yu. A. Plastinin

SPECTROSCOPIC INVESTIGATIONS OF THE EMISSION OF HOT NITROGEN

This paper treats the emission spectrum of very hot nitrogen in the visible and near infrared regions of the spectrum 5450 — 8200 Å. The spectrum was excited by reflecting a shock wave from the tube end /1/. This method has been used much lately in spectroscopic investigations of gases. Measurements in hot nitrogen over the wavelength range indicated are of interest when studying the first positive system of nitrogen $N_2(1+)$. Few such measurements have been obtained in pure nitrogen /2—4/. Allen's study /2/ embraced the spectral region $\lambda < 0.7\mu$, Wurster /3/ investigated the range 0.74—1.25 μ , and Wray /4/ obtained photoelectric measurements of the intensity at different points of the spectrum 7200—10400 Å. Allen's results for 10400 Å are given in /5/. The chief aim of /2—4/ was to determine the square of the matrix element Re^2 of the first positive system of $N_2(1+)$. It was shown in /4/ and /5/ that the values of Re^2 given in /2/ and /3/ diverge considerably in both absolute values and the pattern of their variation with wavelength. This discrepancy is discussed in /5/, but no conclusions are reached; further studies therefore seem appropriate. From an analysis of /2—4/ one concludes that their results are marred by a lack of any photographic record of the emission spectrum of the hot gas, and by the use of spectral apparatus of average dispersion. It is therefore possible that radiation from foreign particles or atomic nitrogen lines are present in the spectral zones isolated by the monochromator. Besides, so far no one has succeeded in obtaining an emission spectrum of nitrogen free from the interference of impurities. The main shortcoming in obtaining photographs in shock-tube experiments is that the photographic material is insufficiently sensitive in the near infrared region of the spectrum. In the present study the photographic sensitivity was increased by several orders of magnitude using a three-stage image converter /6/, which enabled nitrogen emission spectra to be resolved at time intervals of the order of several tens of microseconds. In addition to photographic recordings, the standard photoelectric method was used to obtain absolute measurements of the radiation intensity. The simultaneous use of these two methods yielded data on Re^2 for the system $N_2(1+)$.

1. INSTRUMENTATION

The experimental set-up included a two-diaphragm steel shock tube, made of chrome-plated high, medium, and low pressure compartments of 80 mm

bore. The low pressure compartment terminated in a stainless steel square section 35×35 mm, connected by an intermediate section with a compartment of circular cross section. The radiation was observed both along and across the tube axis from corundum apertures at the end of the shock tube. Lateral apertures were used in most of the experiments; the observation axis was 4 mm from the end surface.

The driver gas was helium under a pressure of 200 atm, and so the intermediate compartment was filled with helium up to 1 atm. The shock tube was equipped with a system to purify the gas being studied (removal of solid foreign particles, drying the gas, freezing out the CO_2). The low pressure was $p_1 = 25$ mm mercury. The velocity of the normal shock wave, measured by means of ionization sensors, was $v = 3450 \pm 30$ m/sec. The given p_1 and v corresponded to a design temperature and pressure behind the reflected shock wave of $T_3 = 7100 \pm 30^\circ \text{K}$ and $p_3 = 34 \pm 0.4$ atm. The gas parameters and composition of hot nitrogen were determined by the usual method /1/, using the thermodynamic functions of nitrogen in /7/. The molar fraction of nitrogen was $z = 0.821$. It follows from /8/ that the design temperature of nitrogen $\sim 7000^\circ \text{K}$ coincides with the measured value; the time-consuming pyrometric investigations of the working conditions of our apparatus could therefore be dispensed with. On the strength of the data in /9/ we established that under our experimental conditions the relaxation processes behind the reflected shock wave ceased after $\leq 0.1 \mu\text{sec}$.

The equipment for the spectral measurements consisted of a glass spectrograph ISP-51 with camera of $f = 270$ mm, an image converter with multislit photocathode /6/, a four-channel diffraction spectrometer with relative aperture 1:7, dispersion 26 \AA/mm to first order and 13 \AA/mm to second, and a condenser of $f = 90$ mm. The entrance slit of the spectrometer was 0.1 mm wide, and the exit slit 1 mm wide. The radiation was recorded in all four channels by means of FEU-38 photomultipliers and OK17-M pulse oscillographs. The receiving-amplifier circuit was graduated by means of a standard tungsten SI 8-300 lamp.

The beam of light from the lateral aperture was split by a semitransparent mirror into two parts, one of which was directed to the entrance slit of the spectrometer, and the other to the entrance slit of the spectrograph.

With this apparatus, the radiation from a given volume of gas could be studied simultaneously by photoelectric and photographic methods. An image-converter photocathode was placed where the spectrum image formed in the focal plane of the spectrograph chamber. The spectrum was photographed from the image-converter screen on highly sensitive film. The spectrograph slit was 0.02 mm wide. The image-converter had a delayed frame-scan circuit, triggered by a signal from an ionization sensor at the end of the shock tube.

2. MEASUREMENT RESULTS

Photographs of the emission spectra of nitrogen in the wavelength range 6300–8500 \AA are shown in Figures 1–3. Photographs were taken at intervals of 33–100 μsec , the exposure time for each frame being $\Delta t = 25$ –80 μsec . The line spectrum of a PRK-2 lamp was used for reference /10/. The optical system was focused such that the resolution power at the middle of the image-converter screen was $\sim 3 \text{ \AA}$.

The following conclusions were reached. Atomic lines of nitrogen, the band spectrum of the nitrogen molecules, and atomic lines of the impurities are all excited in the spectrum. The following atomic lines were identified:

Element	Wavelength, Å
N . . .	8216, 8185, 7468, 7442, 6723, 6645
O . . .	8446, 7773
K . . .	7699, 7665
Ca . . .	7326, 7203, 7148, 6494, 6462, 6439

One notes the presence in the spectrum of the intense oxygen line 7773 Å, due to the use in the experiments of industrial nitrogen, which contains 0.3–0.8 % O.

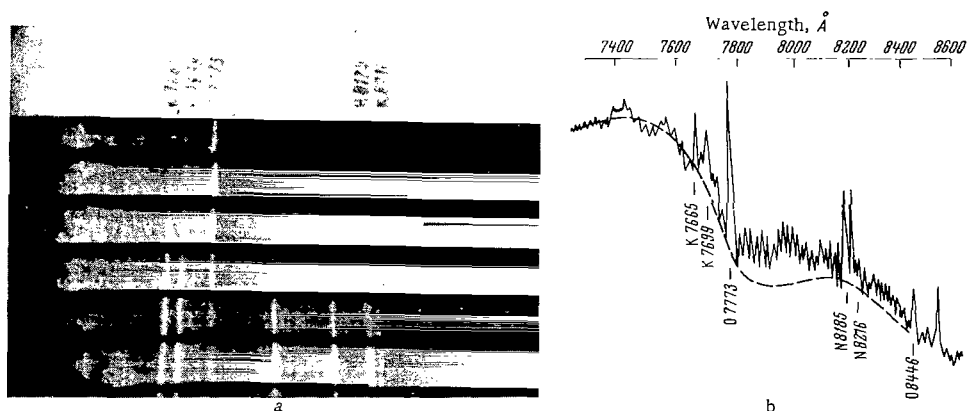


FIGURE 1. Frame scan of the nitrogen emission spectrum (a) for wavelengths 7300–8500 Å, $\Delta t = 25 \mu\text{sec}$, and microphotogram of the emission spectrum (b) (the second frame):

1—theoretical curve.

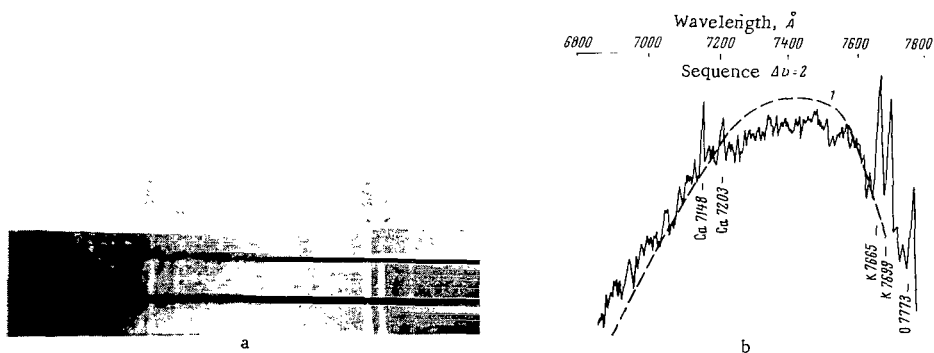


FIGURE 2. Frame scan of the nitrogen emission spectrum (a) for wavelengths 6800–7800 Å, $\Delta t = 80 \mu\text{sec}$, and microphotogram of the emission spectrum (b) (the second frame):

1—theoretical curve.

Figures 1—3 indicate that the number of impurity lines and their intensity increase sharply with time. Thus, traces of K lines can be seen on the spectrogram of the first frame in Figure 1, while in subsequent frames their intensity increases sharply. The lines of the other easily excitable element Ca appear much later in the spectrum than the K lines. Unlike the K and Ca lines, the intensity of the O lines is almost constant from the time the spectrum is first photographed. The differences in behavior of the radiation intensity of the K, Ca, and O lines are probably due to the fact that the K and Ca atoms originate at the walls of the shock tube, while oxygen is present in the gaseous phase throughout the radiating gas. Additional observations of the K, Ca, and O lines from the end aperture corroborate this opinion. The emission spectrograms established that during the first $25\mu\text{sec}$ a few weak impurity lines are present.

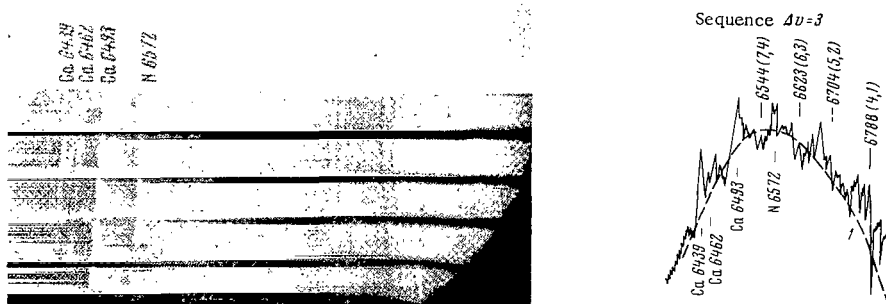


FIGURE 3. Frame scan of the nitrogen emission spectrum (a) for wavelengths $6400-7200\text{\AA}$, $\Delta t = 80\mu\text{sec}$, and microphotogram of the emission spectrum (b) (the second frame):

1—theoretical curve.

A clearly expressed band structure was observed in the nitrogen spectrum, and this seems to correspond to the first positive system of the nitrogen molecules. This interpretation is based on the following considerations:

- 1) the theoretical distribution of the radiation intensity corresponds to that observed in the whole wavelength interval;
- 2) a detailed analysis of the band spectrum structure established that the distances between the intensity peaks almost coincide with the distances between the edges of the branches of the bands of the system $\text{N}_2(1+)$ (2, 0), (3, 1), etc., which can be determined from data on the rotational structure /13/;
- 3) the variation of the oxygen concentration in nitrogen between 0.3 and 0.8% does not affect the spectrum and the relative distribution of the intensity with wavelength. The corresponding photoelectric measurements of the absolute intensity indicate that the intensity remains invariable when the oxygen concentration is varied within these limits;
- 4) The bands of the red system of cyanogen are absent from the emission spectrum. It follows in particular from Figure 1 that the strong cyanogen bands near $\lambda = 8000\text{\AA}$ are not observed, and therefore the emission of bands belonging to this system does not affect the intensity measurements.

Figures 1—3 present microphotograms of emission spectra and the results of calculating the blackening density, allowing for the spectral sensitivity of the converter radiation receiver. The spectral absorption index of the first positive system of nitrogen was calculated by a computer using the formula /11/

$$K_{\lambda} = A_{\lambda} [N_2], \quad (1)$$

where

$$\begin{aligned} A_{\lambda} = & 2.69 \cdot 10^{-14} \frac{g_e''}{\Delta \lambda} \exp \left[-\frac{1.438}{T} \left(\frac{10^4}{\lambda_{00}} - T_e'' \right) \right] \times \\ & \times \int_{\lambda - \Delta \lambda/2}^{\lambda + \Delta \lambda/2} \frac{1}{\lambda'} \left[\exp \left(\frac{1.438 \cdot 10^4}{\lambda' T} \right) - 1 \right] \sum_{\lambda_{v'v''} > \lambda'} \left\{ \frac{q_{v'v''} \text{Re}^2(\lambda_{v'v''})}{|B_{v'} - B_{v''}|} \right\} \times \\ & \times \exp \left[-\frac{1.438}{T} \left(\frac{B_{v'} \cdot 10^4}{(B_{v'} - B_{v''}) \lambda'} + G'(v) - \frac{10^4 B_{v'}}{(B_{v'} - B_{v''}) \lambda_{v'v''}} \right) \right] d\lambda'; \\ & \lambda_{v'v''} = \lambda_{00} \cdot 10^4 / [10^4 + \lambda_{00} (G'(v) - G''(v))]; \\ & B_v = B_e - \alpha_v \left(v + \frac{1}{2} \right); \\ & G(v) = \omega_0 v - \omega_0 x_0 v^2 + \omega_0 y_0 v^3 + \omega_0 z_0 v^4. \end{aligned} \quad (2)$$

Here, Q is the total statistical sum disregarding the nuclear spin; $\text{Re}^2(\lambda_{v'v''})$ is the square of the matrix element of the dipole moment, at. units; $q_{v'v''}$ is the Franck-Condon factor; λ_{00} is the wavelength of the center of the band (0, 0); T_e'' , g_e'' are the energy and statistical weight of the lower electron state; ω_0 , $\omega_0 x_0$, $\omega_0 y_0$, $\omega_0 z_0$ are molecular constants; $\Delta \lambda$ is the averaging interval; $[N_2]$ is the concentration of N_2 molecules; λ is the wavelength, μ .

The single primes indicate the upper electron state, and the double primes the lower state. The value $\text{Re}^2 = \text{const}$ was used in the calculations, in addition to the latest, most accurate values of the Franck-Condon factor, given in /12/. They were calculated for the potential curves of states $A^3\Sigma$ and $B^3\Pi$ of the nitrogen molecules, determined by the Klein-Rydberg-Ritz method. The molecular constants were taken from a handbook /7/.

$\lambda, \text{\AA}$	Intensity	$\lambda, \text{\AA}$	Intensity
5450	4.16; 3.6	7260	18.1; 19.3; 25.2; 26.9
6000	20.8; 23.5; 17.2; 15.7; 16.6	7373	16.0; 27.2; 27.8; 20.6
6532	30.6; 36.0 36.0;	7490	32.0; 32.4
6780	12.2	7613	23.7; 31.0; 31.0; 19.2
6800	20.0	7738	11.6; 16.0
6870	12.3; 15.6; 11.3	7767	12.0
6884	15.8; 15.1; 14.3		

It is seen from Figures 1—3 that the theoretical calculation describes satisfactorily the special features of the intensity distribution in the emission spectrum, such as the maxima of the intensities of sequences $\Delta v = 2$ and 3, the sharp drop in intensity at the long-wave end of the sequences, and the smooth drop at the short-wave end.

The values of the absolute intensities obtained by the photoelectric method are given in the table ($I_\lambda = 1 \text{ w/cm}^2 \cdot \mu \cdot \text{sterad}$). The spectral range isolated by the spectrometer was 26 \AA for wavelengths $> 0.64 \mu$ and 13 \AA for wavelengths $< 0.64 \mu$.

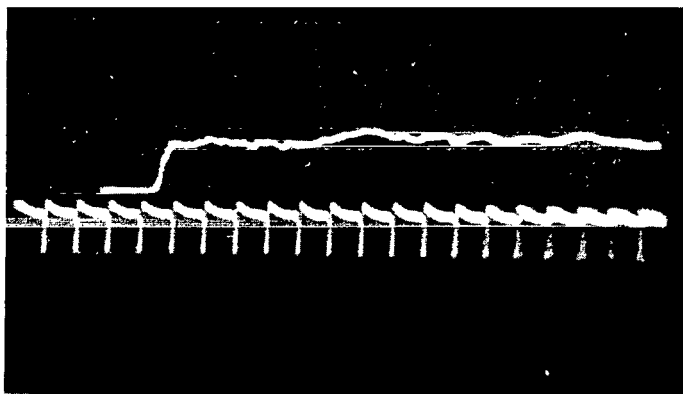


FIGURE 4. Oscillogram of the nitrogen emission, recorded at right angles to the tube axis.

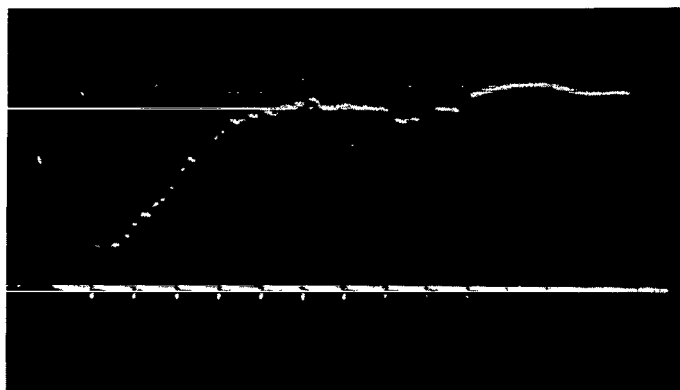


FIGURE 5. Oscillogram of the nitrogen emission, recorded from the end of shock tube.

Figure 4 represents an oscillogram of the signal from the photomultiplier, characteristic for all the investigated regions of the spectrum. The lower beam represents the time base, with a peak-to-peak distance of $10 \mu\text{sec}$.

The values obtained for the absolute intensities (cf. the table) were used to determine the square of the matrix element of the first positive system of nitrogen by the formula

$$\text{Re}^2 = \frac{I_\lambda}{(K_\lambda / \text{Re}^2) B_\lambda l}, \quad (3)$$

where K_λ was calculated by means of relations in /1, 2/; B_λ is Planck's function; l is the thickness of the radiating gas layer; I_λ is the radiation intensity.

The formula holds for an optically thin gas layer. To test this assumption, the intensity was measured during recordings of the radiation at the end of the shock tube. The corresponding radiation oscillogram is shown in Figure 5. A linear form is observed on the oscillogram for 25 μ sec, a fact indicating that the radiation intensity and the thickness of the radiating gas are related linearly [13, 14].

The results of determining the square of the matrix element over the wavelength range 5450–8500 Å are given in Figure 6, together with values

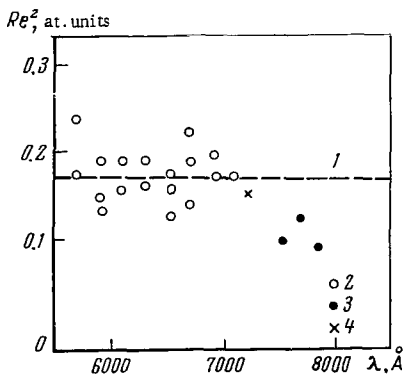


FIGURE 6. Re^2 as a function of λ for the first positive system of nitrogen:

1—averaged values of the present paper by photographic and photoelectric methods; 2—Allen's values [2]; 3—Wurster's values [3]; 4—Wray's values [4].

of Re^2 obtained from the relative distribution of the radiation intensity when processing the microphotograms of Figures 1 and 3. A relative relationship was normed with the aid of data on Re^2 for the wavelength 7490 Å, obtained by the photoelectric method. It is seen from Figure 6 that, according to the relative and absolute measurements, the value of the square of the matrix element is constant over the whole wavelength range studied: $Re^2 = 0.19 \pm 0.05$ at. units.

In order to compare our data with the results of [2–5] the latter must be recalculated to allow for the new values of the factors $q_{v'v''}$ [12]. The results of such calculations for the data of [2–4] are represented in Figure 6. The data of Allen [2] and Wray [4] agree satisfactorily with the values of Re^2 in this study. Wurster's data [3], on the other hand, yield considerably lower values of the matrix element. Nicholls [15] established a strong dependence of Re on the mean internuclear distance, using the values of $q_{v'v''}$ for the potential Morse curve [16]. However, if the latest values of the Franck-Condon factors are used [12], the matrix element of the first positive system of nitrogen is constant rather than variable. This conclusion agrees with the results of the present study.

The author acknowledges the help given him by G. G. Baula.

Bibliography

1. Rakhmatulin, Kh. A. and S. S. Semenov, editors. *Udarnye trubyy* (Shock Tubes).—IL. 1962.
2. Allen, R., J. Camm, and J. Keck. *Radiation from Hot Nitrogen*.—*J. Quant. Spectr. Radiative Transfer*, Vol. 1, No. 3/4. 1961.
3. Wurster, W. H. *Measurements of the Transition Probability for the First Positive Band System of Nitrogen*.—*J. Chem. Phys.*, Vol. 36, No. 8. 1962.
4. Wray, K. L. and T. J. Connolly. *Nitrogen and Air Radiation in the IR*.—*J. Quant. Spectr. Radiative Transfer*, Vol. 5, No. 1. 1965.

5. Keck, J.C., R.A. Allen, and R.L. Taylor. Electronic Transition Moments for Air Molecules.—*J. Quant. Spectr. Radiative Transfer*, Vol. 3, No. 4. 1963.
6. Butslov, M.M. Elektronno-opticheskie preobrazovateli dlya izucheniya sverkhbystrykh protsessov (Image Converters for Studying Ultrarapid Processes).—*Uspekhi nauchnoi fotografii*. Vol. 6, *Trudy Soveshchaniya po vysokoskorostnoi fotografii i kinematografii*, Moskva-Leningrad, Izdatel'stvo AN SSR. 1959.
7. Glushko, V.P., editor. Termodinamicheskie svoistva individual'nykh veshchestv (Thermodynamic Properties of Individual Substances).—Moskva, Izdatel'stvo AN SSSR. 1962.
8. Kudryavtsev, E.M., N.N. Sobolev, L.N. Tunitskii, and F.S. Fauzilov. Pirometricheskoe issledovanie sostoyaniya gaza za otrazhennoi udarnoi volnoi (Pyrometric Study of the Gas State behind a Reflected Shock Wave).—*Trudy FIAN*, Vol. 18. 1962.
9. Logan, D.G. Relaxation Phenomena in Hypersonic Aerodynamics, Collection of translations.—*Mekhanika*, No. 1. 1959.
10. Atlas spektra rtuti (Atlas of the Mercury Spectrum).—Alma-Ata, Izdatel'stvo AN KazSSR. 1959.
11. Plastinin, Yu.A. and G.G. Baula. Secheniya pogloshcheniya elektronnykh sistem dvukhatomnykh molekul N_2 , O_2 , N_2 , NO , C_2 , CN . Fizicheskie izmereniya v gazovoi dinamike (Absorption Cross Sections of Electronic Systems of the Diatomic Molecules N_2 , O_2 , N_2 , NO , C_2 , CN . Physical Measurements in Gas Dynamics).—Collection of papers edited by A.S. Predvoditelev "Issledovanie po fizicheskoi gazovoi dinamike," Moskva, Izdatel'stvo "Nauka." 1966.
12. Zare, R.N., E.O. Larsow, and R.A. Berg. Franck-Condon Factors for Electronic Band Systems of Molecular Nitrogen.—*J. Molecul. Spectrosc.*, Vol. 15, No. 2. 1965.
13. Diecke, G.H. and D.F. Heath. The First and Second Positive Bands of N_2 .—*Johns Hopkins Spectroscop. Rept.* No. 17. 1959.
14. Keck, J.C., J.C. Camm, B. Kivel, and J. Wenting. Radiation from Hot Air.—*Ann. Phys.*, Vol. 7, No. 1. 1959.
15. Turner, R.G. and R.W. Nicholls. An Experimental Study of Band Intensities in the First Positive System N_2 . The Transition in the First Moment.—*Canad. J. Physics*, Vol. 32, No. 6. 1954.
16. Nicholls, R.W. Franck-Condon Factors to High Vibrational Quantum Numbers N_2 and N_2^+ .—*J. Res. Nat. Bureau Standards*, Vol. 65 A, No. 5. 1961.

V. A. Bashilov, V. P. Shevelev

FLOW STRUCTURE OF IONIZED GAS IN AN ELECTROMAGNETIC SHOCK TUBE

1. THE DISCHARGE PROCESS IN A CONIC DISCHARGE CHAMBER

The process taking place inside a discharge chamber and causing the flow of high-temperature plasma in an electromagnetic shock tube, strongly affects the behavior of the whole flow. In particular, a plasma "piston" forms in the discharge chamber, and leads to the appearance of a shock wave.

A conic chamber made of a transparent material was used to study the process which brings about plasma flow. The process in the chamber was recorded by means of SFR cameras, which took single films and made a continuous recording. The process was recorded both inside the discharge chamber itself and at its junction with the plexiglass section of the shock tube.

A number of papers [1—3] have shown that a pinch effect must be observed during the discharge in a conic chamber. Only a small number of experimental studies exist, on the basis of which a conclusion could be drawn about the actual discharge mechanism in a conic discharge chamber.

The experiments indicated that the following occurs (Figure 1): first, a narrow luminous band appears along the cone axis; 6—8 μ sec later the luminous zone starts to broaden symmetrically, until after $\sim 10 \mu$ sec it fills the whole cone; 4—5 μ sec later a glow appears in the region behind the annular electrode. A clearly visible revolving pinch then becomes visible in the discharge chamber itself. The pinch revolves with constant angular velocity, its period being approximately 10 μ sec. The radius of revolution of the pinch remains constant during the first 30 μ sec and equal to the radius of the discharge chamber; it then starts to decrease, until at the end of the half-period of the discharge the pinch disintegrates completely. The pinch rotation takes place in a cone filled with luminous plasma. However, photographs show that the plasma luminosity in the pinch is much greater than the luminosity of the surrounding medium. The rotation of the pinch probably contributes to the symmetry of the plasma efflux from the cone. No shock waves were seen converging to the chamber center.

The rotating pinch exists for a fairly long period, and for roughly the same period a stable flow pattern can be observed at the exit from the cone. The process near the chamber during the plasma efflux in the shock tube was recorded in detail. The field of view of the recording instrument was 20 cm. By inserting a frame, photographs of the process were obtained at the junction of the tube with the gap. The plasma appears in the region

behind the annular electrode approximately $10\mu\text{sec}$ after the discharge commences. Near the tube walls a narrow, pale ejection appears, which gradually shrinks to the center of the tube, forming a cone with a glowing vertex. The oblique shocks converging to the tube center gradually become distinct, and the general pattern of the plasma flow from the conic chamber during this period resembles the pattern of supersonic flow from a nozzle. The angle at the vertex of the luminous cone increases, the vertex itself becomes blurred, and after $\sim 12\mu\text{sec}$ the regular geometrical configuration disappears. After another $5\mu\text{sec}$, the pattern is restored. This restoration was found to be linked with the second half-period of the discharge current.

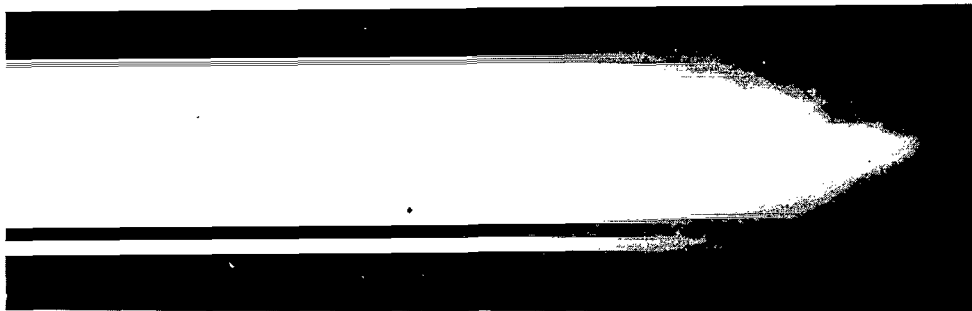


FIGURE 1. Rotating mirror photograph of the process in the discharge chamber. The axis of the camera mirror lies at right angles to the tube axis.

2. THE PLASMA FLOW STRUCTURE FOR DIFFERENT INITIAL DISCHARGE CONDITIONS

To elucidate the character of the plasma flow at different instances of time the process was photographed by two synchronized SFR cameras, one of which made a continuous recording and the other a series of photographs. The first camera served to measure the propagation velocity of the glow front, and the second to determine the instantaneous flow pattern. The exposure time was $0.5\mu\text{sec}$ per frame.

At first, the plasma flow in the tube was observed at a distance of 30 cm from the annular electrode. The driver gases used were air, hydrogen, carbon dioxide, argon, nitrogen, and also mixtures of these gases. The air was evacuated from the tube to a pressure of $1 \cdot 10^{-3}$ mm mercury, after which the tube was filled with the driver gas to the required pressure. The voltage in the discharge chamber varied between 3 and 5 kv. It was established that for an initial pressure of 0.1–0.5 mm mercury the plasma motion from the discharge area is accompanied by a gradual alignment of the leading boundary of the plasma and the formation of a plane glow front. The lower the initial pressure, i. e., the higher the plasma flow velocity, the earlier is the alignment achieved. Thus, for an initial pressure of 0.5 mm mercury (in the air) the plane front was observed ~ 30 cm from the annular electrode, while for a pressure of 0.1 mm this distance decreased to ~ 20 cm. For an initial gas pressure of 1 mm and above, the leading front of the plasma glow near the discharge chamber ceases to appear plane.

For higher initial tube pressures the plasma efflux from the cone is not accompanied by the formation of a distinct and stable pattern, and there are no oblique shocks at the exit from the cone. As the plasma moves further along the tube, the leading front of the plasma glow ceases to have a distinct boundary.

The investigation of the plasma flow pattern at large distances from the discharge chamber showed that for low initial pressures (0.1–0.5 mm mercury) of the driver gas the leading front of the plasma remains plane up to a distance of 1.5 m from the discharge chamber (no investigations were conducted at larger distances). For higher initial pressures the leading front of the plasma flow did not have a distinct shape at large distances from the annular electrode, and the formation of "tongues" and diffuse ejections from the brightly glowing region was observed.

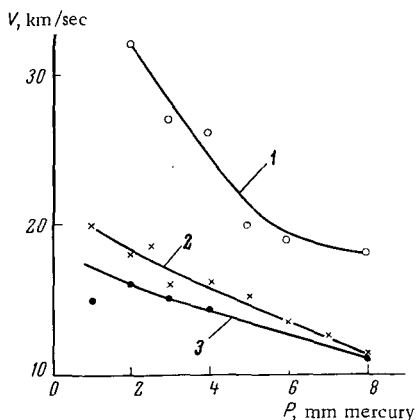


FIGURE 2. Glow front velocity as a function of the initial pressure in the shock tube:

1—hydrogen; 2—air; 3—argon.

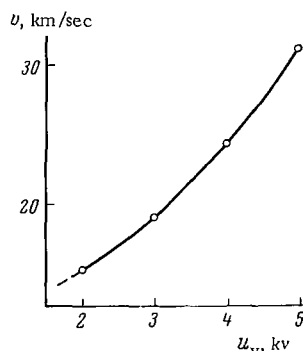


FIGURE 3. Glow front velocity as a function of the voltage on the capacitor battery, for air.

The photorecordings enabled curves to be plotted of the variation in the velocity of the leading glow front (Figure 2). The experiments established that a change of initial pressure does not affect the front velocity very much. Thus, a variation in pressure from 0.1 to 1 mm mercury in air only yielded a 40% change in the front velocity. No regular pattern was observed in the glow front velocity along the tube. The velocity attenuation changed for different initial pressures. Nevertheless, over a certain initial portion of the tube (up to 30 cm from the annular electrode) the plasma was accelerated, after which the velocity decreased gradually. An increase in the voltage applied to the discharge chamber from 2.5 to 5 kv caused a linear increase in the glow front velocity, while the pattern of its variation along the tube remained unchanged. The dependence of the front velocity on the discharge voltage is shown in Figure 3.

The dependence of the glow front velocity on the discharge parameters was studied for different driver gases. It was established that the velocities in hydrogen and air differ by approximately 25% and vary as a function of the initial pressure between 13 and 18 km/sec for a voltage of 3 kv applied to the discharge chamber. The velocities in CO₂ and argon were somewhat lower (~10–14 km/sec).

The photographs could not shed any light on the nature of the glow at the leading front of the plasma flow. The glow front was mostly identified with the shock front, assuming that the gas glow was due to its being heated behind the shock front [4, 5]. A study of plasma flow along the tube showed however that the leading front of the glow is not always plane, as it should be for the propagation of a shock wave.



FIGURE 4. Rotating mirror photograph of the propagation process of the glow front in the top part of the shock tube over a portion enclosed by light filters, for $p = 7$ mm mercury.

The fluid was dyed to aid studies of the front structure. Sodium chloride was introduced at the central electrode of the discharge chamber, and the process was photographed in the monochromatic light of a sodium doublet.

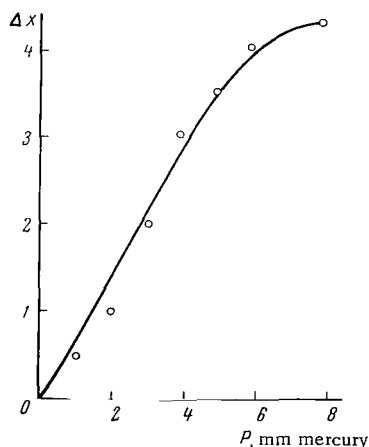


FIGURE 5. Distance between the glow front and the boundary of the sodium-colored region, as a function of the initial pressure of air

The part of the tube being photographed was enclosed by SES-10 and OS-14 light filters which excluded the spectrum range 5800—6000 Å. The length of tube covered by light filters was 8 cm, and the total field of vision of the SFR camera was 50 cm. The film used was sensitive to the red range of the spectrum (Panchrome-13); a color film of sensitivity 45 GOST* units was also used. During the discharge, the central electrode material was vaporized, and the gas discharge plasma was forced out of the conic chamber and moved along the tube. Photographs were taken at different points of the shock tube for different initial discharge conditions (Figure 4). At initial pressures of 0.1—0.5 mm mercury and voltages of 3.5—5 kv applied to the discharge chamber, there was no difference in the recorded glow whether or not

* [Gosudarstvennyi obshchesoyuznyi standart — All-Union State Standard.]

the tube was enclosed by light filters. At a pressure of about 1 mm and above and at a distance of 50 cm from the discharge chamber, a small lag is observed between the glow of the sodium-colored plasma and the leading glow front of the plasma flow. Figure 5 shows a curve of the value Δx of this lag as a function of the initial discharge conditions. On the tube section near the discharge chamber up to a distance of ~ 50 cm from the annular electrode, the leading glow front and the beginning of the sodium fluorescence almost coincide even at pressures above 1 mm mercury. As the motion continues along the tube the leading glow front starts to move away from the boundary of the sodium luminescence, and the lag increases smoothly with increasing distance from the conic discharge chamber. At any fixed observation point this distance becomes larger for higher initial gas pressures in the chamber. A similar pattern is observed when the voltage applied to the discharge chamber is reduced: the lower this voltage, the higher is Δx at a fixed observation point and for a given pressure.

The photographs show that the propagation velocities of the leading glow front and the sodium luminescence are very close, and the lines corresponding to them on the recording are almost parallel.

The experiments indicated that for all operating conditions of the apparatus the radiation intensity of the gas-discharge plasma considerably exceeds the luminosity of the shock-heated gas.

These results agree with measurements of the plug length by continuously recording the emission spectra of ionized gas from an electromagnetic shock tube [6].

3. THE INTERACTION OF THE PLASMA FLOW WITH A SOLID

Some papers, such as [7], established that in discharge shock tubes the time of flow past a model considerably exceeds the computed value for a shock wave with corresponding velocity. This discrepancy is normal, since the existence of two zones has been established in a plasma flow, namely, that of the shock-heated gas and that of the gas-discharge plasma, the latter exceeding the former in its dimensions by a factor of 10–15.

The flow past differently shaped bodies was studied using the IAB-451 Schlieren unit with an SFR camera taking separate films. Satisfactory Schlieren photographs of the flow of ionized gas in discharge tubes are difficult to obtain, in view of the strong plasma glow. To obtain a satisfactory Schlieren photograph, the optical system between the exit slit of the Schlieren unit and the entrance slit of the SFR camera was adjusted. The two-line framing inset together with the conversion system produced an image of the model in a scale such that a working field of vision of 13 cm diameter was represented on a frame of 10 mm diameter. To that end RO-2 and Industar-23 objectives with focal distances of 75 and 110 mm respectively were placed between the shadow apparatus and the SFR camera. Two knife edges, each 0.4 mm wide, were inserted at right angles to the flow in the IAB-451 instrument to produce a slit of height 8 mm. These adjustments enabled a satisfactory Schlieren photograph of the flow past the models to be obtained.

The window in the plexiglass section was made of polished optical glass of type K8. The glass was washed after every experiment, and the film of copper and soot removed.

The light source was an IFK-200 pulse lamp with a bank of capacitors of $200\mu\text{f}$ capacity and 3 kv voltage. To initiate breakdown, a specially made spark generator with delay circuit was used in the lamp. The generator was triggered by a pulse from the SFR panel.

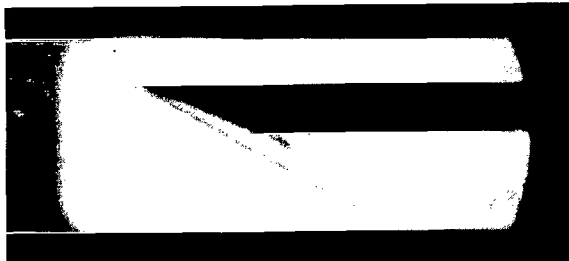


FIGURE 6. Flow past a wedge:

Exposure time 1 μsec ; initial air pressure 2 mm mercury.

Plasma flow past models was studied for different initial discharge conditions, the tube pressure varying between 0.5 and 5 mm mercury and the voltage applied to the discharge chamber between 3 and 5 kv. The photographs show that the flow past solids of different geometrical shapes in an electric discharge shock tube is the same as in an ordinary shock tube for supersonic gas flows past a body.

Figure 6 shows a typical photograph of the flow past a wedge at an angle of attack of 15° ($p = 2$ mm mercury, $V = 3$ kv). A weak disturbance wave appears at one side of the edge of the wedge, while at the other is an oblique compression shock. This shock is reflected from the tube wall, i.e., we observe a typical flow pattern past the wedge of a shock wave followed by the gas.

The experiments indicated that the inclination of the oblique shock is unaltered when the flow is of a gas-discharge plasma. This means that the Mach number of this flow is almost the same as that behind the shock wave. The shock angle increases with time (a fact indicating a decrease in Mach number) until the shock at the model disappears after $80\mu\text{sec}$. The time of flow past the wedge coincides with the time during which the discharge current flows /7/.

Studies of plasma flow past solids showed that a supersonic plasma flow ($M \sim 3.5$ in our conditions) exists in the electric-discharge shock tube. Another important result was that no substantial difference was observed between the Mach numbers of the plasma flow behind the shock wave and the flow of gas-discharge plasma as a whole.

Bibliography

1. Kholev, S.R. and L.I. Krestnikova. Eksperimental'noe issledovanie napravlenogo potoka gaza pri impul'shom razryade (Experimental Study of a Directed Gas Flow in Impulsive Discharge).—Izvestiya Vuzov, Fizika, No. 1. 1960.
2. Vasil'ev, V.I., V.S. Komel'kov, Yu.V. Skvortsov, and S.S. Tserevitinov. Ustoichivyi dinamicheskii tokovyi shnur (Stable Dynamic Current Pinch).—Zhurnal Tekhnicheskoi Fiziki, Vol. 30, No. 7. 1960.
3. Allen, R.A., J.C. Keck, and J.C. Camm. Nonequilibrium Radiation and the Recombination Rate of Shock-Heated Nitrogen.—Phys. Fluids, Vol. 5, No. 3. 1962.
4. Kolb, A.C. Magnetically Confined Plasmas.—Phys. Rev., Vol. 112, No. 2. 1958.
5. Kolb, A.C.—Proc. Fourth Internat. Conf. Ionization Phenomena in Gases, Uppsala. 17–21 August, 1959.
6. Bashilov, V.A. Spektroskopicheskoe issledovanie protsessov, proiskhodyashchikh v elektromagnitnoi udarnoi trube (Spectroscopic Investigation of the Processes Taking Place in an Electromagnetic Shock Tube).—Sbornik: "Fizicheskaya gazodinamika, termodinamika i gorenje," Moskva, Izdatel'stvo "Nauka." 1965.
7. Ladyzhenskii, M.D. and L.G. Chernikova. Issledovaniya raspredeleniya udarnykh voln v razryadnoi trubke (Shock-Wave Distribution in a Discharge Tube).—PMTF, No. 2. 1961.

V. A. Bashilov

***ELECTRON CONCENTRATION BEHIND A SHOCK
FRONT AND IN A GAS-DISCHARGE PLASMA IN
A MAGNETOHYDRODYNAMIC SHOCK TUBE***

Time-resolved emission spectra of ionized gas formed in an electromagnetic shock tube were obtained in [1].

This paper presents the electron concentration, derived from measurements of the halfwidth of the H_β line assuming Stark broadening of the hydrogen lines.

The influence of the following different side effects, which cause a broadening of the spectral lines, will be estimated:

1) instrument broadening, caused by the finite slit width in the instrument for the spectral decomposition of light. Photographs of the plasma spectra were taken with a slit width of 0.2 mm, which gave an instrument broadening $\sim 6 \text{ \AA}$ for the IOP-51 spectrograph with camera $F = 300 \text{ mm}$;

2) Doppler broadening, i. e., a variation in the frequency of an emitter moving at a high velocity according to the formula $\nu = \nu_{\min} (1 - v/c)$, where v is the velocity of the emitter in the direction of observation. The Doppler halfwidth is estimated by the formula

$$\Delta\lambda_D = \frac{2kT \ln 2}{mc^2} v_{\min};$$

with the obviously overestimated value of 20000°K for the temperature (at a front velocity of 20 km/sec), we obtain for the hydrogen atom

$$\Delta\lambda_D = 0.25 \text{ \AA};$$

3) shock broadening, appearing only at very high pressures.

These effects can be neglected for a halfwidth of $H_\beta \sim 40 \text{ \AA}$.

The spectra obtained on the spectrograph for different initial discharge conditions were processed as follows. The continuous spectrum of a tungsten lamp was photographed on the same film through a nine-step attenuator. The characteristic curves of the film were then plotted for three points with wavelengths 6560, 4860, and 4340 \AA (all the spectra processing was conducted on an MF-4 microphotometer). The value of γ for each spectrum range was determined on the basis of these curves. The H_α and H_β lines of the spectrum under observation were then measured photometrically.

Using the characteristic curves, we passed from blackening values to values of the intensity. The halfwidth of the lines was determined as follows:

$$\frac{J_{0.5}}{J_0} = 0.5: \lg \frac{J_{0.5}}{J_0} = \lg 0.5 = 0.301; \lg J_{0.5} = \lg J_0 - 0.301.$$

We found the value of the maximum blackening, namely $\lg J_0$. This value was marked on the characteristic curve, the value 0.301 was subtracted from it, and the blackening value $S = \lg J_{0.5}$ was determined from the characteristic curve. The distance (in Å) was then determined for two such points, located to the right and left of the line center.

It later became possible to simplify the determination of the line halfwidth, since the values of J_0 and $J_0/2$ for the lines obtained were situated in the region of normal blackenings, and therefore

$$S_{0.5} = S_0 - \gamma 0.301.$$

Knowing γ for the wavelengths of the lines H_α and H_β , and having determined S_0 for the maximum line intensity, the blackening for $S_{0.5}$ can be found, and hence the halfwidth of the line.

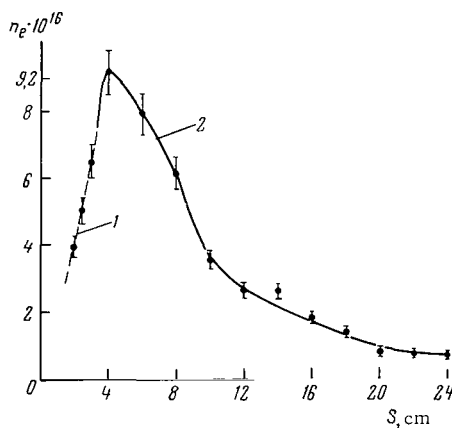


FIGURE 1. Electron concentration behind the shock front and in the gas-discharge plasma:

1—region of shock-heated gas; 2—region of gas-discharge plasma.

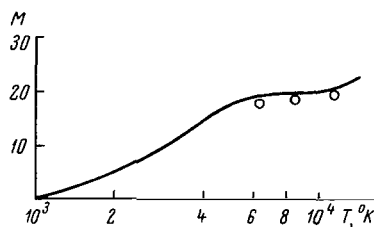


FIGURE 2. The temperature behind the shock front in hydrogen for $p_0 = 4$ mm mercury:

○ — experimental points obtained on the basis of Sach's equation.

The transition from the measured halfwidths to the concentrations of the charged particles is realized as follows. Since satisfactory agreement is observed between theoretical and experimental values of the concentrations for contours of equal halfwidths, the concentrations were calculated (without a detailed comparison of the contours) by formulas derived theoretically and corroborated by numerous experiments in both electric arcs and shock tubes [2, 3]. The line halfwidth for Holtsmark broadening are:

without allowing for the electrons

$$\delta_w = 15.6 \alpha N^{1/3}, \text{ sec}^{-1};$$

allowing for the electrons

$$\delta_w = 25 \alpha N^{1/2}, \text{ sec}^{-1}.$$

Here, α are the effective Stark constants, equal to 3.9 for H_α , to 10.5 for H_β , and to 21 for H_γ .

The concentrations of charged particles were estimated from the H_β lines. The hydrogen line contour was measured every $1 \mu\text{sec}$, and a curve of the electron concentration along the plug was plotted (Figure 1). In addition, the electron concentration in the gas-discharge plasma was estimated. Figure 1 shows the considerable rise in concentration linked with the influx of gas-discharge plasma, followed by the gradual drop in concentration as the gas-discharge plasma moves away from the shock front.

Knowing the velocity of the shock front, one can link the variation in electron concentration with the equilibrium temperature by Sach's formula, and then compare this variation with the theoretical variation, using the conservation laws. The theoretical and experimental results are given in Figure 2.

The following conclusions can be drawn from a comparison of Figures 1 and 2:

the values of the concentrations coincide (within the error limits of the method) with the theoretical values, calculated from the conservation laws on the shock;

the coincidence is observed up to the moment of arrival of the gas-discharge plasma. The concentration of electrons in it is 2 to 3 times greater than the concentration of electrons in the plug.

The measurement of the electron concentration showed that there exists some transition region from the gas-discharge plasma to the pure gas, the concentration increasing smoothly in the direction of the gas-discharge plasma. This is probably due to the diffusion of electrons from the gas-discharge plasma to the pure gas.

Bibliography

1. Bashilov, V.A. Spektroskopicheskie issledovaniya protsessov, proiskhodyashchikh v elektromagnitnoi udarnoi trube (Spectroscopic Study of Processes Taking Place in an Electromagnetic Shock Tube).—Sbornik: "Issledovaniya po fizicheskoi gazodinamike." Moskva, Izdatel'stvo "Nauka." 1955.
2. Greim, H., A. Kolb, and K. Shen. Stark Broadening of Hydrogen Lines in Plasma.—Phys. Rev., Vol. 116. 1959.
3. Kitaeva, V.F. and N.N. Sobolev. Ob ushirenii linii vodoroda v plazme dugi i udarnoi trubki (Broadening of Hydrogen Lines in the Arc Plasma and the Shock Tube).—Doklady AN SSSR., Vol. 137, No. 5. 1961.

T. V. Bazhenova, Yu. S. Lobastov

*RATE OF THERMAL IONIZATION OF NITROGEN
AT 3000—5000°K*

The time taken for an equilibrium degree of ionization to be established in nitrogen at 3000—5000°K was determined from the absorption by nitrogen of centimeter radio waves behind a shock wave in a square $7 \times 7 \text{ cm}^2$ shock tube. The high-pressure chamber was 125 cm long, and the low-pressure chamber 600 cm long. The velocity of the incident shock wave was measured by means of two piezoelectric pressure-sensitive elements on an OK-17-M oscillograph. Control measurements of the velocity of the reflected shock and the structure of the gas column behind it were obtained in some of the experiments with the aid of an IAB-451 optical shadow instrument and a drum photometer. The accuracy of the velocity measurement was 1 %.

The microradio-wave absorption was measured in a special plexiglass section, from the end of which the shock wave was reflected. The absorption of radio waves of wavelengths 1.6 and 0.8 cm, directed through the measuring section in two mutually perpendicular directions, was measured simultaneously; the width of the radio-wave beams did not exceed 20 mm. The determination of the free-electron concentration and the effective collision frequency from the above measurements was described in detail in /1—3/.

The time taken to attain an equilibrium degree of ionization in nitrogen was measured for initial pressures in the low-pressure chamber of 1—5 mm mercury behind the incident shock wave with $M_0 \sim 9$, and behind the reflected wave for incident-shock Mach numbers of 5.5—6.8. The temperature and pressure, calculated from the conservation laws, were $\sim 4000^\circ\text{K}$ and 0.13 atm for an equilibrium composition behind the incident wave, and 3500—4500°K and 1—2 atm behind the reflected wave /4/.

The radio-wave absorption oscillograms are shown in Figure 1. The apparatus resolution, determined from the time of radio-beam shuttering by the shock wave, is less than $10 \mu\text{sec}$ (Figure 1, a), and the time taken to attain a constant absorption level is 60—70 μsec . After the reflected shock wave (Figure 1, b) reaches the radio beam, whose center is located 20 mm from the end, a gradual increase is observed in the absorption of radio waves during the next 100 μsec , after which a constant level is attained. A further increase in absorption is linked with the influx of a secondary wave, produced by the interaction of the reflected wave with the contact surface /3/. The reflected wave propagates with a velocity of 0.5 mm/ μsec with respect to the shock-tube walls /5/, and therefore the gas behind the reflected wave overlaps the radio-beam section for 40 μsec . Control experiments in air showed that bifurcation during the reflection of the shock wave does not noticeably affect the absorption of radio waves.

This is probably linked with the fact that a distortion to the reflected wave front only exists in a narrow region near the front /6/. The increase in radio-wave absorption during $60\mu\text{sec}$ is due to the establishment of equilibrium ionization of nitrogen.

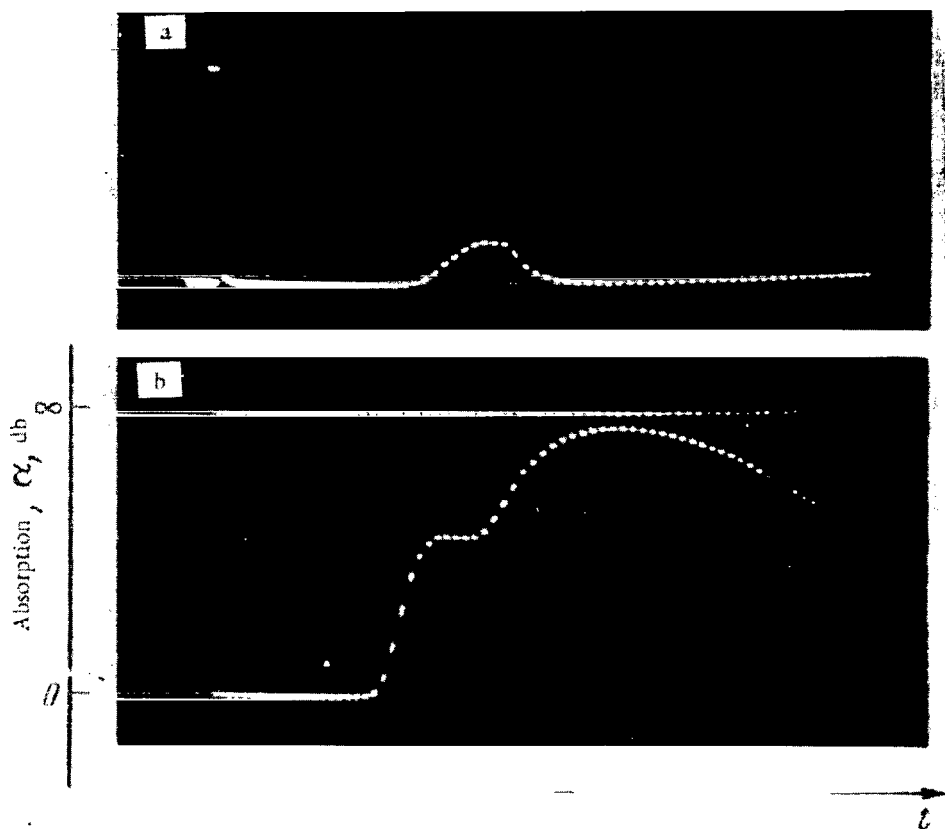


FIGURE 1. Oscillogram of radio-wave absorption:

Peak-to-peak distance is $10\mu\text{sec}$; a — behind the incident shock; b — behind the reflected wave.

The free-electron concentration n_e , measured after the first maximum on the absorption curve, is between 10^{11} and 10^{12}cm^{-3} for $M_0=6-6.8$, $p_0=2\text{ mm mercury}$ (Figure 2). These values of n_e agree with the computed curve /4/.

The time taken to attain an equilibrium degree of ionization under atmospheric-pressure conditions and over the temperature range studied, is $60-300\mu\text{sec}$ (Figure 3). At 4500°K this time is an order of magnitude higher than the time for the thermal ionization of air. By comparison, Figure 3 shows the ionization time of air under the same conditions (in a coordinate frame linked with the gas stream) using data obtained earlier behind the incident shock wave /7/. The experimental data on the ionization time of air agree satisfactorily with the values calculated in /7, 8/ for the

reaction $N + O \rightleftharpoons NO^+ + e$ (cf. Figure 3, curve 4), whose rate constant equals $3.10^{-3}T^{-3/2} \text{ cm}^{-3}$. It was shown in /7/ that the ionization time of air for $T = 3000-5000^\circ\text{K}$ is mainly determined by the formation time of the nitrogen and oxygen atoms. The high values obtained in this paper for the ionization time of nitrogen indicate that not only the formation of nitrogen atoms, but the ionization process itself also represent a limiting process.

Two possible ionization reactions for nitrogen are analyzed in /9/:

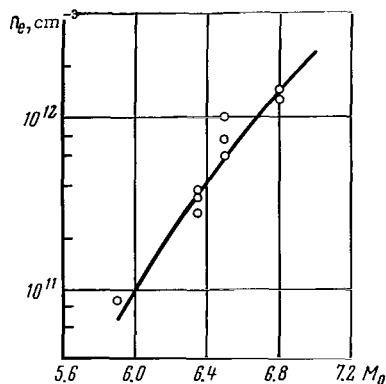


FIGURE 2. Variation of n_e as a function of M_0 .

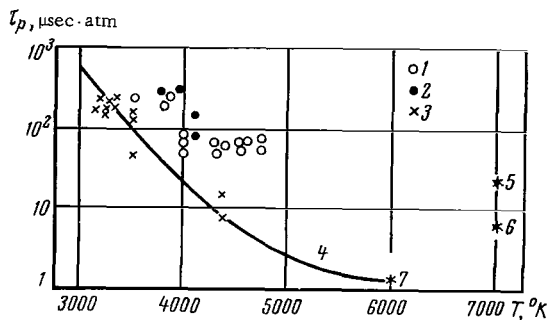


FIGURE 3. Time to establish an equilibrium degree of ionization of nitrogen and air as a function of the equilibrium temperature T :

1—nitrogen behind the reflected wave; 2—nitrogen behind the incident wave; 3—air behind the incident wave; 4—following the data of /8, 9/; 5, 6, 7—following the data of /9/.

In a laboratory frame of coordinates, the time taken to attain an electron concentration near to equilibrium at a shock velocity of 6.6 km/sec and $p_0 = 4$ mm mercury, is /9/ 0.4 and 0.1 μsec respectively for reactions (1) and (2). In a coordinate frame linked with the gas and under atmospheric-pressure conditions, this time is 24 and 6 μsec for $T = 7000^\circ\text{K}$ (cf. Figure 3, points 5 and 6). The ionization time of air, calculated in /9/ for the reaction $N + O \rightleftharpoons NO^+ + e$, is 1.6 μsec for $T = 6000^\circ\text{K}$ at atmospheric pressure (cf. Figure 3, point 7).

The experimental data indicate that the ionization time of nitrogen for $T = 4000^\circ\text{K}$ is an order of magnitude higher than the ionization time of air and agrees with the computed values of /9/.

Bibliography

1. Lobastov, Yu.S. Usovorshenstvovanie metoda radiovolnovogo zondirovaniya gaza, nagretogo udarnoi volnoi (Improving the Radio-Wave Method of Studying a Gas Heated by a Shock Wave).—Sbornik: "Fizicheskaya gazodinamika i svoistva gazov pri vysokikh temperaturakh," Moskva, Izdatel'stvo "Nauka," 1964.
2. Bazhenova, T.V. and Yu.S. Lobastov. Kontsentratsiya elektronov i chislo soudarenii elektronov s molekulami vozdukha za udarnoi volnoi (Electron Concentration and the Number of Electron Collisions with Air Molecules behind a Shock Wave).—Sbornik "Fizicheskaya gazodinamika i svoistva gazov pri vysokikh temperaturakh," Moskva, Izdatel'stvo "Nauka," 1964.
3. Lobastov, Yu.S. Eksperimental'noe opredelenie elektronnykh kontsentratsii i effektivnykh chastot stolkovenii s neitral'nymi chastitsami v vozdukhe, N_2 , O_2 , Ar, CO, and CO_2 za udarnymi volnami (Experimental Determination of the Electron Configuration and Effective Collision Frequencies with Neutral Particles in Air, N_2 , O_2 , Ar, CO, and CO_2 behind Shock Waves).—Sbornik "Issledovaniya po fizicheskoi gazodinamike," Moskva, Izdatel'stvo "Nauka," 1965.
4. Lazarev, P.P. Raschet gazodinamicheskikh i termodinamicheskikh parametrov gazov za padayushchei i otrazhennoi udarnymi volnami (Gas-Dynamic and Thermodynamic Parameters of Gases behind Incident and Reflected Shock Waves).—Trudy FIAN imeni Lebedeva. Vol. XXX, Moskva, Izdatel'stvo "Nauka," 1964.
5. Bazhenova, T.V., O.A. Predvoditeleva, and T.V. Nadezhina. Poteri pri otrazhenii udarnykh voln v udarnoi trube (Losses for Shock-Wave Reflection in a Shock Tube).—Sbornik: "Fizicheskaya gazodinamika i svoistva gazov pri vysokikh temperaturakh," Moskva, Izdatel'stvo "Nauka," 1964.
6. Zaitsev, S.G., A.P. Shatilov, E.V. Lazareva, and L.I. Trukhanova. Issledovanie protsessa vzaimodeistviya otrazhennogo razryva s pogranichnym sloem potoka za padayushchei volnoi (Interaction Process of a Reflected Shock with the Boundary Layer of the Flow behind the Incident Wave).—Sbornik "Fizicheskaya gazodinamika i svoistva gazov pri vysokikh temperaturakh," Moskva, Izdatel'stvo "Nauka," 1964.
7. Bazhenova, T.V. and Yu.S. Lobastov. K voprosu o mekhanizme termoionizatsii vozdukha (Mechanism of the Thermal Ionization of Air).—Sbornik "Fizicheskaya gazodinamika i svoistva gazov pri vysokikh temperaturakh," Moskva, Izdatel'stvo "Nauka," 1964.
8. Lin, S.C. and J.D. Teare. Rate of Ionization behind Shock Waves in Air, II. Theoretical Interpretations.—Phys. of Fluids, Vol. 6. 1963.
9. Hammerling, P., J. Teare, and B. Kivel. Nonequilibrium Electrical and Radiation Properties of High Temperature Air, Nitrogen and Oxygen.—Proc. Fourth Internat. Conf. Ionization Phenomena in Gases, Uppsala, Vol. 2. 1959.

G. P. Petrova, E. K. Chekalin

ARGON PLASMA FLOW IN A CHANNEL WITH A TRANSVERSE MAGNETIC FIELD

The investigation of the flow of ionized plasma in a transverse magnetic field is an important problem in constructing an MHD [magnetohydrodynamic] generator.

It is of interest in this connection to study the boundary-layer effect in a nonisothermal plasma channel flow in the presence of a magnetic field, on the current flow between the electrodes.

A direct study of plasma flow in channels is very difficult. Shock tubes /1—3/ cannot simulate fully the conditions near the channel walls and electrode surfaces in real MHD generators, in view of the short duration of the plasma flow.

This paper studies the magnetohydrodynamic properties of a steady argon plasma flow in a channel with cooled walls.

1. DESCRIPTION OF THE APPARATUS

A steady argon plasma flow was created by means of an electric-arc DC plasmatron /4/. The water-cooled anode of the plasmatron consisted of a conic brass nozzle with throat and exit diameters of 5 and 5.4 mm respectively. The pressure in the arc chamber varied between 4.5 and 5 atm for different working conditions of the plasmatron, and the rate of discharge of argon was 25—30 m³NTP/hr.

First, the plasmatron was connected through joint gaskets with a 23 mm long quartz chamber of 25 mm diameter and a diffuser. Two tungsten electrodes of 1 mm diameter and 4 mm apart were mounted in the quartz chamber perpendicular to the axis of symmetry of the apparatus and the poles of the electromagnet. The electrodes were placed 14 mm from the nozzle exit (Figure 1). The quartz chamber and the diffuser were not cooled, and the tungsten probes were heated strongly.

Later, we used a cylindrical quartz channel of inner diameter 6 mm, which acted as a continuation of the plasmatron nozzle. The channel was enclosed in a quartz shell and cooled by water. A separate unit of two cooled brass electrodes was fastened to the end of the channel, the electrodes being isolated from each other by 5 mm thick talc-chloride washers. The inner diameter of the electrode unit was equal to the diameter of the quartz channel. The electrodes were 15 mm long and 4 mm wide. The channel was fastened to the anode of the plasmatron and to the electrode unit by means of refractory asbestos washers.

The electrodes were thoroughly insulated from the whole apparatus and cooled by distilled water to prevent shunting of the electrodes in the direction of the water cooling. The layout of the plasmatron with channel and electrodes is shown in Figure 2. The screening casing with a 4 mm thick wall was made of Armco iron, and prevented the magnetic field from influencing the plasmatron arc current. The same figure shows the layout of the electrodes and poles of the electromagnet (view from the channel end). The electromagnet poles had a cross section of $14 \times 16 \text{ mm}^2$, and the maximum strength of the magnetic field was 4500 gauss. The magnetic field strength in the gap was measured by a coil of 1.5 mm radius with $n = 50$ turns. The field in the gap was found to be homogeneous to an accuracy of 10 %.

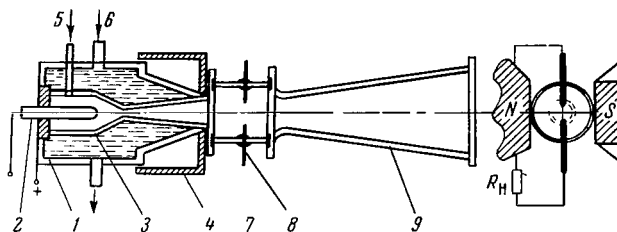


FIGURE 1. Layout of the plasmatron with quartz chamber and exit cone:

1—arc chamber; 2—cathode; 3—nozzle; 4—magnetic screen; 5—argon supply; 6—water cooling; 7—quartz chamber; 8—tungsten probes; 9—diffuser.

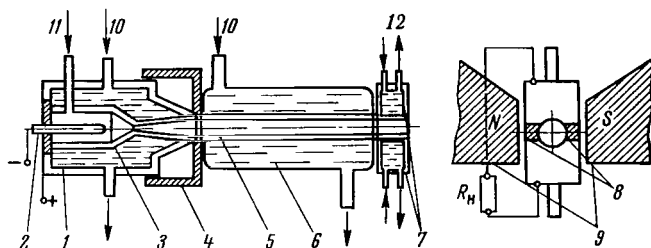


FIGURE 2. Layout of the plasmatron with quartz channel and electrode unit:

1—water-cooled arc chamber; 2—tungsten cathode; 3—nozzle anode; 4—screening casing; 5—quartz channel; 6—water-cooled quartz jacket; 7—brass electrodes; 8—insulating talc-chloride washers; 9—poles of the electromagnet; 10—water; 11—argon; 12—distilled water.

Figure 3 gives the current-voltage characteristics for two different load resistances in the plasmatron circuit— for the cases of plasma flow in the channel and free discharge of the jet into the atmosphere. The graph indicates that the current-voltage characteristics for these cases coincide within the accuracy limits. The inclusion of a magnetic field did not affect the values of the current, arc voltage, and argon rate of discharge.

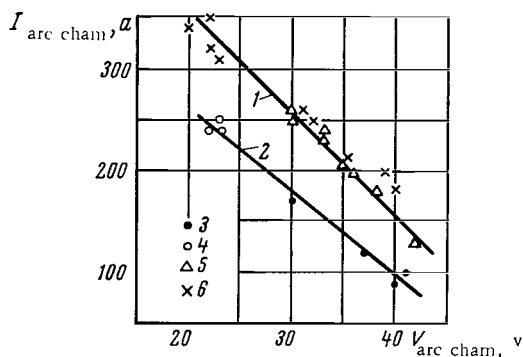


FIGURE 3. Current-voltage characteristics of the electric-arc plasmatron:

1— $R_H = 0.1 \Omega$; 2— $R_H = 0.14 \Omega$; 3—free discharge of the jet from the nozzle into the atmosphere, $R_H = 0.14 \Omega$, $Q_{Ar} = 24.2 \text{ m}^3 \text{ NTP/hr}$; 4—plasma flow in the channel, $R_H = 0.14 \Omega$; $Q_{Ar} = 23.5 \text{ m}^3 \text{ NTP/hr}$; 5—free discharge of the jet into the atmosphere, $R_H = 0.1 \Omega$; $Q_{Ar} = 21.4 \text{ m}^3 \text{ NTP/hr}$; 6—plasma flow in the channel, $R_H = 0.1 \Omega$, $Q_{Ar} = 24.5 \text{ m}^3 \text{ NTP/hr}$.

2. EXPERIMENTAL RESULTS

The emf induced by the flowing plasma and the current in the electrodes circuit were both investigated for various magnetic fields and different working conditions of the plasmatron.

The values of the emf were measured by an M-193 voltmeter and an ENO-1 oscillograph with an input impedance of 0.5 megaohm. In the absence of a magnetic field the plasma flow induces a potential difference on the electrodes varying from experiment to experiment, and probably due to the nonuniform combustion of the plasmatron arc or a disturbance in the coaxial alignment of the nozzle and electrodes.

Tests of two types of electrode showed that the scatter of the initial potential difference is maximum for thin tungsten electrodes. This is probably due to the fact that when electrodes are introduced in a free jet of relatively small diameter, even small deviations from the symmetry can cause changes in the temperatures and velocities of the probes (in a jet of such small diameter the temperature and velocity gradients are considerable). In addition, during a prolonged operation the wire probes became very hot. For large water-cooled electrodes in the channel, the value of the initial potential difference was much smaller and more stable than in the first variant. These electrodes were capable of operating for long periods (all the experiments were conducted with the same electrode unit).

Oscillograph measurements established that the voltage on the electrodes has a variable component, the amplitude of whose oscillations is of the same order of magnitude as the emf; the frequency of these oscillations is

constant and of the order of several kc. The inclusion of an RC circuit ($R = 200 \Omega$, $C = 0.1 \mu f$) enabled these oscillations to be shunted. As a result, the values of the emf measured on the oscillograph and the voltmeter almost coincided.

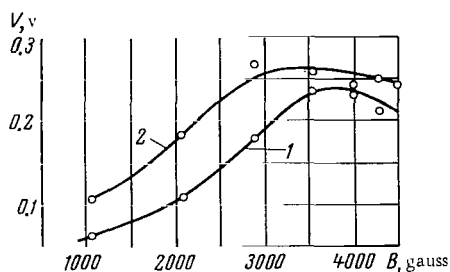


FIGURE 4. Emf on disconnected wire probes as a function of B :

1— $p_{\text{arc}} = 4.53 \text{ atm}$; $i_{\text{arc chan}} = 260 \text{ a}$, $v_{\text{arc chan}} = 32 \text{ v}$, $Q_{Ar} = 20 \text{ m}^3 \text{ NTP/hr}$; 2— $p_{\text{arc}} = 5 \text{ atm}$, $i_{\text{arc chan}} = 301 \text{ a}$; $Q_{Ar} = 23.5 \text{ m}^3 \text{ NTP/hr}$.
 $p_{\text{arc}} = 4.77 \text{ atm}$, $v_{\text{arc chan}} = 28.6 \text{ v}$; $i_{\text{arc chan}} = 250 \text{ a}$, $v_{\text{arc chan}} = 30 \text{ v}$, $Q_{Ar} = 22 \text{ m}^3 \text{ NTP/hr}$.

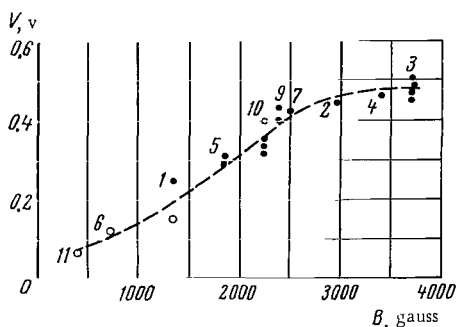


FIGURE 5. Emf on cooled electrodes in a 58mm long channel as a function of B :

The plasmatron was started several times in order to measure the emf for given magnetic field strength B and given working conditions of the apparatus, and during each of its operating periods the magnetic field direction in the gap was altered several times by switching the polarity of the supply source at the terminals of the electromagnet winding. After each operating period the channel and the electrode unit were thoroughly cleaned. The values of the emf in the different experiments were averaged.

Curves of the emf induced on the wire probes are shown in Figure 4. Their characteristic feature is the nonlinearity of the dependence $V = f(B)$ and the existence of maxima. The latter is probably explained by the appearance of a noticeable leakage current between the probes on the inner surface of the quartz chamber.

Figure 5 represents the emf on the cooled electrodes as a function of B . The numbers on the graph represent the sequence in which the points were obtained in the course of the study. The curve in Figure 5 is similar in shape to the curves in Figure 4.

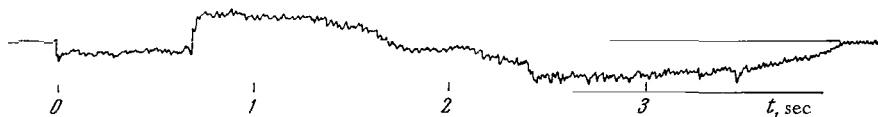


FIGURE 6. Typical oscillogram of the current in the circuit of cooled electrodes.

The current in the circuit of cooled electrodes was measured by an N-700 recording oscillograph. Use was made of galvanometers with a sensitivity to direct current of 1400 mm/ma , and an internal resistance of 36Ω , which

served simultaneously as external load in the channel electrodes circuit. The response of such a galvanometer is 40 cps. Figure 6 shows a typical oscillogram of the current in the electrodes circuit. The undeflected-beam loop can be seen. After the inclusion of the plasmatron arc, but in the absence of a magnetic field, one observes a certain deviation (over a period of 0.7 sec), corresponding to the initial current on the electrodes in the stream of burning plasma. The same photograph shows the beam deviation due to a transverse magnetic field in two opposite directions, but equal magnitude.

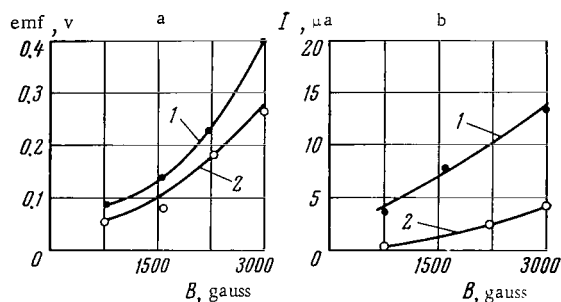


FIGURE 7. Emf and current in the circuit of cooled electrodes as a function of the magnetic field strength:

1—shaft channel (38 mm), $V_{\text{arc cham}} = 32$ v, $I_{\text{arc cham}} = 255$ a, $Q_{\text{Ar}} = 23.1$ m³NTP/hr; 2—long channel (58 mm), $V_{\text{arc cham}} = 31$ v; $I_{\text{arc cham}} = 255$ a, $Q_{\text{Ar}} = 22.7$ m³NTP/hr.

The emf and the current on the electrodes have been plotted in Figure 7 as functions of the magnetic field strength for two lengths of the quartz channel, namely 58 and 38 mm. The emf and the current in the electrodes circuit are seen to decrease for increasing channel length.

3. DISCUSSION OF THE RESULTS

The reason for the nonlinear dependence of the emf on the magnetic field strength B is not sufficiently clear. Such a nonlinear dependence was observed in experiments with models of MHD generators [5, 6]. The working medium was the combustion products of a fuel with an oxygen-nitrogen mixture. The voltage on the electrodes (in open circuit) was of the order of several tens of volts, and the corresponding magnetic induction was of the order of 10 kgauss. The authors noted that for a magnetic induction of 14 kgauss the experimental value of the emf was roughly 15% lower than that obtained by assuming a linear relationship between the emf and B . This discrepancy is explained by the voltage drop on the electrodes and the leakage currents along the surface of the insulator separating the electrodes.

The effect of channel length on the induced emf and the current in the circuit of cooled electrodes (cf. Figure 7) is easily explained by the intense cooling of the plasma in the channel and the development of a boundary layer in it.

In fact, the longer the channel, the stronger the cooling and the lower the average temperature of the plasma in the region between the electrodes.

For two channels of lengths l_1 and l_2 respectively we have

$$\frac{U_1}{U_2} = \frac{T_1}{T_2} \frac{p_2}{p_1},$$

where $U_{1,2}$ is the average velocity of the plasma flow; $T_{1,2}$ is the average temperature; $p_{1,2}$ is the pressure.

For any channel length the pressure near the exit of the stream from the electron unit approximates the atmospheric pressure (cf. Figure 2), so that $p_1 \simeq p_2$.

It follows from here that the flow velocity in the electrode unit will decrease with an increase in channel length, and the emf will therefore decrease.

Figure 7 implies that the decrease in emf and the drop in plasma conductivity caused by the cooling of the flow along the channel affect strongly the value of the short-circuiting current. Thus, if the cooled channel is lengthened by 50 % for $B = 3000$ gauss, it yields a drop of 70 % in the value of the current and only 30 % in the open-circuit emf.

When assessing the results it should be borne in mind that the experiments were conducted with small-diameter channels, and therefore the effect of heat losses in the channel on the various characteristics of the plasma in the magnetic field was considerable.

Bibliography

1. Nagamatsu, H. and R. Sheer. Magnetohydrodynamic Results for Highly Dissociated and Ionized Air Plasma.—Phys. of Fluids, Vol. 4. 1961.
2. Sakuntala, M., A. Von Engel, and R. Fowler. Ionic Conductivity of Highly Ionized Plasmas.—Phys. Rev., Vol. 118. 1960.
3. Makarov, Yu. V. Nekotorye issledovaniya protsessov v magnitogidrodinamicheskoi udarnoi trube s konicheskoi razryadnoi kameroi (Processes in a Magnetohydrodynamic Shock Tube with a Conic Discharge Chamber).—Sbornik "Fizicheskaya gazodinamika i svoistva gazov pri vysokikh temperaturakh," Moskva, Izdatel'stvo "Nauka." 1964.
4. Petrova, G. P. Issledovaniya nekotorykh fizicheskikh svoistv plazmennoi strui argona (Some Physical Properties of an Argon Plasma Jet).—Sbornik "Fizicheskaya gazodinamika i svoistva gazov pri vysokikh temperaturakh," Moskva, Izdatel'stvo "Nauka." 1964.
5. Way, S., S. M. De Corso, R. L. Hundstad, G. A. Kemeny, W. Stewart, and W. E. Young. Experiments with MHD Power Generation.—J. Eng. Power, Vol. 83. 1961.
6. Way, S. Comparison of Theoretical and Experimental Results in a Magnetohydrodynamic Generator.—Progress. Astron. J. Rocketry, Vol. 3. 1961.

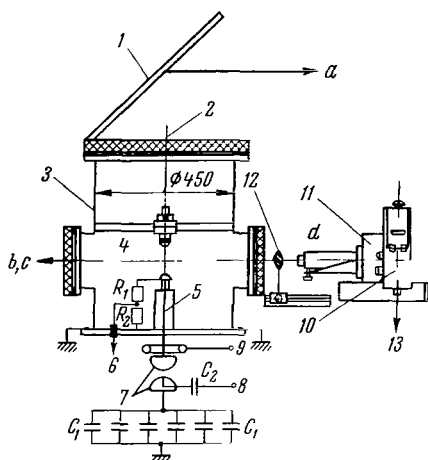
E. K. Chekalin, V. S. Shumanov

RADIATION OF AN EXPLODING WIRE IN VACUUM

The electric explosion of thin wires has attracted much attention lately /1/ in connection with its many possible applications.

Of particular interest is the use of exploding wires as a source of powerful radiation tubes in both the visible and ultraviolet regions of the spectrum for optical pumping of lasers /2/. However, the radiation of exploding wires has so far been insufficiently studied.

The study of the radiation of exploding wires in a gaseous atmosphere is made difficult both by the luminosity of the surrounding gas in the explosion process, and by the absorption of the radiation of the exploding wire in the surrounding gas. Figure 1 presents the vacuum chamber, the



Layout of the experimental apparatus:

1—mirror; 2—end window; 3—vacuum chamber; 4—copper wire; 5—high-voltage electrode; 6—terminal of the pulse voltage divider; 7—air spark gap; 8—from the SFR panel; 9—terminal of the Rogowski loop; 10—SFR camera; 11—ISP-51 spectrograph; 12—condenser lens; 13—to the SFR panel

arrangement of the measuring instruments, and the elements of the electric circuit of the discharge loop. The electric explosion of the wires was realized in vacuum. A copper wire 4 of 0.3 mm diameter and 100 mm length was placed vertically between special clamps (electrodes) along the axis of the vacuum chamber 3. The initial vacuum in the chamber was about $3 \cdot 10^{-5}$ mm mercury. The impulsive discharge of the battery of capacitors ($C_1 = 40 \mu\text{f}$) was triggered by an air spark gap 7 from the SFR panel across the transition capacitor C_2 . The discharge current circuit consisted of the high-voltage battery of capacitors C_1 , the air spark gap 7, a central conductor 5 connecting the spark gap with the lower electrode in the vacuum chamber, the wire 4, an upper electrode and the cylindrical casing of the vacuum chamber 3. The discharge current was measured by the Rogowski loop 9, and the voltage on the wire by the pulse ohmic divider R_1 and R_2 , which was placed inside the vacuum chamber and had a vacuum sealed coaxial terminal 6.

In the experiments, the initial voltage on the battery of capacitors was 30 kv. The discharge period was $45 \mu\text{sec}$, which corresponds to a frequency of 22 kc. The maximum discharge current was 150 ka.

The SFR camera, placed on one side of the wire (position b, c in Figure 1), both took single films and took a rotating mirror photograph of the explosion process through a plexiglass window.

In position a , the SFR camera made a motion-picture record along the vacuum chamber axis through the end window 2.

The emission spectrum of the expanding plasma cloud was obtained by means of an ISP-51 spectrograph 11, combined with an SFR camera 10. The arrangement of the spectrograph and the SFR is similar to that in /3/. The emission spectrum, restricted in height by the horizontal slit, was focussed on the film in the SFR camera such that the wavelength axis of the spectrum λ was perpendicular to the direction of the mirror rotation. As a result, the time resolution of the spectrum was obtained.

Figure 2 presents photographs of the plasma expansion in vacuum and a rotating mirror photograph of the emission spectrum of the exploding wire. The time scale on photographs a, b, c, d is the same.

The photographs in Figure 2 were obtained in different experiments, but in view of the satisfactory reproducibility of the results they can be compared.

It is seen in Figure 2, a that the cloud of expanding plasma possesses cylindrical symmetry, and that annular glow layers are observed in the radial direction. The leading boundary of the glow, sharp at first, becomes blurred with time. Inside the plasma cloud, $28\mu\text{sec}$ after the commencement of the process, a region of bright luminosity with a clear-cut boundary is formed anew.

Inhomogeneities are also observed in the direction of the wire axis, both on the leading boundary and inside the cloud of luminous plasma (Figure 2 b, c). The rotating mirror photograph of the motion of the leading boundary of the glow front was realized across a horizontal slit, on which the image of the middle part of the wire was projected.

The continuous spectrum record (Figure 2, d) showed that the spectral lines belong both to the copper atoms (most of the lines) and to the material of the electrodes in which the wire is fastened.

It is seen on the spectrum record that initially there is a continuous spectrum, probably caused by the glow of the finest liquid particles of the wire in the plasma, and also by the electron bremsstrahlung accompanying the electric breakdown of the metal vapors of the exploding wire. Individual strongly broadened spectral lines of copper are clearly seen on the background of the continuous spectrum. The variation in the glow intensity of the spectral lines corresponds to the amplitude of the discharge current.

After the first half-period of the discharge current ($18\mu\text{sec}$) there appears in the red region a continuous spectrum with a sharp leading front, whose intensity decreases in the direction of the short-wave region of the spectrum. At the middle of the second half-period ($32\mu\text{sec}$) there appears again an intense continuous spectrum, likewise with a sharp leading front. On the background of the continuous spectrum the lines of the absorption spectrum are clearly visible. After $20\mu\text{sec}$ two spectral lines in the red region are inverted. Thereafter the lines of the electrodes material flash, corresponding to maxima of the discharge current.

A comparison of Figures 2 b, c, d , show that the continuous spectrum after 18 and $32\mu\text{sec}$ appears at the moment the glow zones inside the plasma cloud (moving from the electrodes) meet at the middle, in the region cut by

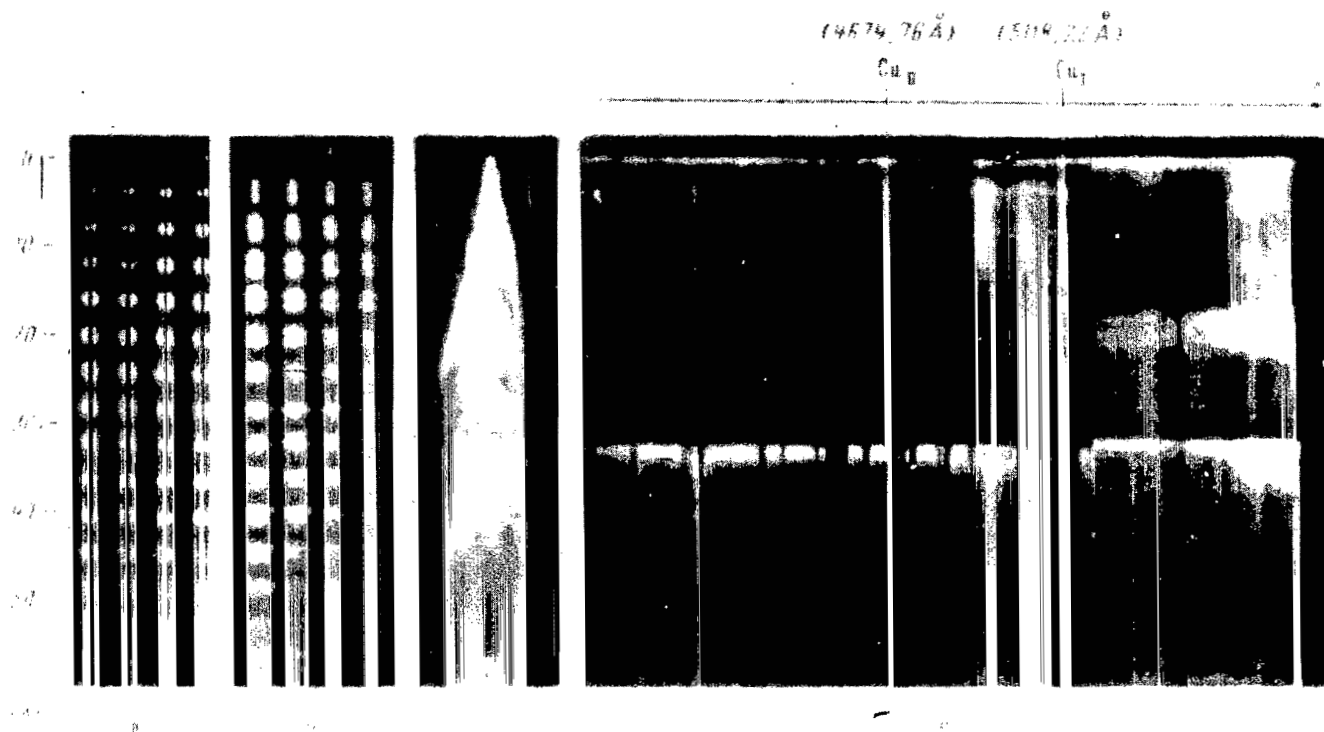


FIGURE 2. Radiation of the plasma of an exploding copper wire of 0.3 mm diameter and 100 mm length for $U_0 = 30$ kv and $p_0 = 3 \cdot 10^{-5}$ mm mercury:

a—motion-picture record along the wire axis; b—motion-picture record on one side of the wire; c—rotating mirror photograph on one side of the wire; d—rotating mirror photograph of the emission spectrum.

the narrow horizontal slit. These moving glow zones are probably produced by flows of electrode material, whose formation is not completely clear. It is mentioned in /4/ that the jets of electrode material are possibly due to the sputtering of the electrodes material in the liquid phase. The actual sputtering is analogous to the process of the electric explosion of metallic wires. The continuous spectrum after 18 and 32 μ sec is therefore apparently of the same nature as the continuous spectrum at the initial stage of the explosion.

The existence of an absorption spectrum indicates that the temperature corresponding to the glow intensity of the continuous spectrum is higher than the electron temperature in the outer layers of the expanding plasma cloud. No absorption spectrum was observed in the red region.

Thus, both the integrated radiation of the plasma of an exploding wire and its spectral distribution are inhomogeneous in time and space.

The appearance of electrode jets is probably the reason for the intense continuous spectrum, against whose background is observed the absorption spectrum of the lines due to the metal in the wire.

These facts complicate somewhat the utilization of exploding wires as a radiation source for practical applications.

Bibliography

1. Chace, W. Exploding Wires.—Physics Today, Vol. 17, No. 8. 1964.
2. Stevenson, M.J., W. Reuter, N. Braslau, P.P. Sorokin, and A.J. Landon. Spectral Characteristics of Exploding Wires for Optical Maser Excitation.—J. Appl. Phys., Vol. 34, No. 3. 1963.
3. Bashilov, V.A. Spektrograf s zerkal'noi razvertkoi (Spectrograph with Rotating Mirror).—Pribory i tekhnika eksperimenta, No. 2. 1965.
4. Meek, J. and J. Craggs. Electrical Breakdown of Gases.—Clarendon Press, Oxford. 1953.

E. K. Chekalin, V. S. Shumanov

ELECTRIC CHARACTERISTICS OF AN EXPLODING WIRE IN VACUUM

The present study aims at measuring the electric characteristics of the explosion of thin metallic wires. The energy necessary for the wire to evaporate in the explosion is transmitted to it almost instantaneously compared with the time necessary for the ordinary evaporation process of metal (which is 10^{-3} sec). The gas in a volume equal to the volume of the wire will therefore be subjected to a very high pressure and temperature for explosion conditions to occur. When the surface forces and magnetic pressure become unable to contain the wire material in its previous volume, an explosive expansion of this material occurs. To avoid the shunting effect of the gas surrounding the wire, and also the complication of the explosion process by the formation of shock waves in the atmosphere surrounding the gas, the wire explosion was realized in vacuum (cf. Figure 1 of the preceding paper).

In most experiments the system had the following parameters: initial voltage of the bank of capacitors $U_0 = 30$ kv; energy stored in the capacitor battery $W_0 = 18$ kj; total inductance of the discharge circuit $L = 1.3\mu$ henry; maximum discharge current $I_{\max} = 150$ ka; duration of the first half-period of the current $\tau/2 = 23\mu$ sec; maximum rate of increase of the current $(dI/dt)_0 = 2.3 \cdot 10^{10}$ a/sec; length of the wire $l = 100$ mm. The variation with time of the discharge current in the series R , L and C circuit is described by the differential equation

$$\frac{d^2 I(t)}{dt^2} + \frac{1}{L} \frac{d(R(t)I(t))}{dt} + \frac{1}{LC} I(t) = 0. \quad (1)$$

This equation is easily solved for constant R , L and C . In our case the wire resistance, which represents the main part of the circuit resistance, varies with time in the course of the explosion process, a fact which considerably complicates the problem. The wire explosion takes a few microseconds in all (see below), and so the energy losses due to heat conduction can be neglected. The radiation losses up to the moment at which the wire melts can also be neglected, since the temperature of the wire surface is not high. Then

$$0.24 I^2(t) R(t) dt = \bar{c} M dT, \quad (2)$$

where \bar{c} is the average specific heat of the wire material; M , T are its mass and temperature.

By solving equations (1) and (2) simultaneously one can find the variation with time of the discharge current and the wire resistance; this assumes a knowledge of the dependence of the wire resistance on temperature, which up to the instant of melting approximately satisfies the relationship

$$R(T) = R_0(1 + \beta T), \quad (3)$$

where β is the temperature coefficient of the resistance.

As in Sobolev's paper*, the following expressions were derived from (2) and (3) for the resistance and temperature of the wire as a function of time:

$$R = R_0 \exp\left(\frac{0.24 \beta R_0}{cM} \int_0^t I^2(t) dt\right); \quad T = \frac{1}{\beta} \left[\exp\left(\frac{0.24 \beta R_0}{cM} \int_0^t I^2(t) dt\right) - 1 \right]. \quad (4)$$

It is very difficult to solve equation (1) in the general case. If we restrict ourselves to the particular case when the current increases linearly with time, we obtain with the aid of (4) equations for determining the resistance and temperature as functions of time. The validity of this assumption is corroborated experimentally (cf. Figures 1 and 2). Under these conditions

$$I(t) = \left(\frac{dI}{dt}\right)_0 \cdot t = \frac{U_0}{L} t \quad (5)$$

and the resistance and temperature are given by

$$R = R_0 \exp(At^3), \quad T = \frac{1}{\beta} [\exp(At^3) - 1], \quad (6)$$

where

$$A = 0.13 \frac{\beta \rho_0}{c\delta} \left(\frac{U_0}{d^2 L}\right)^2;$$

ρ_0 is the resistivity of the wire material; δ , d are the density of its material and its diameter.

Therefore, the resistance and temperature of the wire increase proportionally to $\exp(At^3)$.

From relations (6) one can obtain the time required to heat the wire to its melting point, i.e.,

$$t_m = \left\{ \frac{\ln[1 + \beta(T_m - T_0)]}{A} \right\}^{1/3} = \left\{ 7.7 \frac{c\delta}{\beta \rho_0} \ln[1 + \beta(T_m - T_0)] \right\}^{1/3} \left(\frac{d^2 L}{U_0}\right)^{1/2}. \quad (7)$$

An approximate calculation of the required times for the other phase transformations of the wire material is very difficult for most metals, in view of the absence of reference data (or the existence of contradictory data) for metals in liquid and vapor states.

Table 1 compares theoretical (calculated by (7)) and experimental values of t_m .

- * Issledovanie elektricheskogo vzryva tonkikh provolochek (Investigation of the Electric Explosion of Thin Wires).—Zhurnal Fizicheskoi Khimii, Vol. 17, No. 11. 1947.

TABLE 1.

	Material					
	copper					aluminum
d , mm	0.11	0.15	0.2	0.25	0.31	0.3
t_m , calculated	0.38	0.57	0.83	1.1	1.49	1.01
t_m , experimental	0.4	0.62	0.90	1.3	1.7	1.1

Figures 1 and 2 give examples of oscillograms of the current and voltage for different wires.

It is clearly seen that the time resolution suffices to distinguish the various phase changes in the material, and also to follow the variation in the resistance at every phase.

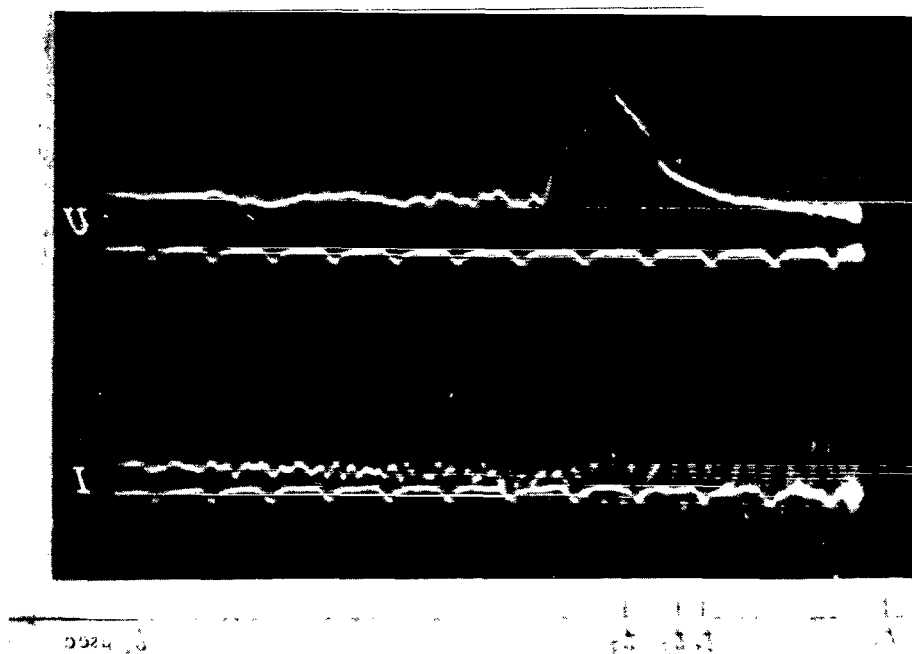


FIGURE 1. Oscillogram of the current I and voltage U during the explosion of a copper wire of 0.1 mm diameter and 100 mm length:

$U_0 = 30$ kv; time markings 0.1 μ sec.

The variation with time of the discharge current in the initial stage of the process is linear. The well-known current pause is absent in these experiments. Only at the instant of wire explosion does one see a small variation in dI/dt on the current oscillogram. Such a variation in the rate of increase of the current is to be expected, since at the explosion time considerable energy is transmitted to the wire from the bank of capacitors, leading to a rapid rise in the temperature of the wire. This

is accompanied by a sharp increase in the wire resistance, and therefore a decrease in dl/dt , the rate of increase of the current.

Later, after the breakdown of the spark gap and the ignition of the arc discharge in the metal vapors, the current variation is mainly determined by the electric parameters of the circuit, since the resistance and inductance of the discharge interval are small compared with the corresponding parameters of the discharge circuit.

The initial voltage drop on the wire is determined by the ratios of the resistances and inductances of the wire and the whole circuit. The wire resistance later increases with increasing temperature. The increase of the wire resistance, and the increase of the discharge current with time, lead to an increase in its voltage potential. The first point t_1 at which the curve slope varies rapidly corresponds to the transition from a solid to a liquid state, since the material conductivity varies discontinuously during the phase transition. At some instant the wire is part solid and part liquid. The second voltage discontinuity is observed at time t_2 , the beginning of the evaporation, after which the wire resistance increases until the voltage gradient along it becomes sufficiently high to ignite an arc in the metal vapors at time t_3 . Thus, for a copper wire of 0.31 mm diameter the oscillogram yields $t_m = (t_1 - t_0) = 1.70 \mu\text{sec}$, while the theoretical value is $t_m \simeq 1.49 \mu\text{sec}$ (cf. the table). The small increase in the experimentally obtained melting time of the wire is due to the lower discharge current at the melting time t_1 as compared with its theoretical value.

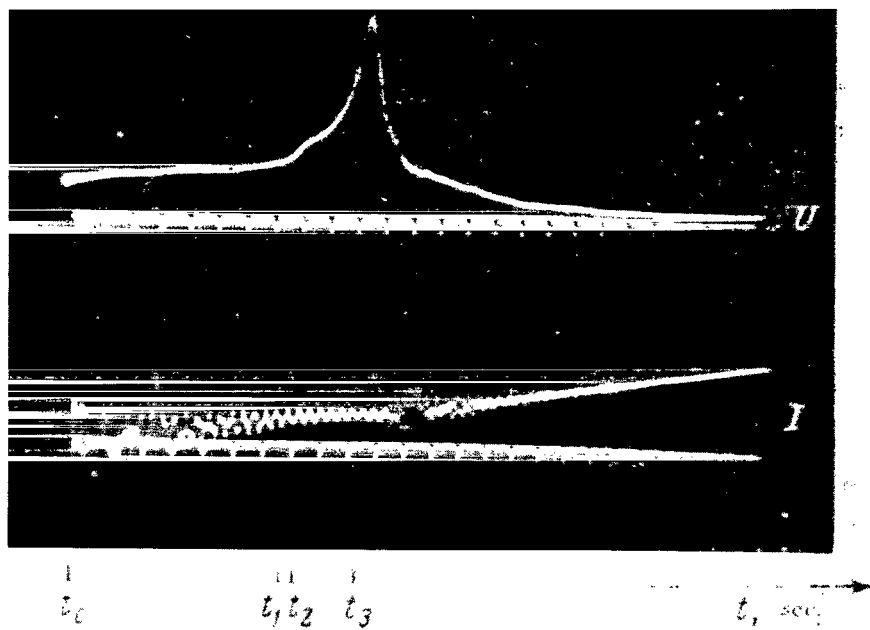


FIGURE 2. Oscillogram of the current I and the voltage U during the explosion of a copper wire of 0.31 mm diameter and 100 mm length:

$U_0 = 30 \text{ kv}$; time markings $0.2 \mu\text{sec}$.

One can derive data on the electrical conductivity of metals for different phase states of the material by analyzing the electric characteristics of the explosion. A study can also be made of the thermophysical properties of metals in liquid and vapor phases at high temperatures and pressures.

V. F. Vygovskii, E. K. Chekalin, V. S. Shumanov

DEFORMATION OF SOLIDS BY AN EXPLODING WIRE

Applications of the electric explosion of a wire were discussed in [1-5]. This paper presents experimental results on achieving permanent joints by means of the electric explosion of a wire.

The experiments were performed on the apparatus shown in Figure 1: discharge voltage $U_0 = 40$ kv, capacity of the bank of capacitors $C_0 = 45 \mu\text{f}$, total inductance of the discharge circuit $L = 1.0 \mu\text{h}$, period of natural oscillations of the discharge circuit $T = 30 \mu\text{sec}$.

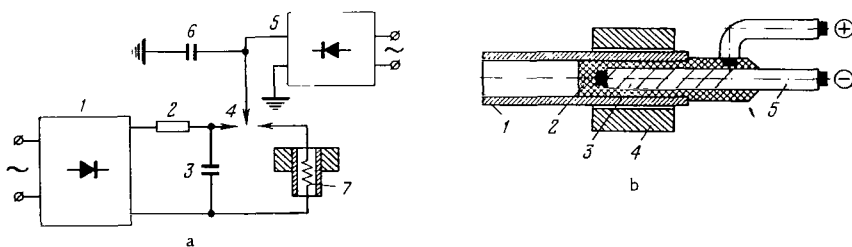


FIGURE 1. Experimental apparatus:

a—electric block diagram of the apparatus: 1—rectifier; 2—charge resistance; 3—bank of capacitors; 4—switching device; 5—igniting device; 6—igniter capacity; 7—wire;
b—layout before the explosion: 1—copper pipe; 2—plasticine; 3—wire; 4—steel ring; 5—forward conductor.

The exploding wire was wound in a spiral on a straight insulated current conductor placed inside a copper tube filled with industrial plasticine (Figure 1, b). The deformation of solids by an exploding wire was studied using a copper pipe (outer diameter $d_{\text{out}} = 20$ mm, wall thickness 3 mm), inserted in a steel ring (outer diameter $D_{\text{out}} = 40$ mm, inner diameter $D_{\text{in}} = 20.5$ mm, height $h = 30$ mm). Two annular grooves on the inner surface of the ring ensured the sealing of the pipe-ring joint.

The pressure pulse generated by the exploding wire and communicated to the copper pipe through the plasticine, deforms it in a radial direction and so welds the pipe with the ring.

The degree of radial deformation H' was studied experimentally as a function of the electric energy W stored in the bank of capacitors (Figure 2). The value of H' characterizes the quality of the pipe-ring joint and is given by

$$H' = \frac{(d'_{\text{in}} - d_{\text{in}}) - (D_{\text{in}} - d_{\text{out}})}{D_{\text{in}}} 100\%,$$

where d'_{in} , d_{in} are the internal diameters of the pipe after and before the wire explosion.

Very strong pipe-ring joints were obtained in the experiments.

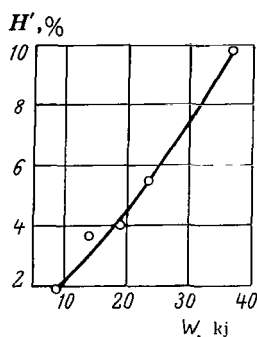


FIGURE 2. Deformation H' as a function of the energy W of the bank of capacitors.



FIGURE 3. Microstructure at the interface of the copper-steel permanent joint.

Magnification $\times 160$.

Figure 3 presents the microstructure of the interface of the pipe-ring joint. The structure of the steel ring consists of perlite and ferrite, mainly located at the grain boundaries. It can be seen from the figure that the pipe material completely fills the inner recess.

Thus, by means of an exploding wire the required degree of deformation of solids is obtained, whereby a joint can be satisfactorily sealed by filling the inner recesses of the ring with copper; this is achieved by using capacitor banks of optimum electric power.

Bibliography

1. Rukhadze, A.A., editor. Sbornik: "Vzryvayushchiesya provolochki" (Collection "Exploding Wires").—IL, 1963.
2. Chace, W. Exploding Wires.—Physics Today, Vol. 17, No. 8. 1964.
3. Rukhadze, A.A., editor. Sbornik "Elektricheskii vzryv provodnikov" (Collection "Electric Explosion of Conductors").—Moskva, Izdatel'stvo "Mir." 1965.
4. Chace, W. Exploding Wires and Their Uses.—New Scientist, Vol. 18, No. 339. 1963.
5. Mountford, N.D.G. Shaping Metal by Explosion.—New Scientist, Vol. 14, No. 284. 1962.

A.S. Predvoditelev

IGNITION THEORY OF TWO-PHASE MIXTURES

I

1. The ignition theory of combustible gas mixtures can be extended to two-phase mixtures. The energy balance equation is easily formed in this case, and consists of the energy in heating the gaseous phase and liquid drops, the energy expended on evaporation, and the energy liberated during combustion of the gaseous phase. In addition, the inequality of the temperatures of the gaseous phase and drops must be accounted for; the latter is lower than the temperature of the remaining medium during the evaporation of the drops. The temperature of the drops remains constant as long as evaporation continues. During ignition the temperature of the gaseous medium must be functionally connected with the fuel concentration. It is also assumed that the kinetics of combustion is known, at least in a general form.

The energy balance equation can thus be established under the condition that a burning zone is formed about the ignition source.

The heating of the gaseous mixture is determined by the integral over the volume of the burning zone:

$$\int C_v \rho \frac{dT}{dt} dv.$$

The drops are heated by heat exchange with the surrounding medium. If φ_1 represents the coefficient of heat transfer of an individual drop (we assume it has the same value for each drop), N the number of drops per unit volume, and S the surface of an individual drop, then the energy expended on heating the drops will be

$$\int \varphi_1 S_1 \Delta T N dv, \quad \Delta T = T - T_d.$$

Suppose the burning rate is $\psi(T, z)$ and the specific heat liberated during combustion is q ; the quantity of heat liberated in the burning zone will then be given by

$$\int q \psi dv.$$

The quantity of heat expended on evaporation (latent heat) is

$$\int N q_1 \psi_1 dv,$$

where q_1 is the latent heat of vaporization and ψ_1 is the rate of evaporation.
The heat liberated by the external heat source is

$$\int \varphi \Delta T dS, \quad \Delta T = T - T_w,$$

where φ is the coefficient of heat transfer from the source to the medium.
Hence, the total heat balance can be written as

$$\int C_v \rho \frac{dT}{dt} dv + \int \varphi_1 S_1 \Delta T N dv = \int q \psi_1 dv - \int q_1 \psi_1 N dv - \int \varphi \Delta T dS. \quad (1)$$

2. Let the derivative dT/dz be designated by ρ , which has a definite meaning during the mixture ignition. Equation (1) is differentiated with respect to the variable z . At the beginning of ignition the product $C_v \rho$ is assumed to depend weakly on the concentration of the combustible constituent z . Hence

$$\int C_v \rho \frac{dP}{dt} dv + \int \varphi_1 S_1 P N dv = \int q \left(\frac{\partial \psi}{\partial z} + \frac{\partial \psi}{\partial T} P \right) dv - \int q_1 \frac{\partial \psi_1}{\partial P} P N dv - \int \varphi P dS. \quad (2)$$

The rate equation is now differentiated with respect to temperature:

$$\frac{d}{dT} \frac{dz}{dt} = \frac{\partial \psi}{\partial T} + \frac{\partial \psi}{\partial z} \frac{1}{P}; \quad \frac{dz}{dt} = \psi,$$

or

$$\frac{dP}{dt} = - \left(\frac{\partial \psi}{\partial T} P^2 + \frac{\partial \psi}{\partial z} P \right). \quad (3)$$

If equation (3) is substituted in equation (2), we obtain

$$\int \varphi_1 S_1 P N dv = \int (C_v \rho P + q) \left(\frac{\partial \psi}{\partial z} + \frac{\partial \psi}{\partial T} P \right) dv - \int q_1 \frac{\partial \psi_1}{\partial T} P N dv - \int \varphi P dS, \quad (4)$$

or

$$\int \varphi P dS = \int (C_v \rho P + q) \left(\frac{\partial \psi}{\partial z} + \frac{\partial \psi}{\partial T} P \right) dv - \int (\varphi_1 S_1 + q_1 \frac{\partial \psi_1}{\partial T}) P N dv. \quad (4a)$$

Using the mean-value theorem, this becomes

$$\overline{\varphi P S} = \overline{(C_v \rho P + q) \left(\frac{\partial \psi}{\partial z} + \frac{\partial \psi}{\partial T} P \right) V} - \overline{(\varphi_1 S_1 + q_1 \frac{\partial \psi_1}{\partial T}) P N V},$$

where the bar indicates the mean value taken over the burning zone.
Designate \bar{P} by P_s . We can then always alter some mean values to satisfy the equalities

$$\begin{aligned} \overline{(C_v \rho P + q) \left(\frac{\partial \psi}{\partial z} + \frac{\partial \psi}{\partial T} P \right)} &= (\overline{C_v \rho P_s} + q) \left(\frac{\partial \psi}{\partial z} + \frac{\partial \psi}{\partial T} P_s \right), \\ \overline{(\varphi_1 S_1 + q_1 \frac{\partial \psi_1}{\partial T}) P N} &= \varphi_1 S_1 \left(\varphi_1 S_1 + q_1 \frac{\partial \psi_1}{\partial T} \right) P_s N. \end{aligned}$$

Taking these relations into account, the last equality can be written as follows:

$$\frac{\varphi S}{V} P_s = (\overline{C_v \rho} P_s + q) \left(\frac{\partial \overline{\psi}}{\partial z} + \frac{\partial \overline{\psi}}{\partial T} P_s \right) - \left(\varphi_1 S_1 + q_1 \frac{\partial \overline{\psi}_1}{\partial T} \right) P_s N. \quad (5)$$

This equality plays an important role in determining the ignition conditions of two-phase mixtures.

II

1. Consider the slow heating of a two-phase mixture, for which the following inequalities can be considered as valid:

$$\frac{\partial \overline{\psi}}{\partial T} P_s \gg \frac{\partial \overline{\psi}}{\partial z}; \quad \overline{C_v \rho} P_s \ll q.$$

With these inequalities, equation (5) can be expressed in the form

$$\frac{\varphi S}{V} = q \frac{\partial \overline{\psi}}{\partial T} - \left(\varphi_1 S_1 + q_1 \frac{\partial \overline{\psi}_1}{\partial T} \right) N \quad (6)$$

or

$$\frac{qV}{\varphi S} \frac{\partial \overline{\psi}}{\partial T} - \left(\varphi_1 S_1 + q_1 \frac{\partial \overline{\psi}_1}{\partial T} \right) \frac{NV}{\varphi S} \simeq 1. \quad (6a)$$

2. Rapid heating of the material leads to the formation and motion of a burning zone. The value of P_s will then satisfy inequalities of the form

$$\frac{\partial \overline{\psi}}{\partial T} P_s \gg \frac{\partial \overline{\psi}}{\partial z}; \quad \overline{C_v \rho} P_s \gg q.$$

On the strength of these inequalities (5) takes the form

$$\frac{\varphi S}{V} = \overline{C_v \rho} \frac{\partial \overline{\psi}}{\partial T} P_s - \left(\varphi_1 S_1 + q_1 \frac{\partial \overline{\psi}_1}{\partial T} \right) N. \quad (7)$$

Hence

$$P_s = \frac{\varphi S}{V} \frac{1}{\overline{C_v \rho} \frac{\partial \overline{\psi}}{\partial T}} + \frac{\left(\varphi_1 S_1 + q_1 \frac{\partial \overline{\psi}_1}{\partial T} \right) N}{\overline{C_v \rho} \frac{\partial \overline{\psi}}{\partial T}}. \quad (7a)$$

Consider the quantity P_s written in the form

$$P_s = \frac{\Delta T}{\Delta z} = \frac{\Delta T}{\tau} \frac{\tau}{\Delta z} = \frac{\Delta T}{\tau \overline{\psi}} = \frac{\Delta T}{\Delta n} \frac{\Delta n}{\tau} \frac{1}{\overline{\psi}},$$

where Δn is the increment in the normal during the formation time of the burning zone. The value of $\Delta n/\tau$ measures the displacement rate g of the burning zone. The temperature gradient is the ratio of the heat flux of the mean heat conductivity of the medium. The displacement rate of

the burning zone and the heat flux Q have the same direction. Therefore

$$P_* = \frac{Q}{\lambda} g \frac{1}{\bar{\psi}}. \quad (8)$$

Substituting (8) in (7a), we obtain

$$g = \frac{\varphi S}{V} \frac{\bar{\lambda} \bar{\psi}}{Q} \frac{1}{\bar{C}_{v\rho} \frac{\partial \bar{\psi}}{\partial T}} + \frac{\left(\varphi_1 S_1 + q_1 \frac{\partial \bar{\psi}_1}{\partial T} \right) N \bar{\lambda} \bar{\psi}}{\bar{C}_{v\rho} \frac{\partial \bar{\psi}}{\partial T} Q}, \quad (9)$$

where the ratio $\frac{\partial \bar{\psi}}{\partial T} / \bar{\psi}$ can be replaced by

$$\frac{\partial \lg \bar{\psi}}{\partial T}.$$

If \bar{a} represents the mean value of the thermal diffusivity of the medium, equality (9) takes the form

$$g = \frac{\varphi S}{V} \frac{\bar{a}}{Q} \frac{1}{\frac{\partial \lg \bar{\psi}}{\partial T}} + \frac{\left(\varphi_1 S_1 + q_1 \frac{\partial \bar{\psi}_1}{\partial T} \right) \bar{a} N}{\frac{\partial \lg \bar{\psi}}{\partial T} Q}. \quad (9a)$$

3. The ratio V/S represents the thickness d of the burning zone. Hence

$$\frac{V}{S} = d = g\tau.$$

However, during the formation time τ of the burning zone the following is valid:

$$\int_0^\tau \psi dt = \bar{\psi} \tau = M.$$

Therefore

$$\frac{V}{S} = g \frac{M}{\bar{\psi}},$$

with the aid of which expression (9a) becomes

$$g^2 = \frac{\varphi \bar{\psi} \bar{a}}{QM \frac{\partial \lg \bar{\psi}}{\partial T}} + \frac{\left(\varphi_1 S_1 + q_1 \frac{\partial \bar{\psi}_1}{\partial T} \right) \bar{a} N}{Q \frac{\partial \lg \bar{\psi}}{\partial T}} g. \quad (10)$$

The heat fluxes, expressed in terms of the coefficient of heat transfer and the average heat conductivity, are equal, so that

$$Q = \varphi \Delta T = \lambda \frac{\Delta T}{\Delta n}.$$

Equality (10) now takes the form

$$g^2 = \frac{\bar{a} \bar{\psi}}{\Delta T M \frac{\partial \lg \psi}{\partial T}} + \frac{\left(\varphi_1 S_1 + q_1 \frac{\partial \bar{\psi}_1}{\partial T} \right) \bar{a} N}{Q \frac{\partial \lg \psi}{\partial T}} g. \quad (10a)$$

Using the identity

$$\Delta T = \frac{\Delta T}{\Delta n} \frac{\Delta n}{\tau} \tau = \frac{Q}{\lambda} g \tau,$$

which is valid here, (10a) becomes

$$g^3 = \frac{\bar{a} \bar{\psi}^2 \bar{\lambda}}{M^2 Q \frac{\partial \lg \psi}{\partial T}} + \frac{\left(\varphi_1 S_1 + q_1 \frac{\partial \bar{\psi}_1}{\partial T} \right) \bar{a} N}{Q \frac{\partial \lg \psi}{\partial T}} g^2. \quad (10b)$$

We have thus obtained a formula for the displacement rate of the burning zone in two-phase mixtures for a constant heat flux from the ignition source.

The burning rate of the gaseous phase can be represented by

$$\psi = F(T) f(z),$$

so that the following equality is thus valid:

$$\frac{\partial \lg \psi}{\partial T} = \frac{\partial \lg F}{\partial T}.$$

Equation (10b) can now be written in the final form

$$g^3 = \frac{\bar{a} \bar{\psi}^2 \bar{\lambda}}{M^2 Q \frac{\partial \lg F}{\partial T}} + \frac{\left(\varphi_1 S_1 + q_1 \frac{\partial \bar{\psi}_1}{\partial T} \right) \bar{a} N}{Q \frac{\partial \lg F}{\partial T}} g^2. \quad (11)$$

The physical meaning of the terms in this expression is easily understood. In the absence of liquid drops the displacement rate of the burning zone is

$$g_0^3 = \frac{\bar{a} \bar{\psi}^2}{M^2 Q \frac{\partial \lg F}{\partial T}}.$$

If the burning rate ψ is almost zero, the evaporation zone moves with velocity g_1 . Formula (11) then yields

$$g_1 = \frac{\left(\varphi_1 S_1 + q_1 \frac{\partial \bar{\psi}_1}{\partial T} \right) \bar{a} N}{Q \frac{\partial \lg F}{\partial T}}.$$

Hence, formula (11) can be rewritten in the simple form

$$g^3 = g_0^3 + g_1 g^2 \dots \quad (11a)$$

III

1. We shall investigate under what conditions equation (11a) has real roots and what is their number.

First, this equation is reduced to canonical form by putting

$$g = y + \frac{g_1}{3}.$$

With this substitution formula (11a) gives

$$y^3 - \frac{g_1^2}{3}y - 2\left(\frac{g_1^3}{27} + \frac{g_0^3}{2}\right) = 0. \quad (12)$$

The canonical cubic equation has the form

$$y^3 + 3py + 2q = 0.$$

Therefore, the following identities are valid in our case:

$$P = -\frac{g_1^2}{9}, \quad q = -\left(\frac{g_1^3}{27} + \frac{g_0^3}{2}\right).$$

The condition for one real root and two imaginary ones is

$$P^3 + q^2 > 0, \quad \left(\frac{g_1^3}{27} + \frac{g_0^3}{2}\right)^2 - \frac{g_1^6}{27^2} > 0;$$

alternatively

$$g_0^3 \left(\frac{g_1^3}{27} + \frac{g_0^3}{4}\right) > 0. \quad (13)$$

The quantity g_0 is always positive. Inequality (13) will therefore only be satisfied when

$$\frac{g_1^3}{27} + \frac{g_0^3}{4} > 0. \quad (13a)$$

It follows that when q_1 is positive we shall have one real root and two imaginary ones.

2. The expression

$$g_1 = \frac{\left(\varphi_1 S_1 \cap q_1 \frac{\partial \bar{\Psi}}{\partial T}\right) \bar{a} N}{Q \frac{\partial \lg F}{\partial T}}$$

will now be transformed. In the stationary case the quantity of heat delivered to one drop can be considered as equal to the latent heat liberated per unit time:

$$\varphi_1 S (T - T_d) = q_1 \Psi_1.$$

With the aid of this equality g_1 takes the form

$$g_1 = \frac{\varphi_1 S (T - T_d) N \bar{a}}{(T - T_d) Q \frac{\partial \lg \bar{F}}{\partial T}} \left[1 + \frac{\partial \lg \varphi_1}{\partial T} (T - T_d) \right].$$

Suppose the heat source for the ignition yields exactly the amount of heat necessary for the evaporation of the drop. Then

$$\varphi_1 S (T - T_d) N V = Q S,$$

and the last formula can be written as follows:

$$g_1 = \frac{\bar{a} S}{V (T - T_d) \frac{\partial \lg \bar{F}}{\partial T}} \left[1 + \frac{\partial \lg \varphi_1}{\partial T} (T - T_d) \right].$$

The ratio V/S can however be expressed as

$$\frac{V}{S} = d = g \tau = g \frac{M}{\bar{\psi}}.$$

Therefore

$$g g_1 = \frac{\bar{a} \bar{\psi}}{M (T - T_d) \frac{\partial \lg \bar{F}}{\partial T}} \left[1 + \frac{\partial \lg \bar{\psi}}{\partial T} (T - T_d) \right]. \quad (14)$$

The factor before the brackets in this formula is identical with the first term of (10a), which is equal to g_0^2 if ΔT is equal to the difference $(T - T_d)$. These differences are not in fact equal in the general case. Introduce γ , defined by

$$\frac{\Delta T}{T - T_d} = \gamma.$$

This quantity equals the ratio of the temperature jump in the burning zone to that near the evaporating drop. Therefore, in accordance with the physical meaning, its minimum value is unity. In practice these two jumps are hardly ever equal, although logically they could be.

With the aid of this expression formula (14) can be written in the form

$$g g_1 = \gamma g_0^2 \left[1 + \frac{\partial \lg \bar{\psi}}{\partial T} (T - T_d) \right]. \quad (14a)$$

Substituting the value obtained for g_1 in (11a), we obtain

$$g^3 = g_0^3 + \gamma g_0^2 \left[1 + \frac{\partial \lg \bar{\psi}}{\partial T} (T - T_d) \right] q, \quad (15)$$

or

$$g^3 - \gamma g_0^2 \left[1 + \frac{\partial \lg \bar{\psi}}{\partial T} (T - T_d) \right] g - g_0^3 = 0. \quad (15a)$$

This cubic equation is in canonical form, where

$$3P = -\gamma g_0^3 \left[1 + \frac{\partial \lg \Psi}{\partial T} (T - T_d) \right], \quad 2q = -g_0^3.$$

The condition for one real and two imaginary roots is

$$\frac{g_0^6}{4} - \frac{\gamma^3 g_0^6 \left[1 + \frac{\partial \lg \Psi}{\partial T} (T - T_d) \right]^3}{27} > 0,$$

or

$$\frac{1}{4} - \frac{\gamma^3 \left[1 + \frac{\partial \lg \Psi}{\partial T} (T - T_d) \right]^3}{27} > 0. \quad (16)$$

The condition for three real roots is

$$\frac{1}{4} - \frac{\gamma^3 \left[1 + \frac{\partial \lg \Psi}{\partial T} (T - T_d) \right]^3}{27} < 0. \quad (16a)$$

Both cases can obviously exist. The first condition corresponds to stable ignition, and the second to unstable ignition. Each case depends on the numerical value of the evaporation rate of the drops and on the value of γ .

The quantity $\frac{\partial \lg F}{\partial T} (T - T_d)$ can be interpreted as the increment in the evaporation rate of drops caused by a temperature gradient at the surface of the drops. If its magnitude is positive and larger than one, stable combustion occurs for all values of γ . If it is positive and smaller than one, stable ignition depends exclusively on the numerical value of γ .

A. S. Predvoditelev

IGNITION CONDITIONS IN COMBUSTIBLE GAS MIXTURES

INTRODUCTION

The large-scale use of gaseous, liquid, and solid fuels in different branches of engineering, has opened a new chapter of knowledge—the physics and chemistry of combustion. Soviet scientists have been foremost in this new science. Homogeneous combustion was mainly studied by Semenov's school, while heterogeneous combustion was developed by the author of this paper and his co-workers. Our understanding of heterogeneous combustion was also advanced by Knorre's school, whose aim was to apply the theory.

The secondary phenomena accompanying combustion in industrial machinery complicate considerably the theoretical analysis. The different processes of fuel combustion have however many common phenomena, reflecting the nature of the combustion process; these enable a theory of the latter to be constructed independently of the type of equipment.

Without such a basic theory it would be impossible to understand, even qualitatively, the maze of combustion phenomena in industrial machinery. Therefore, in the absence of such theories the engineering of furnace machinery is doomed to an extremely slow development, which is quite incompatible with our rate of technical progress.

The main phenomena of homogeneous combustion are spontaneous ignition, induced ignition, normal propagation of the flame, turbulent combustion, and detonation.

Several problems connected with the ignition of burning mixtures are treated in this paper from a new point of view.

The physics of homogeneous combustion devotes considerable attention to the so-called limiting phenomena, which are usually divided in two classes—limiting phenomena at spontaneous ignition and at induced ignition. From the purely physical point of view the two phenomena are almost identical. The difficulties in their description are only due to the chemical treatment of the phenomena.

We propose in this paper a new method to describe the phenomena of spontaneous and induced ignition in quiescent gas mixtures.

1. THE CRITERIA OF SPONTANEOUS IGNITION

Consider a slowly heated closed vessel, filled with a combustible gas mixture. We shall analyze the factors on which the ignition of this mixture depends.

As long as a chemical reaction has not yet started, no direct relation exists between the temperature and composition of the mixture. Only after the beginning of the chemical reaction does such a connection appear, since the heat released during this reaction depends on the quality of burnt material, and therefore also on the mixture composition. This is what determines basically the conditions for thermal ignition of gas mixtures.

To solve the problem, we shall determine the rate of the chemical reaction by the change in the components of the gas mixture.

If the concentration of a component is z , a sufficiently general equation of chemical kinetics can be written in the form

$$\frac{dz}{dt} = \alpha_0 F(T) f(z). \quad (1)$$

The function $F(T)$ may coincide in a particular case with the Arrhenius function.

In addition, the energy balance equation must be satisfied over the volume of the system.

The variation in the quantity of heat contained in a gas of volume V during heating is

$$\int c_v \rho \frac{dT}{dt} dV.$$

This variation must be compensated, first by the heat liberated by the chemical transformations, expressed as

$$\int q \alpha_0 F(T) f(z) dV,$$

where q is the specific heat of the chemical reaction, and second by the heat transferred from the walls to the gas:

$$\varphi S (T_w - T_s),$$

where T_s is the temperature of the gas mixture near the wall.

If the wall is assumed to be uniformly heated, the balance equation is

$$\int c_v \rho \frac{dT}{dt} dV = \int q \alpha_0 F(T) f(z) dV + \varphi S (T_w - T_s). \quad (2)$$

Equation (1) and (2) do not form a closed system, and do not give the condition for the ignition of a volume of gas mixture. During ignition, as mentioned above, a direct link must exist between the temperature and the mixture composition at any point in the volume, i. e., a relationship of the form

$$T = f(z). \quad (3)$$

The three equations (1)–(3) must hold simultaneously from the ignition time.

When the first equation is differentiated with respect to the temperature T , and the second one with respect to the variable z , where

$$\psi(T, z) = f(z) F(T) \quad \text{and} \quad \frac{dT}{dz} = P,$$

we obtain

$$\begin{aligned} \frac{dP}{dt} &= -\alpha_0 P \frac{\partial \psi}{\partial z} - \alpha_0 \frac{\partial \psi}{\partial T} P^2, \\ \int c_v \rho \frac{dP}{dt} dV &= \int \alpha_0 q \left[\frac{\partial \psi}{\partial z} + \frac{\partial \psi}{\partial T} P \right] dV - \varphi S P_s. \end{aligned}$$

The derivative dP/dt can be eliminated from the last equation to yield

$$\varphi S P_s = \int \alpha_0 (q + c_v \rho P) \left[\frac{\partial \psi}{\partial z} + \frac{\partial \psi}{\partial T} P \right] dV. \quad (4)$$

Were the gas mixture heated at an infinitely slow rate, the temperature and concentration would be the same everywhere in its volume. Equality (4) can be integrated for this particular case and written as

$$\frac{\alpha_0 q V}{\varphi S P} \left(1 + \frac{c_v \rho}{q} P \right) \left(\frac{\partial \psi}{\partial z} + \frac{\partial \psi}{\partial T} P \right) = 1. \quad (4a)$$

For slow heating, relation (4a) is valid at any instant. To find the ignition condition, the gas pressure P at the ignition time must be known.

Consider several particular cases. Suppose P satisfies the conditions

$$\frac{\partial \psi}{\partial T} P \gg \frac{\partial \psi}{\partial z}, \quad \frac{c_v \rho}{q} P \ll 1. \quad (4b)$$

Equation (4a) then yields the relation

$$\frac{\alpha_0 q V}{\varphi S} \frac{\partial \psi}{\partial T} \simeq 1. \quad (4c)$$

When the reaction at the ignition time is of zero order, relation (4c) becomes

$$\frac{\alpha_0 q V}{\varphi S} \frac{\partial F}{\partial T} = 1. \quad (5)$$

This relation was derived by Semenov.

A second case is also possible, when only the first of inequalities (4b) is satisfied, while the second one is replaced by

$$\frac{c_v \rho}{q} P = \frac{c_v \rho}{q} \frac{dT}{dz} = 1.$$

This equality implies that in every element of the ignition volume the quantity of heat which heats the gas is equal to the heat liberated during the

chemical reaction. Bearing this in mind, we can write relation (4a) as

$$\frac{\alpha_0 q V}{\varphi S} \frac{\partial \psi}{\partial T} = \frac{1}{2}. \quad (6)$$

These criteria do not hold for rapid heating. In this case the ignition process is necessarily accompanied by the formation of a burning zone and its propagation inside the gas. The integration of equation (4) must therefore be taken over the burning zone volume. The surface S must likewise enclose the whole burning zone. Integrating the right side of (4) with the aid of the mean-value theorem, we obtain

$$\varphi S P_s = \alpha_0 (q + \overline{c_v \rho P}) \left[\frac{\overline{\partial \psi}}{\partial z} + \frac{\overline{\partial \psi}}{\partial T} P \right] V. \quad (7)$$

In the case considered the process of formation of the burning zone must always be associated with a very high pressure P . The following inequalities must therefore be satisfied:

$$\frac{\overline{\partial \psi}}{\partial T} P \gg \frac{\overline{\partial \psi}}{\partial z}, \quad \frac{\overline{c_v \rho}}{q} P \gg 1.$$

Taking this into account, equality (7) is rewritten as

$$\frac{\alpha_0 V}{\varphi S P_s} (\overline{c_v \rho P}) \frac{\overline{\partial \psi}}{\partial T} P = 1. \quad (8)$$

The mean values of P , $c_v \rho$ and $\partial \psi / \partial T$ are selected to satisfy the equalities

$$\overline{c_v \rho P} = \overline{c_v \rho} P_s, \quad \frac{\overline{\partial \psi}}{\partial T} \overline{P} = \frac{\overline{\partial \psi}}{\partial T} P_s.$$

Similar identities will always be meaningful if the burning zone is sufficiently thin. Relation (8) can then be represented in the form

$$\frac{\alpha_0 V}{\varphi S} \frac{\overline{\partial \psi}}{\partial T} \overline{c_v \rho} P_s = 1. \quad (9)$$

This formula can be transformed to a more interesting form using the following identities:

$$P_s = \frac{\left(\frac{dT}{dt} \right)_s}{\left(\frac{dz}{dt} \right)_s}, \quad \alpha_0 \frac{\overline{\partial \psi}}{\partial T} = \frac{dz}{dt} \frac{\partial \lg F}{\partial T} = \left(\frac{dz}{dt} \right)_s \frac{\partial \lg F}{\partial T}.$$

Equality (9) then takes the form

$$\frac{V}{\varphi S} \frac{\partial \lg F}{\partial T} \overline{c_v \rho} \left(\frac{dT}{dt} \right)_s = 1. \quad (10)$$

The derivative $(dT/dt)_s$ can be easily expressed in terms of the displacement rate of the isothermal front. By definition

$$g = - \frac{dT}{dt} \frac{1}{\frac{dT}{dn}}, \quad g \frac{dT}{dn} = - \frac{dT}{dt}.$$

From Fourier's equation we obtain

$$Q = -\lambda \frac{dT}{dn}, \quad \frac{dT}{dn} = -\frac{Q}{\lambda},$$

and therefore

$$\left(\frac{dT}{dt} \right)_s = g \frac{Q_s}{\lambda}.$$

If this expression is substituted in (10) it yields

$$g = \frac{\bar{a} S \Phi}{\frac{\partial \lg \bar{F}}{\partial T} V' Q_s}, \quad (10a)$$

where \bar{a} represents $\lambda/\rho c_v$.

Let ΔT be the temperature difference between the surfaces of the burning zone. Hence

$$Q_s = \varphi \Delta T.$$

Formula (10a) can now be written as follows:

$$g = \frac{\bar{a}}{\Delta T} \frac{\frac{S}{\frac{\partial \lg \bar{F}}{\partial T}}}{V}. \quad (11)$$

The surface S is equal to the sum of the surfaces enclosing the burning zone:

$$S = S_1 + S_2.$$

If the thickness of the burning zone is d , its volume is

$$V = S_1 d.$$

Relation (11) then becomes

$$g = \frac{\bar{a}}{\Delta T} \frac{\frac{S_1 + S_2}{\frac{\partial \lg \bar{F}}{\partial T}}}{d}. \quad (11a)$$

If the thickness of the burning zone is very small then, without considerable error, we may write

$$g = \frac{\bar{a}}{\Delta T} \frac{\frac{2}{\frac{\partial \lg \bar{F}}{\partial T}}}{d}. \quad (12)$$

A fundamental result is now drawn from this expression. Consider the following relations for the burning zone:

$$d = g\tau, \quad M = \int_0^{\tau} \dot{z} dt = \bar{z}\tau,$$

where τ represents the formation time of the burning zone, and M the quantity of burnt gas.

With these better relations formula (12) can be expressed in the form

$$g = \frac{\frac{2\bar{a}\bar{z}}{\partial \lg F}}{\Delta T \frac{\partial \lg F}{\partial T} M} \quad (12a)$$

Thus, if conditions are created under which g satisfies equality (12a), the ignition process of the combustible gas mixture commences.

2. THE PRESSURE RANGE FOR IGNITION

Experience shows that gas mixtures cannot be ignited at all concentrations and pressures. The question therefore arises how to interpret these phenomena: to what extent do they depend on the chemical nature of the gas mixture and to what extent are they determined by the physical conditions. The solution of this problem is important for both the theory and practice of gas burning; the design of any device for gas burning must take these phenomena into account.

On the strength of the Maxwell distribution of thermal velocities, the gas mixture must always contain molecules with relative thermal velocities capable of starting the chemical process. This phenomenon is not observed because the direct and inverse processes lead to instantaneous concentrations of the reaction products with an associated lifetime which is impossible to detect by conventional means. With a rise in temperature the concentrations and lifetimes become observable; what is more, the rate of the direct process may exceed that of the inverse process. We can thus conclude that no component of the gas mixture can be completely expended.

Following this idea, some equilibrium concentrations of the components must exist in any gas mixture. This equilibrium is kinetic, i.e., the concentrations of the reacting components in a given time interval vary within definite, sufficiently narrow limits. If the time interval is lengthened with the aid of the temperature, it is possible to isolate in this cyclic process a specific link in one direction.

The existence of cyclic reactions in the gas affects the total pressure so that it will fluctuate about some mean pressure. The amplitudes of these vibrations are usually very small and in practice cannot be directly measured.

The simplest equations describing pressure fluctuations caused by cyclic reactions are the Volterra equations.

Let p_1 represent the partial pressure of the active center. This is created due to molecular collisions at high relative velocities, and can

lead under suitable temperature conditions to the development of the chemical process. The quantity p_2 is the partial pressure of the gas minus the concentration of the active center. The following equality will then hold:

$$p = p_1 + p_2.$$

When the gas is not ignited its pressure p fluctuates with time about some mean value.

The Volterra equations can be written in the form

$$\frac{dp_1}{dt} = p_1(\alpha_1 - \beta_1 p_2), \quad \frac{dp_2}{dt} = -p_2(\alpha_2 - \beta_2 p_1).$$

If the first equation is multiplied by β_2 and the second by β_1 , and the resulting two equations then added, the following is derived:

$$\beta_2 \frac{dp_1}{dt} + \beta_1 \frac{dp_2}{dt} = \alpha_1 \beta_2 p_1 - \alpha_2 \beta_1 p_2.$$

Now multiply the first equation by α_2/p_1 and add the results. This yields

$$\alpha_2 \frac{dp_1}{dt} \frac{1}{p_1} + \alpha_1 \frac{dp_2}{dt} \frac{1}{p_2} = -\alpha_2 \beta_1 p_2 + \alpha_1 \beta_2 p_1.$$

When these latter two equations are added, we have

$$\beta_2 \frac{dp_1}{dt} + \beta_1 \frac{dp_2}{dt} - \alpha_2 \frac{d \lg p_1}{dt} - \alpha_1 \frac{d \lg p_2}{dt} = 0.$$

This equality is easily integrated and yields

$$\beta_2 p_1 + \beta_1 p_2 - \alpha_2 \lg p_1 - \alpha_1 \lg p_2 = \text{const.}$$

or alternatively

$$F(p_1, p_2) = e^{-\beta_1 p_1} e^{-\beta_2 p_2} p_1^{\alpha_2} p_2^{\alpha_1} = \text{const.}$$

In the (p_1, p_2) -plane the integral represents a closed oval curve, which reduces to a point under certain conditions. A definite value of the total pressure corresponds to every pair of points on this curve. This pressure will fluctuate with a period corresponding to the time taken to make a circuit of the oval curve.

Suppose z represents the concentration of the active center, where

$$z = \frac{p_1}{p}.$$

The Volterra equations, expressed in terms of z , will now have the form

$$\left. \begin{aligned} \frac{dp_1}{dt} &= \alpha_1 p z - \beta_1 p^2 (1 - z) z, \\ \frac{dp_2}{dt} &= -\alpha_2 p (1 - z) + \beta_2 p^2 (1 - z) z. \end{aligned} \right\} \quad (13)$$

If the first equation is multiplied by the molecular weight m_1 of the active center, the second by the molecular weight m_2 of the second component

(which may be the mean molecular weight of any gas mixture), and the notation

$$M = m_1 p_1 + m_2 p_2$$

introduced, equation (13) may be combined to yield

$$\begin{aligned} \frac{dM}{dt} &= [\alpha_1 m_1 z - \alpha_2 m_2 (1 - z)] p + [m_2 \beta_2 (1 - z) z - m_1 \beta_1 z (1 - z)] p^2 = \\ &= F_1(T, z) p + F_2(T, z) p^2. \end{aligned} \quad (14)$$

The following additional notation is introduced:

$$U = \frac{dT}{dM}.$$

Consider a slow variation in the temperature near the ignition point. The mean temperature T of the gas is at first independent of z , since there is no ignition reaction and no heat is liberated, although the number of active centers will increase slowly. At the ignition temperature z must assume a critical value, since it determines the beginning of the chemical reaction of combustion. The mean temperature will then depend on the variable z , and therefore on the variable M as well.

The natural assumption which can be made about the ignition conditions reduces to the assertion that the relationship between the mean temperature of the gas and M has a minimum, i. e.

$$\frac{dT}{dM} = U = 0. \quad (15)$$

For the case considered condition (4a) can be rewritten as follows:

$$\frac{qV}{\Phi S} \left(1 + \frac{c_v \rho}{q} U \right) \left[\left(\frac{\partial F_1}{\partial T} + \beta F_1 \right) p + \left(\frac{\partial F_2}{\partial T} + 2\beta F_2 \right) p^2 \right] = 1.$$

When condition (3) is observed, it follows that

$$\left[\left(\frac{\partial F_1}{\partial T} + \beta F_1 \right) p + \left(\frac{\partial F_2}{\partial T} + 2\beta F_2 \right) p^2 \right] = \frac{\Phi S}{qV}, \quad (16)$$

where β represents the coefficient of volume expansion of the gases, given by

$$\beta = \left(\frac{1}{p} \right) \left(\frac{dp}{dT} \right).$$

We shall determine the beginning of ignition with respect to the temperature T , and pressure p . Obviously, this temperature and pressure satisfy (16).

If T , is kept constant and the pressure increased, the mixture will burn. Finally, at a pressure corresponding to the second root of equation (16), the mixture will again be nonignitable.

Thus, for every composition of the combustible mixture there exist temperature and pressure regions of nonignition. Although we started from Volterra's equations in establishing the kinetic equality (14), the

whole course of our reasoning, leading to the existence of two ignition limits with respect to the pressure, shows that this phenomenon is wholly determined by second-order reactions. Therefore, whatever model of chemical transformations we attempt to construct, given the two ignition limits in terms of pressure, the leading reaction must always be of second order.

Following Semenov it can be shown that there exist ignition regions defined by curves having three roots with respect to the pressure. According to our reasoning, a third-order leading reaction must exist in this case.

3. THE CONCENTRATION LIMITS OF INDUCED IGNITION

The reasoning of the preceding section can be extended to the case of induced ignition. Consider a closed volume, such as a sphere, filled with a combustible gas mixture. Let a heat source, whose temperature exceeds the ignition temperature of the combustion gas mixture, be placed at the center of this volume. As before, φ is the coefficient of heat transfer from the heat source to the gas, and S is its surface. With the ignition of the gas mixture a burning zone of thickness d appears about the heat source. Equality (7), written in the form

$$\frac{\varphi S p_s}{Sd} = (q + \overline{c_v \rho P}) \left[\left(\frac{\partial \overline{F_1}}{\partial z} p + \frac{\partial \overline{F_2}}{\partial z} p^2 \right) + \left(\overline{P \frac{\partial \overline{F_1}}{\partial T}} + \overline{\beta F_1 P} \right) p + \left(\frac{\partial \overline{F_2}}{\partial T} P + 2 \overline{\beta F_2 P} \right) p^2 \right],$$

will then hold for this zone. The mean values are chosen to satisfy the identities

$$\overline{c_v \rho P} = \overline{c_v \rho} P_s, \quad \overline{P \frac{\partial \overline{F_1}}{\partial T}} = \frac{\partial \overline{F_1}}{\partial T} P_s, \quad \overline{\beta F_1 P} = \overline{\beta F_1} P_s, \\ \frac{\partial \overline{F_2}}{\partial T} \overline{P} = \frac{\partial \overline{F_2}}{\partial T} P_s, \quad \overline{\beta F_2 P} = \overline{\beta F_2} P_s,$$

so that this equality now takes the form

$$\frac{\varphi S p_s}{Sd} = (q + \overline{c_v \rho} P_s) \left\{ \left(\frac{\partial \overline{F_1}}{\partial z} p + \frac{\partial \overline{F_2}}{\partial z} p^2 \right) + P_s \left[\left(\frac{\partial \overline{F_1}}{\partial T} + \overline{\beta F_1} \right) p + \left(\frac{\partial \overline{F_2}}{\partial T} + 2 \overline{\beta F_2} \right) p^2 \right] \right\}. \quad (17)$$

This relation holds for the gas ignition, i.e., for the formation about the heat source of a combustion front propagating throughout the gas volume. It is also valid when a burning zone, which is incapable of propagating throughout the gas volume, is formed about the heat source. The latter can be realized for very small values of P_s . Since this magnitude (according to equality (17)) depends on the pressure, it is obviously possible to attain minimum values of P_s . The displacement rate of the burning zone

will then be very low, and the whole gas volume will only ignite after a large time interval. In fact, P_s can be expressed by

$$P_s = \frac{\Delta T}{\Delta M} = \frac{\lambda \Delta T}{d} \frac{d}{\lambda \Delta M} = \frac{Q}{\lambda} \frac{d}{\tau \Delta M} = \frac{Qg}{\lambda \frac{\Delta M}{\tau}},$$

where τ is the formation time of the burning zone.

It follows from the identities obtained that for given reaction rate and heat flux, P_s depends on the displacement rate of the combustion front. For low P_s the displacement rate g of the front will likewise be small.

The pressure for which P_s attains a minimum value is termed the minimum pressure of the gas mixture.

For the minimum value of P_s formula (17) can be approximated to the following:

$$\frac{\varphi S P_s}{S d} = q \left[\frac{\partial \bar{F}_1}{\partial z} p + \frac{\partial \bar{F}_2}{\partial z} p^2 \right]. \quad (18)$$

The following equalities clearly hold:

$$\begin{aligned} \varphi S \Delta T = Q &= -q \frac{d\bar{M}}{dt} S d = -q (\bar{F}_1 p + \bar{F}_2 p^2) S d, \\ \frac{\varphi}{d} P_s &= \frac{\varphi S \Delta T}{S d \Delta M} = -\frac{q (\bar{F}_1 p + \bar{F}_2 p^2)}{\Delta M}. \end{aligned}$$

Equation (18) therefore becomes

$$\bar{F}_1 + \bar{F}_2 p = -\Delta M \left(\frac{\partial \bar{F}_1}{\partial z} + \frac{\partial \bar{F}_2}{\partial z} p \right), \quad (19)$$

where ΔM is the minimum quantity of reacting material about the heat source.

Hence, it follows that

$$P_{\min} = -\frac{\bar{F}_1 + \Delta M \frac{\partial \bar{F}_1}{\partial z}}{\Delta M \frac{\partial \bar{F}_2}{\partial z} + \bar{F}_2}. \quad (20)$$

However, according to (14)

$$\begin{aligned} F_1(T, z) &= -\alpha_2 m_2 + (\alpha_2 m_2 + \alpha_1 m_1) z = -b + b_1 z, \\ F_2(T, z) &= (\beta_2 m_2 - \beta_1 m_1) (1 - z) z = a^* (1 - z) z. \end{aligned}$$

These relations enable (20) to be rewritten in the form

$$P_{\min} = \frac{(-b + b_1 \Delta M) + b_1 \bar{z}}{-a^* [-\Delta M - (1 - 2\Delta M) \bar{z} + \bar{z}^2]}. \quad (21)$$

The roots of the quadratic expression in this equation are positive for all values of ΔM , however small. We can therefore write

$$p_{\min} = \frac{\left(\frac{b}{a^*} - \frac{b_1}{a^*} \Delta M\right) - \frac{b_1}{a^*} \bar{z}}{(z - c_1)(z - c_2)}, \quad (22)$$

where c_1 and c_2 are the roots of the quadratic expression. This equality implies the existence of lower and upper limits subject to the following inequality:

$$\frac{b}{a^*} - \frac{b_1}{a^*} \Delta M - \frac{b_1}{a^*} \bar{z} > 0.$$

Formula (22) was corroborated experimentally.

G. D. Salamandra

VIBRATIONAL FLAME PROPAGATION IN A TUBE

The vibrational propagation of a flame is a self-oscillating process. Any self-oscillating system consists of the oscillating system proper, an energy source, and some mechanism supplying the energy to the oscillating system. In the case of the vibrational propagation of a flame, the oscillating system is represented by the gas along which the flame propagates. The energy source is the heat energy liberated during combustion. (The possibility of maintaining oscillations by means of thermal energy was first noted by Rayleigh /1/.) The mechanism supplying the energy to the system remains an open question. Its explanation is of considerable interest, since it may provide a means for controlling the process. The present paper deals with this question.

We investigated the vibrational propagation of the flame in circular tubes of 30 mm diameter, and cross section $36 \times 36 \text{ mm}^2$ and $50 \times 50 \text{ mm}^2$. Combustible mixtures consisted of rapidly burning hydrogen-oxygen mixtures and slowly burning carbon monoxide-air mixtures. The process was photographed in the first case by a high-speed SFR camera, and in the second case by the SKS-1 camera. The motion picture record was supplemented by the continuous photography of the process. The gas flow ahead of the flame front was visualized by the method described in /2/. The Töpler method was used for the photography. Both conventional black-and-white and color Schlieren photographs of the process were obtained, the latter with the aid of a lattice of color filters /3/. Figure 1 shows the development of the combustion process of an hydrogen-oxygen mixture, containing 67% O_2 and 33% H_2 . On the left is the continuous time scan of the process in a tube of 30 mm diameter and 167 mm length, and on the right a series of instantaneous photographs of the same process in a tube of $50 \times 50 \text{ mm}^2$ cross section. The flame front was recorded on the photographs in the form of a dark zone against a grey background. Artificially created inhomogeneities, moving together with the gas, are clearly visible ahead of the flame front.

The following conclusions were drawn from an analysis of the photographs:

- 1) the gas ahead of the flame is brought into motion by compression waves generated by the flame front. The gas velocity is constant along each of the disturbances;
- 2) the gas motion ahead of the flame front can be considered as one-dimensional.

The gas motion ahead of the flame front was calculated by the method of characteristics. The construction of the characteristics for a plane isentropic gas flow in a bounded space was treated in detail in /4, 5/. The method of characteristics was used in /6/ to calculate the gas state ahead of the flame front, propagating in long tubes, when the combustion

is accompanied by the formation ahead of it of a shock wave or a transition into detonation. This method gave results agreeing satisfactorily with experimental results.

For combustion in short tubes, the calculation is complicated somewhat by the necessity of allowing for the influence of the waves reflected from both the tube end and the flame front. Figure 2 represents a part of the wave diagram of the process shown in Figure 1, a. The abscissa represents the distance x , and the ordinate the time t . The flame is represented by the bold line.

The position of the walls is indicated by vertical lines with coordinates $x = 0$ and $x = 167$ mm. The figures I, II, III designate the artificially created inhomogeneities. The (x, t) -plane is covered by a grid of characteristics, constructed as follows.

The slope of the characteristic $O-O_0$ starting from point O is determined by the sound velocity in the undisturbed gas, equal to 394 m/sec. This characteristic intersects the wall at O_0 . The region O, O_0, x corresponds to the state of rest. To construct the characteristic starting from point 1 it is necessary to know the gas velocity v and the sound velocity a at this point. The gas velocity ahead of the flame front is determined from the time record of the process /6/. The sound velocity was determined from the characteristic in the (v, a) -plane (Figure 3). Due to a suitable selection of the scale, this characteristic represents a straight line inclined at an angle of 45° to the coordinate axes. Knowing the value of v and a at 1, we draw a straight characteristic starting from point 1 in the (x, t) -plane (cf. Figure 2). Its equation is $dx/dt = v + a$.

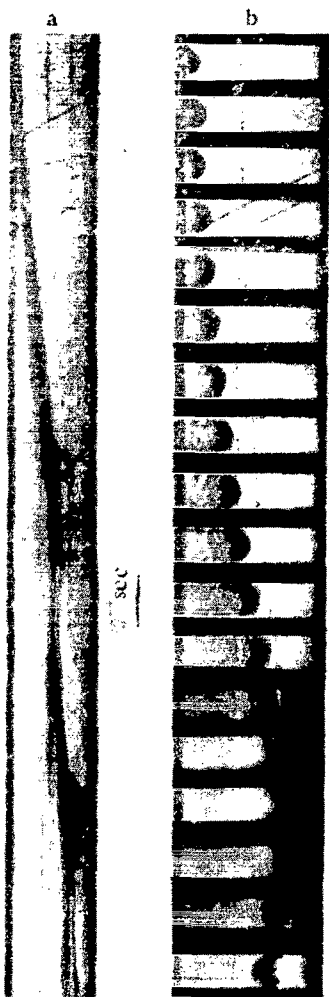


FIGURE 1. Combustion of a hydrogen-oxygen mixture containing 67% O_2 and 33% H_2 :

a—continuous time scan of the process; b—series of instantaneous photographs. Rate of photography 200000 frames/sec; 1—flame; 2—artificially created inhomogeneity.

Through O_0 we draw a straight characteristic of the second family $dx/dt = -a_0$, where a_0 is the sound velocity in fresh air. The intersection of the two straight characteristics determines the point O_1 . The characteristic starting from 2 is constructed similarly. The point O_2 lies at the intersection of the characteristics starting from points 2 and O_1 . The slope of the characteristic O_1, O_2 is determined by the sound velocity at O_1 , equal to the sound velocity at 1. To find the values of v and a , necessary for constructing the characteristic O_1, I_1 we draw the straight line $v - v_1 = -(2/\gamma - 1) \times (a - a_1)$ through point 1 in the (v, a) -plane. This straight line, making an angle of 90° with the characteristic 1, ..., 7, intersects the ordinate axis at I_1 , whose coordinates are the required values. The slope of the characteristic O_2, I_2 is determined by the coordinates of the point of intersection of the characteristics in the (v, a) -plane, drawn from points I_1 and O_2 . The remaining characteristics are plotted in the same manner.

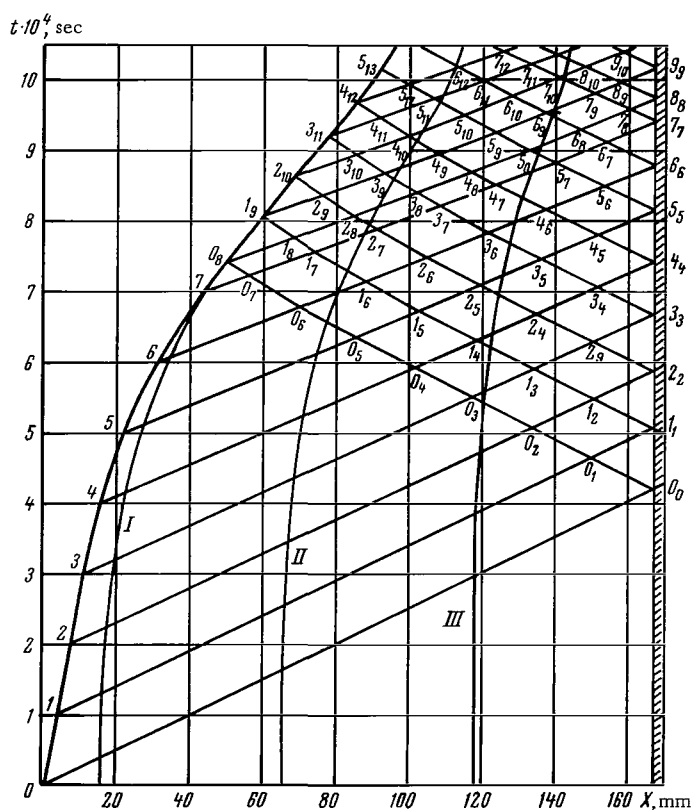


FIGURE 2. Wave diagram of the process shown in Figure 1, a.

From the wave diagram of the process it is possible to construct the distribution of the gas velocities between the flame front and the tube end at any moment. The corresponding construction for five different moments

is given in Figure 4, where the abscissa axis represents the distance traveled by the flame from the ignition point, and the ordinate axis represents the gas velocity. The vertical line indicates the flame position at the instant under consideration. The horizontal line is drawn at a level corresponding to the flame velocity at the given time. The points indicate the experimentally obtained gas velocities, with which the calculation agrees satisfactorily. Note the coincidence of the oscillation phases at all sections along the tube; this is characteristic for a standing wave in a medium at rest.

The compression waves propagating in the burning medium affect the shape of the flame front by altering the quantity of gas burning

in it. Although the question of the interaction between the compression waves and the flame front is of great interest, sufficient data does not yet exist on the variation of the flame front shape during vibrational combustion.

It is known that Schlieren photography visualizes regions in which the first derivative of the refraction index differs from zero. Since the gradient of the refraction index is maximum in the zone of heating, this zone is always recorded in the Schlieren photographs. From its variation one obtains an idea about the variation in the flame front shape (assuming that during interaction with the acoustic waves the burning zone is deformed in the same manner as the heating zone). The photographs in Figure 5 (on p. 155) show that this is not so. According to the filter arrangement in the lattice used in the experiments, the undisturbed field of the Schlieren photograph is red [gray background], the region of small gradients of the refraction index is green [fringes], and the region of large gradients is blue [band between fringes]. When interpreting color Schlieren photographs one must bear in mind that due to the finite width of the lattice strips every color includes certain angles of deviation. The wider the lattice strips, the

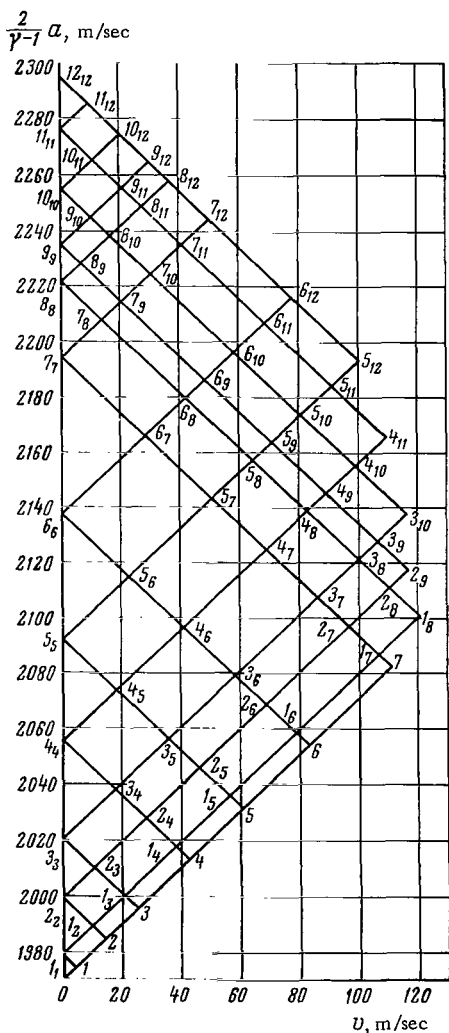


FIGURE 3. Characteristics in the (v, a) -plane.

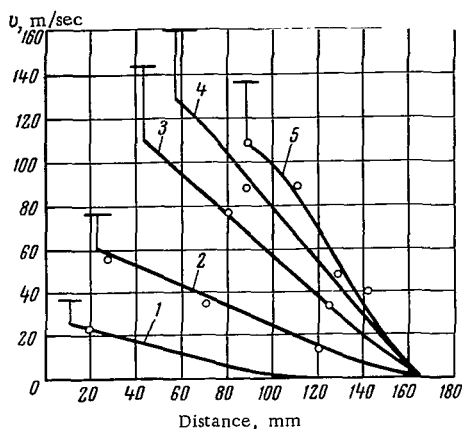


FIGURE 4. Distribution of the gas velocities between the flame front and the end of the tube at different instances of time:

1— $3 \cdot 10^{-4}$ sec; 2— $5 \cdot 10^{-4}$; 3— $7 \cdot 10^{-4}$; 4— $8 \cdot 10^{-4}$; 5— 10^{-3} .

larger the region of deviations corresponding to the same color. We used a lattice of strip width 0.5 mm.

The Schlieren photograph shows that the development of the process is accompanied not only by a variation in the total width of the zone recorded on the photograph, but also by a redistribution of the regions with different refraction-index gradients inside this zone. The leading boundary of the heating zone, which is habitually used for outlining the shape of the flame front, varies much more slowly than the combustion zone. For a detailed study of the flame front structure the number of filters in the lattice must be increased.

The following conclusions can be drawn from here.

1. For the vibrational propagation of a flame in a tube, the gas ahead of the flame front is set in motion by the disturbances generated by the front. The problem of the gas motion ahead of the flame front can be considered as one-dimensional. The calculations of the gas state ahead of the flame front by the method of characteristics agree satisfactorily with experimental results.

2. For a more detailed study of the flame front structure in the case of vibrational combustion it is necessary to use color Schlieren photographs.

Bibliography

1. Lord Rayleigh. Theory of Sound, Vol. II.—Dover Publications, New York, 1896.
2. Salamandra, G.D. and I.K. Fedoseeva. Izmerenie skorosti gaza v srede, sposobnoi k vosplameneniyu (Gas Velocity in an Inflammable Medium).—IFZh, Vol. 7, No. 7. 1964.
3. Salamandra, G.D. Poluchenie tsvetnykh teplerogramm bystroprotekayushchikh protsessov s pomoshch'yu pribora IAB-51 (Obtaining Color Schlieren Photographs of Rapid Processes Using the IAB-51 Instrument).—In this collection, p. 153.
4. Kochin, N.E., I.A. Kibel', and N.V. Roze. Teoreticheskaya gidromekhanika (Theoretical Hydromechanics).—Part II, Moskva, Gostekhizdat, 1948.
5. Zel'dovich, Ya.B. and Yu.P. Raizer. Fizika udarnykh voln i vysokotemperaturnykh gidrodinamicheskikh yavlenii (Physics of Shock Waves and High-temperature Hydrodynamics).—Moskva, Izdatel'stvo Fiziko-Matematicheskoi Literatury. 1963.
6. Salamandra, G.D. Formirovanie potoka gaza pered frontom plameni (Formation of a Gas Flow ahead of the Flame Front).—Sbornik "Issledovaniya po fizicheskoi gazodinamike," Moskva, Izdatel'stvo "Nauka." 1966.

G. D. Salamandra

OBTAINING COLOR SCHLIEREN PHOTOGRAPHS OF RAPID PROCESSES USING THE IAB-451 INSTRUMENT

Optical methods for visualizing inhomogeneities in transparent media have found many applications in various fields of science and engineering. One of the most widely used optical methods is the Töpler Schlieren method, which enables one to visualize regions in which the refraction-index gradient differs from zero.

The optical inhomogeneities are represented in Schlieren photographs by differently illuminated zones against a uniform grey background, corresponding to the undisturbed field.

By means of a simple modification of Töpler's scheme color photographs can be obtained on which the inhomogeneities are differently colored, each color corresponding to a definite gradient of the refraction index. Since the eye is more sensitive to a variation in color than to a variation in background illumination, color photographs give considerably more information about inhomogeneities than the usual black-and-white ones. They are particularly convenient for interpreting processes near the boundary of a solid. The color photographs enable estimates to be made rapidly of the distribution of refraction-index gradients in an inhomogeneity, and often allow a quantitative assessment to be made as well. To obtain a color Töpler image, the illuminating part of Töpler's scheme must be adjusted somewhat by placing a prism on the path of the beam from the light source to the first lens. This prism disperses the incident light into a spectrum $/1-5/$. Alternatively, the knife edge can be replaced by a lattice of color filters $/4, 6/$.

When the first method is used, the knife edge in the focal plane of the second lens is replaced by a slit cutting out a part of the spectrum. As long as the medium is homogeneous, the image plane will be monochromatic. If an inhomogeneity is placed on the beam path, a part of the spectrum is shifted and light of a different wavelength passes through the slit. Color zones appear in the image plane, i.e., the image of the given optical inhomogeneity. The second method is simpler, since the illuminating part of the scheme remains unaltered. The lattice replacing the knife edge is placed such that in the absence of an inhomogeneity the image of the light source appears at the center of the middle strip. When an optical inhomogeneity appears in the instrument's field of vision, the light rays passing through the inhomogeneity are shifted through some angle, thus causing the image of the light source to appear on a different lattice strip.

Differently colored zones, corresponding to the image of the optical inhomogeneity, appear in the image plane against the colored background, which designates the location of the undeflected rays. In view of the finite

width of the lattice strips, a single color will embrace a certain range of deviation angles. Depending on the shape of the light source used, the lattice takes the form either of differently colored narrow strips (for a line course of light), or of colored rings (for a point source of light).

In spite of the obvious advantages of color Schlieren photographs over black-and-white ones, color photography has so far not been widely applied because very few Schlieren instruments produced in Russia are suitable for color photography. Such instruments are very difficult to set up under laboratory conditions. No less difficult is the preparation of color lattices. Lattices produced photographically are unsuitable for obtaining color photographs. Lattices consisting of strips of colored optical glass are even more difficult to make, since the number and width of the strips, as well as their alternation must be varied in accordance with the nature of the object studied. Another factor hindering the development of color Schlieren photography is the unavailability of color films of the required sensitivity for photographing high-speed phenomena.

To obtain color Schlieren photographs of rapid processes using the IAB-451 instrument, it was first necessary to find a simple method of preparing color lattices, and then to select the light source and developing conditions to ensure the recording of high-speed phenomena on photographic material of low sensitivity. Our experiments established that foil filters are satisfactory for the preparation of color lattices. Simple attachments enable both strips and rings of any dimensions to be easily punched from foil filters.

When photographing high-speed processes at rates of up to 4000 frames per sec, the light source comprised a light-pressure DRSh-1000 mercury lamp. Alternatively, the IFP-800 flash bulb was used in conjunction with a high-speed SFR camera, with a rate of several thousand frames per second.

In the first variant the process was recorded on a reversible OTs-2 film of sensitivity 22 GOST* units, and in the second one on a negative film of sensitivity 35 units. The negative film was developed with the aid of thallium salts, which increase the light sensitivity of the film several times in the course of its development /7-9/.

Figure 1 shows a series of instantaneous Schlieren photographs of the vibrational propagation of a flame in a mixture of carbon monoxide and air. The photographs were taken by an SKS-1 camera at a rate of about 3000 frames per sec. The color filters of the lattice are so arranged that the undisturbed field is colored red [gray background], the region of small gradients of the refraction index in white [fringes], and the region of large gradients in blue [center band]. The variation in the flame front structure during vibrational combustion can be followed on the photographs, which is not the case with black-and-white photographs.

Figure 2 shows a series of Schlieren photographs of the flame propagation near the closed end of the tube. The photographs were taken by a high-speed SFR camera, at a rate of about 300000 frames per sec. The photographs clearly show the flame front and the compression waves running ahead of it, which cannot be resolved on black-and-white photographs.

* [Gosudarstvennyi obshchesoyuznyi standart—All-Union State Standard.]

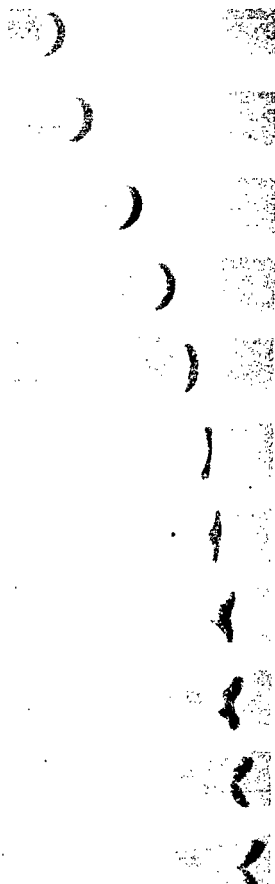


FIGURE 1. Schlieren photographs of the vibrational propagation of the flame:

Rate of photography about 3000 frames per sec.

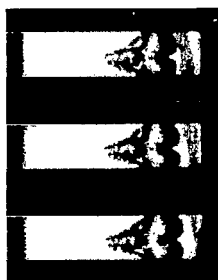


FIGURE 2. Schlieren photographs of the flame propagation in a stoichiometric mixture of hydrogen and oxygen:

Rate of photography about 300000 frames per sec.



FIGURE 5*. Series of Schlieren photographs of the vibrational propagation of a flame in a mixture of carbon monoxide and air in a tube of cross section $36 \times 36 \text{ mm}^2$:

Rate of photography about 3000 frames per sec.

- [This figure refers to the previous paper.]

Bibliography

1. Schardin, H. Schlierenverfahren and ihre Anwendungen.—Ergebn. exakten Naturwiss., Vol. 20. 1942.
2. Holder, D.W. and R.J. North. Colour in the Wind Tunnel.—Aeroplane, Vol. 82. 1952.
3. Holder, D.W. and R.J. North. A Schlieren Apparatus Giving an Image in Colour.—Nature, Vol. 169, No. 4298. 1952.
4. Holder, D.W. and R.J. North. Schlieren Methods. Notes on Applied Science.—London, Dept. of Scient. and Indust. Research, No. 31. 1963.
5. Vasil'ev, L.A. Uovershenstvovanie pribora IAB-451 (Improving the IAB-451 Instrument).—Nauchnye Doklady Vysshei Shkoly, Mashinostroenie i Priborostroenie, No. 4. 1953.
6. Anashev, M.D., V.D. Mikhailenko, and N.F. Belyaeva. Primenenie tsvetnogo rastra dlya kolichestvennykh issledovaniy shliir opticheskim metodom Teplera (Use of Color Photography for the Quantitative Study of Schlieren Photographs by Töpler's Optical Method).—Trudy Instituta dvigatelei, No. 6, Moskva, Izdatel'stvo AN SSSR. 1962.
7. Garnov, V.V. and V.V. Shchauro. Vysokoskorostnaya fotografiya samosvetyashchikhsya protsessov na tsvetnoi plenke (High-Speed Photography of Self-luminous Processes on Color Film).—ZhN i PFiK, Vol. 8, No. 4. 1963.
8. Mikhailov, V.Ya. Vliyanie uslovii proyavleniya na svetochuvstvitel'nost' i balans tsvetnoi negativnoi plenki (Influence of the Developing Conditions on the Light Sensitivity and Balance of a Color Negative Film).—ZhN i PFiK, Vol. 1, No. 1. 1956.
9. Mikhailov, V.Ya. Aerofotografiya i obshchie osnovy fotografii (Air Photography and Fundamentals of Photography).—Moskva, Geodezizdat. 1959.

N. K. Fedoseeva

APPARATUS FOR PROJECTING STILLS

Various optical-mechanical instruments have been invented for studying rapid processes (detonation, shock waves, explosion, etc.), and several million frames per second can be obtained with their aid. High-speed spark photography is also used widely [1-3]. However, the films are unsuitable for motion-picture projection, since the frames are arranged nonlinearly and nonuniformly spaced (see Table).

Camera	Frames/sec	Film width, mm	Arrangement of frames	Frame dimensions, mm	Number of frames
SSKS-1	$2 \cdot 10^5$	190	5, 9 or 15 rows	15.22-3.6.6	330-4800
FP-36	$2.5 \cdot 10^4$	320	Horizontal	7.5.7.5	
SFR-2M	$5 \cdot 10^5 - 2.5 \cdot 10^6$	35	Two series, four series	$\varnothing 10$	60
				$\varnothing 5$	240
LV-1	$2 \cdot 10^6 - 33.3 \cdot 10^6$	35	One series, two series	$\varnothing 12$	30
				$\varnothing 5$	150
ZhLV	$3 \cdot 10^4 - 4.5 \cdot 10^6$	35	One series, two series, four series } on two films	$\varnothing 15$	125
				$\varnothing 10$	300
UVIS	10^5	35	One series (nonuniform frequency)	$\varnothing 5$	1500
				—	300

By projecting rapid processes, one can study their dynamics, gain an insight into the physical essence of the phenomena, and observe the processes slowed down by as much as a fraction of tens of thousands.

To obtain a motion-picture film the original film must be reprinted such that the arrangement of the frames and the intervals between them correspond to the specifications of a standard film.

It is seen from the table that the majority of cameras operate with a 35 mm film, and for such cameras we have assembled an apparatus whose optical layout is similar to that described in [4].

The stills were rephotographed by a KSR-1 cinecamera with mirror obturator capable of taking stills as well. In order to utilize fully the film area ($16-22 \text{ mm}^2$), the stills were enlarged during reprinting. The general layout of the apparatus is shown in Figure 1. The illuminator 1 of the film consisted of a condenser and an STs-63 lamp (12 v, 35 w), whose heating was controlled by a rheostat.

The 35 mm film was held by the cassette of a "Kiev-2" camera. The unit holding the film being projected was held by a special device 3, shown in Figure 2. Pintles 4 were placed on the prop 1 (Figure 2) with which to fasten the cassette holding the film 2 and the frame 3.

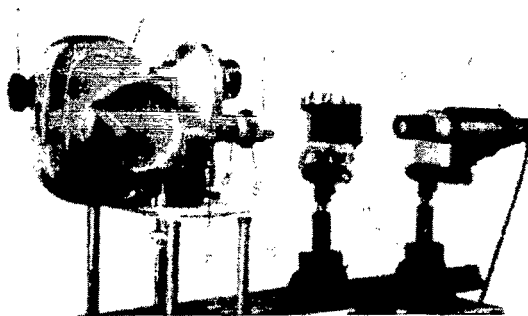


FIGURE 1. General view of the apparatus for projecting films.

The illuminator and the film holder were mounted on an optical bench 10 on special props 11, to enable adjustments to be made in three directions.

The image of each frame on the film 2 (cf. Figure 2) was formed by a system of lenses 4 and 8 in the focal plane of the cinecamera 5. The optical

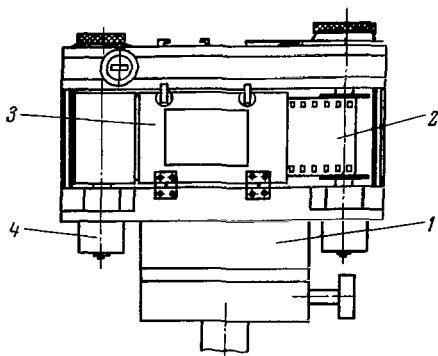


FIGURE 2. Layout of the unit holding the film being projected.

system was focused by moving lens 8, and diaphragmed by the diaphragm of lens 4. When the frames were reprinted from the film of the SFR camera (in the case of two-series framing), the lenses Yu-8 and Yu-11 were selected as lenses 4 and 8. The Yu-11 was the working lens of the cinecamera 5. The "Moment-1" central action shutter 9 was fastened between them on adapters. The shutter, which ensured exposures of up to $1/250$ sec, was opened before the photography. When the handle 7 was rotated the mirror obturator crossed the optical channel. The frame setting was controlled visually

by a direct-focusing magnifying glass 6, so enabling each subsequent frame to be set in a fixed position on the screen.

After the next frame was set, the shutter was closed, the obturator opened the optical channel, and the photography started.

In view of the high speeds of the processes studied and the small number of frames on the SFR film, every frame had to be repeated three times. This did not impair the smooth motion of the object on the screen.

The exposure time during reprinting was selected by trial and error. A "Micrat-200" film was used for reprinting. In this way, we obtained films of the interaction between a shock wave and a flame front, the vibrational propagation of a flame in a tube (at a frequency of $5 \cdot 10^5$ frames/sec), etc.

Bibliography

1. Inform. Sbornik. NIKFI, No. 3. 1960.
2. Dubovik, A.S. Fotograficheskaya registratsiya bystroprotekayushchikh protsessov (Photorecording Rapid Processes). — Moskva, Izdatel'stvo "Nauka". 1964.
3. Salamandra, G.D. and I.K. Sevast'yanova. Ustanovka dlya vysokoskorostnoi iskrovoi s'emki (Apparatus for High-Speed Spark Photography). — IFZh, Vol. 3, No. 9. 1960.
4. Garnov, V.V. and A.S. Dubovik. Ob ekranizatsii snimkov sverkhskorostnoi registriruyushchei ustanovki SFR (Photographic Projection by the High-Speed SFR Recording Apparatus). — PTE, No. 5. 1960.

S. G. Zaitsev, E. V. Lazareva, E. I. Chebotareva

THE BOUNDARY LAYER BEHIND A SHOCK WAVE IN ARGON AND NITROGEN

When solving various problems of physical gas dynamics in shock tubes one must allow for the influence of the boundary layer on the shock front and stream.

The effect of the boundary layer on shock-wave damping, the variation in the stream parameters behind the wave and the length of the plug were studied theoretically in /1-3/. The boundary layer behind the shock wave was assumed to be either completely laminar or completely turbulent. These papers cannot pretend to describe correctly the processes accompanying shock-wave motion, since they do not take into account phenomena on the contact surface, whose influence on the plug and shock front was corroborated experimentally; the process of the opening of the diaphragm is likewise not considered.

A full treatment of this phenomenon must include the transition of a laminar layer into a turbulent one.

The boundary layer in the shock tube was studied with thin-film probes /4-7/ and interferometric methods /7-8/. The results showed that at a certain distance from the shock front the heat fluxes increase sharply as a result of the transformation of the laminar boundary layer into a turbulent one. The interferometric method was used to determine the density distribution in the boundary layer, its thickness and rate of increase. The process can be better understood by measuring the density profile in the boundary layer of different gases over a wide range of Mach numbers, in addition to the parameters ahead of the shock front, and then comparing these data with the values calculated under general assumptions.

We describe below the experimental determination of the boundary-layer thickness and the density distribution in it for nitrogen and argon, where $p_0 = 10$ and 50 mm mercury, $M_s = 2.5-9$.

1. INTERFEROMETRIC METHOD OF DENSITY MEASUREMENT

The Mach-Zender interferometer for studying gas streams can be used to determine the density distribution in the stream. The standard interferometric method of determining the density profile behind a shock wave is based on the assumption of small deformation of the light-wave front (the variation in the angle γ of the normal to the wave front after passing through an inhomogeneity is much smaller than the angle ω between the

interfering beams). This condition, which is usually fulfilled for the main stream, makes the relations given below inapplicable in the immediate vicinity of a wall. As a result, the region within 0.2—0.3 mm of a wall is inaccessible to measurements.

Consider the case when the direction of the bands coincides with the direction of the density gradient in the stream. The interference pattern then makes it possible to determine in a zero approximation the variation of the density field, given by

$$\Delta\rho = \rho(y_1) - \rho(y_2) = \frac{\Delta\lambda}{lk}, \quad (1)$$

where l is the length of the ray path in the stream studied; k is the Gladstone-Dale constant; Δ is the optical path difference, determined from the relation

$$\Delta = \frac{\xi}{S}; \quad (2)$$

S is the band width; ξ is the shift (Figure 1).

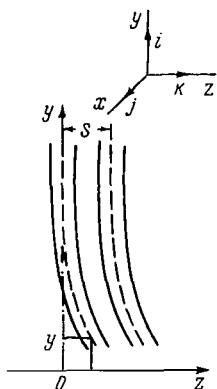


FIGURE 1. Density measurement in the boundary layer with fringes oriented perpendicular to the fairing.



FIGURE 2. Density measurement in the boundary layer with fringes oriented parallel to the fairing.

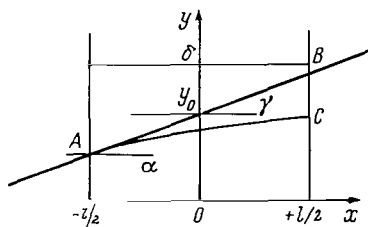


FIGURE 3. Ray propagation in a layer of variable density.

If the density gradient is perpendicular to the direction of the interference fringes, this causes a change in the distance between them. Different methods are therefore required to interpret such interferograms.

In the boundary layer behind the shock wave there is a density gradient both perpendicular and parallel to the wall. As a result, the interference fringes oriented along the wall (Figure 2) form a fan in the boundary layer. When determining the density profile in section Z_0 by formula (1) it is assumed that the fringe width is invariable. The error introduced by this assumption does not exceed 5% for density-ratio measurements.

We shall estimate the error in the density caused by the bending of the light ray due to an inhomogeneity. Its magnitude is determined by the variation in the refractive index along the ray trajectory in the volume studied, and the variation in geometrical length of the ray path $AC-AB$ (Figure 3).

Let the ray propagate along the straight line AB in the absence of a density gradient, in a gaseous medium of refractive index n_1 . The equation of this line is

$$y - y_0 = \alpha x. \quad (3)$$

When a density gradient appears, the ray trajectory is deflected from AB in the direction of density increase (line AC). If $n = n(y)$, we can represent the equation of the light-ray propagation in a medium of variable density, in the form

$$\sqrt{1 + (y')^2} \frac{dn}{dy} = \frac{d}{dx} n y' \frac{1}{\sqrt{1 + (y')^2}} \quad (4)$$

This equation will be solved under the following assumptions:

- 1) the slopes of AB and AC coincide at point A , since the actual variations in the experimental values of the refractive index did not exceed 0.01 %;
- 2) $n(y)$ has the form

$$n(y) = n(y_0) + N(y - y_0), \quad (5)$$

where

$$N = \frac{1}{n(y_0)} \frac{\partial n}{\partial y} \Big|_{y=y_0}.$$

In the experiments considered, $\partial n / \partial y < 0$ for the coordinate frame used (cf. Figure 3).

If (5) is substituted in (4), then

$$y'' + N[1 + (y')^2]^{3/2} = 0. \quad (6)$$

For the actual density gradients $|y' - \alpha| < 1$.

In the apparatus used $|\alpha| < 10^{-2}$. The solution of (6) takes the form

$$y - y_0 = \frac{N}{2} \left(x + \frac{l}{2} \right)^2 + \alpha x \quad (7)$$

to an accuracy of terms of order $(y' - \alpha)^3$.

The light ray propagating along AC continues beyond point C along a straight line coinciding with the tangent to AC at C ; this line intersects AB at the point E . Therefore, in the approximation adopted, the inhomogeneity considered does not disturb the plane in which the interference pattern is localized. The angle between AB and EC $\gamma \simeq (\Delta n / \Delta y) l$. For the regions of the boundary layer studied, $y \geq 0.2$ mm and $\gamma < 10^{-3}$. When using interference fringes of width S equal to $\simeq 0.2$ mm (magnification of the interference

pattern 1:1), the angle ω between the interfering beams, determined from

$$\omega = \frac{\lambda}{S},$$

will be $\simeq 10^{-3}$. Thus, starting at a distance $y < y^*$ for which $\gamma \simeq 0.1 \omega$, one must account for the wave-front distortion, and therefore use a different method to interpret the interferograms. In this paper $y^* \simeq 0.2-0.3$ mm.

The optical path difference caused by the inhomogeneity is determined by the relation

$$\Delta = \int_{AC} n(y) \sqrt{1 + (y')^2} dx - \int_{AB} n_1 \sqrt{1 + \alpha^2} dx. \quad (8)$$

Substituting (5) and (7) in (8), using values satisfying $N \ll 1$, $a \ll 1$ in the experiments, and restricting ourselves to terms of order N^2 , we obtain

$$\Delta = (n(y_0) - n_1) \left(1 + \frac{\alpha^2}{2} \right) l + \alpha \frac{\Delta n}{\Delta y} \frac{l^2}{2} + \left\{ \frac{1}{n(y_0)} \frac{dn}{dy} \right\}_{y=y_0}^2 \frac{l^3}{3}. \quad (9)$$

The first term of this equation corresponds to the variation in the optical path difference caused by a change of refractive index, the variation of this index along the trajectory being neglected. The second term corresponds to the variation in the optical path difference caused by a change of refractive index along an invariable trajectory AB ; the third term allows for the variation in the geometrical length of the ray path due to the $AC - AB$ density gradient (cf. Figure 3).

With the aid of the Gladstone-Dale relation between the refractive index and density, (9) takes the form

$$\Delta \rho = \rho_1(y_0) - \rho_1 = \frac{\Delta}{kl} (1 - \varepsilon_1), \quad (10)$$

where

$$\varepsilon_1 = \left\{ \frac{1}{n(y^*)} \frac{dn}{du} \right\}_{u=y^*}^2 \frac{l^2 n(y^*)}{3(n(y^*) - n_1)}.$$

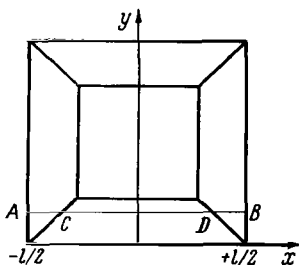


FIGURE 4. Ray propagation in the boundary layer.

Relation (10) enables one to estimate the error when the density variation is determined from the interferograms by relation (1).

In this paper, for $y^* \simeq 0.2$ mm, $\max \varepsilon_1 \leq 3\%$. Obviously, as y varies from y^* to δ (the boundary layer thickness), the value of ε_1 drops to zero.

Consider the boundary-layer effect due to the cover glass, on the density measurement in the stream, including the boundary layer on the upper and lower walls. It is assumed that the density distribution in the boundary layer on the cover glass is the same as on the upper and lower walls in the layers.

The optical path difference for the ray AB (Figure 4), caused by the stream, can be written as

$$2k \int_0^{l/2-u} \Delta \rho(\xi) d\xi + 2k \int_0^y \Delta \rho(\xi) d\xi = \Delta.$$

In this relation, the density on segment CD is taken as invariable in the direction of ray propagation and determined by the distance from the wall. On segments DB and AC the density varies due to the effect of the side walls $y = \pm l/2$. To estimate these terms we used the density distribution in the boundary layer obtained by analyzing the interferograms on the basis of (1), i.e., disregarding the effect under consideration.

The density variation is represented in the form

$$\Delta\rho(y) = \frac{\Delta}{kl} - \varepsilon_2,$$

where

$$\varepsilon_2 = \frac{2}{l-2y} \int_0^y \Delta\rho(\xi) d\xi.$$

Its magnitude is maximum for measurements outside the boundary layer, and determined by the relation

$$\varepsilon_2 = \frac{2}{l-2\delta} \int_0^\delta \Delta\rho(\xi) d\xi.$$

In our experiments $\varepsilon_2 \leq 1\%$.

2. SHOCK-TUBE DENSITY MEASUREMENTS NEAR A WALL IN SUPERSONIC HIGH-TEMPERATURE STREAMS

When measuring the density distribution in a boundary layer, the axis of the probing beam and the upper and lower walls of the chamber must be parallel to within 0.1° . Otherwise, the effects associated with the oblique incidence of the ray on a region of variable density (the second term of (9)) would unnecessarily complicate the treatment.

A coarse alignment of the chamber walls and the probing beam was realized by a level, and the fine adjustment by a collimator in front of the first dividing plate of the interferometer. The main position of the interferometer is where the images of the collimator cross wire coincide in the two channels. A plane-parallel plate is then placed on the lower wall of the chamber (with the cover glass removed). When the probing beam and the horizontal walls of the chamber are not parallel, the collimator cross wires diverge; they are then brought into coincidence by a small rotation of the shock tube. This method provides an alignment accuracy of 0.1° . A symmetrical interference pattern of the process is obtained on the film, and its symmetry is a criterion of the necessary alignment accuracy.

To increase the contrast between the fringes and weaken the background created by the luminosity of the object being studied, diaphragms were placed before the lens, which focused the interference pattern on the film. The measurements were realized in monochromatic light with $\lambda = 4990 \text{ \AA}$. The image of the chamber walls on the interferograms was sufficiently

sharp, and the error in determining its position did not exceed 0.1 mm.

The boundary layer behind the shock front was investigated by interferograms with fringes oriented parallel (horizontal fringes) and perpendicular (vertical fringes) to the upper and lower walls of the chamber. When vertical fringes were used, the interferograms were recorded on a fixed film. Thus, each photograph gives an interference pattern of the process in the measuring chamber at a given instant of time. To study the variation in the boundary layer along the plug, a number of interferograms were taken under the same working conditions, but at different times during which the light source functioned. The reproducibility of the working conditions was not lower than 0.1 M , and the light source was a spark of duration $10\mu\text{sec}$.

When horizontal fringes were used, the interference fringes were oriented parallel to the upper and lower walls of the chamber. The film moved at a speed of $0.117\text{ mm}/\mu\text{sec}$ in the propagation direction of the shock wave, and the area of measuring chamber projected on it was restricted by means of an optical slit oriented parallel to the shock front. The photography thus gives the variation with time of the interference pattern at a given section. The light source was an IFP-800 flash lamp of flash duration $\sim 800\mu\text{sec}$. Since the density increases gradually in the boundary layer, the fringes passing through the boundary layer region are inclined at an angle of inclination which decreases toward the main stream. When the interferograms were processed, we measured the displacement of the fringe center at a distance y from the wall relative to the center of this fringe on the shock front. As in the method with vertical fringes, the relationship $\rho_1/\rho(y)$ was established by means of formula (1), and the boundary layer thickness determined.

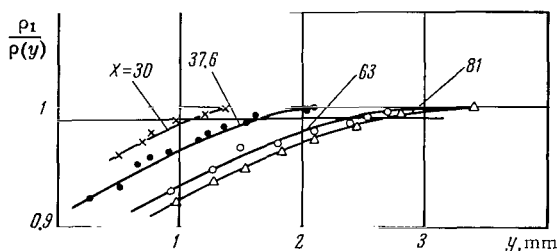


FIGURE 5. Density variation in the boundary layer:

Nitrogen. $M_s = 8.9$; $p_0 = 30$ mm mercury; x is the distance from the shock front.

The second method is more convenient when investigating the layer as a whole (dependence of the layer thickness on x , etc.), and the first method is best for a detailed study of the density variation at the initial development stages of the layer.

The density in the wall region was calculated by the formula

$$\rho(y) = \rho_1 + \frac{\lambda}{kl} \frac{\xi}{S}, \quad (11)$$

where ξ is the displacement of the fringe center at a distance y from the wall relative to the fringe center in the main stream; S is the fringe width, measured in the main stream. The measured values of ξ were corrected to allow for fringe distortions caused by glass imperfections. The results were represented in the form of the relationship $\rho_1/\rho(y) = f(y)$ (Figure 5). The thickness of the boundary layer was taken as the distance from the wall corresponding to $\rho_1/\rho(y) = 0.99$.

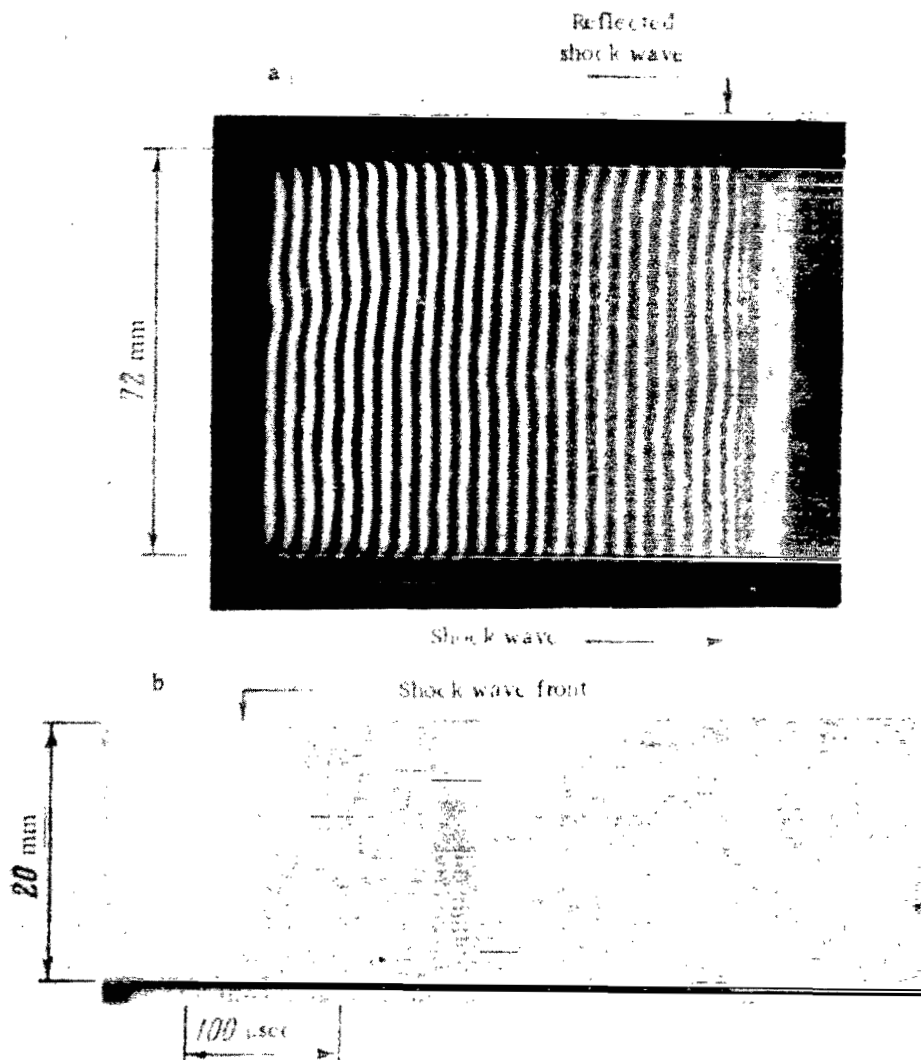


FIGURE 6. Interferogram of the stream behind the shock wave:

a—carbon dioxide: $M_s = 4$; $p_0 = 10$ mm mercury. The fringes are oriented perpendicular to the wall;
b—nitrogen: $M_s = 3.5$; $p_0 = 50$ mm mercury.

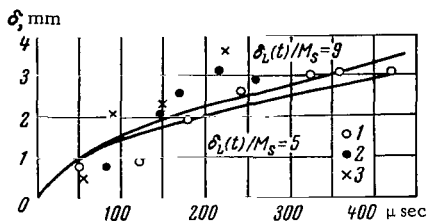


FIGURE 7. Variation of the boundary layer thickness with time, in argon:

$\rho_0 = 0.216 \cdot 10^{-4} \text{ g/cm}^3$, $T_0 = 300^\circ\text{K}$, $a_0 = 319 \text{ m/sec}$; 1— $p_0 = 10 \text{ mm mercury}$; $M_s = 4.8$; $u_1^* = 1070 \text{ m/sec}$; $T_1 = 2470^\circ\text{K}$; $\rho_1 = 0.518 \cdot 10^{-4} \text{ g/cm}^3$; $p_1 = 289 \text{ mm mercury}$; $\mu = 0.963 \cdot 10^{-3} \text{ g/cm} \cdot \text{sec}$; $Re_B = 0.146 \cdot 10^6$; 2— $p_0 = 10$; $M_s = 6.3$; $u_1^* = 1455$; $T_1 = 4010$; $\rho_1 = 0.55 \cdot 10^{-4}$; $p_1 = 500$; $\mu = 0.132 \cdot 10^{-2}$; $Re_B = 0.155 \cdot 10^6$; 3— $p_0 = 10$, $M_s = 10$, $u_1^* = 2420$; $T_1 = 9020$; $\rho_1 = 0.637 \cdot 10^{-4}$; $p_1 = 1155$; $\mu = 0.222 \cdot 10^{-2}$; $Re_B = 0.229 \cdot 10^6$.

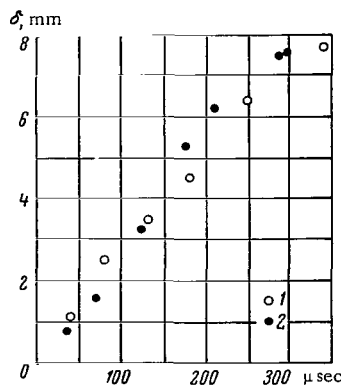


FIGURE 8. Variation of the boundary layer thickness with time, in argon:

$\rho_0 = 0.108 \cdot 10^{-3} \text{ g/cm}^3$, $T_0 = 300^\circ\text{K}$; 1— $p_0 = 50 \text{ mm mercury}$; $M_s = 5.8$; $u_1^* = 1150 \text{ m/sec}$; $T_1 = 3440^\circ\text{K}$; $\rho_1 = 2.65 \cdot 10^{-4} \text{ g/cm}^3$; $p_1 = 2150 \text{ mm mercury}$; $\mu = 0.119 \cdot 10^{-2} \text{ g/cm} \cdot \text{sec}$; $Re_B = 0.818 \cdot 10^6$; 2— $p_0 = 50$; $M_s = 6.2$; $u_1^* = 1430$; $T_1 = 3820$; $\rho_1 = 2.75 \cdot 10^{-4}$; $p_1 = 1870$; $\mu = 0.128 \cdot 10^{-2}$; $Re_B = 0.840 \cdot 10^6$.

The above method for determining the density profile near the wall was used to study the boundary layer on a cool wall, past which flows a high-temperature supersonic stream of nitrogen or argon. The measurements in nitrogen were conducted for shock front Mach numbers of 2—6. Over this range the refraction changes caused by dissociation processes could be neglected. It was possible to use values of the constant k (relation (1)) measured at room temperatures, since the variation in the polarizability of the molecules caused by the excitation of the vibrational levels can be neglected within the accuracy limits of the method.

In streams of dissociated gas the Gladstone-Dale constant k is determined by the component refractions and the stream composition. The density profile therefore cannot be found by the method described, since the variation in the boundary-layer density is accompanied by a variation in composition. Fringe bending near the wall enables the boundary-layer thickness to be determined in this case as well.

In argon, the boundary layer was measured for $M_s < 13$. Over the range $9 < M_s < 13$ only its thickness was measured, since here the ionization processes cause a considerable variation in k . Figure 6 shows typical interferograms, used to determine the boundary-layer density profile and thickness.

The values of the boundary layer thickness in argon are given in Figures 7 and 8. The initial parameters ahead of the front and the stream parameters are given in the captions, where p_0 is the pressure (in mm mercury) ahead of the shock front; $M_s = u_s/a_0$ is the Mach number of the shock front; u_1^* is the stream velocity (in m/sec) in a coordinate frame linked with the tube; T_1 , ρ_1 , p_1 , μ are respectively the temperature, density, pressure, and

viscosity in the stream; Re_s is the boundary-layer Reynolds number, determined by

$$Re_s = u_s \left(\frac{\rho_1}{\rho_0} - 1 \right)^2 \frac{\rho_0 x}{\mu_1}.$$

The stream parameters were obtained by solving the shock-front conservation equations.

The method used to determine the density has a constant absolute error. As a result, the relative error in measuring the density profile increases with a decrease in the absolute value of the stream density. The boundary layer thickness in streams of lower density will therefore be underestimated.

The values of the boundary layer thickness in nitrogen are given in Figures 8–10. The initial conditions ahead of the shock front and the stream parameters are given in the captions.

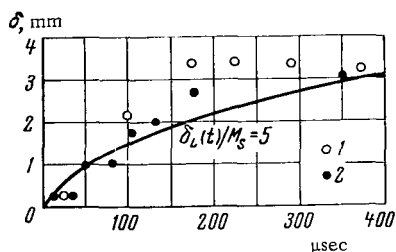


FIGURE 9. Variation of the boundary layer thickness with time, in nitrogen:

$\rho_0 = 0.150 \cdot 10^{-4}$ g/cm³, $T_0 = 300^\circ\text{K}$, $O_0 = 353$ m/sec; 1— $p_0 = 10$ mm mercury; $M_s = 5.1$; $u_1^* = 1470$ m/sec; $T_1 = 1670^\circ\text{K}$; $\rho_1 = 0.837 \cdot 10^{-4}$ g/cm³; $p_1 = 310$ mm mercury; $\mu = 0.552 \cdot 10^{-3}$ g/cm·sec; $Re_s = 1046 \cdot 10^6$; 2— $p_0 = 10$; $M_s = 5.4$; $u_1^* = 1570$; $T_1 = 1820$; $\rho_1 = 0.863 \cdot 10^{-4}$; $p_1 = 350$; $\mu = 0.598 \cdot 10^{-3}$; $Re_s = 1.100 \cdot 10^6$.

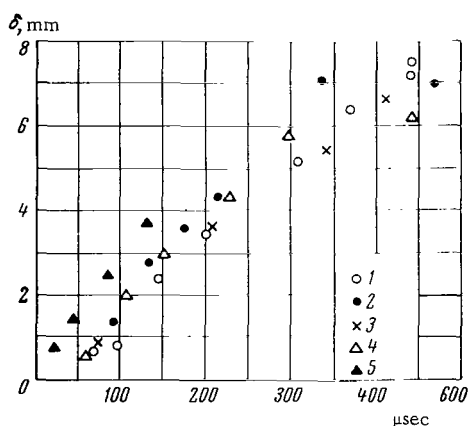


FIGURE 10. Variation of the boundary layer thickness with time, in nitrogen:

$\rho_0 = 0.750 \cdot 10^{-4}$ g/cm³, $T_0 = 300^\circ\text{K}$; 1— $p_0 = 50$ mm mercury; $M_s = 2.7$; $u_1^* = 690$ m/sec; $T_1 = 690^\circ\text{K}$; $\rho_1 = 2.70 \cdot 10^{-4}$ g/cm³; $p_1 = 412$ mm mercury; $\mu = 0.318 \cdot 10^{-3}$ g/cm·sec; $Re_s = 1.557 \cdot 10^6$; 2— $p_0 = 50$; $M_s = 3.6$; $u_1^* = 980$; $T_1 = 1010$; $\rho_1 = 3.25 \cdot 10^{-4}$; $p_1 = 730$; $\mu = 0.406 \cdot 10^{-3}$; $Re_s = 2.67 \cdot 10^6$; 3— $p_0 = 50$; $M_s = 3.7$; $u_1^* = 1010$; $T_1 = 1050$; $\rho_1 = 3.30 \cdot 10^{-4}$; $p_1 = 770$; $\mu = 0.416 \cdot 10^{-3}$; $Re_s = 2.79 \cdot 10^7$; 4— $p_0 = 50$; $M_s = 4.0$; $u_1^* = 1120$; $T_1 = 1160$; $\rho_1 = 3.63 \cdot 10^{-4}$; $p_1 = 930$; $\mu = 0.440 \cdot 10^{-3}$; $Re_s = 3.63 \cdot 10^7$; 5— $p_0 = 50$; $M_s = 5.6$; $u_1^* = 1640$; $T_1 = 1930$; $\rho_1 = 4.38 \cdot 10^{-4}$; $p_1 = 1880$; $\mu = 0.620 \cdot 10^{-3}$; $Re_s = 5.75 \cdot 10^7$.

In the course of our investigation we measured the density in the main stream behind the shock front up to the contact region. The measurements showed that when hydrogen or helium is used in the high-pressure chamber, the density behind the shock wave propagating in carbon dioxide, nitrogen, or argon, fluctuates 3% about the mean value ρ_1 . Toward the contact region ρ_1 remains invariable or increases within 3 to 5%. When an oxygen-hydrogen-helium mixture is used in the high-pressure chamber, the

variation pattern of the density in the plug remains the same as for hydrogen or helium, but the fluctuation increases. The fluctuation is affected by the method of igniting the oxygen-hydrogen-helium mixture. If the ignition is distributed (e.g., when a glow-lamp filament is placed along the whole high-pressure chamber), the fluctuations are a minimum.

3. DISCUSSION OF THE RESULTS

The values obtained for the boundary layer thickness in nitrogen and argon point to the existence of two growth regimes of the boundary layer behind the shock front. If the layer thickness increases according to $\delta(t) \simeq t^n$, then $n = 1/2$ for the first regime. This is realized in the present experiments for $p_0 = 10$ mm mercury.

Figures 7 and 9 give the calculated values of the boundary layer thickness $\delta_L(t)$ for an assumed fully laminar, boundary layer. The method of calculation was that used in [9]. A comparison shows that the boundary layer thickness for $p_0 = 10$ mm mercury lies within 20–30 % of the calculated value.

CONCLUSION

It was shown that for boundary-layer Reynolds numbers below $1.1 \cdot 10^6$ and $0.3 \cdot 10^6$ for the nitrogen and argon streams respectively, the variation of $\delta(t)$ agrees satisfactorily with the growth law of a fully laminar boundary layer.

Bibliography

1. Mirels, H. Restriction of the operating time of a Shock Tube due to the Turbulent Boundary Layer at the Wall.—Russian translation in *Raketnaya tekhnika i kosmonavtika*. Vol. 2, No. 1. 1964.
2. Mirels, H. Test Time in Low-Pressure Shock Tubes.—*Phys. Fluids*, Vol. 6, No. 9. 1963.
3. Dem'yanov, Yu. A. Vliyaniye pogranichnogo sloya na kharakter techeniya gaza v trube za dvizhushcheisya udarnoi volnoi (Boundary-Layer Effect on the Gas-Flow Pattern in the Tube behind a Moving Shock Wave).—*PMM*, Vol. 21, No. 4. 1954.
4. Chabai, A. and R. Emrich. Measurement of Wall Heat Transfer and of Transitions to Turbulence during Hot Gas and Rarefaction Flows in a Shock Tube.—*Dissertation Abstr.*, Vol. 19, 2629-30. 1959.
5. Marrone, P. V. and R. A. Hartunian. Thin Film Thermometer Measurements in Partially Ionized Shock-tube Flows.—*Phys. Fluids*, Vol. 2, No. 6. 1959.
6. Hartunian, R. A., A. L. Russo, and P. V. Marrone.—Boundary-layer Transition and Heat Transfer in Shock Tubes.—*J. Aerospace Sci.*, Vol. 27, No. 8. 1960.

7. Martin, W.A. An Experimental Study of the Turbulent Boundary Layer behind the Initial Shock Wave in a Shock Tube.—J. Aerospace Sci., Vol. 25, No. 10. 1950.
8. Stever, H., E. Witmer, and W. Hermann. Development of the Boundary Layer behind a Shock Wave.— In: "Boundary Layer and Heat Transfer Problems," Görtler, H. and W. Tollmien, editors. [Russian Translation 1960.]
9. Mirels, H. Attenuation in a Shock Tube due to Unsteady-boundary-layer Action.— NACA Tech. Note No. 3278. 1956.

R. G. Nemkov

A DELAY CIRCUIT FOR TRIGGERING SHOCK-TUBE RECORDING INSTRUMENTS, AUTOMATICALLY CONTROLLED BY THE SHOCK-WAVE VELOCITY

In shock-tube experiments it is sometimes necessary to vary the delay T of the trigger pulse according to some law depending on the shock-wave velocity v :

$$T = T(v). \quad (1)$$

Suppose we wish to light a flash bulb at the exact instant that a shock wave passes through a section $c - c'$ (Figure 1) of the shock tube. The simplest procedure would be to place a probe at section $c - c'$ to trigger the bulb. However, this is sometimes impossible, e.g., when the time to light the bulb (to its maximum luminosity), although stable, is too small compared with the time taken for the wave to pass the section. A probe located upstream from section $c - c'$ (cf. Figure 1) is then used, and the problem is to delay the pulse generated by it for a time

$$T(v) = \tau(v) - \tau', \quad (2)$$

where $\tau(v)$ is the time for the wave to travel a distance l ; τ' is the delay time for lighting the bulb. This problem is most simply solved by means of phantastrons.

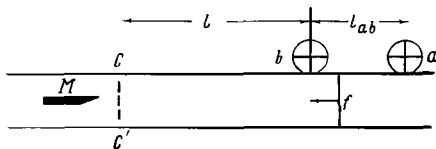


FIGURE 1. Arrangement of the probes along the shock tube:

a, b — probes; f — shock-wave front, propagating to the left; M — model placed in the section under consideration.

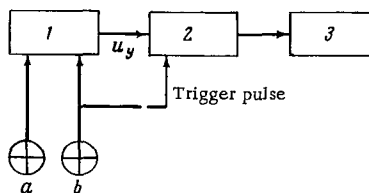


FIGURE 2. Block diagram of the delay circuit:

1—control circuit; 2—phantatron; 2—flash bulb.

Only one such study is known to us /1/. A description is given below of a delay circuit (simpler than that described in /1/, where two phantastrons are used) designed especially for shock-tube experiments.

Figure 2 represents the block diagram of this delay circuit. The delay τ_{ph} of the phantastron is a linear function of its controlling voltage (Figure 3), so that

$$\tau_{ph} = c_{ph}(u_{ph} - V), \quad (3)$$

where c_{ph} is a constant.

Suppose the control circuit (Figure 4) is also designed to memorize the wave velocity at section $a - b$ of the shock tube, in the sense that its output voltage u_y will be proportional to the passage time of the wave Δt , i. e.,

$$u_y = c_y \Delta t, \quad (4)$$

where c_y is constant.

It is seen from the block diagram that

$$u_{ph}(t) = u_{ph}^0 + u_y(t), \quad (5)$$

where u_{ph}^0 is the initial control voltage of the phantastron.

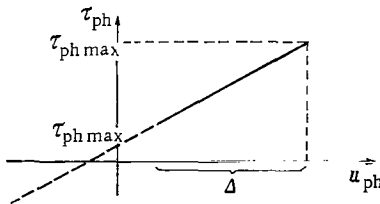


FIGURE 3. The phantastron delay τ_p as a function of its controlling voltage u_{ph} .

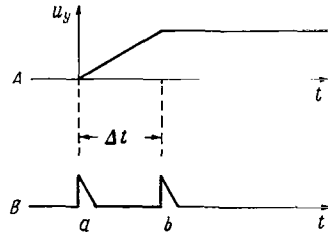


FIGURE 4. Diagram of the functioning of the control circuit:

A—output pulse as a function of time;
B—probe pulses.

The phantastron delay varies linearly with Δt . If u_{ph}^0 equals V , we obtain a delay varying according to the law $T = c/v$, where $c = c_{ph} c_y$ is some constant, obtained by selecting c_{ph} and c_y equal to 1. Finally, for values of u_{ph}^0 to the left of V , we can satisfy the given relation (2) in some region Δ (cf. Figure 3).

Figure 5 represents a schematic diagram of the delay. The signals from probes a and b are amplified in the Kandiak triggers /2/ (the tubes $T_1 T_2$ and $T_7 T_8$), which are here threshold amplifiers with an adjustable triggering threshold, starting at 0.1 v. A similar application of the Kandiak trigger is given in /3/. We have then a buffer stage (tubes T_3 and T_4), which prevents the possibility of repeated triggering from the vibration of the probes, and induction from the trigger pulse circuits. The tubes T_4 , T_5 , T_6 belong to the control circuit, and T_{10} , T_{11} to the phantastron. The constants c_{ph} and c_y in relations (3) and (4) can be altered by suitably selecting C_{ph} and R_y . The knob in the grid circuit of the trigger on tube T_4 is to set it in the initial position, indicated by MN-8. The potentiometer

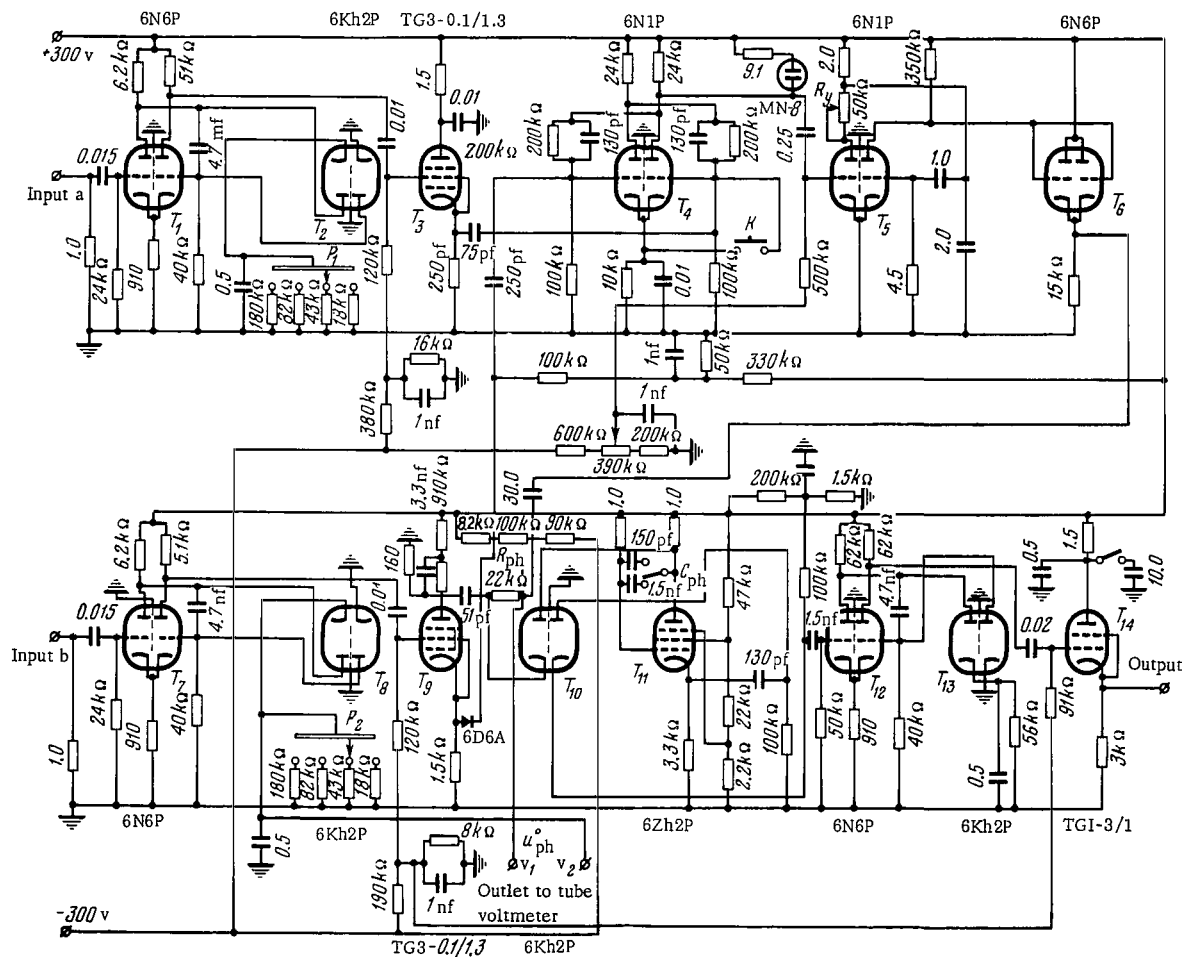


FIGURE 5. Schematic diagram of the delay circuit.

R_{ph} is to enable u_{ph}^0 to be varied. Finally, the tubes T_{12}, T_{13} form a second Kandiak trigger, triggering the output at TGI 1-3/1 (Tube T_{14}).

Such a delay was used in conjunction with Naboko in experiments on the development of the Mach line slope for flow past a half-wedge. The basic parameters of the scheme were $l = 45$ cm; $l_{ab} = 68.5$ cm; $R_y = 18$ k Ω ; $c_{ph} = 1000$ pf; $u_{ph}^0 = -10$ v; flash bulb (IFP-500); diameter of the piezocrystals 10 mm. The nonlinearity of the phantastron delay, i. e., of the function (3), and the unavoidable scatter in triggering the different parts of the circuit, are negligibly small compared with the inconstancy of the shock-wave velocity and the inaccuracy of Δt caused by the finite dimensions of the piezocrystals.

Bibliography

1. Mishin, G. P. Avtomaticheskoe upravlenie fantastronnymi skhemami zaderzhki (Automatic Control by Phantastron Delays).—PTE, No. 2. 1964.
2. Kandiak, K. A Sensitive Pulse Trigger with a Stable Threshold.—Proc. Inst. Electr. Engrs., 101(81):2. 1954.
3. Berzin, A. K., R. P. Meshcheryakov, and R. G. Nemkov. Novaya skhema kontrolya maksimal'noi energii x-luchei (A New Scheme for Controlling the Maximum Energy of X-Rays).—Izvestiya Tomskogo Politehnicheskogo Instituta, Vol. 87. 1957.

M. V. Gusev, V. A. Gordyushin, V. D. Lobanov

PULSE COUNTING CHRONOMETER FOR SHOCK-VELOCITY MEASUREMENTS

Many problems are being studied with apparatus employing shock waves in gases. The gas state behind the shock wave is calculated from the conservation laws, using the initial pressure p_0 in front of the shock wave (measured in each experiment) and the shock velocity V_0 .

The shock velocities are mostly determined by recording the change in pressure, temperature, or illumination in a shock wave as it passes by sensors [1]. The pulses from two sensors positioned along the path of the shock wave are recorded by an oscilloscope or a chronometric device of the IV-13M type. The average speed is calculated from the time interval between the pulses and the distance between the sensors.

A determination of the time interval by the sweep of the oscilloscope or a chronometric device is linked with the development of the photographic materials and their analysis under a microscope. Thus, information concerning the operational regime of the device during the experiment cannot be obtained during the experiment itself. To eliminate this shortcoming, there has been much laboratory experimentation in designing instruments which permit the time interval between pulses to be obtained during the experiment [2, 3].

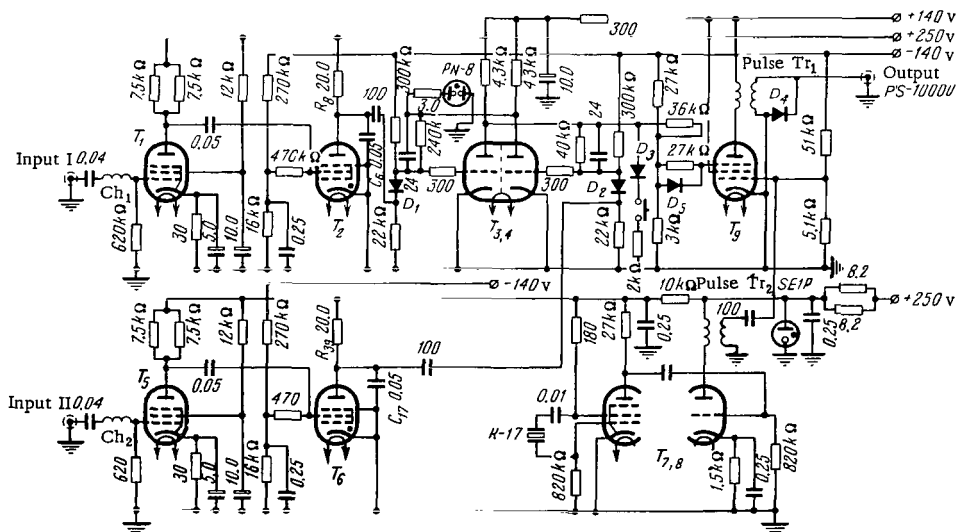


FIGURE 1. Principal schematic diagram of pulse-counting chronometer.

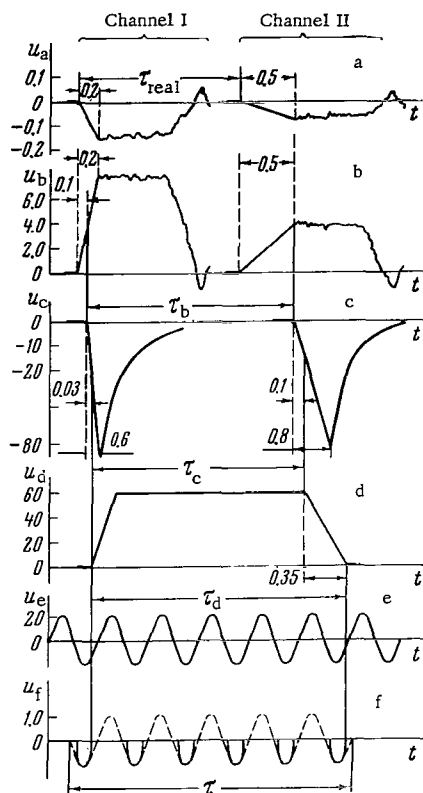


FIGURE 2. Diagram of the output voltage from the instrument blocks:

a—shape and characteristics of the signals of the piezoelectric pressure sensors; b—amplifying stages (T_1 and T_5 —6E5P); c—pulse-shaping stages (T_1 and T_6 —TGI—0.1/1.3); d—trigger (T_3 and T_4 —6N6P); e—regulated generator (T_7 and T_8 —6F1P); f—coincidence circuit (T_9 —6Zh2P).

arriving at the trigger (Figure 2, d), the signals from the thyratrons alternately open it up (Channel I) and cut it off (Channel II) with their leading edges. A rectangular voltage pulse arises at the trigger output and opens up the coincidence circuit (Figure 2, f). At this moment, the coincidence circuit becomes passable for sinusoidal oscillations of frequencies 1 MHz coming from the generator. This generator is regulated by a quartz resonator of the K-17 type (Figure 2, e). Negative pulses of duration $0.4\mu\text{sec}$ and repetition frequency 1 MHz are obtained at the output of the coincidence circuit and recorded by the PS-10000 scaler.

Piezoelectric transducers, which were designed in our laboratory [4], are now being used as a pulse-counting chronometer, and the pulse counter used here is the standard scaler of the PS-10000 type.

The chronometer counts the pulses with a frequency of 1 MHz which arrive between two pulses from the piezoelectric transducers; it is a two-channel electronic shaper of the pulses from the piezoelectric transducers into rectangular pulses, which are equal in length to the time interval between the leading edges of the pulses from these sensors.

The principal schematic design is shown in Figure 1. The voltage diagrams (by blocks) of this design (Figure 2) clarify the operational procedures of the blocks and their functions.

The signals from the sensors (Figure 2, a) at the separating inputs of Channels I and II open up the thyratrons of the shaping blocks (Figure 2, c) by their leading edges after amplification in the first cascade (Figure 2, b). As a result of thyatron shaping, the instrument effects a single operation during the discharge time and pileup of the capacitance charge $C_{6,17}$ at the anodes T_2 and T_6 . This time is regulated by the proper selection of $R_{8,38}$ and $C_{6,17}$, so that it is much longer than the time for a signal from the piezoelectric sensor, i. e., the time for attenuation of the wave processes in the shock tube. On

MEASUREMENT ERRORS

The systematic error of a pulse-counting chronometer with an internal generator is determined by the discrepancy with the real frequency of the generator taken for the frequency readings.

This discrepancy depends mainly on the tuning precision of the generator and the temperature coefficient of the frequency drift. For a generator with shock-wave excitation of oscillations, the tuning becomes a rather tedious matter, and requires very precise apparatus.

Therefore, we selected a generator which is regulated by a high-precision K-17 quartz resonator.

The K-17 quartz resonator has the following parameters: natural frequency $f = 10^6 \text{ Hz} \pm 7 \text{ Hz}$; temperature coefficient $+1.0 \cdot 10^{-6} \text{ Hz} \cdot \text{deg}^{-1}$ in the range $20-50^\circ$. With these parameters, an error of $1 \mu\text{sec}$ is possible in measuring a time interval of $10^6 \mu\text{sec}$, due to the difference of $\pm 7 \text{ Hz}$ between this frequency and the calculated one. The systematic error due to a change in temperature of the crystal up to 50° is less than $+1 \mu\text{sec}$ for each second of the measured time interval. No special means were taken in this case to stabilize the temperature of the quartz resonator, except for removing it from possible heat sources. The measurements showed that the temperature of the chassis near the resonator did not exceed 40°C . This provided the basis on which to disregard errors of the generator in measuring time intervals up to $10^3 \mu\text{sec}$.

Random errors of the chronometer are determined according to the stability of the stage signals, in both voltage potential and duration of the leading edge, since the stages of the device trigger the input pulses from the leading edges (see Figure 2).

The piezoelectric transducers for triggering both channels of the chronometer eliminate untimely actuation of either channel.

The random error for this circuit is determined by the ratio between the input voltages and the triggering thresholds in stages, as well as the discrepancy in the durations of the leading edges of the input voltages.

In determining the error, the triggering threshold of each stage is calculated according to the technological characteristics of the tubes used. The power bands of the transducers, which depend on the regime in the shock tube, are measured by a cathode-ray oscilloscope, the IO-4.

The deviation in the durations of the leading edges are measured by determining the input voltages in stages.

As for the first amplifying stages of both channels, it was understood that they transmit the leading edge of a pulse from the sensor without distortions, since the pass band of the amplifier is 5 MHz , which is much greater than the frequency corresponding to the leading edge of the input pulse (about 3 MHz).

For the shaping block, the thyratrons were identical in triggering threshold. The possible deviation in the potentials of the sensors was $\pm 25 \%$. In this respect, the duration of the leading edge depended on the speed V_0 of the shock wave, and varied from 0.35 ± 0.15 to $0.15 \pm 0.1 \mu\text{sec}$ for $V_0 = 1000$ and 4000 m/sec , respectively. The time τ_{rel} between the beginning of the leading edges of the pulses at the input of the amplifiers of both channels was taken as the real time. These pulses pass through the amplifying stage without distortions. Since all subsequent blocks actuate

the input pulses from the leading edges, the delays in the actuation of the first channel produce a negative error, while those of the second channel produce a positive error.

The variations in the delay for both channels are determined, not only by the duration t of the leading edges, but also by the ratio k between the output voltage of each stage and the triggering threshold of the subsequent stage.

Thus, the absolute error, e.g., for the shaping stage, is expressed as follows:

$$\pm \Delta \tau = \pm \Delta \tau_a - \frac{t_{Ib} \mp \Delta t_{Ib}}{k_{Ib}} + \frac{t_{IIc} \pm \Delta t_{IIc}}{k_{IIc}},$$

where the subscripts a, b, c, etc., denote the stages; subscripts I and II refer to the channels of the design; t is the duration of the leading edge of a pulse; Δt is the deviation in the duration of the leading edge; $k = U_{in}/U_{th}$, where U_{th} is the triggering threshold of the stage and U_{in} is the voltage at its input.

Let us write the expression for the absolute error of the blocks, from the amplifying to the trigger stage, and then examine the effect on the error of the shortness of the measured time interval for the period of oscillations of the generator.

The absolute error for the stage from a to d is

$$\begin{aligned} \pm \Delta \tau = & \pm \tau_a - \frac{t_{Ib} \mp \Delta t_{Ib}}{k_{Ib}} + \frac{t_{IIb} \pm \Delta t_{IIb}}{k_{IIb}} - \frac{t_{Ic} \mp \Delta t_{Ic}}{k_{Ic}} + \\ & + \frac{t_{IIc} \pm \Delta t_{IIc}}{k_{IIc}} - \frac{t_{Id} \mp \Delta t_{Id}}{k_{Id}} + \frac{t_{IIId} \pm \Delta t_{IIId}}{k_{IIId}}. \end{aligned}$$

When $\Delta \tau_a = 0$ and the values of $t, \pm \Delta t$ and k are those presented in the Table for $V_0 = 1000 - 4000$ m/sec (respectively), we can calculate the values of $\pm \Delta \tau$.

TABLE

Stage	Sign of error	$t, \mu\text{sec}$		$\Delta t, \mu\text{sec}$		ChI	ChII
		$V_0 = 1000$ m/sec	$V_0 = 4000$ m/sec	$V_0 = 1000$ m/sec	$V_0 = 4000$ m/sec		
b	+	0.35	0.15	0.15	0.1	2.0	1.0
	-					1.0	2.0
c	+	0.7	0.7	0.1	0.1	5.35	5.35
	-						
d	+	0.25	0.25	0.1	0.1	∞	1.0
	-						

Since the duration of a rectangular pulse from the trigger is considered as the time between the appearance of the beginning of the leading edge and the end of the trailing edge, $t_{Id} = 0$. The values presented above (measured for many experiments) permit us to calculate the following for shock-wave velocities of 1000—4000 m/sec:

$$\Delta \tau_{\max} = \begin{cases} + (0.788 - 0.612) \\ - (0.287 - 0.112) \end{cases} \mu\text{sec}.$$

Considering that the electronic tube (Stage f) is open the entire time from the beginning of the leading edge to the end of the trailing edge of a trigger signal, as well as the fact that only the negative part of the sine-wave of the generator is transmitted in the PS-10000 device, we can expect a difference between the measurable and measured time of one pulse in the scaler, with a maximum random error of $\Delta\tau_{\max} = \begin{cases} +0.788 \\ -0.287 \end{cases} \mu\text{sec}$, since $\Delta\tau_{\max} < T$ is the period of the oscillations of the generator.

Thus, for any measurable time interval, the maximum possible random error is $\pm 1 \mu\text{sec}$. The relative error δt in this case is a value connected linearly with the measurable time, and is equal to 1 % for an interval of $100 \mu\text{sec}$.

Bibliography

1. Rakhmatulin, Kh. A. and S. S. Semenova, editors. Sbornik "Udarnye truby" (Shock Tubes).— I. L. 1962.
2. Boronin, A. P. and T. G. Ignat'eva. Impul'snye zondovye izmereniya v udarnoi trube (Pulse Probing Measurements in Shock Tubes).— Sbornik "Fizicheskaya gazodinamika i svoystva gazov pri vysokikh temperaturakh," Moskva, Izdatel'stvo "Nauka." 1964.
3. Kabanov, G. L. Izmerenie skorosti udarnykh voln v razryzhennykh gazakh (Shock-velocity Measurements in Rarefied Gases).— Sbornik "Fizicheskaya gazodinamika i svoystva gazov pri vysokikh temperaturakh," Moskva, Izdatel'stvo "Nauka." 1964.
4. Guser, M. V. and O. I. Luneva. P'ezoelektricheskii datchik davleniya (Piezoelectric Pressure Sensors).— Sbornik "Issledovaniya po fizicheskoi gazodinamike," Moskva, Izdatel'stvo "Nauka." 1965.

M. V. Gusev, V. D. Lobanov, V. A. Gordyushin

AN INSTRUMENT FOR CONTROLLING THE HIGH-SPEED PHOTORECORDING OF THE PHASES OF A PROCESS

High-speed Schlieren photography of flow patterns associated with shock waves necessitates the use of triggered photorecorders, since the ordinary high-speed SFR photorecorder cannot be synchronized with a shock-wave formation process. When the SFR is used, photographs are taken at the chance coincidence of two processes: the arrival of the shock wave in the experimental section, and the rotation of the SFR mirror into position when the image of the experimental section is incident on one of the SFR frames. Simultaneously, a third process must take place, namely, the opening of the SFR shutter, if a constant light source is used in the Töpler arrangement, or the flash bulb operation, whose flash duration τ must be less than the period T of rotation of the SFR mirror.

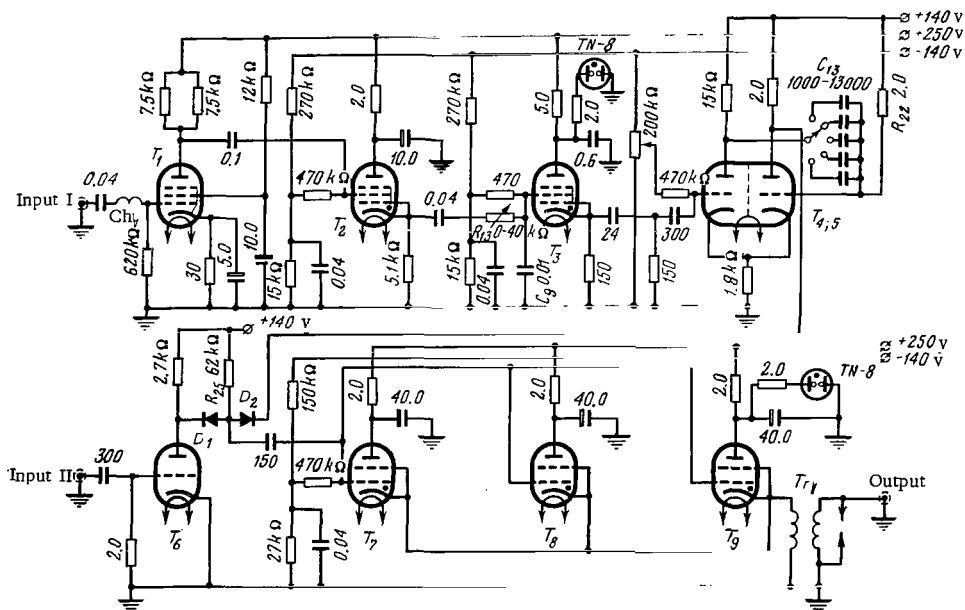


FIGURE 1. Basic diagram of the instrument.

The use of SFR recorders under the probability recording conditions described above is efficient if the recording probability is sufficiently high. The recording probability depends on the rpm of the mirror, and the number of frames considered sufficient for evaluating the phase being studied [1, 2]. When studying expanding flows in a shock tube we used the

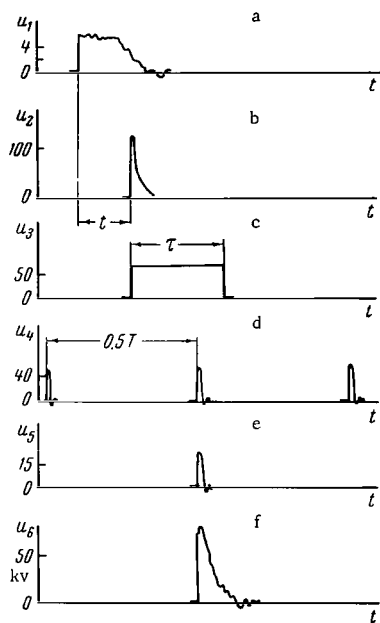


FIGURE 2. Diagram of the output voltage from the instrument blocks:

a—amplifying stage (T_1 —6E5P); b—thyatron stage for shaping and delaying the pulse (T_2 and T_3 —TGZ—0.3/1.3); c—multivibrator ($T_4, 5$ —6N1P); d—phase-shifting stage (T_6 —6N6P); e—coincidence circuit (D_1, D_2, R_{25}); f—thyatron stage of the control pulse (T_7, T_8, T_9 —TGI—0.3/1.3).

mirror (Figure 2, d), a pulse of positive voltage appears at the output of the coincidence circuit (Figure 2, e), which is then used to trigger the thyatron block. As a result, a control pulse (Figure 2, f) was only obtained when the phase under observation coincided with the corresponding position of the SFR mirror. The pulse from the pickup of the SFR mirror was taken from the outlet synchronization on the SFR control panel during its functioning under controlled conditions. To bring this pulse in correspondence with the resolving pulse of the triggered multivibrator, it passed through the phase-shifting stage of the circuit (T_6 1/2 6N6P).

After its transformation in a high-voltage transformer (T_p), the control pulse triggered the flash bulb of the IAB-451 instrument (bulb IFP-500). The film in the SFR was exposed while the source was luminous.

SFR camera under probability recording conditions. The photorecorder functioned in conjunction with an electronic circuit controlling the coincidence of the process studied with the required position of the SFR mirror (Figure 1). The shock-wave position relative to the experimental section was controlled by a piezoelectric transducer [2], placed ahead of the experimental section. The pulse from the transducer was amplified in the first stage (Figure 2, a) and shaped by the thyatron stage (Figure 2, b), which also enabled the pulse to be delayed. The delay time t depends on the integrating circuit R_6C_4 and varied between 100 and $1500\mu\text{sec}$. The leading edge of the pulse overruns the triggered multivibrator. The return of the multivibrator to the initial position is determined by the time constant of the circuit $R_{17}C_{10}$ (cf. Figure 1). At the multivibrator output we obtain a rectangular resolving pulse of controllable width τ (Figure 2, c), which is selected equal to the duration of the process studied. (By delaying the pulse from the piezoelectric transducer during a time t the leading edge of the rectangular pulse has already been made to coincide with the beginning of the process phase being studied in the experimental section.)

The resolving pulse is fed to the coincidence circuit D_1, D_2, R_{25} (Figure 1), and when a pulse reaches it simultaneously from the pickup located on the SFR

The flash of the IFP-500 bulb was selected to satisfy $\tau \leq (1/2)T$, since the SFR mirror was two-way; T is the period of rotation of the mirror.

In the scheme described the beginning of recording does not have to be synchronized with the first frame, since the process studied required 10—15 frames when using one series of a two-series lens insert and an SFR mirror rotation speed of 30,000 rpm. This made it possible to dispense with additional pulse shaping from the SFR mirror pickups and, for a pulse width of $50\mu\text{sec}$, to start recording the process from any one of the first six frames (for the above rotation speed).

The flash shows whether the image of the process was incident on the film, and when necessary to repeat the experiment without having to develop the film. This was impossible previously.

Bibliography

1. Ionov, V.P., G.N. Nikolaev, M.V. Gusev, and O.I. Luneva. Izuchenie potokov gaza v udarnoi trube s pomoshch'yu skhemy Teplera i skorostnogo kadrovogo fotografirovaniya (Shock-tube Investigation of Gas Streams Using Schlieren High-Speed Frame Photography).—Sbornik "Fizicheskaya gazodinamika i svoistva pri vysokikh temperaturakh," Moskva, Izdatel'stvo "Nauka." 1964.
2. Gusev, M.V. and O.I. Luneva. P'ezoelektricheskii datchik davleniya (Piezoelectric Pressure Sensors).—Sbornik "Issledovaniya po fizicheskoi gazodinamike," Moskva, Izdatel'stvo "Nauka." 1965.

V.M.Eroshenko, A.V.Morar, Yu.N.Terent'ev

FRONT NATURE OF THE REACTION SURFACE WITH THE MEDIUM

A new theory of heat propagation in chemically reacting media was suggested by Mikhel'son /1/ and developed by Predvoditelev /2, 3/, who found a method of studying self-consistent combined processes.

The method resolves existing difficulties in analyzing heat and mass exchange between the surrounding medium and a solid, on whose surface a reaction of material takes place (sublimation, erosion, fusion, combustion, etc.). The different phenomena are combined and proceed as a front, as, e.g., wave processes. The somewhat unusual physical model of front processes is based on the experimental fact that in such phenomena one can always find a surface whose displacement obeys the laws of motion of a wave front. Such a surface could be the isothermal surface on which material reaction takes place. Its motion obeys not the laws of smoothing processes, such as Fourier's law, but the laws of motion of a front, such as Huyghen's principle.

The concept of a front is considerably wider than that of a wave. A front was found to be formed only when heat transfer or diffusion of mass is accompanied by some additional processes, combined with the main transfer processes. A study of front processes enables quantitative and qualitative relations to be established between the quantities controlling the reaction rate of the material and the geometry of the reaction surface; the analysis is conducted in a region immediately adjacent to the reaction surface. To determine the distribution of transformed material or latent-heat liberation during the reaction, but far from the reaction surface, boundary-value problems must be formulated. Thus, the problem considered involves the formulation of two basically different mathematical problems. In our opinion, a complete solution of this problem cannot be determined by boundary-value problems alone.

We shall consider Predvoditelev's method in more detail. Excluding the equilibrium states, all the natural phenomena can be represented by two basically different processes, namely, propagation and smoothing. The latter process is studied by introducing the concept of a surface of equal states; the isothermal surface for heat-smoothing processes, the surface of equal concentrations or densities for material-diffusion processes, etc. The motion of such surfaces obeys parabolic partial differential equations. Neither the medium properties nor its state suffer a discontinuity across a surface of equal states, even for discontinuous initial values. Quite different are surfaces of equal states appearing as a propagation process develops, i.e., the fronts of a wave transfer. They represent possible

discontinuity surfaces in the medium state on which the initial discontinuities are conserved during the entire development time of the process. The front surface is characteristic for some wave propagation, and its motion is described by a Hamilton-Jacobi partial differential equation. The solution is based on Huyghen's idea that at any instant of time the wave front propagating from a source may be regarded as the envelope of the fronts of spherical waves originating from different points of the initial surface. The interpretation of the front as the envelope of a given family of surfaces leads to Monge's representation of the front surface as consisting of the contact lines of the enveloping surface with the enveloped surfaces. The equation of the enveloping surface, which moves in space and is the front of some propagation process, can be written as

$$\xi = V(xyz) + gt; \quad (1)$$

$\xi = \text{const}$ represents a continuous set of wave surfaces. An arbitrary function $\Phi(\xi)$ defines a continuous sequence of surfaces selected from this set, and satisfies a system of partial differential equations describing the waves. This function enables the normal displacement velocity of the front surface to be found in the form

$$g_{\xi} = - \frac{\partial \xi}{\partial t} / |\vec{\nabla} \xi| = - \frac{g}{H_v}, \quad (2)$$

where H_v is the first scale factor of the function $V(x, y, z)$.

The displacement velocity of the front is easily found from the wave equation describing the wave process. However, some phenomena can be described by the model of wave processes propagating in a front, but which are treated by heat-conduction or diffusion equations describing smoothing processes.

Consider the reaction surface of a material in combined processes. Let the equation of heat conduction from a source and the general equation of kinetics of an additional process be given. We transform the given system of differential equations to the variable ξ , and then solve them relative to the normal front velocity given by (2). Using physical considerations, the quantitative relations of the different processes are established, e.g., between the temperature and quantity of transformed material. The system of equations is therefore reduced to an ordinary equation for the function $g_{\xi} = -g/H_v$, which is then analyzed. This program is now applied to the dynamic melting of solids in a gas-dynamic stream. The heat propagation during melting must obey

$$\left. \begin{aligned} c_v \rho (\partial T / \partial t) &= k \Delta T + q (\partial M / \partial t), \\ \partial M / \partial t &= f(M). \end{aligned} \right\} \quad (3)$$

The first equation of this system is the equation of heat conduction from a source, where q designates the specific heat liberated or absorbed during the transformation of 1 g solid material; the second equation controls the reaction rate of the material, M representing the quantity of transformed phase of the material per unit volume. A combined process

is regarded as one in which the basic quantities determining it are interrelated. In our case these are the temperature T and mass M . Therefore, in combined processes they must be connected by the functional relationship dM/dT , which is always assumed to exist in these processes. Assumptions relative to higher order derivatives will be made later. The first of equations (3) now takes the form

$$\partial T / \partial t = (a / \alpha) \Delta T, \quad (4)$$

where $a = k/c_v \rho$ is the thermal diffusivity, and

$$\alpha = 1 - \frac{q}{c_v \rho} (dM / dT). \quad (5)$$

Since a frontal character has been assumed, all the quantities characterizing the process will depend on the curvilinear characteristic ξ . Transforming to the variable ξ [4], we obtain

$$g_\xi = - \frac{a}{\alpha} \left(\frac{\Delta V}{H_v} - H_v P \right), \quad (6)$$

where we have used relation (2) and introduced the notation

$$P = \left(\frac{d^2 T}{d\xi^2} / \frac{dT}{d\xi} \right). \quad (7)$$

In view of the existence of the first derivative of M , we can rewrite the second equation of (3) as

$$\frac{dM}{dT} \frac{\partial T}{\partial t} = f(M). \quad (8)$$

Differentiating (8) with respect to time, this equation becomes

$$\frac{d^2 M}{dT^2} \left(\frac{\partial T}{\partial t} \right)^2 + \frac{dM}{dT} \left(\frac{\partial^2 T}{\partial t^2} \right) = \frac{df}{dM} \frac{dM}{dT} \left(\frac{\partial T}{\partial t} \right). \quad (9)$$

To simplify the following analysis, we shall make assumptions about the value of the second derivative of M with respect to T . If melting has not started, no relation exists between the temperature T and mass M . These two quantities become related only when melting commences. Suppose the point in the (M, T) -plane corresponding to the initial time is an inflexion point of the function $M = M(T)$. The following condition must then be fulfilled:

$$d^2 M / dT^2 = 0. \quad (10)$$

If (10) holds throughout melting, (9) can be replaced by

$$\partial^2 T / \partial t^2 = \frac{df}{dM} (\partial T / \partial t). \quad (11)$$

Transforming (11) to the variable ξ , and using (2) with notation (7), we obtain

$$P g_\xi H_v = - \frac{df}{dM}. \quad (12)$$

Hence, equation (6) becomes

$$g_{\xi}^2 + \frac{a}{\alpha} \frac{\Delta V}{H_v} g_{\xi} + \frac{a}{\alpha} \frac{df}{dM} = 0, \quad (13)$$

where df/dM is determined by the kinetics of the reaction.

The quadratic equation (13) is solved for g_{ξ} :

$$g_{\xi} = -\frac{1}{2} \frac{a}{\alpha} \frac{\Delta V}{H_v} \left(1 + \sqrt{1 - 4 \frac{a}{\alpha} \left(\frac{H_v}{\Delta V} \right)^2 \frac{df}{dM}} \right). \quad (14)$$

The minus sign before the radical has been discarded, since it is physically meaningless under certain conditions. In fact, the phenomenon can exist even if the derivative df/dM vanishes. When the sign before the radical is negative the equality $df/dM=0$ leads to the vanishing of the velocity g_{ξ} as well, which is inadmissible.

We now assume that

$$\frac{\alpha}{a} \left(\frac{H_v}{\Delta V} \right)^2 \frac{df}{dM} \ll 0.25, \quad (15)$$

i.e., the second term under the radical can be neglected.

This inequality is satisfied if any one of the cofactors of (15) is small. The value of each can be determined for the particular phenomenon considered. Thus, if (15) is valid, then

$$g_{\xi} = -\frac{a}{\alpha} \frac{\Delta V}{H_v}. \quad (16)$$

We shall represent the quantity α in a more convenient form. If the unit volume of material did not consume latent heat of transformation in its transition to the liquid phase, the material would heat to a temperature T_q given by

$$\rho q = c_v \rho (T_q - T_0), \quad (17)$$

where T_0 is the initial temperature.

Under the action of the gas-dynamic stream a certain quantity ΔM of transformed material is detached from this unit volume, taking with it $q\Delta M$ calories of heat. This quantity is completely restored as a result of melting, and the volume of material will remain unchanged and heat to the stagnation temperature of the stream T_{00} . The corresponding quantity of heat is $c_v \rho (T_{00} - T_0)$. Here and in the following, we use mean values of the specific heat and density. The energy balance equation is

$$c_v \rho (T_q - T_0) - c_v \rho (T_{00} - T_0) + q\Delta M = 0. \quad (18)$$

Hence,

$$[(T_q - T_0)/(T_{00} - T_0)] = 1 - \frac{q}{c_v \rho} \frac{\Delta M}{(T_{00} - T_0)}. \quad (19)$$

For the complete removal of the transformed material by the gas-dynamic stream, no considerable error is introduced if we take

$$\alpha \approx \frac{T_q - T_0}{T_{00} - T_0}. \quad (20)$$

Consider now the conclusions which can be drawn about the motion of a surface of given initial geometry. If we consider a spherical body, we have

$$r = \sqrt{x^2 + y^2 + z^2}. \quad (21)$$

For this function the first and second scale factors are respectively

$$H_v = 1; \quad \Delta V = \frac{2}{r}. \quad (22)$$

Allowing for (22), equation (16) can be written as

$$g_{\xi} = -(2a/\alpha r). \quad (23)$$

For a spherically symmetric body, g_{ξ} clearly represents the rate of variation of its radius, i.e.,

$$g_{\xi} = \frac{dr}{dt} = -(2a/\alpha r). \quad (24)$$

Hence, simple transformations yield

$$\frac{d(4\pi r^2)}{dt} = (dS/dt) = -\frac{16\pi a}{\alpha}, \quad (25)$$

where S is the surface area of the spherical particle.

If the values of a and α are substituted, then

$$\frac{dS}{dt} = -\frac{16\pi k}{c_v \rho} \left(\frac{T_{00} - T_0}{T_q - T_0} \right). \quad (26)$$

It follows that for condition (15), constant values of k , c_v and ρ , and steady gas flow past the spherical particle, the reaction surface area of the material varies at a constant rate. This was established experimentally in 1882 by the Russian scientist Sreznevskii /4/ while studying the evaporation rate of liquid drops. He established that the evaporation rate from a unit surface of the drop is inversely proportional to the drop radius, and that the rate of change (decrease) of the drop surface is constant, i.e., $dS/dt = \text{const}$. The applicability of Sreznevskii's law to all natural phenomena preceded by a front will be established below. This law will be considered as governing the strong physical interaction of two combined processes: heat transfer in a solid, and the transformation of material on its surface with heat liberation or absorption.

We shall now prove Sreznevskii's law by a different procedure. The reaction surface of the material can move in space, varying its area according to a linear law for constant or variable curvature. Only experiments can show whether this is realized in practice. A specific formula

can however be derived theoretically. Consider a spherical body, for which equation (14) (allowing for (22)) becomes

$$\frac{dr}{dt} = -\frac{a}{\alpha r} \left(1 + \sqrt{1 - \frac{\alpha}{a} \frac{df}{dM} r^2} \right). \quad (27)$$

Integrating and performing a number of elementary transformations, we obtain

$$\psi(r) = \psi(r_0) \exp \left\{ \frac{df}{dM} t \right\}, \quad (28)$$

where

$$\psi(r) = \frac{\{\exp \sqrt{1 - \beta r^2}\}}{1 + \sqrt{1 - \beta r^2}} \quad (29)$$

and

$$\beta = \frac{\alpha}{a} \frac{df}{dM}. \quad (30)$$

If (15) holds as before, i. e., βr^2 is small compared with unity, then

$$\sqrt{1 - \beta r^2} = 1 - \frac{1}{2} \beta r^2 - \frac{1}{8} (\beta r^2)^2 - \dots, \quad (31a)$$

$$\exp \left\{ -\frac{1}{2} \beta r^2 \right\} = 1 - \frac{1}{2} \beta r^2 + \frac{1}{8} (\beta r^2)^2 - \dots \quad (31')$$

If the first two terms of (31a) and the first three of (31') are retained and substituted in (29), then

$$\psi(r) = [\exp (4 - \beta r^2) / 8]. \quad (32)$$

Hence, equation (28) can be transformed to the form

$$r^2 = \frac{4a}{\alpha j} - \left(\frac{4a}{\alpha j} - r_0^2 \right) \exp \{jt\}, \quad (33)$$

where $j = (df/dM)$, and expression (30) replaces β .

Expressing equality (33) in terms of the surface S of the sphere, we obtain

$$S = \frac{16\pi a}{\alpha j} - \left(\frac{16\pi a}{\alpha j} - S_0 \right) \exp \{jt\}. \quad (34)$$

For sufficiently small values of the product jt the exponential function in expression (34) can be expanded in a series. This results in the approximate equality

$$S = S_0 - Gt, \quad (35)$$

where

$$G = \left(\frac{16\pi a}{\alpha} + S_0' \right). \quad (36)$$

Equation (35) expresses Sreznevskii's law, i. e., the linear relationship between the body surface and time. This derivation enables another law to be derived which is obeyed under definite conditions by the motion of the reaction surface of the material.

Expression (36) yields the following value of the initial Gaussian curvature of the surface of a spherically symmetric body:

$$\frac{4\pi}{S_0} = \frac{1}{r^2} = \frac{j}{(G/4\pi) - 4(a/\alpha)}. \quad (37)$$

This equation implies that if the phenomenon under observation develops according to Sreznevskii's law, the reaction rate of the material varies such that the Gaussian curvature of the surface remains constant. This can be realized only if there exists a plane dividing the sphere into two parts, in which the material is transformed at different rates. This is observed in the presence of natural convection, or when the material reaction takes place in a moving medium. The integration of (27) is possible only when α is independent of the radius r of the spherical particle. The Sreznevskii law is therefore more general than the conservation law of the Gaussian curvature of the reaction surface, and can be satisfied in the form of (26), while the Gaussian curvature of the surface can vary.

There is one corollary from the laws established, concerning the geometry of the moving reaction surface of the material. Gauss' famous theorem asserts that the total (Gaussian) curvature of the surface depends only on the linear elements (and their first- and second-order derivatives) on the surface, and therefore does not change with the deformation of the surface. It follows that every surface of constant Gaussian curvature is applicable to (can be deformed into) any other surface of the same curvature. We recall that two surfaces S and S^* are isometric, i. e., the surface S is applicable to the surface S^* (or S^* represents a deformation of S) if their line elements are equal. It follows from Gauss' theorem that developable surfaces (surfaces enveloping the ∞ -family of tangent planes to a space curve), cones, and cylinders are applicable to a plane. Thus, since the material transformation takes place under specific conditions, fulfilling the Sreznevskii law and conserving the Gaussian curvature of the surface, the motion of the reaction surface can be represented as an uniform and continuous deformation of the whole surface or individual parts of it. If the solid possesses spherical symmetry, the surface is transformed with time in such a way that symmetry will be preserved for the front and back of the surface, subject to different exchange conditions with the surrounding medium. For bodies of conical, cylindrical, or any other developable surface the dynamic transformation of the material will proceed such that even when Sreznevskii's law is obeyed and the Gaussian curvature is conserved for the whole surface or its individual parts, the body shape can be altered substantially by deformation (e.g., transformed into a plane).

The results listed represent only some of the advantages of the proposed model, whose simplicity considerably facilitates the study of many phenomena of various combined processes.

The theoretical model proposed does not contradict published data or our own experimental results, which are considered below.

One of the first papers emphasizing the importance of Sreznevskii's law was /5/, where the law was applied to the evaporation kinetics of liquid drops and volatile solid bodies. Zubkov /6/ observed the evaporation kinetics of naphthalene and camphor spheres, over an air-velocity range of 0.5—10 m/sec, and air temperature of 15—120°. These air temperatures enabled both pure sublimation and evaporation through a liquid phase to be studied. The investigations showed that there is no difference between the evaporation kinetics of naphthalene in liquid and solid phases, i. e., that although the decrease in material per unit time is different, the process is the same qualitatively. This is understandable in the frame of the model discussed. Figure 1 shows consecutive stills of an evaporating naphthalene sphere. The evaporation proceeds at different rates on different portions of the surface. A zone of minimum evaporation rate is clearly visible, and it divides the surface of the sphere into front and back parts. The zone of minimum evaporation is situated where the impinging stream divides. By observing the shape of the front and back parts, the naphthalene was seen to evaporate at different but comparable rates. According to Zubkov's data, in a first approximation, both the front and back parts preserve a spherical shape during evaporation. In addition, Zubkov's calculations of the radii of the front and back surfaces showed that they vary linearly, i. e., following Sreznevskii's law. Similar results were obtained by Aksel'rud /7/ for compressed saltpeter spheres and sodium chloride dissolved in a liquid stream. Figure 2 represents successive stages in the dissolution of the saltpeter spheres. A comparison of Figures 1 and 2 indicates that both processes obey the same law.



FIGURE 1. Successive stills of the evaporation of naphthalene spheres for low subsonic speeds of the air stream.

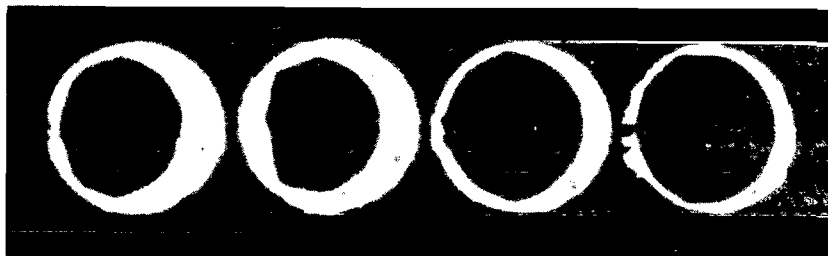


FIGURE 2. Successive stages in the dissolution of saltpeter spheres:
Aksel'rud's experiments.

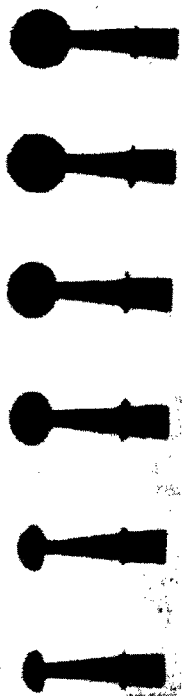


FIGURE 3. Typical shapes of naphthalene spherical models during sublimation in a subsonic stream.

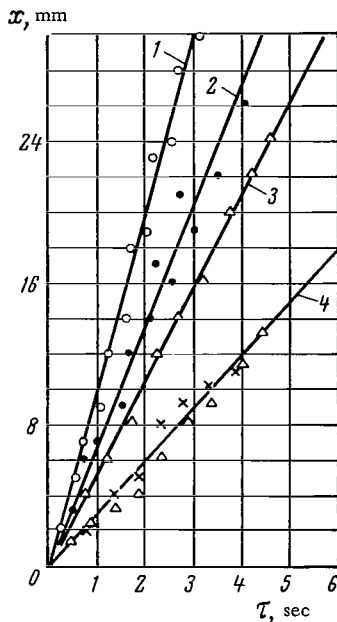


FIGURE 4. Displacement of the stagnation point of lead conical models, as a function of time in a gas-dynamic stream:
1—cone with apex angle 10° ; 2— 20° ;
3— 30° ; 4— 40° .

The authors of this paper conducted experimental studies of the sublimation of naphthalene models for air speeds between 50 and 270 m/sec (subsonic speeds) and Mach numbers $M=1.7$ (supersonic speeds), and stream stagnation temperatures between 60 and 150°C . The results showed that the sublimation of the spherical particles obeys Sreznevskii's law, and that the Gaussian curvature of the front part of the surface is conserved. The center of the radius of curvature moves according to a linear law. The air stream at the back part of the spherical model was considerably disturbed by the holder; we have accordingly refrained from analyzing this part of the model. Figure 3 shows typical shapes of naphthalene spherical models during sublimation at high subsonic speeds of the gas. The shape of the models remains qualitatively unchanged during their sublimation in a supersonic stream. The surface variation of the front part of the sublimating model are presented in the following paper [8].

Donald [9] described the melting of hemispherical ice models in a hot humid air stream, and pointed to the linear displacement of the leading stagnation point. His photographs of the process show that the dynamic transformation of the material is preceded by a front in accordance with

Sreznevskii's law, and conserves the Gaussian curvature of the melting surface.

We conducted experiments on the melting of cylindrical ice models with hemispherical heads, placed lengthwise in a water stream. Sreznevskii's law was obeyed, and the Gaussian curvature of the hemispherical nose surface and the cylindrical part of the model surface was conserved.

The numerous experiments conducted at the Power Institute im. Krzhizhansvskii on the melting of various metals and alloys in gas-dynamic streams corroborate the front character of the displacement of the reaction surface. The shortening of the conic sample along its axis obeyed a linear function of time, undisturbed by the variation in cone angle. If the cone length versus time is plotted, a straight line is obtained whose slope decreases with increasing cone angle (Figure 4).

Experimental characteristics of the dynamic melting and sublimation of axisymmetrical bodies, data on the contraction of the models, and values of the radius of the models' noses are given in /10/. The varying geometry of the reaction surface of the material draws attention to the complex interconnected processes taking place. The approximate theoretical calculation of the reaction surface does not, in our opinion, elucidate the true development mechanism of the investigated phenomenon. Stetson's results seem to indicate that the phenomenon of dynamic melting and sublimation developed according to the model of front dynamic processes.

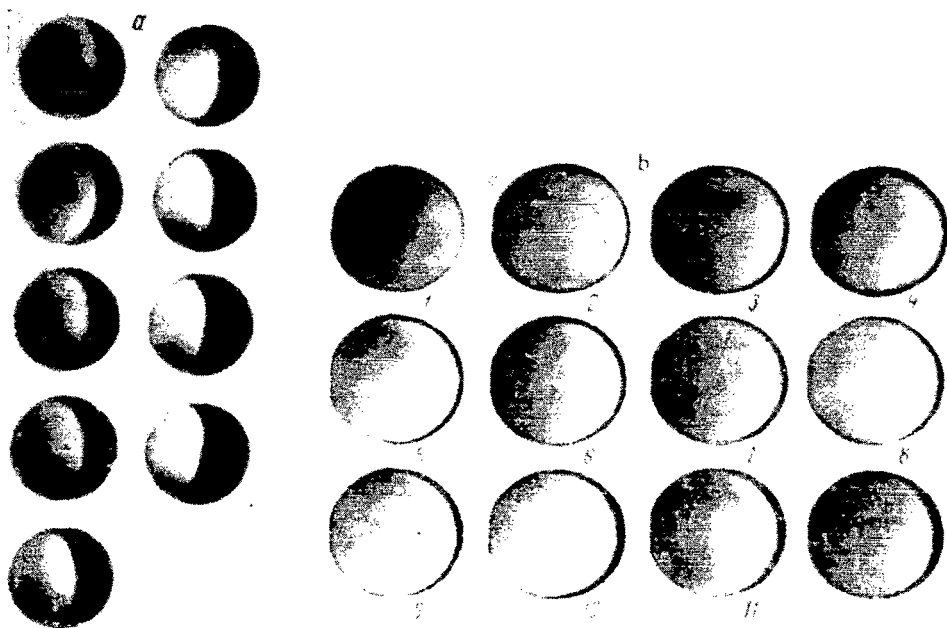


FIGURE 5. Successive stages in the burning of a coal particle :

a—sphere $\phi 7$ mm in an oxygen stream: $M = 1.3$; $T^* = 820^\circ\text{C}$. Time interval 0.5 sec between the stills;
b—sphere $\phi 7$ mm in an air stream; $M = 3$; $T^* = 870^\circ\text{C}$. Time interval 5 min between the stills.

We conducted an experimental study of the combustion of spherical and cylindrical coal particles in a supersonic air and oxygen stream for $M = 1.3-3.5$ and stream stagnation temperatures between 780 and 950°. The results (Figure 5) show that the model of front processes is also applicable to combustion processes. The area of the reaction surface of the spherical coal particle varied linearly with time; it was also established that the Gaussian curvature is conserved on the front and back parts. These observations are illustrated in Figures 6 and 7. The results obtained are qualitatively similar to those of Blinov and Khaikin on the combustion of carbon in low-speed gas streams. Their results are discussed in detail by Predvoditelev /3/ from the viewpoint of front processes.

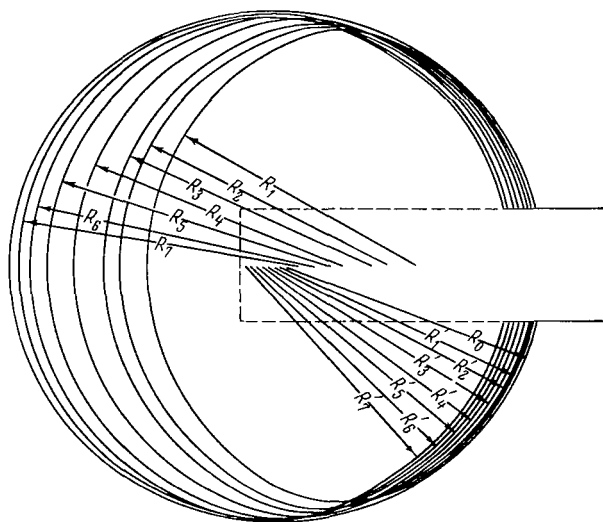


FIGURE 6. Outlines of the successive combustion stages of a sphere in a supersonic oxygen stream:

$M = 1.4$; $T^* = 820^\circ\text{C}$.

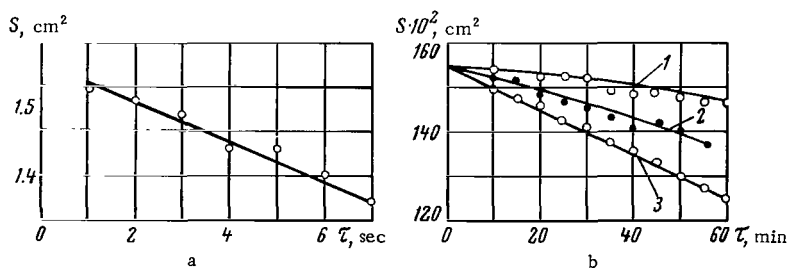


FIGURE 7. Variation in the surface area of spherical models $\phi 7$ mm from coal particles during combustion in a stream of air and oxygen:

a—oxygen; $M = 2$; $T^* = 820^\circ\text{C}$; b—air: $M = 2.5$; 1— $T^* = 820^\circ\text{C}$; 2— $T^* = 860^\circ\text{C}$; 3— $T^* = 950^\circ\text{C}$.

Of considerable interest are the experimental results on the interaction between graphite spherical bodies and a high-enthalpy supersonic stream ($M = 2.4$) of air, argon, and nitrogen /11/. The paper presents data on the stable surface shape acquired by the cylindrical graphite bodies in a plasma jet of air and two other gases at stagnation temperatures above 8000° and stream speeds about 3000 m/sec. The authors established that graphite rods rapidly acquired a stable conic surface geometry with a sharp nose, which remained invariable throughout the experiment. These results are illustrated in Figure 8. They also presented data on the contraction of the sample and the removal of transformed mass as a function of time, and showed that both phenomena are described by linear relationships. The experiments were therefore found to obey both laws of motion of the reaction surface of the material in combined processes developed by a front.

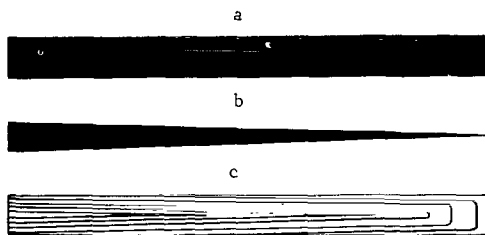


FIGURE 8. Variation in the geometry of cylindrical graphite bodies during interaction with a supersonic high-enthalpy stream of gases:

a, b—photographs of the graphite rod before and after the interaction with the gas stream; c—outline of the variation in the cylinder surface for a time interval of 1 min.

Bibliography

1. Mikhel'son, V.A. O fizicheskoi teorii plameni Bunzena (Physical Theory of the Bunsen Flame).—ZhRfKhO, Vol. 22, 3A, 1890.
2. Predvoditelev, A.S. O frontovom protsesse ispareniiya i sublimatsii sfericheskikh chastits (Front Process of Evaporation and Sublimation of Spherical Particles).—Trudy Odesskogo Gosudarstvennogo Universiteta im. I.I. Mechnikova, Seriya Fizicheskikh Nauk., Vol. 150, No. 7, 1960.
3. Predvoditelev, A.S. O gorenii sfericheskikh chastits (Combustion of Spherical Particles).—Trudy Odesskogo Gosudarstvennogo Universiteta im. I.I. Mechnikova, Seriya Fizicheskikh Nauk., Vol. 150, No. 7, 1960.
4. Sreznevskii, B.I. Ob isparenii zhidkostei (Evaporation of Liquids).—ZhRfKhO, Vol. 14, 7A, 1882.
5. Fedoseev, V.A. Kinetika ispareniiya kapel' zhidkosti (Evaporation Kinetics of Liquid Drops).—Trudy Odesskogo Gosudarstvennogo Universiteta im. I.I. Mechnikova, Seriya Fizicheskikh Nauk., Vol. 150, No. 7, 1960.

6. Zubkov, V.I. Ob isparenii sharikov tverdykh tel v potoke gaza (Evaporation of Solid Spheres in a Gas Stream).—Doklady AN SSSR, Vol. 123, No. 5. 1958.
7. Aksel'rud, G.A. K voprosu o kinetike rastvoreniya tverdoi chastitsy, dvizhushcheysya v potoke zhidkosti (Dissolution Kinetics of a Solid Particle, Moving in a Gas Stream).—Zhurnal Fizicheskoi Khimii, Vol. 28, No. 10.
8. Eroshenko, V.M. and Yu.N. Terent'ev. Analiz sublimatsii tverdykh tel v sverkhzvukovom Potoke (The Sublimation of Solids in a Supersonic Stream).—In this collection, p.196.
9. Donald, J. The Melting of Ice in a Hot Humid Stream of Air.—J. Fluid Mech., Vol. 8, part I. 1960.
10. Stetson, N. Issledovanie ablyatsii konicheskikh modelei (Investigation of the Ablation of Conic Models).—VRT, No. 2. 1966.
11. Christensen, D. and R.D. Buhler. On the Stable Shape of an Ablating Graphite Body.—J. Aero. Sci., Vol. 26, No. 1. 1959.

V. M. Eroshenko, Yu. N. Terent'ev

THE SUBLIMATION OF SOLIDS IN A SUPERSONIC STREAM

The sublimation of bodies in a supersonic stream was studied in a continuous open-circuit wind tunnel with Eiffel chamber. The air parameters in the experiments were: pressure in the stilling chamber 1 atm; static pressure in the jet $p_{st} = 0.2$ atm; Mach number $M = 1.7$. The outlet area of the De Laval nozzle was 27×27 mm. Air from the atmosphere entered an electric stove through a filter. It was then heated to the required temperature, passed through the stilling chamber and flowed out through the De Laval nozzle into the low-pressure chamber. The necessary pressure drop in the low-pressure chamber was created by RMK-4 fore-vacuum pumps. Chemically pure naphthalene was used for studying the sublimation. The selection of naphthalene was due to its intense sublimation at relatively low temperatures. To eliminate, or at least decrease to the minimum, the mechanical removal of material by the impinging air stream, models of sufficient mechanical strength were manufactured by compression in a hydraulic press at a pressure $p = 2000$ kg/cm². This method enabled them to be processed mechanically on different lathes.

The shape and dimensions of the models are given in Figure 1. Before the experiment the models were stuck on the thread end of a wooden holder. The wood acted as heat insulator and reduced the distortion of the temperature fields inside the model. To reduce the effect of the holder on the flow past the models, its thread end was made as thin as possible. Figure 2 illustrates how the models were introduced into the stream. A two-position lever was mounted in the low-pressure chamber for introducing the models in the working section of the stream. The model and the holder were kept in the refrigerator of the low-pressure chamber until the required conditions were created in the apparatus. In this way, the initial given dimensions of the model and its initial temperature could be preserved. The gas-dynamic stream was considered thermally stationary if in the course of 10 min the temperature in the stilling chamber varied by no more than 0.3°. The sublimation of the models in the supersonic stream was observed through the optical windows of the low-pressure chamber by means of an IAB-451 instrument. Simultaneously, the different stages of the process were photographed over fixed time intervals. The sublimation of the models was investigated for stagnation temperatures of 20–85°C.

Figure 3 shows Schlieren photographs of the different stages of the evaporation of spheres. The photographs of the variation in the surface of the sphere were processed on a small microscope with scale divisions of 0.01 mm. Consequently, it was possible to determine with sufficient

accuracy the coordinates of the model contour at different stages of its evaporation. This is illustrated in Figure 4. Besides the experimental points, the figure shows circles whose radius equals that of the initial sphere, but relative to a point situated at a distance from the initial center equal to the displacement of the leading stagnation point of the surface. It is seen from Figure 4 that the experimental points characterizing the front surface of the model at different sublimation times are located near the arcs of the circle of initial radius, plotted by the method described above.

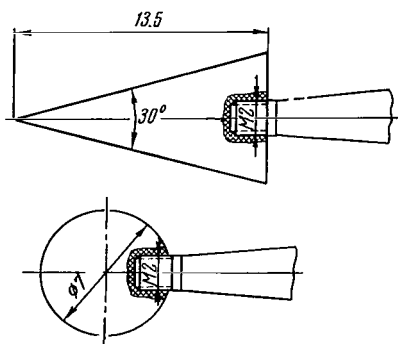


FIGURE 1. Naphthalene samples.

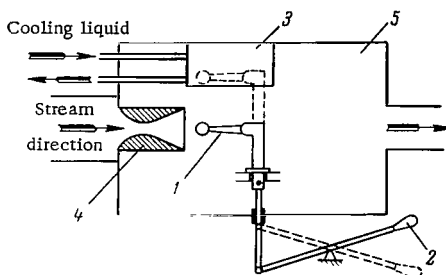


FIGURE 2. Scheme of the mounting and introduction of models in the stream:

1—model; 2—lever for introducing the model in the stream; 3—refrigerant; 4—De Laval nozzle; 5—low-pressure chamber.

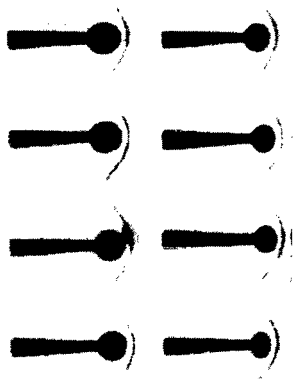


FIGURE 3. Schlieren photographs of the successive stages of the evaporation of naphthalene spherical samples.

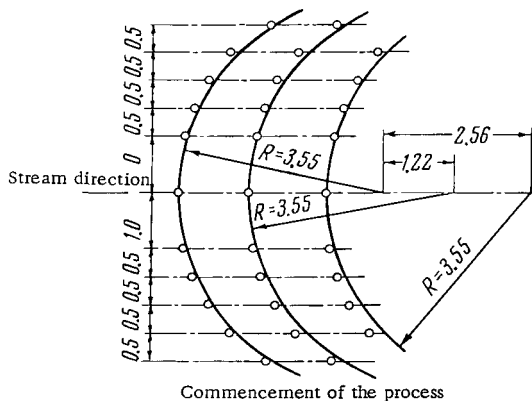


FIGURE 4. Contours of the successive evaporation stages of naphthalene spherical models.

Thus, when a sphere evaporates in a supersonic stream, the front surface of the model conserves a spherical shape with its initial radius. In other words, the front surface evaporates as if the center of a sphere with constant radius (equal to its initial value) moves downstream. A similar pattern was observed for models of 7 and 10 mm diameter and other stagnation temperatures. The radius of the front part of the sphere remained unchanged up to very extensive evaporation. In many experiments the displacement of the leading stagnation point reached 70–85% of the value of the initial radius, without any change in the total curvature of the spherical model surface. Experimental plots of $\Delta h = f(\tau)$ are given in Figure 5, with Δh representing the distance between the leading stagnation point of the model at the initial moment of the process and the stagnation point corresponding to some instant τ during evaporation. The relationship $\Delta t = f(\tau)$ is linear, i. e., for given shape and dimensions of the model the displacement velocity of the leading stagnation point remains almost constant for invariable stream parameters.

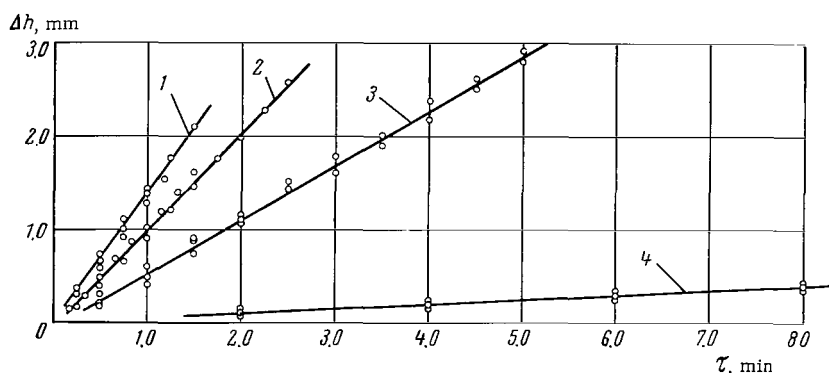


FIGURE 5. Displacement with time of the leading stagnation point of a naphthalene sphere:

1— $T^* = 85^\circ\text{C}$; 2— $T^* = 75^\circ\text{C}$; 3— $T^* = 65^\circ\text{C}$; 4— $T^* = 35^\circ\text{C}$.

Figure 5 shows that the increase in stagnation temperature is accompanied by a sharp increase in the sublimation rate. It is difficult to draw quantitative conclusions about the evaporation kinetics of the back part of the model surface, in view of the influence of the holder on the flow pattern. Nevertheless, the experimental results indicate that the back part of the surface evaporates much slower than the front part. At relatively low stagnation temperatures of the stream the evaporation rate of the front part of the surface is roughly twice that of its back part. This ratio increases from two to five with a rise in stagnation temperature. A comparison of the curves $\Delta h = f(\tau)$ for spheres of 7 and 10 mm diameter, under identical flow conditions (cf. Figure 6) shows that higher displacement velocities of the front point correspond to lower values of the diameter.

Figure 7 shows photographs illustrating the development with time of the evaporation of conical models. These photographs show that the front part of the cone evaporates far more than its back and side parts. The variation in the cone surface during its evaporation in a supersonic air stream was estimated quantitatively by a microscope.

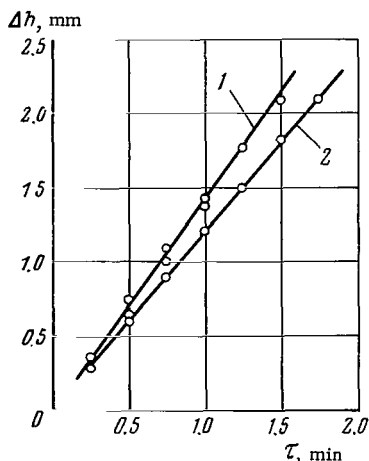


FIGURE 6. Displacement of the leading stagnation point of naphthalene spheres of different initial diameters under identical flows conditions:

1—sphere ϕ 7 mm; 2— ϕ 10 mm.

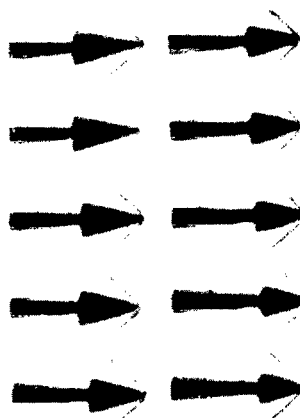


FIGURE 7. Schlieren photographs of the successive stages in the evaporation of conical naphthalene models.

Curves of $\Delta h = f(\tau)$ for conical models are given in Figure 8, where Δh represents the distance between the cone apex at the initial moment of the process and the leading stagnation point at some instant τ of the evaporation. The relationship $\Delta h = f(\tau)$ is linear for spherical models. For conic models a decrease (from 2 to 5 %) with time in the displacement velocity of the leading stagnation point was observed. However, since this decrease was of the same order of magnitude as the mean experimental error, the relationship $\Delta h = f(\tau)$ can also be considered as linear in this case. It follows from Figure 8 that an increase in the stagnation temperature of the impinging stream is accompanied by a sharp increase in the evaporation rate of the conical model. Comparing the curves $\Delta h = f(\tau)$ for the cone and sphere, we conclude that under identical conditions the displacement velocity of the leading stagnation point is much higher for the cone than the sphere. It is characteristic for the evaporation of the conical model that its nose is rounded with time, acquiring the shape of a paraboloid of revolution. In addition, when the stagnation temperature of the stream is low (30°), the initial angle of the model remains unchanged; at higher values of the stagnation temperature (75°) the cone angle increases. Such an increase in cone angle is due to an intense evaporation of the front part of the model surface.

The contours of the successive evaporation stages of the cones for stagnation temperatures of 30 and 75° are shown in Figure 9.

The experimental results on the sublimation of spherical particles in a supersonic stream agree with the conclusions drawn from a theoretical model of the front motion of the surface of evaporating material /1/.

The experimental results on the sublimation of spherically symmetric bodies in a supersonic stream are similar to those for spherical bodies at low subsonic stream velocities /2/. Although the total curvature of the surface of the front and back parts remained constant in the course of the sublimation experiments described in /2/, the total curvature of the

spherical front and back regions varied with time. In addition, both the total surface of the spherical particle studied, and its front and back surfaces, varied linearly with time.

Thus, the results of /2/ are qualitatively similar to our results and can be explained by the front model of the motion of the evaporation surface.

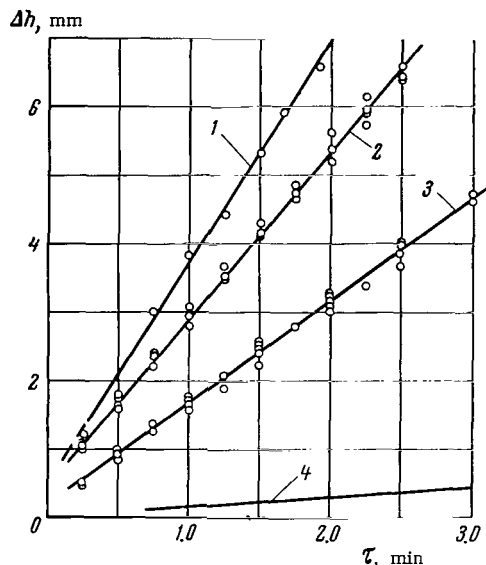


FIGURE 8. Displacement velocity of the leading stagnation point of the cone as a function of time for different stagnation temperatures:

1— $T^* = 85^\circ\text{C}$; 2— $T^* = 75^\circ\text{C}$; 3— $T^* = 50^\circ\text{C}$; 4— $T^* = 30^\circ\text{C}$.

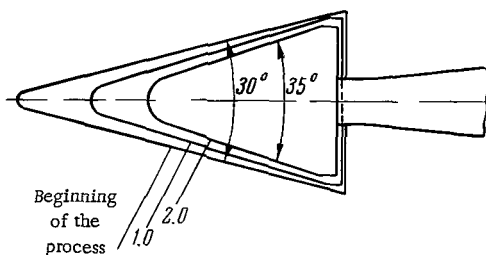


FIGURE 9. Contours of the successive sublimation stages of naphthalene cones for stream stagnation temperatures of 30° and 75°C .

We shall now consider in more detail the motion of the leading stagnation point of conical bodies by the model describing the front process. The following equation was obtained in /1/ for this model:

$$g_\xi^2 + \frac{a}{\alpha} \frac{\Delta V}{H_v} g_\xi + \frac{a}{\alpha} \frac{df}{dM} = 0, \quad (1)$$

where g_{ξ} is the normal displacement velocity of the reaction surface of the material; a is the thermal diffusivity; H_v and ΔV are the first and second scale factors of the reaction surface V ; df/dM is the derivative of the function controlling the reaction kinetics with respect to the quantity of transformed material. The quantity α is defined as

$$\alpha = 1 - \frac{q}{c_v \rho} \frac{dM}{dT} \approx \frac{T_q - T_{cr}}{T_{00} - T_{cr}}, \quad (2)$$

where q is the latent heat of transformation of the material; c_v , ρ are the heat capacity and density; T_{cr} is the critical temperature at which the material transformation starts; T_{00} is the stagnation temperature of the gas flowing around the body. The temperature T_{cr} is defined as the temperature to which the transformed part of the material would be heated in the absence of latent-heat absorption during the reaction. Its value is given by the formula

$$\rho q = c_v \rho (T_q - T_{cr}). \quad (3)$$

If the cone is approximated by a paraboloid of revolution, we have

$$V = z + \frac{br^2}{R^2}, \quad (4)$$

where $r = \sqrt{x^2 + y^2}$; R is the radius at the cone base; b is the distance from the cone apex to the base.

This means that the evaporation of the cone is determined by the velocity of the reaction surface of the material in the direction of the solid residue. The first and second scale factors of the surface V have the form

$$H_v = 1 + \frac{4b^2 r^2}{R^4}; \quad \Delta V = \frac{4b}{R^2}. \quad (5)$$

We shall now consider the displacement velocity of the reaction surface along the z -axis, for which

$$H_v = 1; \quad g_{\xi} = \frac{dz}{dt}. \quad (6)$$

If the mass variation per unit volume obeys the linear law

$$\frac{\partial M}{\partial t} = kM, \quad (7)$$

where k is a proportionality constant, then

$$\frac{df}{dM} = \frac{\partial M}{\partial t} \frac{1}{M}. \quad (8)$$

In a steady state the cone apex is transformed into a sphere. The product $\pi b^2 M g_{\xi} H_v$ can therefore be considered as the flux of transformed mass across a surface of area πb^2 . This product must be equal to $\partial M / \partial t$. Therefore, from (8), we obtain

$$\frac{df}{dM} = -\pi b^2 g_{\xi} H_v. \quad (9)$$

For a cone of unit volume we have

$$\pi R^2 b / 3 = 1; \quad R^2 = 3 / \pi b. \quad (10)$$

With the aid of (10), (9) takes the form

$$\frac{df}{dM} = -\frac{3b}{R^2} g_{\xi} H_v. \quad (11)$$

Allowing for (5), (6), and (11), we can write equation (1) in the form

$$g_{\xi}^2 + \frac{ba}{\alpha R^2} g_{\xi} = 0. \quad (12)$$

When formula (6) is substituted for g_{ξ} ,

$$\frac{dz}{dt} = -\frac{ba}{\alpha R^2}. \quad (13)$$

Integration of this equation yields

$$z = -\frac{ba}{\alpha R^2} t + \text{const.} \quad (14)$$

It is easily shown that the constant has the value b , if the coordinate frame is selected as follows:

$$\begin{aligned} z = 0 &\rightarrow r = R; \\ r = 0 &\rightarrow z = b. \end{aligned}$$

As a result (14) becomes

$$\Delta h = z - b = -\frac{ba}{\alpha R^2} t. \quad (15)$$

The quantity Δh is determined when processing the experimental material. Let the generatrix of the cone have a common point with some section of the paraboloid of revolution formed by a plane passing through the z -axis, and let that point be $z = 0$, $r = R$. Then,

$$\frac{dz}{dr} = -\frac{2b}{R} \approx \text{ctg} (180 - \theta) = \text{ctg} \theta, \quad (16)$$

where θ is the cone semiangle.

With the aid of (16) one can express (15) in the form

$$\Delta h = \frac{a}{\alpha R} \frac{\text{ctg} \theta}{2} t \quad (17)$$

or

$$\Delta h = \frac{a}{R} \frac{\text{ctg} \theta}{2} \frac{T_{00} - T_{cr}}{T_q - T_{cr}} t, \quad (18)$$

if the value of a is replaced by the approximate value in formula (2).

This is the final form of the equation which must be obeyed by the law of variation of the cone length. To use it, we must determine T_{cr} and T_q . Suppose a critical temperature T_{cr} exists below which no sublimation of the material is observed. This temperature corresponds to the melting temperature in metals. For sublimating bodies it also depends on the manufacture of the material. The more friable the material, the lower the sublimation temperature. Its value will be highest for a compressed sublimating material with a polished surface.

In our experiments the samples were made of compressed naphthalene, which hardly sublimated during many hours in a gas-dynamic stream at temperatures around 25°. This temperature was adopted as the critical sublimation temperature. To calculate T_q by formula (3), one must determine the heat of material transformation (i.e., the heat of sublimating 1 g material) as follows. Before a molecule leaves the solid material, it must do work in order to approach the surface. This work is equivalent to the escape of a molecule from the sphere of influence of the other molecules (namely, a distance from the surface larger than the radius of influence of the cohesion forces), and is equal to the heat of fusion. After the molecule has reached the surface, it must do work against the surface forces. Only after these forces have been overcome can it evaporate. This work is identified with the heat of evaporation or sublimation.

Designate by Q the total latent heat of evaporation, by q_s the sublimation heat, and by q_f the heat of fusion. The following equality holds:

$$Q = q_s + q_f. \quad (19)$$

The total latent heat of evaporation of naphthalene is 75 cal/g, and the heat of fusion 35 cal/g. The sublimation heat of naphthalene is therefore $q_s = 40$ cal/g. The temperature difference $T_q - T_{cr}$ is determined by formula (3) and equals 121°K. The thermal diffusivity of naphthalene for mean values of k , c_v , and ρ is $a = 22.6 \cdot 10^{-4} \text{ m}^2/\text{hr}$.

With these values, the motion of the leading stagnation point of the naphthalene conical model is

$$\Delta h = 9.4 \cdot 10^{-4} (T_{00}^* - 298) t. \quad (20)$$

By this formula the tangents of the sublimation lines of naphthalene were calculated; they were also determined experimentally for gas-dynamic streams with different stagnation temperatures. The experimental contours of the front stagnation point are shown in Figure 9. The experimental and theoretical results are given in the following table, where $T_{00, \epsilon}^*$, $T_{00, \tau}^*$ are the experimental and theoretical stagnation temperatures, °C; m_1 is the tangent of the sublimation lines (experiment); m_2 , m_2' are the tangents calculated by (20) for $T_{00, \epsilon}^*$ and $T_{00, \tau}^*$ respectively:

$T_{00, \epsilon}$	$T_{00, \tau}^*$	m_1	m_2	m_2'	$T_{00, \epsilon}$	$T_{00, \tau}^*$	m_1	m_2	m_2'
30	28	0.00027	0.00047	0.00028	75	—	0.00450	0.00475	—
50	—	0.00263	0.00240	—	85	—	0.00570	0.00572	—

Satisfactory agreement is observed between the theoretical and experimental results. Thus, in addition to examining the qualitative laws of sublimation in a gas-dynamic stream, we have established the suitability of the model of front processes for analyzing the complex phenomenon of heat and mass exchange.

Bibliography

1. Eroshenko, V.M., A.V. Morar, and Yu.N. Terent'ev. Frontovoi kharakter poverkhnosti prevrashcheniya veshchestva pri vzaimodeistvii s vneshnei sredoi (Front Nature of the Reaction Surface with the Medium).—In this collection, p. 183.
2. Zhubkov, V.I. Ob isparenii sharikov tverdykh tel v potoke gaza (Evaporation of Solid Spheres in a Gas Stream).—DAN SSSR, Vol. 123, No. 5. 1958.

*Yu. N. Vorontsov, V. M. Eroshenko, A. V. Morar,
Yu. N. Terent'ev*

A METHOD FOR VISUALIZING ISOTHERMAL SURFACES

In recent years, interest has grown in methods of reducing the disintegration of the structure of solids by aerodynamic heating. It is important in this connection to be able to visualize the process of propagation of the heat front in the solid for an invariable surface geometry.

To this end, we conducted a series of experiments in a supersonic wind tunnel, using spherical models made of polytetrafluoroethylene [Teflon] and placed in an air stream with $T^* = 600 - 900^\circ\text{K}$ and $M = 2.5$.

Polytetrafluoroethylene is a dense substance in which amorphous and crystalline zones are uniformly distributed. The degree of crystallinity depends on the manufacturing conditions of the samples and varies between 50 and 70 %. The crystallites of polymers differ however in several respects from the crystals of simple substances. Thus, the transition of the polymer crystallites into an amorphous state takes place over a wide temperature range, without any discontinuous variation in the properties of the substance. The melting temperature of the crystallites is accordingly defined as the temperature above which no crystallites are present in the sample [1]. The melting temperature of the crystallites of polytetrafluoroethylene is 327°C , and the glass point of the amorphous zones is 120°C .

Under normal conditions polytetrafluoroethylene is a white opaque material. When heated above 327°C all the crystallites melt completely and the substance becomes transparent. Up to 415°C polytetrafluoroethylene does not pass from a state of high elasticity to a viscous one. At 415°C polytetrafluoroethylene starts to decompose slowly, the process being accelerated with a rise in temperature. The decomposition of the material in the experiments was negligible, although the stagnation temperature of the stream sometimes reached 900°K ; this was due to the fact that the models were only kept in the stream for a short while (less than 2 min).

The models studied were spheres of 7 mm diameter. Porcelain and brass rods were used as holders. Figure 1 shows the successive stages of the motion of the recrystallization front of the spherical model.

The models were photographed in reflected light with weak background lighting. The experimental conditions were identical for porcelain and brass holders.

Figure 1, a, b show how the holder material affects the propagation of the heat flux from the rear zone into the model. The holder material substantially affected the time necessary for the spherical model to become translucent. The geometry of the moving surface separating the highly elastic region and the region with crystalline zones was not noticeably affected.

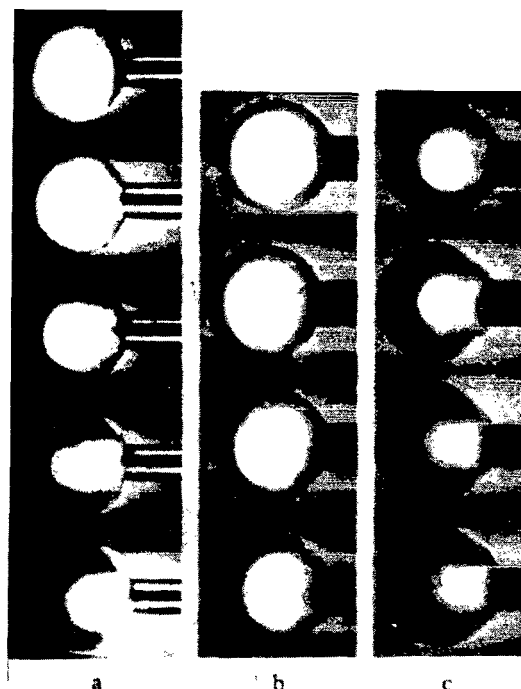


FIGURE 1. Successive stages in the motion of the isothermal translucent surface of polytetrafluoroethylene in spherical models of $\phi = 7$ mm for $M = 2.5$ and $T_{00}^* = 770^\circ\text{K}$:

a—brass holder; b, c—porcelain holder. The time interval between the frames is 10 sec.

In the course of the experiment the relationship between the velocity of motion of the heat front and the gradual translucence of the model material was recorded, as well as the time interval between the introduction of the model in the stream and the instant at which the entire model became translucent. The experimental results are shown in Figures 2 and 3.

Measurements of the radius of the frontal zone of the surface of the translucent heat front (cf. Figure 1) and the analysis of the experimental results (cf. Figure 2) yielded the following information:

the radius of curvature of the isothermal surface of the translucent front remains for a long time constant and equal to the radius of the spherical model;

the velocity of motion of this front surface is linear for a long time;

the radius of the spherical surface of the melting front of the polymer crystallites begins to vary at the same time that the velocity of motion of the leading point of the front begins to deviate from the linear values (cf. Figure 2);

for the brass holder, the displacement velocity of the leading point of the front deviates from the linear law before the radius of the spherical surface of the heat front varies from its constant value. The displacement velocity is more clearly expressed in this case.

It is seen from Figure 3 that for stream stagnation temperatures over the range 600–900°K, the time of complete recrystallization of a spherical polytetrafluoroethylene model varies according to a near-exponential law. At temperatures above 900°K the recrystallization is independent of the stream stagnation temperature, and is determined only by internal processes, i.e., the maximum recrystallization rate.

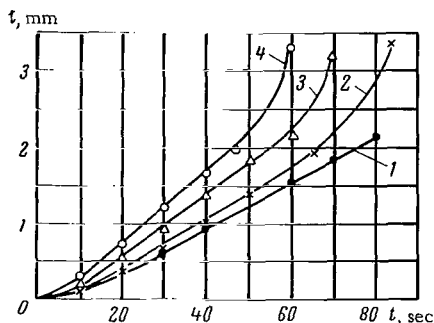


FIGURE 2. Velocity of motion of the isothermal translucent surface in a spherical model for $M=2.5$: 1— $T_{00}^*=763^\circ\text{K}$; 2— 793° ; 3— 813° ; 4— 833° .

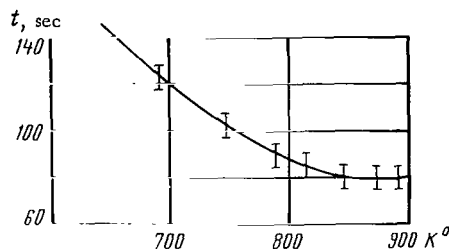


FIGURE 3. Total time taken by a polytetrafluoroethylene sphere to become translucent as a function of the stagnation temperature of the stream.

Near the phase transition point (327°C) there was a plane stationary recrystallization boundary (cf. Figure 3, the left-hand branch of the curve), which assumed a spherical shape as the stagnation temperature increased, and started to move inside the model according to the laws described above. The appearance of a plane boundary at the reaction surface of the material under the conditions of a gas-dynamic flow has also been observed in naphthalene sublimation experiments, but so far this effect lacks a satisfactory explanation.

With the exception of the region affected by the holder (the end of the process), the phase transition proceeds under invariant Gauss curvature of the reaction surface of the material, while the leading point of this surface moves at a constant velocity, the area varying according to a linear law, i.e., the process obeys Sreznevskii's law [2]. The experimental results agree satisfactorily with the conclusions drawn from the theory based on the model of the motion of the front of an isothermal surface, on which the additional processes of material transformation combined with the process of heat equalization take place [3].

The method proposed for visualizing isothermal surfaces is also suitable for bodies of fairly complex configuration and arbitrary law of heat exchange. The method is simple and is useful in calibration experiments when studying the ablation of various substances in gas-dynamic high-enthalpy streams.

Bibliography

1. Chegodaev, D.D., et al. *Ftorplasty (Fluoroethylene Polymers)*.—Moskva, Fizmatgiz. 1960.

2. Sreznevskii, V. Ob isparenii zhidkosti (Evaporation of Liquids).—ZhRfKhO, Vol. 14. 1882.
3. Predvoditelev, A.S. O frontovom protsesse isparenii i sublimatsii sfericheskikh chastits (Front Process of Evaporation and the Sublimation of Spherical Particles).—Trudy Odesskogo Gosudarstvennogo Universiteta, Seriya Fizicheskikh Nauk, No. 7. 1960.

National Aeronautics and Space Administration

WASHINGTON, D. C. 20546

OFFICIAL BUSINESS

**POSTAGE AND FEES PAID
NATIONAL AERONAUTICS AND
SPACE ADMINISTRATION**

040 001 '58 51 3DS 69304 00903
AIR FORCE WEAPONS LABORATORY/WLIL/
KIRTLAND AIR FORCE BASE, NEW MEXICO 87117

ATTN: E. LUD KOPMAN, CHIEF, TECH. LIBRARY